AN IMAGING STUDY OF THE PHOTODISSOCIATION OF OZONE IN THE HUGGINS BAND AND O(^{1}D) REACTION AND DEACTIVATION

A Dissertation

Presented to the Faculty of the Graduate School

of Cornell University

In Partial Fulfillment of the Requirements for the Degree of

Doctor of Philosophy

by

Clarice Agnes Krebs Kelleher

January 2013

AN IMAGING STUDY OF THE PHOTODISSOCIATION OF OZONE IN THE HUGGINS BAND AND O(^{1}D) REACTION AND DEACTIVATION

Clarice Agnes Krebs Kelleher, Ph. D.

Cornell University 2013

Velocity mapped imaging (VMI) is used to study the photodissociation and reaction dynamics in both single and crossed molecular beams. In this dissertation the focus of these techniques is on questions of atmospheric importance but the results also contribute to an understanding of reactions that take place by multiple pathways.

The first part of the dissertation focuses on the dissociation of ozone in the Huggins band. Velocity – mapped images and O(^{3}P$_2$) yield spectra are analyzed to determine the relative O_2 electronic and vibrational populations and to provide an estimation of the rotational population as characterized by a temperature. O_2 images are also obtained to gain insight into the REMPI detection of O_2 and the spectroscopy of the two lowest Rydberg states of O_2, $d\ ^1\Pi_g$ and $C\ ^3\Pi_g$.

The second part of the dissertation describes the development of a crossed molecular beam apparatus. The apparatus allows for the use of VMI techniques for deactivating and reactive collisions with state-selective detection methods. Initial results for the electronic deactivation of O(^{1}D) to ground state O(^{3}P) on collision with O_2 and N_2 are reported. Within the dual-beam apparatus, a delayed detection method is developed to minimize background.

In the final part of the dissertation, the vibrational and rotational distribution of NO from the O(^{1}D) + N_2O reaction is determined through analysis of the NO spectra between 220 – 246nm. An explanation is suggested for the differences in NO

vibrational distribution observed in our apparatus compared to those of others who have also investigated this reaction.

BIOGRAPHICAL SKETCH

The author was born in Harford, NY in 1981 to Michael and Ann Kelleher. In 1984 her brother Philip was born. The author and family lived in upstate New York for most of the author's life and her parents remain there still. Her early education, at Immaculate Conception School and Dryden Public High School, initiated an interest in science. This is especially due to Mrs. Sperry, Mrs. Hickey and Mrs. Michaels. In 2000, she went to college at The College of the Holy Cross, in Worcester, MA where she did undergraduate research with Dr. R. Taylor. She met Charles Ulrich in Worcester, whom she married in 2007. 2004 brought a move back to Ithaca to start graduate school at Cornell University. In 2008, she moved to Atlanta, GA to complete work towards her degree after moving the Houston lab to Georgia Institute of Technology. In 2011, the author and husband, Charles, had a beautiful little girl, Savanna.

To Uncle Michael

To Da

ACKNOWLEDGMENTS

I have been blessed with so many wonderful people in my life who have contributed in many different ways throughout my education.

My family has been supportive and inspirational throughout my education. Charles and Savanna, my loves, have been amazing throughout the whole process. Charles has always supported me, both within the writing process and getting me out of the house to enjoy life. Without his IT support this dissertation would have taken much longer. Savanna reminds me every day how much there always is to learn and love. Your smile makes everything better. I owe so much to my parents who always helped me to believe I could do anything. Their love and support has helped shape me into the person I am. Philip, is the best brother, his artistic influences have helped me to see the world beyond science. Thank you to Nanny and Da, Grandma Ruth and PaPa, and the rest of my family; not many people are as lucky as I am to have such a great family. You have all inspired my life in a unique way and help me to achieve my goals.

Thank you to Paul Houston for his inspiration, guidance and help throughout my degree process. He is an amazing scientist and individual, inspiring me to work hard without losing perspective. Thank you to my committee members, Floyd Davis, Gregory Ezra and Jwoong Park, for their support and discussions. Professor Davis and his research group were especially helpful while I was at Cornell; our joint group meetings were always insightful and fun. Floyd's continued support throughout and since is very much appreciated.

Paul's group past and present has been an invaluable part of the work involved in this dissertation. Mark Lambert taught me a lot about working in a laser lab. I owe much to Jun "Jack" Chen for his knowledge and friendship. Onur Tokel unpacked all

the boxes and made the long hours in the lab more entertaining. My close work with Paul, Jack and Onur made this dissertation possible. Ben and all the previous members have taught me so much and made the lab work more fun.

My friends at Cornell whose special bond in G20 and cooking Thursdays helped me through those first few years of graduate school, I will never forget. Especially Showey without our walks, I do not know where I would be today. Thank you to the close friends I have gained throughout my life including Erica, Amy R, Abby, Amy G, Aimee, Joe, Emily, and many others, you all have helped and taught me so much along the way.

TABLE OF CONTENTS

TABLE OF FIGURES

TABLE OF TABLES

CHAPTER 1

INTRODUCTION

Human nature leads us to be constantly exploring the world around us, both for practical reasons and to satisfy our desire to understand how and why things behave as they do. Two major influences on our life are the sun, our largest source of energy, and the atmosphere, the air we breathe. Therefore, it is natural that we should study the effect of this energy on the molecules and atoms that form our atmosphere. Subjecting a molecule to light can cause an array of results, including breaking bonds, opening new reaction pathways, and internal excitation. The study of such effects can help us to gain a better understanding of the molecule. Since light's interaction with matter is the cause of much of the molecular dynamics and chemical kinetics in our atmosphere, it reasonable to use light to study questions about molecular systems.

1.1 Photodissocitation

Photodissociation results when the light incident on a molecule excites it in a way that allows it to break, or dissociate, into fragments. For example, in the atmosphere ultraviolet light causes ozone to dissociate to O and O_2. Studying a photodissociation event allows one to obtain knowledge about the parent molecule and its photo-products. The results are more complicated than just the identification of the photo-products. Since energy and momentum must be conserved any "extra" energy, not used in the bond breaking process, will be partitioned between the various photo-

fragments. This energy can excite the fragments internally as well as give them translational energy. The energy the products receive will affect how they interact with other atoms or molecules around them.

Our ability to control and observe photodissociation events provides the initial step for understanding our atmosphere. Important aspects of the control include selecting the energy of the initial molecule, and the properties of the light causing the event. Detecting the energy and other properties of the resulting fragments is also a key to understanding what has happened. The development of tools for this control and detection has greatly increased the information that can be gained from a photodissociation event, as can be seen from the following brief history.

The first detailed study of product velocity and angular distributions from a molecular photodissociation event was reported nearly simultaneously by Bush et al.[1] and by Diesen et al.,[2] who used a technique called photodissociation translational spectroscopy. Bush et al.[1] dissociated a molecular beam of Cl_2 with linear polarized light and then detected the Cl atoms with a mass spectrometer. The rotationally and vibrationally cold Cl_2, prepared by the molecular beam source, and the well-defined light photon allowed for a well-defined photodissociation event. Through conservation of momentum and energy, the velocity distribution of the Cl atom was used to determine the internal Cl electronic energy states, and the angular distribution was used to determine whether the dissociation occurred via an absorption dipole that was parallel or perpendicular to the molecular bond.

The development of laser methods to detect products in a state specific manor made it possible to obtain much more information about a system. Two commonly

used techniques are Laser Induced Fluorescence (LIF)[3,4] and Resonance Enhanced Multiphoton Ionization (REMPI).[4,5] In LIF, a laser is tuned to excite, or probe, a particular internal energy state of the molecule of interest, and the fluorescence is then detected from the excited state. The intensity of fluorescence is proportional to the number of molecules in the probed state. REMPI uses a laser to excite a molecule to an excited state, with one or more photons, and then another photon(s) ionizes the molecule. The ions are then detected, and their number is proportional to the number of molecules in the probed state. The benefit of these methods is that they give detailed information about a single state and so with the use of conservation of momentum and energy, the information about the possible partner fragment states can be determined. A limitation is that since only one state is detected at a time the experiment may need to be repeated to detect other states. Since the signal for a single state can be small, it is sometimes not possible to detect ones with low population. A benefit of REMPI over LIF is that is that it is possible to collect every ion, whereas it is not possible to detect all of the fluorescence and REMPI allows for the determination of the mass to energy ratio for the molecule.

If one takes advantage of the Doppler Effect, equation 1, the absorption frequency profile can be used to determine both the speed distribution, which gives rise to the width of the Doppler profile, as well as the angular distribution, which gives rise to the shape of the Doppler profile.

$$\nu = \nu_0 [1 - {}^{v}/_{c}] \tag{1}$$

In equation (1), ν is the frequency of light actually absorbed or emitted, ν_0 is the frequency that would be absorbed or emitted if the molecule were not moving with

respect to the light, v is the relative velocity of the molecule, and c is the speed of light. Obtaining Doppler profiles at a series of laser polarizations of a product molecule with respect to polarization direction of the light that excited the parent molecule can be used to determine whether the parent molecule absorbed light via a dipole parallel or perpendicular to its principle axis.

Since the Doppler profile is probed along a line, it is really a 1D projection of the 3D product sphere.[6,7] In 1987, Chandler and Houston[8] developed an ion-imaging method in which the 2D projection of the entire 3D sphere of one of the photo-products was detected at once. In their experiment Chandler and Houston dissociated CH_3I in a molecular beam and detected the CH_3 (v = 0) product. The CH_3 (v = 0) product can be produced with either the ground state of the iodine atom, I, or an electronically excited state, I*. Reconstruction of the image showed peaks from both channels. The relative population of the channels is proportional to the relative size of the peaks, and the velocity for each channel is based on the distance of the peak from the center of the image and on the measured time of flight for the ion to reach the detector. The angular distribution was also readily available.

A limitation of the initial ion imaging experiments was image "blurring" that occurred because of the finite dissociation volume created by the cross-section of the laser and the molecular beam. Products in this volume having the same velocity arrived at the detector at different places. This "blurring" negatively affects the resolution of velocity of the products. Velocity mapped imaging (VMI) uses electrodes as an electrostatic lens to focus the ions such that all ions of the same velocity reach the detector at the same location.[9,10] Eppink and Parker developed VMI

and demonstrated its efficacy with the detection of O from the dissociation of O_2. The increased resolution can be seen through the clarity of the rings in the O^+ image.

Another improvement in ion imaging was the development of the real-time ion counting method by Chang et al.[11] This method increases the resolution of the images by ignoring low level background and selecting the single maximum pixel for each ion and ignoring neighboring pixels.[11] This method is helpful since it helps overcome the fact that generally a single ion will trigger several pixels around it.

1.2 Vector Correlation

An important aspect to understand the extent of information that can be obtained from studies of photodissociation utilizing methods such as Doppler Profiles and Ion Imaging is the correlation of vectors within the dissociation systems. It is clear that determining the dynamics of a photodissociation event is useful in understanding how the photodissociation works for a specific system, such as obtaining the product distribution of the fragments. This can also be used to aid in determining other details of a system such as the symmetry of the dipole transition moment in the parent molecule, the lifetime of the dissociation, and information about the product(s) not detected. Vector correlations occur within the fragment, between the parent molecule and fragment, as well as between the parent molecule, fragment and lab frame. The correlations can be used to determine the dynamics and other details of a system. More information is available through the vector correlations then from individual vectors.[12-15]

Although there are many vector correlations within a photodissociation event, only the most pertinent for the studies within this dissertation will be discussed here, $\hat{E}$-μ-v, $\hat{E}$-μ-J, v-J, and $\hat{E}$-μ-(v-J). The polarization of the dissociation laser is represented by $\hat{E}$, μ is the transition dipole moment of the parent molecule, v is the recoil velocity of the photofragment, and J is the rotational vector of the photofragment.

The $\hat{E}$-μ-v correlation can be used to obtain information about how the photofragment leaves the parent molecule as well as about the lifetime of the photodissociation. The absorption probability of the parent molecule is proportional to $|\mu \cdot \hat{E}|^2 = \cos^2[\alpha]$, where α is the angle between $\hat{E}$ and μ. Thus, even if the parent molecules are not initially aligned with respect to the lab frame, the dissociating laser preferentially excites those molecules whose rotation brings them into alignment during the laser pulse.[12-15] Figure 1.1 demonstrates an example of what can happen in a diatomic molecule. Generally only one photo-product would be detected at a time through the use of Ion-Imaging or other detection methods to determine v and β. The photo-fragments will have an angular distribution given by equation (2).[12-15]

$$I(\theta) = {}^{1}/_{4\pi}\,(1+\beta P_2[\cos[\theta]]),\ \beta = 2P_2\cos[X]. \qquad (2)$$

θ is the angle, in the lab frame, between $\hat{E}$ and v. X is the angle, in the molecular frame, between μ and v. β is the anisotropic parameter which gives the relationship between μ and v. It will never be above 2, a parallel transition, and never below -1, a perpendicular transition. For a parallel transition v goes in a direction parallel to μ and for a perpendicular transition v goes in a direction perpendicular to μ, assuming rapid dissociation relative to rotation.

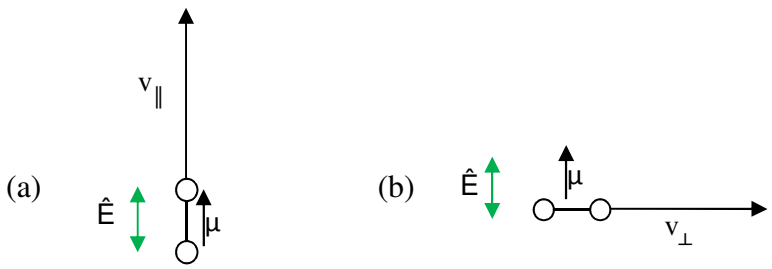

Figure 1.1: The dissociation laser is polarized in the vertical direction ($\hat{E}$) depicted by the green arrows and preferentially dissociates those parent molecules with their μ directed up or down (as these do). (a) Demonstrates a molecule with μ parallel to the molecular bond while for (b) μ is perpendicular to the bond. The fragments then separate traveling the direction v from the parent based on the anisotropic parameter (β) for the fragment. Each photofragment will travel in a different direction based on the type of transition and its relationship with μ. Often with a diatomic molecule the fragments will move parallel (a) or perpendicular (b) compared to μ. The angle between $\hat{E}$ and v will be changing with a $\cos^2$ function based on the preferential absorption. The products will expand in a sphere from the dissociation origin. For (a) a parallel transition β = 2 and the fragments will be preferentially distributed to the north and south poles. For (b) a perpendicular transition, β = -1 and the fragments will preferentially recoil left and right. (v is only shown for one fragment but the other would travel in the opposite direction conserving momentum and energy).

The relationship between μ and v is based on the type of transition that takes place, which is affected by the relationship between the symmetry of the parent molecule and the photo-fragment. It is important to note that the relationship with the lab frame will be lost if the rotation of the parent molecule is faster than the dissociation process.[12-15]

One can see evidence of the $\hat{E}$-μ-v correlation by looking at an image as in Figure 1.2. In this example ozone is dissociated by 285 nm polarized vertically with respect to the image. O(^{1}D) from the dissociation is detected by 2+1 REMPI. As can be seen the strongest part of the signal is centered at the north and south poles.

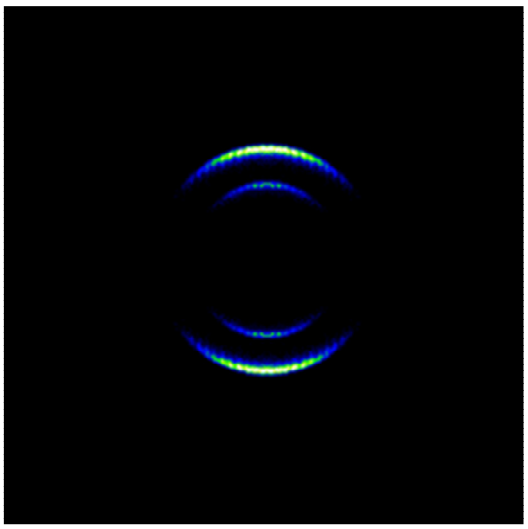

Figure 1.2: $O(^1D)^+$ 2+1 REMPI from the 285 nm dissociation of ozone with vertically polarized light. The rough images have been centered and symmetrized about the x and y axes.

An application of the Ê-μ-v correlation will be demonstrated in Chapter 3 where vertically polarized light is used to dissociate O_3 to create a molecular beam of $O(^1D)$ for deactivation and reaction.

Although less pertinent here, the Ê-μ-J, v-J, and Ê-μ-(v-J) are closely related to the Ê-μ-v correlation and can also be determined through Doppler Profiles or Ion Imaging. Motion within a molecule, such as rotation, caused by photodissociation can also be determined within the lab frame. There is a correlation between Ê-μ-J which relates the photofragment's rotation to the lab frame. For example the intensity of light from LIF changes as a function of polarization which includes a reliance on J that is clearly seen in equation (3).[12,13]

$$I = CS \sum_{k_d k_a k} A_0^{(k)} \epsilon(k_d, k_a, k, 0; \Omega) \omega(k_d, k_a, k; J_i J_e J_f) \quad (3)$$

In equation (3) the sum is over k_d, k_a, and k. C is proportional to population of initial state i in the photo-fragment, the number of molecules that get excited by the probe

laser. S is the line strength of the transition from state i to state e times the line strength from state e to state f. The J's are the rotational quantum numbers of the various states. The k's are the multipole moments associated with absorption and detection photons. For example, for an electronic dipole transition all the k's will be summed for k = 0, 2. Ω comes from the transition that is taking place and is based on the state of the photofragment. $A_0^{(k)}$ are multipole moments, depending on the transition that is occurring. They are coefficients that are combinations of the angular momentum operators J that are present in the molecule. They can be used to determine J for a fragment compared to the parent molecule.[12] The correlation of J to the lab frame can be seen through the emission or absorption of polarized light by the photofragment.

Both the Ê-μ-v and Ê-μ-J correlations relate the fragment with the lab frame, but if the photodissociation event is long compared with the parent molecule rotation or if there is a predissociation step, the correlation to the lab frame is lost. However, as might be supposed based on the previous two correlations discussed, J and v are also correlated within themselves.[12,14] This correlation can be used to obtain information about the fragment and the photodissociation event even when correlation to the lab frame is lost. The correlation depends on the geometry of the parent molecule and dynamics of the photodissociation event.

All of the correlations can be brought together when the correlation to the lab frame is not lost due to rotation of the parent molecule before dissociation. In these cases the correlation Ê-μ-(v-J) can be explained theoretically and determined through experimental processes. The benefit of this is that through the combination of

experiment and theory the relationship between v and J can be determined for the fragment. Their relationship to the parent molecule and to the lab frame is identified as well. This correlation can be approached both classically, for the limiting cases of v perpendicular or parallel to J, and quantum mechanically, for the limiting cases as well as for all angles between v and J.[12-15] It is clear the more information can be gained from utilizing vector correlations within a photodissociation event then without.

1.3 Previous work: Ozone Photodissociation

The developments in photodissociation studies have led to the ability to gain a wealth of knowledge on molecular systems. For practical purposes this can help determine the intricate workings of the atmosphere and how human activities might have an effect on it. For many years it has been known that ozone is an important constituent of the atmosphere, both because its presence in the upper atmosphere protects us from ultraviolet light and because its presence in the lower atmosphere causes smog. Numerous studies of its creation and destruction have been carried out. In 1930, Chapman came up with an initial cycle (1, 2, 3) with (3) being the main pathway for ozone destruction, but this turned out to be too simple.[4,16,17]

$$O_3 + h\nu \rightarrow O_2 + O \quad (1)$$

$$O_2 + O + M \rightarrow O_3 + M \quad (2)$$

$$O_3 + O \rightarrow 2\,O_2 \quad (3)$$

A better picture of the stratospheric ozone cycle is given in Figure 1.3 which takes into account some of the secondary collisions and steps leading to its catalytic destruction that affect the overall O_3 concentration.[17]

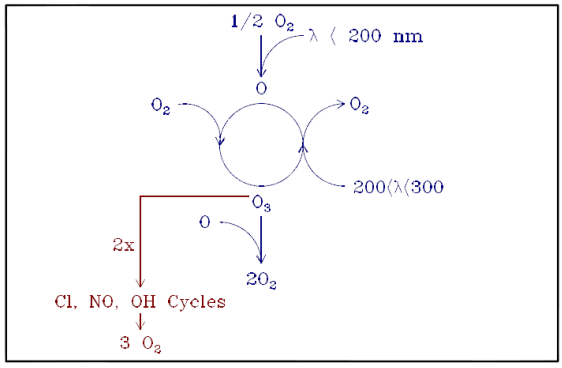

Figure 1.3: The ozone cycle. Figure reprinted with permission from reference 17. Copyright @ 2004 World Scientific Co.

The concentration of ozone in the stratosphere, the ozone layer, is important because it limits how much UV in the 200 – 360 nm range reaches the lower atmosphere and earth's surface. Ozone molecules continually cycle through the mechanism given in Figure 1.3, thus absorbing much of the UV light before it reaches the earth's surface.[17] A benefit of ozone is that it filters out light that otherwise would damage DNA because the peak of DNA absorption is similar to that of ozone.[17,18] Ozone's absorption in the ultraviolet limits the energy of photons that reach the lower atmosphere, thus affecting the photochemistry that can occur there. Any change in the ozone concentration will change the amount of UV reaching the lower atmosphere and surface which makes it important to fully understand the ozone cycle. Ozone in the lower atmosphere is also important but in a negative way because it contributes to pollution.[16,17,18]

The ozone cycle also affects atmospheric chemistry through its photo-fragments. One can see that $O(^1D)$ is an important species since its concentration is closely tied with ozone. $O(^1D)$ is reactive and has a long radiative lifetime,

approximately 150 sec,[15] so it often collides before it radiates. Some collisions lead to the catalytic destruction of ozone while others influence different aspects of atmospheric chemistry. In the stratosphere, $O(^1D)$ is known to react with many molecules including N_2O and OH.[16,17] The reaction of $O(^1D)$ with N_2O, shown below and discussed in more detail in Chapter 4, has a channel (4) that is neutral in the ozone cycle but the other (5) results in the catalytic destruction of ozone.

$$O(^1D) + N_2O \rightarrow O_2 + N_2 \quad (4)$$

$$\rightarrow 2\ NO \quad (5)$$

The production of NO (5) not only destroys the $O(^1D)$ but then can go on to react with ozone, causing the catalytic destruction of ozone.[16,17] For practical purposes, understanding effects of human actions on the atmosphere is important. A clear example of this is the studies of the effect of CFC emission, initially determined by Molina and Rowland.[19] Further studies of atmospheric chemistry related to ozone helped to bring about an understanding of the dangers of releasing CFCs into the atmosphere and prompt regulation of their emission. Beyond their part in the ozone cycle, the excited states of O_2 ($a^1\Delta_g$) and ($b^1\Sigma_g^+$) are important for atmospheric chemistry in their own right as they contribute to the airglow of the atmosphere of Earth, Venus and Mars. The major atmospheric source of the excited O_2 in the daytime is the UV dissociation of ozone. Excitation from the transfer of energy from collision of ground state $O_2(X\ ^3\Sigma_g^-)$ with $O(^1D)$ also contributes.[20]

Determining products and their respective yields from ozone dissociation is the first step in understanding the details of the ozone cycle. Previous studies examining ozone dissociation, both in the main Hartley band[16,17,21,22] and the Huggins

band,[16,22,23,24-36] have led to detailed information about the photodissociation system, but they have also raised new questions.

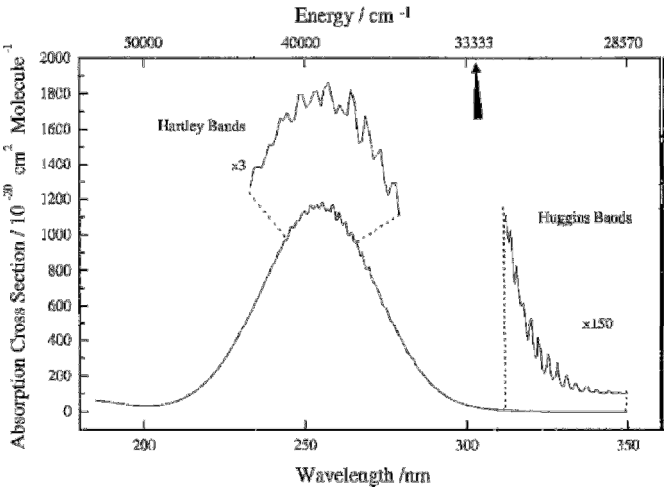

Figure 1.4: The UV absorption of ozone in the Hartley and Huggins band at 226 K. Figure reprinted with permission from reference 24. Copyright JCP 2001, American Institute of Physics.

Absorption via the $^1B_2 - {}^1A_1$ absorption transition in the Hartley band (200 – 310 nm), shown in Figure 1.4, results in the dissociation to the two main spin-allowed channels.[16]

$$O_3 \rightarrow O_2 (X^3\Sigma_g^-) + O (^3P) \quad (6)$$

$$O_3 \rightarrow O_2 (a^1\Delta_g) + O (^1D) \quad (7)$$

The ratio between the two is 0.9:0.1 in favor of the singlet channel (7). The spin allowed singlet channel (6) comes from a direct dissociation while the triplet channel (7) from a curve crossing in the exit channel.[25] The production of $O(^1D)$ in this range will be used in Chapters 3 and 4 to create $O(^1D)$ in a molecular beam to study its deactivation and reaction.

Absorption in the Huggins band (310 – 360 nm), also shown in Figure 1.4, although less efficient than the Hartley band, is still important and complicated. It

may be particularly important in the troposphere where the shorter UV wavelengths have been absorbed by O_2 and O_3 higher in the atmosphere.[25] Ozone absorption in the Huggins band has diffuse vibrational structure which has several assignments.[24,28-31] It leads to dissociation through the ground state channel, (6) from above, and the spin – forbidden channels 8, 9 and 10. There is still some question as to the mechanisms of dissociation in this band, whether it is to the same upper state as the Hartley band[16,30,31] or to another, 2^1A_1.[24]

$$O_3 \rightarrow O_2\,(a^1\Delta_g) + O(^3P) \qquad (8)$$

$$O_3 \rightarrow O_2(b^1\Sigma_g^+) + O(^3P) \qquad (9)$$

$$O_3 \rightarrow O_2(X^3\Sigma_g^-) + O(^1D) \qquad (10)$$

This complexity of the system has been demonstrated by several groups through studies of the yields of the various products. $O(^1D)$ and $O(^3P)$ yield have been studied[24-40] with focus being on the $O(^1D)$ since there is discrepancy in the fall off region and it is so important atmospherically. Production of $O_2(a^1\Delta_g)$ has been studied and often compared with $O(^1D)$ yield.[33-38] It appears that from 310 – 319 nm there is a transition range in which the singlet channel (7) is still produced from vibrationally excited O_3 demonstrated by the temperature dependence of the $O(^1D)$ production.[33-37] At wavelengths of 320 nm and longer this temperature dependence decreases but $O(^1D)$ is still produced at a yield of approximately 10%, suggesting the presence of channel (10). The yield of $O_2(a^1\Delta_g)$ has been shown to have a dependence on wavelength and temperature that is similar to $O(^1D)$. Time-of-flight studies have been done in this region[34-38] for $O_2(a^1\Delta_g)$ and $O(^1D)$[38] which show peaks at the proper kinetic energy to come from channels (8) and (10), respectively. Denzer et al.[38] also

saw evidence that the spin-forbidden channel increasing with respect to the spin-allowed channel when the detection was on resonance with an ozone absorption peak. O'Keeffe et al.[26] were the first to observe channel (4) through the detection of $O_2(b^1\Sigma_g^+)$. They also detected $O(^3P)$ from ozone photolysis in the 310 nm to 335 nm range. At a single wavelength, 322.64 nm they obtained the internal energy distribution of the O_2 fragments from ozone photolysis from the core-sampled velocity release profile of the $O(^3P_0)$ fragment. They observed three peaks, Figure 1.5, which can be accounted for by channels 6, 8, and 9 with the highest relative population being associated with $O_2(a^1\Delta_g)$.[26]

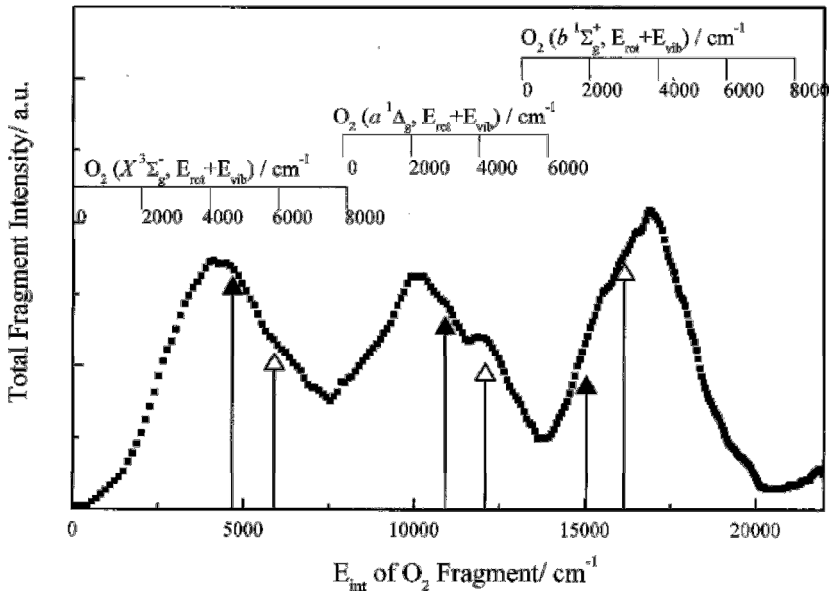

Figure 1.5: The experimental intensity as a function of internal energy distribution of O_2 from the TOF signal of $O(^3P_0)$ from Ozone dissociation at 322.64 nm. The ladders indicate the calculated energy of the O_2 electronic states partnered with $O(^3P_0)$ The opened and closed arrows represent the most probable value for the rotational energy distribution for the fragment for v = 1 and v = 0, respectively. Figure reprinted with permission from reference 26. Copyright JCP 1999, American Institute of Physics

The Donovan group also saw evidence, through $O(^3P_0)$ time-of-flight (TOF) studies, that the ratio of the relative yield of channels 6, 8, and 9 changed based on whether the ozone absorption was resonant with a vibrational band or not. Their findings indicate that a different mechanism may be responsible for dissociation leading to $O_2(b^1\Sigma_g^+)$ compared with $O_2(X\ ^3\Sigma_g^-)$ or O_2 $(a^1\Delta_g)$.[26]

Horrocks et al.[39] used time-of-flight mass spectroscopy and REMPI to measure the translational anisotropy and rotational angular momentum orientation of $O_2(a^1\Delta_g)$ 301 – 311 nm. They found the anisotropy parameter, β, depended both on the rotational state probed and the photolysis wavelength. The $O(^1D)$ anisotropy as a function of wavelength was also determined[40] from 298 – 320 nm. For both $O_2(a^1\Delta_g)$ and $O(^1D)$, β is found to decrease as the photolysis approaches the limit of the spin - allowed channel (2).

Recent calculations to aid in understanding the experimental results of the $O(^1D)$ yield have been reported by Grebenshchikov et al.,[31] with the main focus being the spin - allowed production channel. These findings, based on a new PES described for the ^1B state of ozone,[30] support the ^1B state being the upper state of the Huggins band absorption. Production of $O(^1D)$ from the $O(^1D) + O_2(a^1\Delta_g)$ channel extends beyond the 310 nm due to thermal excitation of the ozone ground electronic state (X) vibrational modes, denoted as $(\nu_1,\nu_2,\nu_3)_X$. At the shorter wavelengths, 310 – 320 nm, the yield is mainly due to one quantum of excitation in the antisymetric stretch (ν_3) with some contribution from one quantum in the symmetric stretch (ν_1). At longer wavelengths two quanta of initial excitation are needed, mainly originating from the $(0,0,2)_X$ state followed by the $(1,0,1)_X$ state and least from $(0,0,2)_X$. The bend mode

plays only a minor role.[31] The shorter wavelengths agree well with experiment but after 320 nm the experimental work shows minimal temperature dependence, which suggests minimal dependence on the initial excitation of ozone above that wavelength. Discussion of similar calculation regarding the $O(^3P)$ channels are currently underway with Dr. Grebenshchikov.

Ozone photodissociation dynamics are interesting and practical to study so the focus of this dissertation will be its dissociation and detection of the products. Despite many studies of the various states produced from ozone photolysis there are still questions as to the relative populations produced in the various channels in the Huggins band. Chapter 2 looks at the dissociation and the resulting relative population of O_2 states in the 321 – 329 nm range of the Huggins band. The results from the population analysis and O_2 ion-images from dissociation are then used to help give insight into portions of the O_2^+ yield spectra that are not well known.

The later parts of this thesis, Chapters 3 and 4, will discuss what happens to the fragments created from photodissociation and how we can use the information about the photodissociation to control and learn about deactivating or reaction collisions. Chapter 3 will focus on using crossed molecular beams for collision experiments to study the deactivation of $O(^1D)$ by other small atmospheric molecules, specifically, N_2 and O_2. Chapter 4 will focus on reactive collisions with a study of $O(^1D) + N_2O$ reaction.

Chapter 4 is based on previously published work and was a collaborative project within the group. It is reprinted with permission from O. Tokel, J. Chen, C. K.

Ulrich, and P. L. Houston, *J. Phys. Chem. A*, **114**, 11292 (2010).

References

1) G.E. Busch, R.T. Mahoney; R.I. Morse, and K. R. Wilson, *J. Chem. Phys.* **51**, 449 (1993)
2) R.W. Diesen, J.C. Wahr and S.E. Adler, *J. Chem. Phys*. **50**, 3635 (1969)
3) R. N. Zare and P. J. Dagdigian, *Science*, **185**, 739 (1974)
4) Houston, P.L. *Chemical Kinetics and Reaction Dynamics,* 2001, McGraw-Hill Companies Inc. New York
5) M.N.R. Ashfold and J.D. Howe, *Ann. Rev. Phys. Chem.* **45**, 57 (1994)
6) J. L. Kinsey, *J. Chem. Phys.* **66**, 2560 – 2565 (1977)
7) R. N. Zare and D. R. Herschbach, *Proc. IEEE.* 173 – 182 (1963)
8) D.W. Chandler, and P.L. Houston, *J. Chem. Phys.* **87**, 1445 (1987)
9) A. Eppink and D.H. Parker, *Rev. Sci. Instr.* **68**, 3477 (1997)
10) D.H. Parker and A.T.J.B. Eppink, *J. Chem. Phys.* **107**, 2357 (1997)
11) B.Y. Chang, R.C. Hoetzlein, J.A. Mueller, J.D. Geiser, and P.L. Houston, *Rev. Sci. Inst.*, **69**, 1665 (1998)
12) P.L. Houston, *J. Phys. Chem.* **91**, 5388 (1987)
13) R.N Dixon, *J. Chem. Phys.* **85**, 1866 (1986)
14) G. E. Hall and P.L. Houston, *Ann. Rev. Phys. Chem.* **40**, 375 (1989)
15) P.L. Houston, *Accounts of Chem. Res.* **22**, 309 (1989)
16) Okabe, Hideo, Photochemistry of Small Molecules. Wiley-Interscience Publication, 1978, New York

17) Houston, Paul L, “Photodissociation Dynamics of Ozone in the Hartley Band,” in "Advanced Series in Physical Chemistry", "Modern Trends in Chemical Reaction Dynamics," X. Yang and K. Liu, editors, Volume 14, Part II. World Scientific Co., 2004, Singapore

18) J. R. Wiesenfeld, *Acc. Chem. Res.* **15**, 110 (1982)

19) M. J. Molina, and F. S. Rowland, *Nature* **249**, 810 (1974).

20) R.P. Wayne, *J. of Photochem.* **25**, 345 (1984)

21) W. N. Hartley, *J. Chem. Soc., Trans.*, **39**, 57 (1881)

22) Y. Matsumi and M. Kawasaki, *Chem. Rev.* **103**, 4767 (2003)

23) W. Huggins and Mrs. Huggins, *Proc. Roy. Soc. London*, 216 – 217 (1890)

24) P. O’Keeffe, T. Ridley, K. P. Lawley, and R. J. Donovan, *J. Chem. Phys*. **115**, 9311 (2001)

25) P. O’Keeffe, T. Ridley, S. Wang, K. P. Lawley, and R. J. Donovan, *Chem. Phys. Lett.* **298**, 368 (1998)

26) P. O’Keeffe, T. Ridley, K. P. Lawley, R. R. J. Maier, and R. J. Donovan, *J. Chem. Phys*. **110**, 10803 (1999)

27) P. O’Keeffe, T. Ridley, H. A. Sherd, K. P. Lawley, R. J. Donovan, and B. R. Lewis, *J. Chem. Phys.* **117**, 8705 (2002)

28) D. H. Katayama, *J. Chem. Phys.*, **71**, 815 (1979)

29) J. A. Joans, *J. Chem. Phys.*, **101**, 5431 (1994)

30) Z-W Qu, H. Shu, M. Tashiro, and R. Schinke, S. C. Farantos, *J. Chem Phys.* **120**, 6811 (2004)

31) S. Y. Gerbenshchikov, and S. Rosenwaks, *J Phys. Chem.* **114**, 9809 (2010)

32) K. Takahashi, M. Kishigami, N. Taniguchi, Y. Matsumi and M. Kawasaki, *J. Chem. Phys.* **106**, 6390 (1997)

33) G.E. Hall, N. Sivakumar, P.L. Houston, and I. Burak, *Phys, Rev. Let,* **56**, 1671 (1986)

34) S. M. Ball, G. Hancock, I. J. Murphy, and S. P. Rayner, *Geophys. Res. Lett.* **20**, 2063 (1993)

35) S. M. Ball, G. Hancock, and F. Winterbottom, *Farad. Disc.* **100**, 215 (1995)

36) S. M. Ball and G. Hancock, *Geophys. Res. Lett.* **22**, 1213 (1995)

37) S. M. Ball, G. Hancock, J. C. Pinot de Moira, C. M. Sadowski, and F. Winterbottom, *Chem. Phys. Lett.* **245**, 1-6 (1995)

38) W. Denzer, G. Hancock, J.C. Pinot de Moira, P. L. Tyley, *Chem. Phys.* **231**, 109 (1998)

39) S. J. Horrocks, G. A. Ritchie, T. R. Sharples, *J. Chem. Phys.* **126**, 044308 (2007)

40) S. J. Horrocks, P.J. Pearson, G.A. Ritchie, *J. Chem. Phys.* **125**, 133313 (2006)

41) G. Hancock, S. J. Horrocks, P. J. Pearson, G. A. D. Ritchie, and D. F. Tibbetts, *J. Chem. Phys.* **122**, 244321 (2005).

CHAPTER 2

OZONE PHOTODISSOCIATION AND O_2 2+1 REMPI DETECTION

2.1 Experiment

Ozone seeded at ~ 1% in Helium was expanded in a skimmed molecular beam and dissociated at wavelengths between 321 – 329 nm. The $O(^3P_2)$ and O_2 products from this dissociation were then detected by 2+1 resonance-enhanced multiphoton ionization (REMPI), resulting in yield spectra and velocity mapped images at several wavelengths for each product.

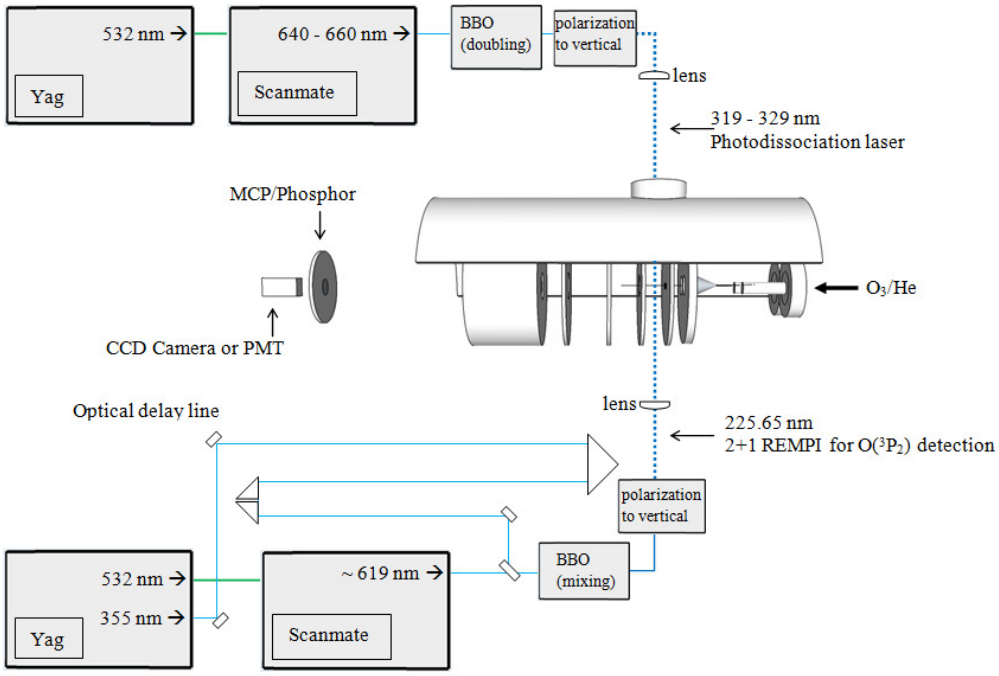

Figure 2.1: A top view of the interaction chamber and laser setup. The chamber is enlarged with respect to the rest of the diagram for ease of viewing. The nozzles are vertically parallel with each other and the nozzles, electrodes, and molecular beam path are centered within the chamber and with respect to the detector.

Ozone, produced in a commercial ozone generator (LG – 7, CD Laboratory) and stored in a trap on silica gel at -78 C, was carried by ultra-high purity Helium (99.999%, Airgas) at a backing pressure of 2 atm. The mixture was supersonically expanded through a nozzle and skimmer into the interaction region, defined as the region between a high voltage repeller and an extractor electrode. One beam of the dual beam time-of-flight mass spectrometer apparatus shown in Figure 2.1 and described previously[1,2] was used for the experiment. In the interaction region, the ozone was crossed perpendicularly by one or two lasers, used for dissociation and detection of O_2 or $O(^3P_2)$. The voltages of the repeller and extractor were set to allow the resulting ions to fly through the center holes of two grounded electrodes and a field-free flight tube to a position-sensitive dual plate MCP/Phosphor set up, to be detected by a PMT, for the spectrum, or by a CCD camera, for velocity mapped images. As the ions moved from the dissociation point to the detector they expended according to the velocity they received from the dissociation. The detector was gated to allow for the detection of either O or O_2 ions based on the time-of-flight of each.

The ozone was dissociated by the doubled light of a Nd:Yag laser (Spectra Physics GCR 230) used to pump a tunable dye laser (Scanmate OPPO). Approximately 2-3 mJ/pulse of 321 – 329 nm light was focused by a 25-cm focal length lens to the center of the ozone beam. For the O_2^+ yield spectra and O_2 ion images this same laser was simultaneously used for the 2+1 REMPI of the O_2, which proceeds through the O_2 $d^1\Pi_g$ or $C^3\Pi_g$ states from O_2 $X\ ^3\Sigma_g^-$, $a^1\Delta_g$, or $b^1\Sigma_b^+$.[3-10] For the O_2 spectrum, the laser was scanned in 0.002 nm steps at a rate of one step per 60 shots at 10 Hz. For the images, the laser was held at the wavelength of interest.

$O(^3P_2)$ was detected by 2+1 REMPI, via the $O(3p^3P_2 \leftarrow\leftarrow 2p^3P_2)$ transition,[12] with 1 mJ/pulse of 225.65 nm light. For $O(^3P_2)$ detection a second laser pulse, focused with a 10-cm focal length lens, intersected the molecular beam parallel to but counter propagating with the first, arriving approximately 5 ns after the dissociation laser. For the probe laser, 25 mJ/pulse of 355 nm from the 3rd harmonic of a Nd:Yag (Spectra Physics GCR 270), was mixed in a BBO crystal with 15 mJ of approximately 619 nm from a tunable dye (R620) laser (Scanmate 2E) pumped by the 532 from the same Nd:Yag laser. For the $O(^3P_2)$ spectrum, the dissociation laser was scanned and the second laser was held at the maximum of the $O(^3P_2)$ REMPI peak. For the $O(^3P_2)$ images the dissociation laser was held at the wavelength of interest while the overlapping probe laser was scanned to cover the Doppler width of the $O(^3P_2)$ detection peak.

2.1.1 O_2 REMPI detection

Two extensively studied wavelengths of ozone dissociation, 266 nm and 298 nm, were used confirm that O_2 excited states were being detected. Both 266 nm and 298 nm dissociate ozone in the Hartley band resulting in 90% $O_2(a^1\Delta_g)$. The resulting spectra were compared with Morrill[3], and simulated in Pgopher.[12]

The O_2 $(d^1\Pi_g\ v=1 \leftarrow\leftarrow a^1\Delta_g v=0)$[3] transition has previously been identified within our experimental range. The ozone molecular beam in the apparatus described above was dissociated with 298 nm vertically polarized light and then 5 – 10 ns later was crossed with the 329.32 – 332.12 nm for the O_2 REMPI detection, obtained from the same laser as above. The 298 nm light was obtained by doubling the output of a

tunable dye laser (Spectra Physics Quanta Ray PDL-2) pumped by the frequency doubled output of a Nd:Yag laser (Spectra Physics GCR). The 298 nm light was focused by a 25-cm focal length lens. An O_2^+ yield spectrum was obtained where the 329 – 332 nm laser was scanned in 0.002 nm steps at a rate of one step per 60 shots at 10 Hz while 298 nm was held at a constant wavelength.

For the other transitions, O_2 ($d^1\Pi_g$ v=2 $\leftarrow\leftarrow$ $a^1\Delta_g$v=0)[3] and O_2 ($d^1\Pi_g$ v=4 $\leftarrow\leftarrow$ $a^1\Delta_g$v=1), a similar experiment was performed but with the dissociation laser at 266 nm and detection either at 318.75 – 324.75 nm or 310.44 – 321.74 nm, respectively. The 266 nm light was obtained from the 4th harmonic of a Nd:Yag laser (Spectra Physics GCR) and reduced with an iris to a 3 mm diameter and approximately 2 mJ/pulse.

2.1.2 Sources of Experimental Background

The $O(^3P_2)$ images can have a background from ozone dissociation by the probe laser alone. This background was only significant when the dissociation laser (321 – 329 nm) did not have enough power to dissociate all of the ozone in the intersection region of the molecular and laser beams, such as dissociation on very small peaks in the O_2^+ spectrum. This background only minimally affects the images since the biggest peak from the 226 nm dissociation of O_3 is slower than the peaks from the 321 – 329 nm dissociation, as shown in Figure 2.2. The area that does overlap has small enough intensity to not play a role.

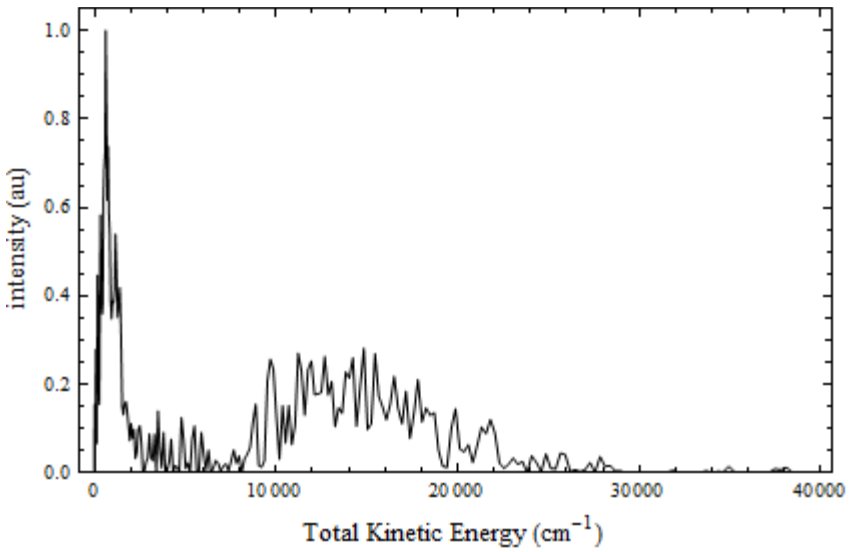

Figure 2.2: Total Kinetic Energy plot of the O($^3P_2$) from the 225.65 nm dissociation of O_3

The other source of background is unavoidable O_2 in the beam resulting from the O_3 generation process. This background does not affect the O($^3P_2$) images and spectra but can affect the O_2 images and spectra. All of this O_2 should be in $O_2(X\ ^3\Sigma_g^-)$ v = 0 and have no velocity component perpendicular to the beam, which means peaks from this can appear in the spectra but in the images it will only be a spot in the center.

2.1.3 Calibrating Spectra and Imaging

The spectrum and image wavelengths from our dissociation laser were shifted to vacuum wavelength based on calibration with two known Xe lines. Xenon (Research grade purity 99.995%, Airproducts) was introduced into the molecular beam and ionized by 3+1 REMPI at 320.450 nm and 323.575 nm.[11,12]

The magnification factor for the experimental set up was determined for conversion of pixels to millimeters in the images. O_2 (99.997% purity, Matheson

Trigas) was introduced into the molecular beam. The 225.65 nm light was used to dissociate it and ionize $O(^3P_2)$ by 2+1 REMPI. The total kinetic energy distribution, Figure 2.3, was compared to literature values[13] to determine the correct magnification factor for the apparatus at the current voltages.

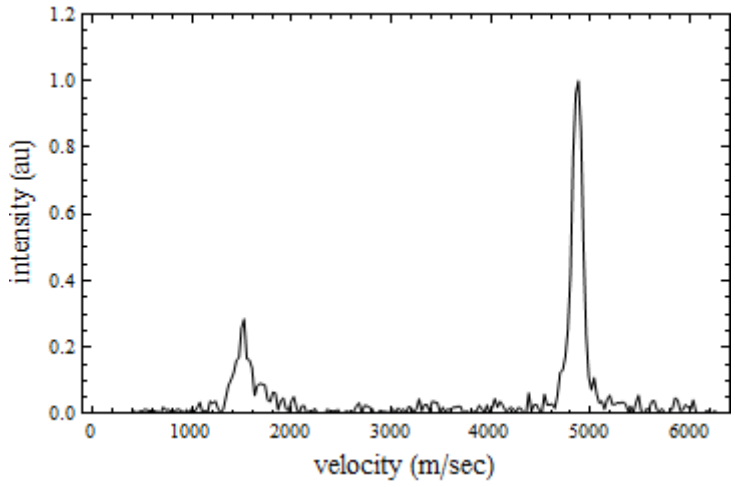

Figure 2.3 2+1 REMPI signal of $O(^3P_2)$ image from the 225.65 nm dissociation of O_2. This uses a magnification factor of 13.45.

A second experiment was also used to check the magnification factor. An image of the "background" $O(^3P_2)$ from O_3 dissociation at 226.65 nm was compared with literature values.[14]

2.2 Image Analysis

All of the resulting images needed initial conversion to a total kinetic energy distribution. The images were first analyzed in BASEX[15] to obtain the speed distribution of the reconstructed 3D image from its 2D projection. They were then converted to velocity using the measured flight time and the magnification factor of

the apparatus. Finally using conservation of energy and momentum, the velocity was converted to total kinetic energy for the dissociation based on the following equations.

$$KE = \frac{1}{2} m_O {v_O}^2 + \frac{1}{2} m_{O_2} {v_{O_2}}^2$$

$$m_1 v_1 = m_2 v_2$$

The anisotropy parameter, β_2, was calculated for the peaks in the images, which are associated with O_2 states, based on the following equation.

$$I(r,\theta) = C[1 + \beta_2 P_2(Cos\theta)]$$

BASEX was used to calculate β for each pixel of the image. This data was then used to determine the average β for each peak in the images, often associated with a specific O_2 state. At low signal intensity there is large error in the calculated β so a weighted average was taken to observe the change in β over the course of the TKE. The following is an example for a single image of how this was done.

First β is calculated as a function of velocity. Grid lines with pixel number are used to determine the β associated with each peak, ignoring the β values where there is no or only background signal, as seen in Figure 2.4.

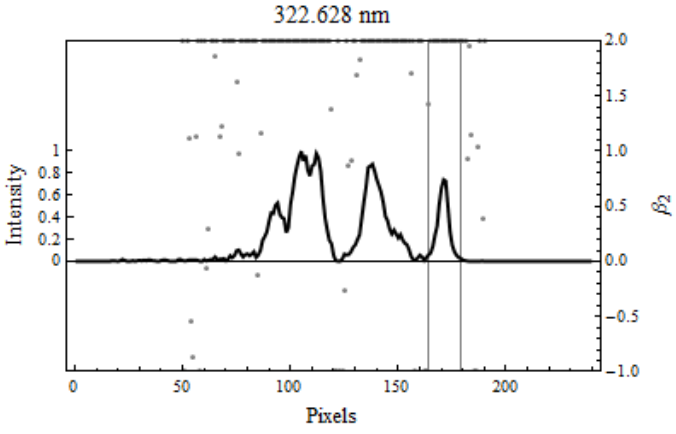

Figure 2.4 A plot of β values per pixel superimposed with the image intensity plot per pixel

The β values where there is little or no signal are unreliable and so were not shown in the figure. The β values within the gridlines for each peak are then averaged to obtain the β for the peak. In some cases, for example if a peak has two distinct parts both the average β for the whole peak and the two β's were reported separately for comparison. Figure 2.5 is an example of plotting the moving average (dashed line) of the β values, demonstrating the change over the course of the image.

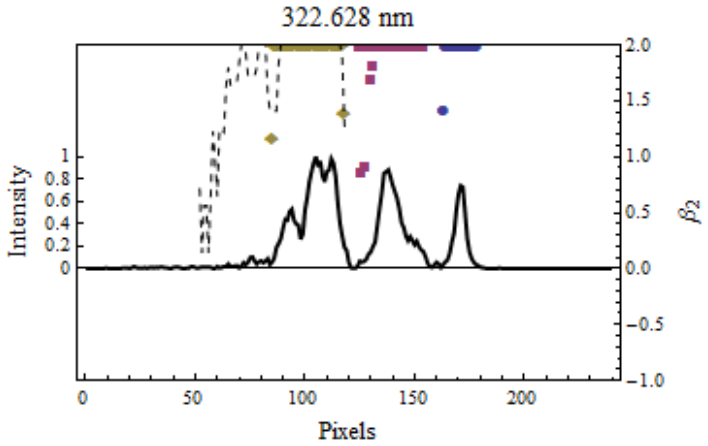

Figure 2.5: This is a plot of the signal intensity (solid line) the weighted average β (dashed lines) and the segments averaged for the reported β (colored points are used for the β values. A different color is used for each β, βa (•), βb (■), βc (◆))

The average β values for each peak are reported in the results section. Plots including the image along with the moving average and the per pixel β for each peak are in Appendix A.

2.3 O(^{3}P) image analysis

The relative O_2 electronic and vibrational populations were determined by fitting the TKE distributions from the images of the sibling O($^3P_2$) products based on

the following equation for the energy and on user entered populations for the vibrational states.

$$KE = E_{hv} - D_0(O_2 - O) - T_{O_2}(v) + ZPE_{O_2} - F_{vO_2}(J) - E_{O(^3P_j)}$$

E_{hv} is the energy of the dissociation photon. D_0 (O_2-O) is the energy in the dissociation of $O_3 \rightarrow O(^3P_2) + O_2(X^3\Sigma_g^-)$.[14,16] T_{O_2} (v) and F_{vO_2} (J) are the internal energy of the O_2 molecule[17-19] and $E_{O(^3P_j)}$ is the internal energy of the O. For $O(^3P_2)$ the E_O is zero. The fit to the images was made by summing a series of Gaussians each representing one O_2 electronic, vibrational and rotational state, where the height of the Gaussian is based on the population, the center energy is based on the energy of the O_2 state, and the width is based on experimental factors, including the line width of the laser and the inherent blurring in the imaging process.

$$\sum_{v=0}^{vXmax}\sum_{J=0}^{100} populationX[v] * e^{-\frac{(x-energyX[v,J])^2}{2*\left(\frac{1+(instrumental\ function*energyX[v,J]}{2*\sqrt{2*Ln2}}\right)^2}}$$

$$+ \sum_{v=0}^{vamax}\sum_{J=0}^{100} populationa[v]$$

$$* e^{-\frac{(x-energya[v,J])^2}{2*\left(\frac{1+(instrumental\ function*energya[v,J]}{2*\sqrt{2*Ln2}}\right)^2}}$$

$$+ \sum_{v=0}^{vbmax}\sum_{J=0}^{100} populationb[v]$$

$$* e^{-\frac{(x-energyb[v,J])^2}{2*\left(\frac{1+instrumental\ function*energyb[v,J]}{2*\sqrt{2*Ln2}}\right)^2}}$$

In the above equation each "energy" function is the KE function given in the previous equation, with T_{O_2} being the energy for the given O_2 state, O_2 ($X\ ^3\Sigma_g^-$), $O_2(a^1\Delta_g)$ or $O_2(b^1\Sigma_g^+)$ respectively. The "instrumental function" in the equation is to account for the band-width of the laser and error within the imaging process, which gave a 10 % error in energy.

$$populationX[v] = \left(\frac{popX_v}{total\ v\ population}\right)(2 + J + 1)\left(\frac{\theta_{Xrot}}{T_{Xrot}}\right)e^{-\frac{(J*(K+1))\theta}{T_{Xrot}}}$$

The fitting assumed that all rotational distributions could be treated as Boltzmann distributions characterized by a temperature. The "population" is then specified by a combination of a rotational temperature and user provided vibration and electronic factors, specified as the fraction of the total vibrational or electronic population. Vibrational levels were included from v = 0 to the maximum v energetically allowed by the reaction for each electronic state. Within each vibrational level, rotational levels from J = 0 – J = 100 were included and a rotational temperature of 500 K was assumed. Initially several rotational temperatures were checked and 500 K resulted in the best fit. The entire fit amplitude was also multiplied by a constant to scale it to the image. Finally, the equations for each vibrational state, for each electronic state and for the sum of all the curves were integrated to find the "area under the curve" such that each reported electronic population is the area under its section of the graph divided by the area under the fit for the entire plot and each reported vibrational plot is the area under its section divided by the area under the fit for the electronic state.

An Example of determining the relative O_2 populations from an O($^3P_2$) Image:

The fraction for the various vibrational populations for the three O_2 electronic states are adjusted to the best fit to the image, Figure 2.6.

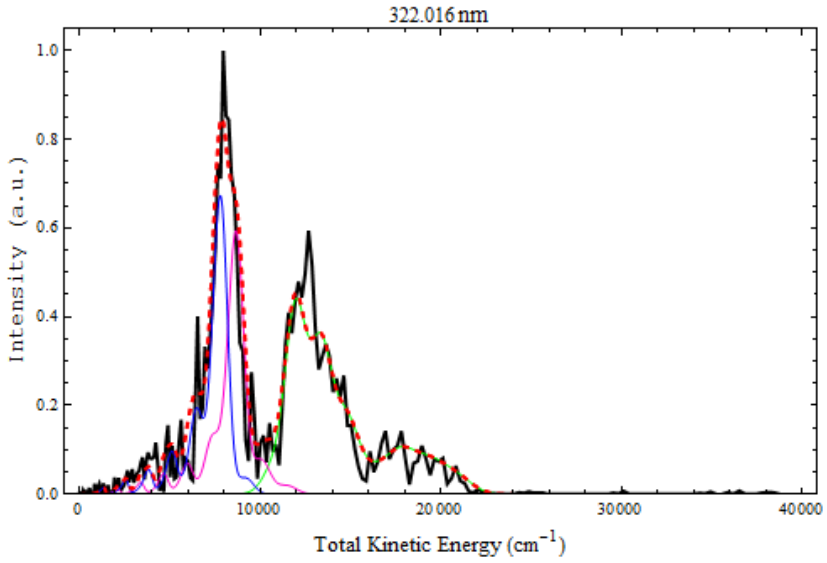

Figure 2.6: The heavy black line is the total kinetic energy of the O($^3P_2$) image from the dissociation of O_3 at 322.016 nm. The green, pink and blue lines are overlay of the O_2 ($X\,^3\Sigma_g^-$), $O_2(a^1\Delta_g)$ and $O_2(b^1\Sigma_g^+)$ respectively. The red dashed line is the sum of all three O_2 ($X^3\Sigma_g^-$), $O_2(a^1\Delta_g)$ and $O_2(b^1\Sigma_g^+)$ states.

This is repeated if there is more than one distinctly different reasonable fit option. For several images the rotational temperature was initially adjusted, 500 K generally seemed best and so was maintained throughout all the fits. Once the best fit(s) were determined the appropriate "area under the curves" were taken to calculate the relative populations which are reported in tables, similar to Table 2.1, for each wavelength and fit. The TKE plots with population fits are found in Appendix B. For many of the wavelengths for the O($^3P_2$) images, there was one distribution that seemed to best fit the data, but for several images there are two possible fits that are difficult to choose between. In the case where there are two equally good fits, it generally occurs that in one fit each "peak" is associated with one O_2 electronic state, and in the second

(better) fit the resulting electronic distribution is not as might be expected. Typically, the highest energy and second highest energy peaks pair with $O_2(X\ ^3\Sigma_g^-)$ while the lowest energy peak is a mix of $O(^3P_2)$ partnered with the $O_2(a^1\Delta_g)$ and $O_2(b^1\Sigma_g^+)$ states.

Table 2.1: The relative fraction of $O(^3P_2)$ associated with each vibrational state of O_2, within the three electronic states O_2 ($X\ ^3\Sigma_g^-$), $O_2(a^1\Delta_g)$ and $O_2(b^1\Sigma_g^+)$ states. This is from the same fit of the $O(^3P_2)$ image from O_3 dissociation at 322.016 nm as in Figure 2.6.

322.016 nm			
v	$O_2(X^3\Sigma_g^-)$	$O_2(a^1\Delta_g)$	$O_2(b^1\Sigma_g^+)$
0	0	0	0.043
1	0.052	0	0.683
2	0.073	0.028	0.148
3	0.089	0.096	0.070
4	0.041	0.662	0.034
5	0.149	0.104	0.017
6	0.269	0.057	0.005
7	0.300	0.033	0
8	0.027	0.016	
9	0	0.005	
10	0	0	
11	0		
12	0		
13	0		
14	0		
15	0		
16	0		

2.4 Results: O_2 Relative Populations

The $O(^3P_2)$ and O_2 REMPI spectra were obtained from the O_3 dissociation in the 321 nm – 329 nm range. Then images were taken of the $O(^3P_2)$ to determine the

$O_2(X\ ^3\Sigma_g^-)$, $O_2(a^1\Delta_g)$, and $O_2(b^1\Sigma_g^+)$ population distributions. The corresponding O_2 images were also taken and used to make assignments in the O_2 spectrum (Section 2.6). The wavelengths for images were chosen based on interesting aspects of the spectra as well as our desire to include a number of different types of peaks in different bands of the O_2 spectra. The $O(^3P_2)$ aspect of the results are reported in this section and discussed in the next while the O_2 spectra and ion-images are discussed in section 2.7-2.8 after a description of their analysis.

The O^+ yield spectra from the two laser experiment is shown in Figure 2.7. The x-axis is the dissociation wavelength and the y-axis is the intensity of the O^+ signal.

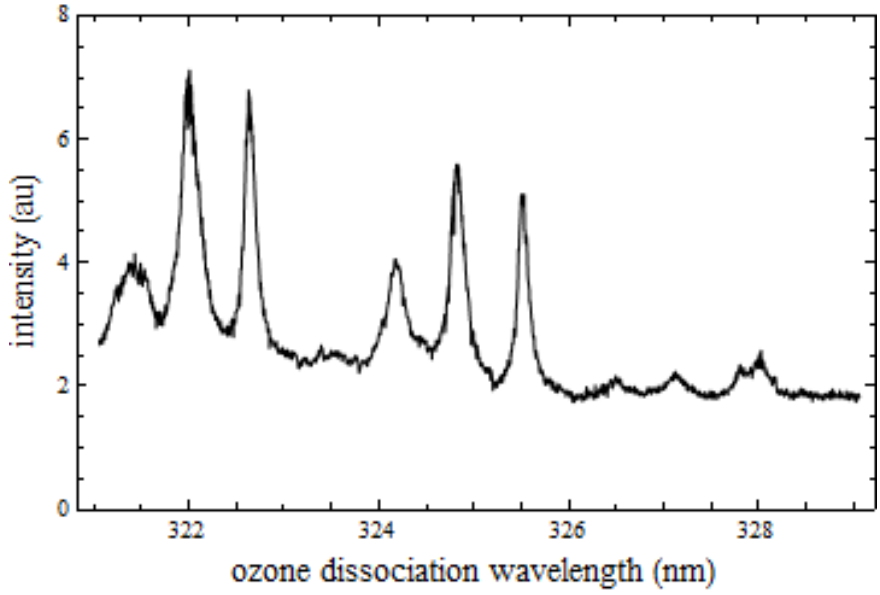

Figure 2.7: O^+ 2+1 REMPI signal using 225.65 nm following O_3 dissociation as a function of dissociation wavelength. The peaks represent dissociation resonant with discrete vibronic bands in the ozone absorption spectrum while signal off the peaks is based on absorption to the continuum leading to dissociation. There may be a small amount of background from probe laser ozone dissociation and $O(^3P_2)$ REMPI.

The overall scan was taken in sections to maintain consistency in the relative intensity of the peaks. The scans were overlapped by 0.2 nm and the laser energies were checked at the beginning and end of each scan.

The O_2 relative electronic state populations are reported in Table 2.2 from the analysis of the $O(^3P_2)$ ion-images.

Table 2.2: The electronic distribution, giving the relative population of O_2 in each of the three electronic states, O_2 ($X\ ^3\Sigma_g^-$), $O_2(a^1\Delta_g)$ and $O_2(b^1\Sigma_g^+)$ following the dissociation of O_3 at wavelengths between 321 – 329nm. For several of the wavelengths there are two or three fits that seems reasonable, in those cases the multiple distributions were included, labeled by consecutive numbers.

Wavelength (nm)	$O_2(X^3\Sigma_g^-)$	$O_2(a^1\Delta_g)$	$O_2(b^1\Sigma_g^+)$
321.199	0.627	0.196	0.177
321.538	0.536	0.264	0.200
322.016 (1)	0.159	0.589	0.252
322.016 (2)	0.484	0.254	0.262
322.628 (1)	0.319	0.294	0.387
322.628 (2)	0.324	0.362	0.314
322.730	0.350	0.410	0.239
323.700	0.563	0.339	0.098
324.192	0.394	0.388	0.218
324.589	0.548	0.297	0.154
324.835 (1)	0.120	0.294	0.586
324.835 (2)	0.367	0.314	0.318
324.906 (1)	0.298	0.382	0.321
324.906 (2)	0.343	0.463	0.194
324.954	0.237	0.299	0.463
325.051	0.301	0.372	0.327
325.567	0.333	0.323	0.344
325.776	0.728	0.162	0.110
326.494	0.720	0.217	0.063
327.157 (1)	0.107	0.451	0.442
327.157 (2)	0.527	0.268	0.205
328.022	0.340	0.288	0.373

The ratio of the three channels varies between the wavelengths, but all wavelengths probed show evidence of all three electronic states. In the cases where two distinctly different fits seem plausible both are reported, numbered sequentially for reference not due to implied importance. There are generally two types of fits, (1) where the three electronic states are more separated and $O_2(X\ ^3\Sigma_g^-)$ accounts for a single broad feature and (2) where $O_2(X\ ^3\Sigma_g^-)$ accounts for the broad feature as well as the fastest narrow peak and $O_2(a^1\Delta_g)$ and $O_2(b^1\Sigma_g^+)$ are more mixed.

It is important to relate the images and relative populations with the spectral region where they occur, as demonstrated in Figure 2.8.

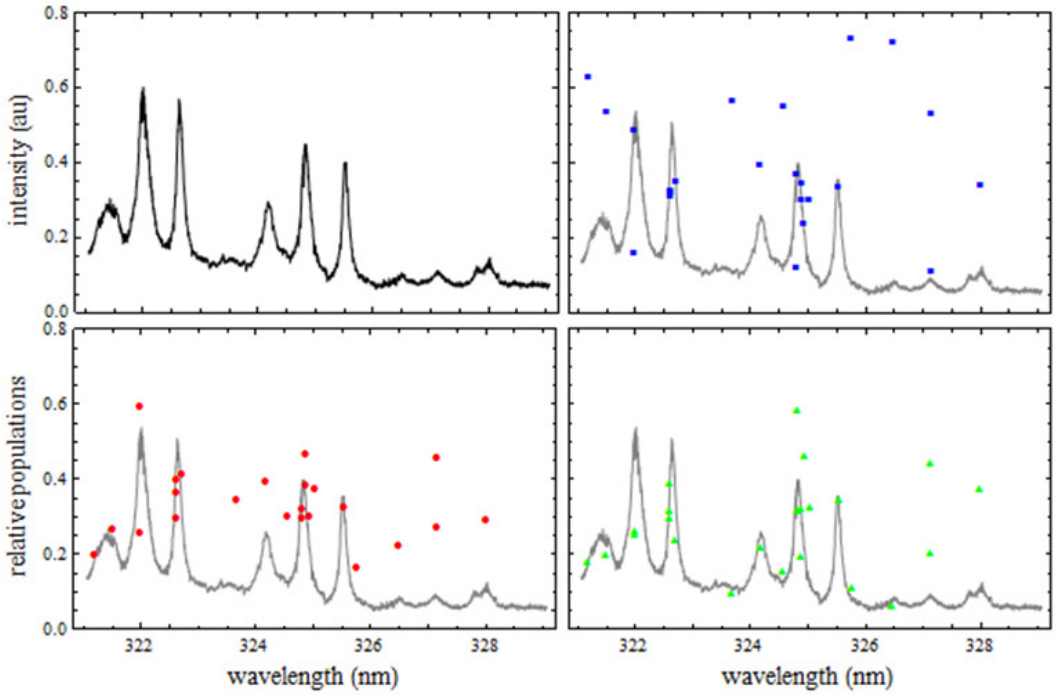

Figure 2.8: Electronic distribution of the relative populations of O_2 ($X^3\Sigma_g^-$) (blue square), $O_2(a^1\Delta_g)$ (red circle) and $O_2(b^1\Sigma_g^+)$(green triangle) from the dissociation of O_3 for several wavelengths between 321nm and 329nm. The populations were determined from analysis of the $O(^3P_2)$ images at the given wavelength. The black and gray lines are the O^+ yield spectra scaled to fit with the population plots.

The $O(^3P_2)$ image fits demonstrate that at all the wavelengths probed the dissociation produces a combination of all three channels.

$$O_3 \rightarrow O(^3P_2) + O_2(X^3\Sigma_g^-) \quad (1)$$

$$O_3 \rightarrow O(^3P_2) + O_2(a^1\Delta_g) \quad (2)$$

$$O_3 \rightarrow O(^3P_2) + O_2(b^1\Sigma_g^+) \quad (3)$$

O'Keeffe et al.[10] also examined the $O(^3P)$ from O_3 dissociation and observed peaks from all three channels. They detected $O(^3P_0)$ and report a single dissociation wavelength, comparable to one in this study, 322.64 nm. They report 31% relative yield to channel (1), 35% to channel (2), and 34% to channel (3). In the current study the dissociation at 322.628nm gave rise to two reasonable fits, neither of which exactly matched the O'Keeffe et al[10] finding, though the first is close, see Table 2.2.

The relative vibrational populations within each electronic state were also determined and reported in Tables 2.3 a - k. As with reporting the electronic distribution, if there are two distinct fits for a given wavelength both are given, the numbers correspond to the numbers in Table 2.2.

Table 2.3: The relative vibrational populations from the $O(^3P_2)$ images. The overall table has been broken into a series of tables (a) – (k) to make it easier to read. Each section of the table is labeled with the dissociation wavelength.

(a)

	321.199			321.528		
v	$O_2(X^3\Sigma_g^-)$	$O_2(a^1\Delta_g)$	$O_2(b^1\Sigma_g^+)$	$O_2(X^3\Sigma_g^-)$	$O_2(a^1\Delta_g)$	$O_2(b^1\Sigma_g^+)$
0	0	0.075	0.316	0.008	0.311	0.437
1	0.034	0.537	0.357	0.074	0.466	0.222
2	0.249	0.238	0.184	0.409	0.165	0.152
3	0.345	0.104	0.087	0.252	0.058	0.106
4	0.211	0.045	0.043	0.173	0	0.053
5	0.096	0	0.014	0.052	0	0.023
6	0.043	0	0	0.024	0	0.006
7	0.019	0	0	0.008	0	0
8	0.003	0		0	0	
9	0	0		0	0	
10	0	0		0	0	
11	0			0		
12	0			0		
13	0			0		
14	0			0		
15	0			0		
16	0			0		

(b)

	322.016 (1)			322.016 (2)		
V	$O_2(X^3\Sigma_g^-)$	$O_2(a^1\Delta_g)$	$O_2(b^1\Sigma_g^+)$	$O_2(X^3\Sigma_g^-)$	$O_2(a^1\Delta_g)$	$O_2(b^1\Sigma_g^+)$
0	0	0	0.043	0	0.148	0.044
1	0.052	0	0.683	0.159	0.266	0.672
2	0.073	0.028	0.148	0.220	0.189	0.153
3	0.089	0.096	0.070	0.271	0.021	0.073
4	0.041	0.662	0.034	0.186	0.284	0.036
5	0.149	0.104	0.017	0.113	0.045	0.017
6	0.269	0.057	0.005	0.051	0.024	0.005
7	0.300	0.033	0	0	0.014	0
8	0.027	0.016		0	0.007	
9	0	0.005		0	0.002	
10	0	0		0	0	
11	0			0		
12	0			0		
13	0			0		
14	0			0		
15	0			0		
16	0			0		

Table 2.3 (continued)

(c)

	322.628 (1)			322.628 (2)		
v	$O_2(X^3\Sigma_g^-)$	$O_2(a^1\Delta_g)$	$O_2(b^1\Sigma_g^+)$	$O_2(X^3\Sigma_g^-)$	$O_2(a^1\Delta_g)$	$O_2(b^1\Sigma_g^+)$
0	0	0.358	0.430	0	0.288	0.395
1	0.760	0.642	0.364	0.755	0.485	0.401
2	0.022	0	0.155	0.022	0	0.165
3	0.020	0	0.038	0.005	0	0.029
4	0.148	0	0.014	0.159	0.129	0.011
5	0.034	0	0	0.041	0.054	0
6	0.015	0	0	0.019	0.044	0
7	0	0	0	0	0	0
8	0	0		0	0	
9	0	0		0	0	
10	0	0		0	0	
11	0			0		
12	0			0		
13	0			0		
14	0			0		
15	0			0		
16	0			0		

(d)

	322.730			323.700		
v	$O_2(X^3\Sigma_g^-)$	$O_2(a^1\Delta_g)$	$O_2(b^1\Sigma_g^+)$	$O_2(X^3\Sigma_g^-)$	$O_2(a^1\Delta_g)$	$O_2(b^1\Sigma_g^+)$
0	0	0.306	0.332	0	0.254	0.230
1	0.293	0.457	0.327	0.018	0.417	0.310
2	0.351	0.162	0.192	0.281	0.285	0.317
3	0.074	0.057	0.090	0.267	0.044	0.124
4	0.269	0.018	0.044	0.223	0	0.018
5	0.012	0	0.014	0.131	0	0
6	0	0	0	0.059	0	0
7	0	0	0	0.021	0	0
8	0	0		0	0	
9	0	0		0	0	
10	0	0		0	0	
11	0			0		
12	0			0		
13	0			0		
14	0			0		
15	0			0		
16	0			0		

Table 2.3 (continued)

(e)

	324.192			324.589		
V	$O_2(X^3\Sigma_g^-)$	$O_2(a^1\Delta_g)$	$O_2(b^1\Sigma_g^+)$	$O_2(X^3\Sigma_g^-)$	$O_2(a^1\Delta_g)$	$O_2(b^1\Sigma_g^+)$
0	0	0.195	0.439	0	0.196	0.474
1	0	0.402	0.351	0.092	0.421	0.299
2	0.438	0.201	0.151	0.270	0.202	0.163
3	0.190	0.081	0.059	0.236	0.108	0.063
4	0.152	0.058	0	0.144	0.046	0
5	0.118	0.039	0	0.120	0.019	0
6	0.071	0.023	0	0.079	0.008	0
7	0.032	0		0.044	0	
8	0	0		0.015	0	
9	0	0		0	0	
10	0	0		0	0	
11	0			0		
12	0			0		
13	0			0		
14	0			0		
15	0			0		
16	0			0		

(f)

	324.835 (1)			324.835 (2)		
v	$O_2(X^3\Sigma_g^-)$	$O_2(a^1\Delta_g)$	$O_2(b^1\Sigma_g^+)$	$O_2(X^3\Sigma_g^-)$	$O_2(a^1\Delta_g)$	$O_2(b^1\Sigma_g^+)$
0	0	0.284	0.312	0	0	0.053
1	0.276	0.508	0.601	0.117	0	0.806
2	0.232	0.112	0.038	0.099	0.034	0.073
3	0.214	0.044	0.026	0.091	0.119	0.051
4	0.157	0.029	0.017	0.066	0.507	0.016
5	0.089	0.017	0.005	0.113	0.254	0
6	0.032	0.006	0	0.340	0.051	0
7	0	0		0.121	0.026	
8	0	0		0.053	0.009	
9	0	0		0	0	
10	0	0		0	0	
11	0			0		
12	0			0		
13	0			0		
14	0			0		
15	0			0		
16	0			0		

Table 2.3 (continued)

(g)

	324.906 (1)			324.906 (2)		
v	$O_2(X^3\Sigma_g^-)$	$O_2(a^1\Delta_g)$	$O_2(b^1\Sigma_g^+)$	$O_2(X^3\Sigma_g^-)$	$O_2(a^1\Delta_g)$	$O_2(b^1\Sigma_g^+)$
0	0.018	0.200	0.339	0	0.107	0.280
1	0.118	0.358	0.457	0.094	0.144	0.505
2	0.156	0.187	0.168	0.121	0.148	0.110
3	0.158	0.100	0.036	0.143	0.148	0.064
4	0.158	0.064	0	0.143	0.205	0.031
5	0.131	0.045	0	0.167	0.185	0.010
6	0.097	0.029	0	0.217	0.064	0
7	0.063	0.014		0.089	0	
8	0.042	0.004		0.026	0	
9	0.029	0		0	0	
10	0.019	0		0	0	
11	0.010			0		
12	0			0		
13	0			0		
14	0			0		
15	0			0		
16	0			0		

(h)

	324.954			325.051		
v	$O_2(X^3\Sigma_g^-)$	$O_2(a^1\Delta_g)$	$O_2(b^1\Sigma_g^+)$	$O_2(X^3\Sigma_g^-)$	$O_2(a^1\Delta_g)$	$O_2(b^1\Sigma_g^+)$
0	0.028	0.193	0.285	0.019	0.329	0.285
1	0.122	0.378	0.600	0.089	0.277	0.600
2	0.128	0.181	0.088	0.132	0.205	0.088
3	0.247	0.097	0.019	0.213	0.103	0.019
4	0.133	0.062	0.005	0.265	0.035	0.005
5	0.109	0.043	0.002	0.114	0.025	0.002
6	0.088	0.028	0	0.068	0.016	0
7	0.057	0.013		0.041	0.008	
8	0.037	0.004		0.025	0.002	
9	0.025	0		0.016	0	
10	0.015	0		0.010	0	
11	0.008			0.005		
12	0.002			0.002		
13	0			0		
14	0			0		
15	0			0		
16	0			0		

Table 2.3 (continued)

(i)

	325.567			325.776		
v	$O_2(X^3\Sigma_g^-)$	$O_2(a^1\Delta_g)$	$O_2(b^1\Sigma_g^+)$	$O_2(X^3\Sigma_g^-)$	$O_2(a^1\Delta_g)$	$O_2(b^1\Sigma_g^+)$
0	0.014	0.009	0.109	0.018	0.103	0.095
1	0.098	0.025	0.228	0.067	0.139	0.159
2	0.102	0.058	0.557	0.139	0.163	0.519
3	0.100	0.127	0.058	0.170	0.213	0.126
4	0.172	0.272	0.035	0.182	0.304	0.079
5	0.211	0.453	0.013	0.158	0.051	0.022
6	0.141	0.036	0	0.117	0.020	0
7	0.074	0.014		0.085	0.006	
8	0.045	0.004		0.042	0	
9	0.028	0.001		0.014	0	
10	0.010	0		0.006	0	
11	0.004			0.002		
12	0.002			0.001		
13	0			0		
14	0			0		
15	0			0		
16	0			0		

(j)

	326.494			327.157 (1)		
v	$O_2(X^3\Sigma_g^-)$	$O_2(a^1\Delta_g)$	$O_2(b^1\Sigma_g^+)$	$O_2(X^3\Sigma_g^-)$	$O_2(a^1\Delta_g)$	$O_2(b^1\Sigma_g^+)$
0	0.057	0.272	0.129	0	0.015	0.184
1	0.159	0.297	0.216	0.031	0.034	0.564
2	0.233	0.191	0.351	0.031	0.059	0.125
3	0.158	0.125	0.169	0.031	0.052	0.080
4	0.130	0.071	0.106	0.030	0.439	0.034
5	0.093	0.029	0.029	0.157	0.255	0.014
6	0.067	0.012	0	0.423	0.087	0
7	0.052	0.004		0.219	0.044	
8	0.033	0		0.055	0.015	
9	0.011	0		0.024	0	
10	0.005	0		0	0	
11	0.002			0		
12	0.001			0		
13	0			0		
14	0			0		
15	0			0		
16	0			0		

Table 2.3 (continued)
(k)

	327.157 (2)			328.022		
v	$O_2(X^3\Sigma_g^-)$	$O_2(a^1\Delta_g)$	$O_2(b^1\Sigma_g^+)$	$O_2(X^3\Sigma_g^-)$	$O_2(a^1\Delta_g)$	$O_2(b^1\Sigma_g^+)$
0	0	0.202	0.256	0	0.083	0.119
1	0.041	0.540	0.394	0.026	0.093	0.167
2	0.172	0.212	0.261	0.071	0.115	0.673
3	0.176	0.046	0.056	0.175	0.142	0.023
4	0.176	0	0.024	0.200	0.145	0.014
5	0.175	0	0.009	0.362	0.341	0.004
6	0.144	0	0	0.098	0.080	0
7	0.116	0		0.043	0	
8	0	0		0.025	0	
9	0	0		0	0	
10	0	0		0	0	
11	0			0		
12	0			0		
13	0			0		
14	0			0		
15	0			0		
16	0					

The angular distributions for the $O(^3P_2)$ images were also determined. The average β for the peaks within each image are reported in Table 2.4, along with the O_2 electronic state associated with the β. In some cases the two population fits result in two possible electronic state assignments to a single peak. Also some peaks are a combination of vibration states from two electronic states.

Table 2.4: The β calculated for each peak of each $O(^3P_2)$ image. The first column is the dissociation wavelength. The next four columns are βa – βd, where the a, b, c, and d represent the order of the βs, a being associated with the fastest peak (or section) and d with the slowest. In general each can be associated with the sibling O_2 product although some are mixed. Unless otherwise noted, βa goes with O_2 ($X^3\Sigma_g^-$), βb with ($a^1\Delta_g$), and βc and βd with ($b^1\Sigma_g^+$).

Dissociation wavelength (nm)	Ba	Bb	Bc	Bd
321.199	1.93	1.59	0.61 ($^1\Delta_g + {}^1\Sigma_g^+$)	1.29
321.538	1.70	0.89	0.78	
322.016	1.57	0.82 ($^3\Sigma_g^-$ or $^1\Delta_g$)	1.34 ($^1\Delta_g + {}^1\Sigma_g^+$)	
322.628	1.96	1.91	1.96	
322.628	2.00	1.98	1.98	
322.73	1.68	0.69 ($^3\Sigma_g^- + {}^1\Delta_g$)	0.80	
322.73	1.68	0.69 ($^3\Sigma_g^- + {}^1\Delta_g$)	1.06	0.66
323.70	1.57	1.21	0.56 ($^1\Delta_g$)	
324.192	1.99	1.73 ($^1\Delta_g + {}^3\Sigma_g^-$)	1.78	
324.192	1.99	2.00 ($^3\Sigma_g^-$+ little $^1\Delta_g$)	1.59 ($^1\Delta_g$)	1.78
324.589	2.00	1.99	1.97	
324.835	1.79	1.64 ($^3\Sigma_g^-$ or $^1\Delta_g$)	1.52 ($^1\Sigma_g^+$ or ($^1\Delta_g$+$^1\Sigma_g^+$)	
324.906	1.79	0.81($^1\Delta_g$ or $^3\Sigma_g^- + {}^1\Delta_g$)	0.99 ($^1\Sigma_g^+$ or $^1\Delta_g$+$^1\Sigma_g^+$)	
324.906	1.77	0.79 ($^1\Delta_g$ or $^3\Sigma_g^- + {}^1\Delta_g$)	0.82 ($^1\Sigma_g^+$ or $^1\Delta_g$+$^1\Sigma_g^+$)	
324.954	1.86	1.75	1.57	
325.051	1.57	0.61	0.55	
325.567	1.46	1.04 ($^3\Sigma_g^-$)	0.25 ($^1\Delta_g$+$^1\Sigma_g^+$)	
325.567	1.34	0.07 ($^3\Sigma_g^- + {}^1\Delta_g$)	0.42 ($^1\Delta_g$+$^1\Sigma_g^+$)	
325.776	1.17	0.64	-0.59	
326.494	1.68	1.22	0.64	
327.157	1.32	-0.12 ($^1\Delta_g$ or $^3\Sigma_g^-$)	0.80 ($^1\Sigma_g^+$ or $^1\Delta_g$+$^1\Sigma_g^+$)	0.21($^1\Sigma_g^+$or $^1\Delta_g$+$^1\Sigma_g^+$)
328.022	1.84	1.32	1.81	

2.5 Discussion

The O^+ yield spectra corresponds well with the O_3 absorption spectra, as shown in Figure 2.9, where the assignments are from O'Keeffe.[20] The vibrational assignments seem reasonable to use as they are also in basic agreement with Shinke[21], despite the difference in the assignment of the upper electronic state.

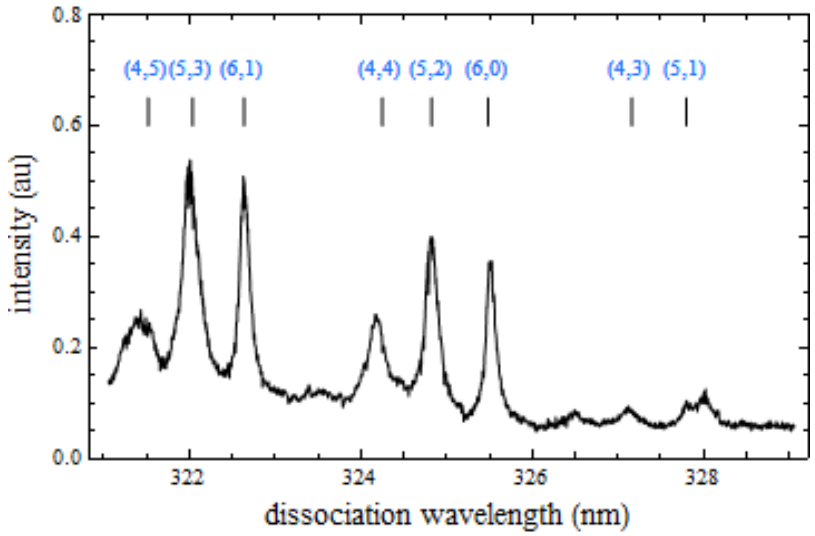

Figure 2.9: O^+ yield spectra from the dissociation of ozone with assignments for the ozone absorption band. The absorption is labeled as (ν_1,ν_2). ν_3 is not included because it is 0 for the assignments given.

The electronic state with the maximum population varies depending on the wavelength of dissociation. These distributions indicate that the spin-forbidden channels and the spin-allowed channel are produced from ozone dissociation in the Huggins band at similar amounts. One thing should be noted about the fits: energetically there is the possibility that either $O_2(X\ ^3\Sigma_g^-)$ or $O_2(a^1\Delta_g)$ could have a bimodal distribution or for $O_2(X\ ^3\Sigma_g^-)$ even a trimodal distribution. As can be seen in

the case of our example 322.016 nm, another option would be that all three peaks could be associated with an $O_2(X\ ^3\Sigma_g^-)$ state partner rather than the two options of fits given. However, given the evidence in previous studies[3,10] of the detection of $O_2(a^1\Delta_g)$ and $O_2(b^1\Sigma_g^+)$ it seems likely that all three states are present.

Understanding the effect of the absorption of ozone may help with understanding the overall production of the three available $O(^3P)$ channels and why the ratios change. The assignments in Figure 2.9 can be used to compare the effect of resonant versus non-resonant absorption of ozone and how the change in ν_1 or ν_2 affects the ratio between the channels. In the resonant case the dissociation occurs via absorption to a discrete ozone vibrational state while the non-resonant case absorption does not occur to a specific state but rather to the continuum. Any change in product ratio based on change in absorption by ozone may be helpful in understanding the dynamics of the dissociation. Care needs to be taken when comparing the various wavelengths because five wavelengths have two distinctly different fits, and the choices can change the appearance of the comparisons. To avoid double counting the wavelengths with two fits and to maintain consistency, the comparisons are made twice, once using fits 1 and once using fits 2.

Resonant absorption in ozone compared with non-resonant absorption for the dissociation may make a difference in the branching ratio between the three channels. O'Keeffe et al.[10] observed an increase in the $O(^3P_0)$ peaks associated with $O_2(a^1\Delta_g)$ and $O_2(b^1\Sigma_g^+)$ for resonant ozone absorption. Four transitions in this work, (5,2), (6,1), (4,4), and (6,0) have resonant images and nearby non-resonant images that can be compared, as shown in Figure 2.10.

Figure 2.10: In all the plots the populations from the dissociation following resonant absorption is green and non-resonant is in blue. (a) (6,1) Fit 1, (b) (6,1) Fit 2, (c) (4,4) (d) (5,2) Fit 1, (e) (5,2) Fit 2, (f) (6,0). (4,4) and (6,0) only have one plot because all wavelengths used have a single fit.

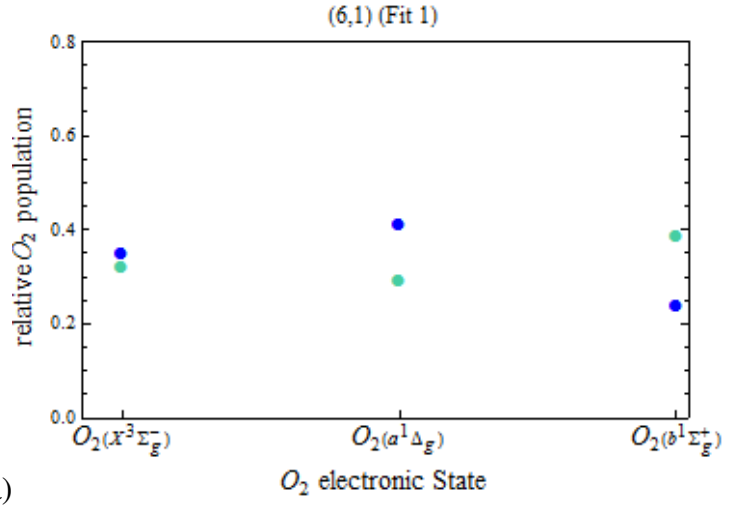
(6,1) (Fit 1)
relative O_2 population
0.0
0.2
0.4
0.6
0.8
$O_2(X^3\Sigma_g^-)$
$O_2(a^1\Delta_g)$
$O_2(b^1\Sigma_g^+)$
O_2 electronic State

(a)

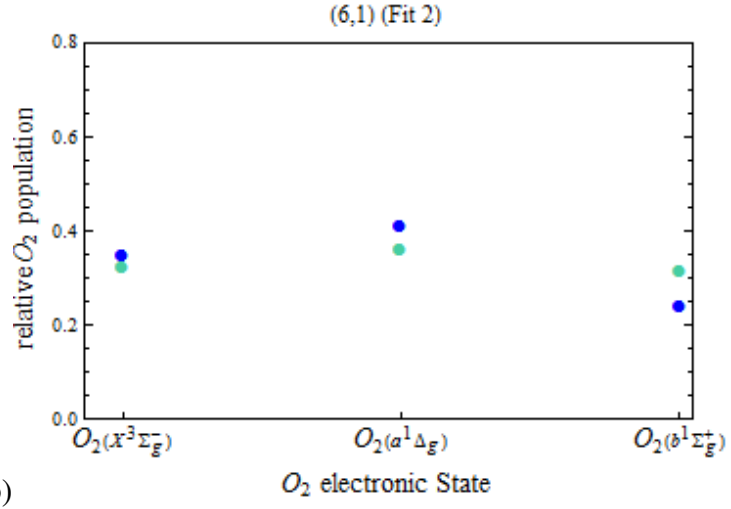
(6,1) (Fit 2)
relative O_2 population
0.0
0.2
0.4
0.6
0.8
$O_2(X^3\Sigma_g^-)$
$O_2(a^1\Delta_g)$
$O_2(b^1\Sigma_g^+)$
O_2 electronic State

(b)

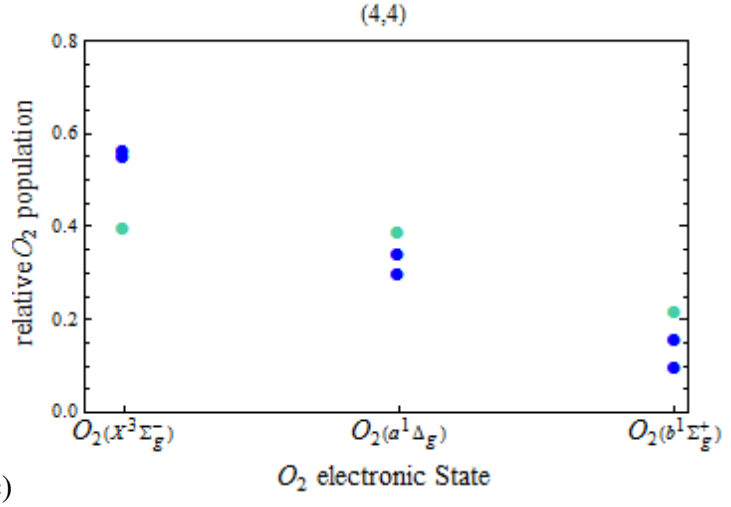
(4,4)
relative O_2 population
0.0
0.2
0.4
0.6
0.8
$O_2(X^3\Sigma_g^-)$
$O_2(a^1\Delta_g)$
$O_2(b^1\Sigma_g^+)$
O_2 electronic State

(c)

Figure 2.10 (continued)

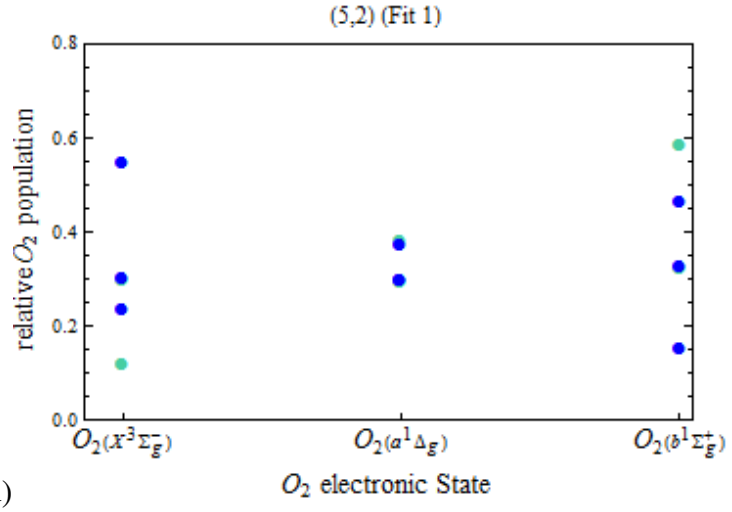

(d)

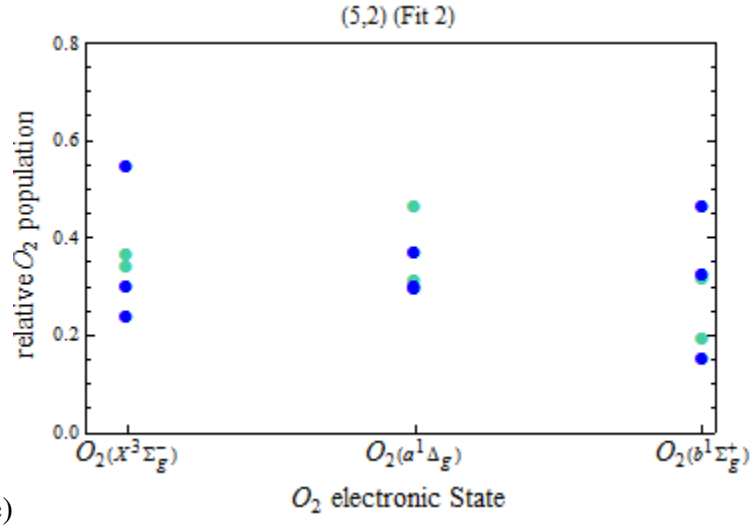

(e)

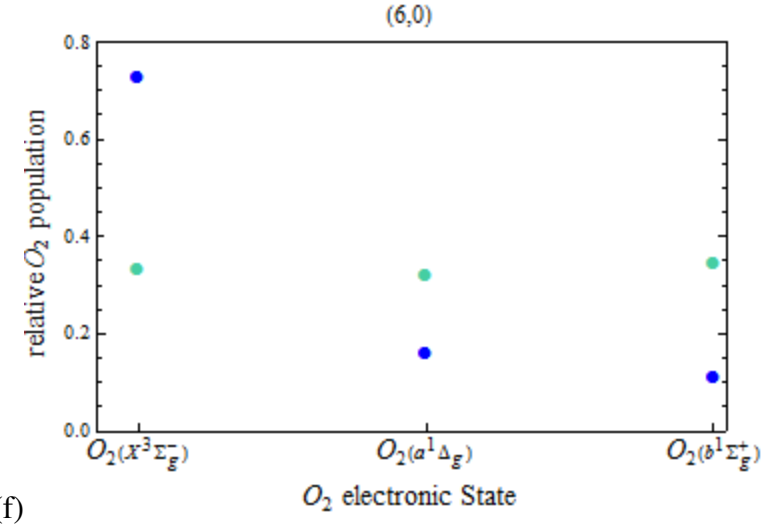

(f)

A specific dependence on resonant absorption is not clear. In general, either $O_2(b^1\Sigma_g^+)$ or $O_2(a^1\Delta_g)$ has the maximum population for resonant peaks, or several states have similar populations. When comparing the $O_2(X\ ^3\Sigma_g^-)$ population between resonant and non-resonant production the non-resonant is always larger. For $O_2(b^1\Sigma_g^+)$ in all but one comparison the largest population is associated with resonant absorption. One can also look at the individual absorption bands. For (5,2) fit 1, $O_2(b^1\Sigma_g^+)$ is the largest for resonant absorption and for non-resonant $O_2(X\ ^3\Sigma_g^-)$. For fit 2 resonant $O_2(a^1\Delta_g)$ is biggest and non-resonant $O_2(b^1\Sigma_g^+)$ is biggest. (6,1) Fit 1 resonant absorption results in the most in $O_2(b^1\Sigma_g^+)$ while for non-resonant $O_2(a^1\Delta_g)$ is biggest. For fit 2 $O_2(a^1\Delta_g)$ has the maximum relative population for both resonant and non-resonant but with a greater difference for non-resonant. $O_2(X\ ^3\Sigma_g^-)$ and $O_2(a^1\Delta_g)$ are similar and more than $O_2(b^1\Sigma_g^+)$ for absorption resonant with the (4,4) band and for non-resonant $O_2(X\ ^3\Sigma_g^-)$ is the maximum relative population. For (6,0) resonant absorption all are similar but for non-resonant $O_2(X\ ^3\Sigma_g^-)$ is the maximum.

Another aspect to consider is the change in population as the excitation in ν_1 or ν_2 increases. Figure 2.11 demonstrates the change in O_2 electronic state production as a function of increasing excitation in ν_1. Based on fit 2 , Figure 2.11 (d – e), there may be a dependence on the ν_1 excitation in ozone, although this is less evident when comparing the populations using fit 1, Figure 2.11, (a – c).

Figure 2.11: The relative O_2 electronic state populations plotted as a function of ν_1 in ozone absorption where (a – c) are for fit 1 and (d – f) using Fit 2.

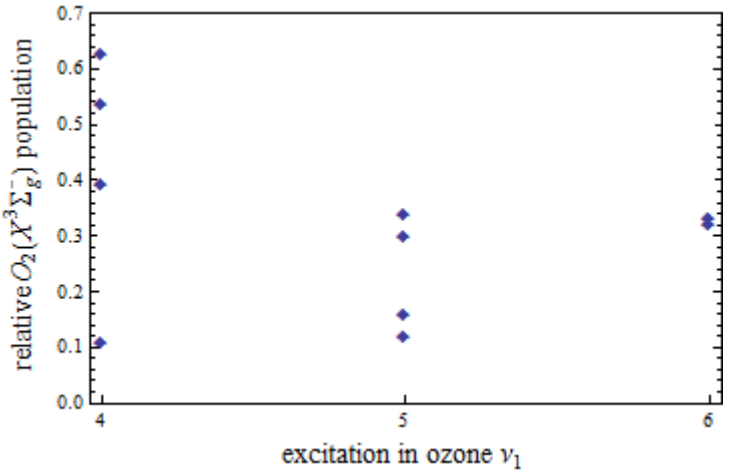
relative $O_2(X^3\Sigma_g^-)$ population
0.0
0.1
0.2
0.3
0.4
0.5
0.6
0.7
4
5
6
excitation in ozone ν_1

(a)

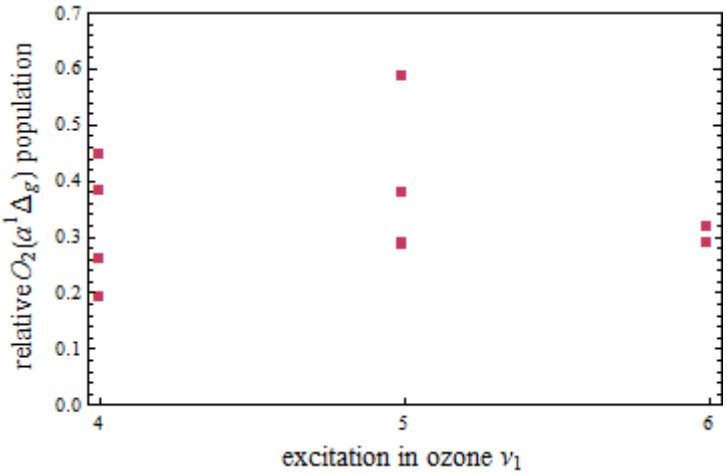
relative $O_2(a^1\Delta_g)$ population
0.0
0.1
0.2
0.3
0.4
0.5
0.6
0.7
4
5
6
excitation in ozone ν_1

(b)

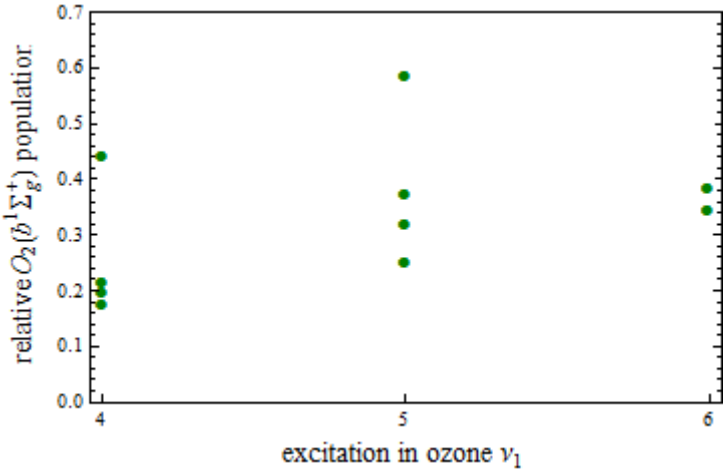
relative $O_2(b^1\Sigma_g^+)$ population
0.0
0.1
0.2
0.3
0.4
0.5
0.6
0.7
4
5
6
excitation in ozone ν_1

(c)

Figure 2.11 (continued)

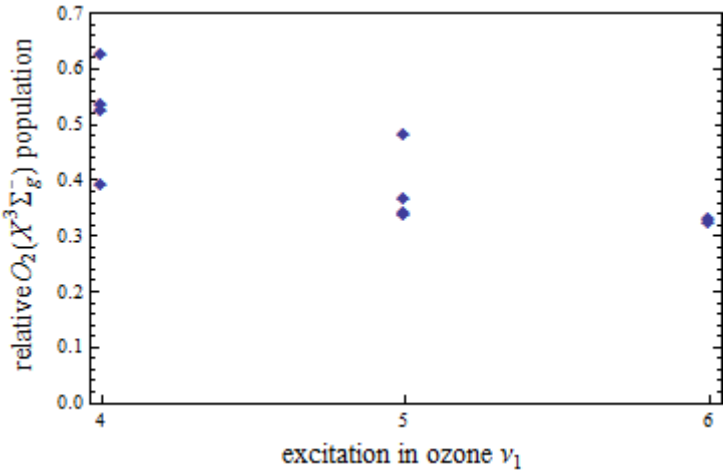

(d)

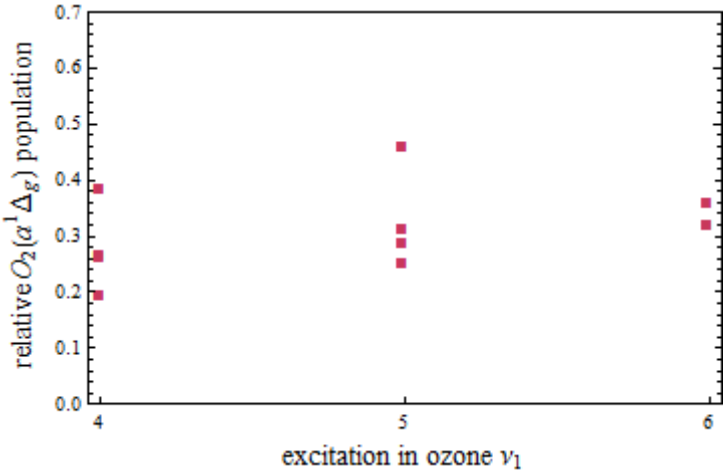

(e)

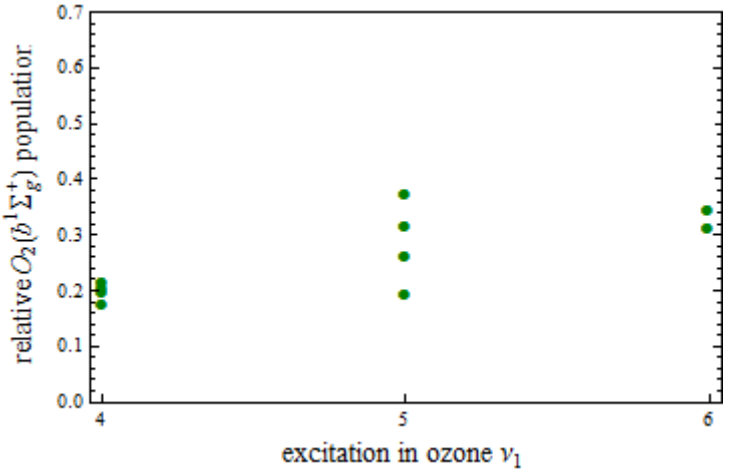

(f)

With few data points for each ν_1 excitation, it is difficult to be certain of any trends but as the excitation in ν_1 increases the relative population of $O_2(X\ ^3\Sigma_g^-)$ appears to decrease while $O_2(a^1\Delta_g)$ and $O_2(b^1\Sigma_g^+)$ appear to increase or remain the same. This could signify that increased vibrational excitation of the ozone leads to electronic excitation in the O_2 products.

One can also look at the effect of exciting ozone in ν_2, seen in Figure 2.12 where (a – c) is for fit 1 and (d – f) is for fit 2. .

Figure 2.12: The relative O_2 electronic state populations plotted as a function of ν_2 in ozone absorption where (a – c) are for fit 1 and (d – f) using Fit 2.

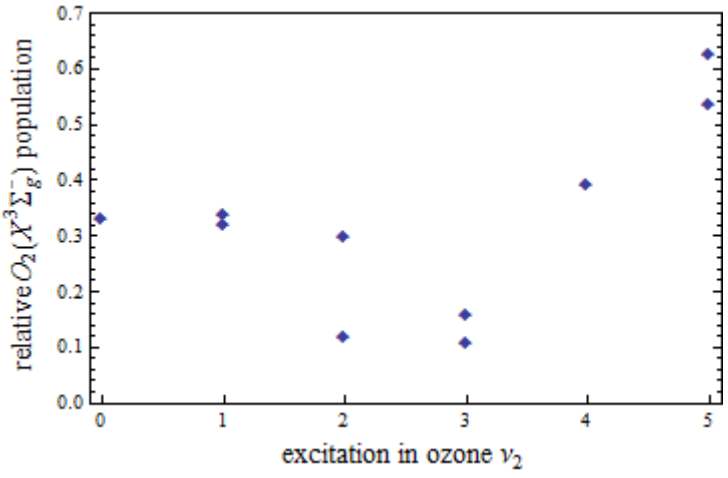
relative $O_2(X^3\Sigma_g^-)$ population
0.0
0.1
0.2
0.3
0.4
0.5
0.6
0.7
0
1
2
3
4
5
excitation in ozone ν_2

(a)

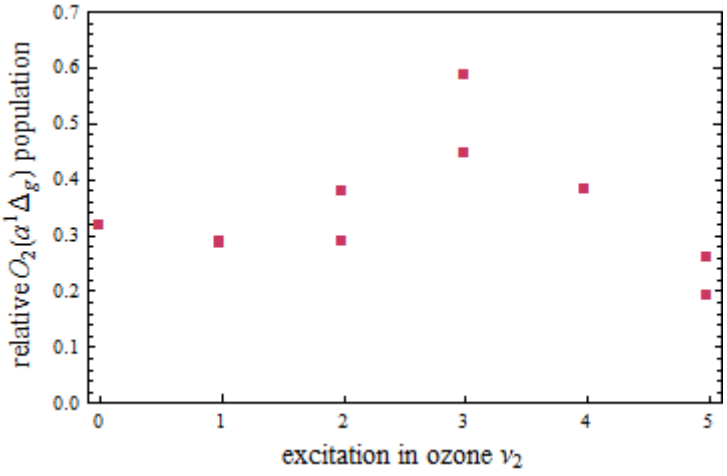
relative $O_2(a^1\Delta_g)$ population
0.0
0.1
0.2
0.3
0.4
0.5
0.6
0.7
0
1
2
3
4
5
excitation in ozone ν_2

(b)

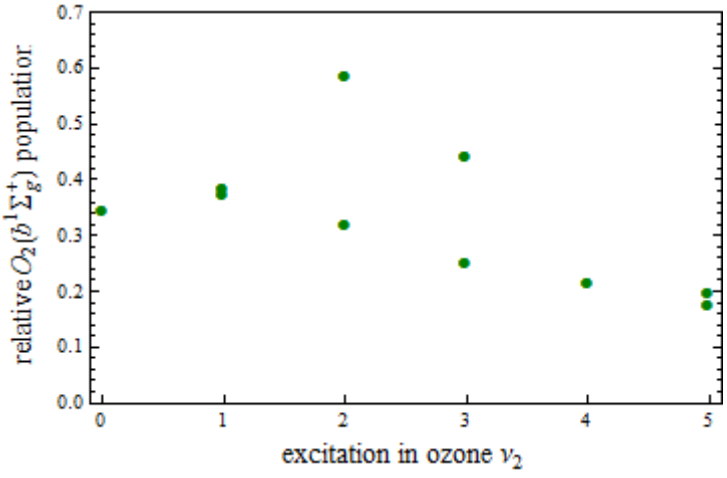
relative $O_2(b^1\Sigma_g^+)$ populatior
0.0
0.1
0.2
0.3
0.4
0.5
0.6
0.7
0
1
2
3
4
5
excitation in ozone ν_2

(c)

Figure 2.12 (continued)

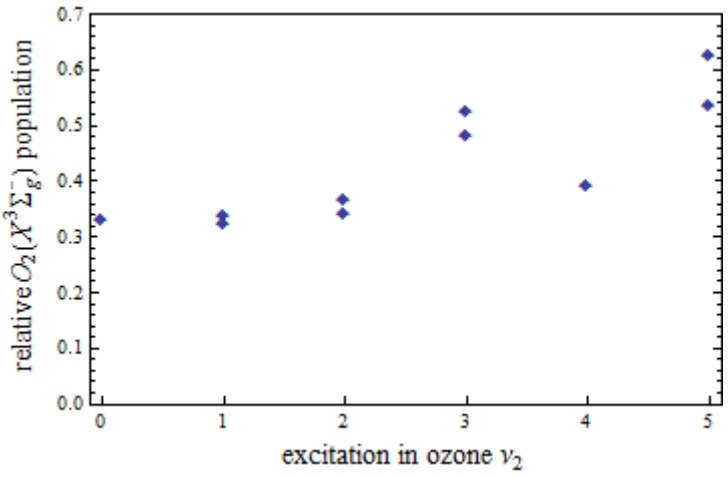

(d)

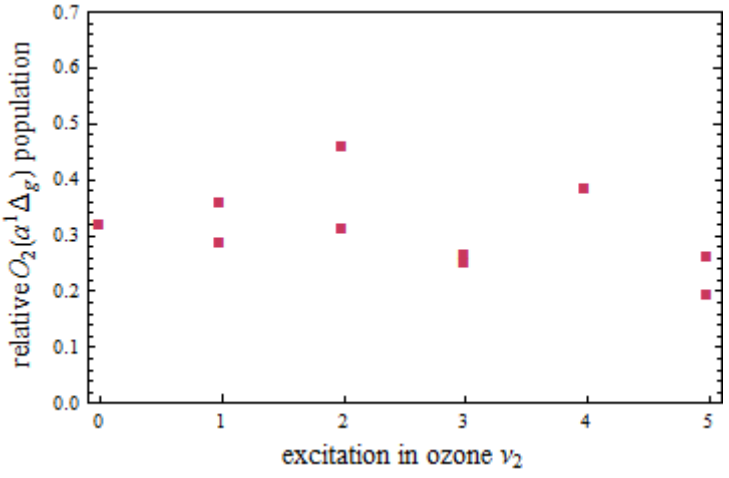

(e)

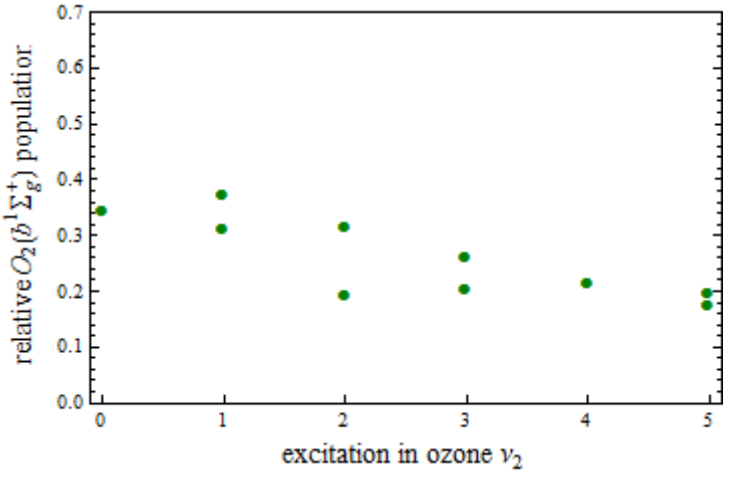

(f)

Excitation in ν_2 is quite different for fit 1 compared with fit 2 and so must be discussed independently. For fit 1, the electronic excitation in O_2 appears to peak around $\nu_2 = 2$ or 3 and ultimately decrease. The population in $O_2(X\,^3\Sigma_g^-)$ dips around 2 or 3 but ultimately increases from 0 to 5. For fit 2, the $O_2(X\,^3\Sigma_g^-)$ population appears to increase while the $O_2(a^1\Delta_g)$ and $O_2(b^1\Sigma_g^+)$ populations remain the same or decrease. This may imply that increased excitation in ν_2, the bend, leads to rotational or vibrational excitation in O_2 rather than electronic. The effect of ozone absorption on the relative vibrational population can be seen in similar graphs in Appendix C. The change in vibrational population as ν_1 or ν_2 change is unclear with the few data points for each one.

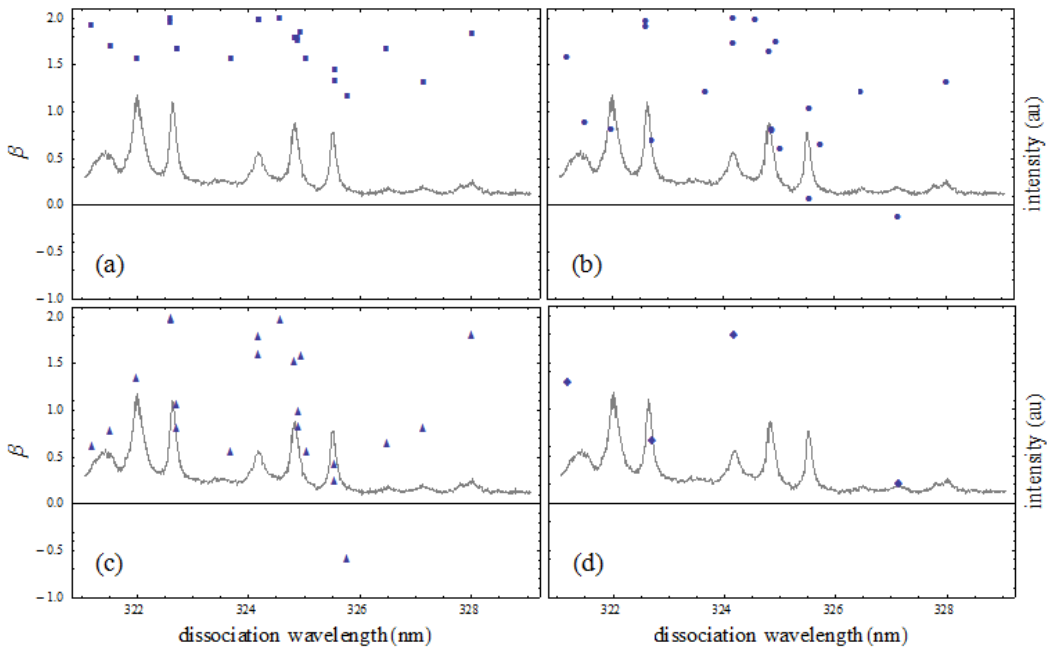

Figure 2.13: The change in β as a function of wavelength, where (a – d) are βa, βb, βc, and βd respectively. The gray line is the O^+ signal intensity. In general βa is associated with $O_2(X^3\Sigma_g^-)$, βb is associated with $O_2(a^1\Delta_g)$, and βc, and βd are associated with $O_2(b^1\Sigma_g^+)$, with some exceptions given in Table 2.4

The anisotropy within the images may be helpful for further understanding. Most of the β are positive with many being close to 2 signifying a parallel transition. In general the β values associated with the spin allowed channel are more positive than those associated with the spin forbidden channels, which can roughly be seen by comparing Figure 2.13 a with b and c. On average at longer wavelengths all the β tend to become less positive although the difference is small, which can be observed in Figure 2.13.

Observing the trends as a function of ozone absorption and O_2 electronic state are the first steps in understanding what is occurring in the dissociation process. The meaning behind the trends is still unclear but future studies both through calculation and experimental could add a more clear definition of the trends and understanding of their meaning. The findings here suggest that the ozone absorption plays a key role in the relative population distribution between the three possible O_2 electronic states.

2.6 Previous work: O_2 REMPI

Despite the importance of O_2 in the atmosphere there are still questions about its absorption spectrum, particularly that from excited vibrational states. In the 321 – 329 nm range, detection by 2+1 REMPI has transitions from the three lower states, O_2 $X\ ^3\Sigma_g^-$, $a\ ^1\Delta_g$ and $b\ ^1\Sigma_g^+$ reaching two upper states, $C\ 3s\sigma_g\ ^3\Pi_g$ and $d\ 3s\sigma_g\ ^1\Pi_g$. The upper states are perturbed by several nearby states, mainly the valence states *II* [a] $(\sigma_g\pi_g^3)\ ^{3,1}\Pi_g$,[3-5,22] respectively. REMPI detection could occur from the lower states to

[a] Based on the notation used in Lewis et. al. the diabatic (crossing) states are labeled I, II, III and the corresponding adiabatic states are labeled 1, 2, 3. At large R, the ordered diabatic and adiabatic become equivalent

the valence states but the ionization step from the valence states is more difficult than from the Rydberg states. A transition to the valance state should produce signal that is an order of magnitude less than a transition to the Rydberg states, so only the Rydberg transitions are considered here. Many REMPI studies have identified transitions in this region and defined the upper states, but there are still questions especially concerning the $C\ ^3\Pi_g$ state and upper vibrational levels of the $d\ ^1\Pi_g$ state.[3-9,11,23]

$C^3\Pi_g$ and $d^1\Pi_g$ are the lowest two gerade Rydberg states from the $O_2^+\ X\ ^2\Pi_g$ core. REMPI studies by Ogorzalez Loo et al,[6,7] Sur et al[8,9] and Johnson at al[11] identified transitions from $X\ ^3\Sigma_g^-$, $a\ ^1\Delta_g$ and $b\ ^1\Sigma_g^+$ to the $C\ ^3\Pi_g$ and $d\ ^1\Pi_g$. Morrill et. al[4] and Lewis et al.[5] reanalyzed the previous studies and new experimental work[3] to determine details of the states and perturbations. They calculated term values for $d\ ^1\Pi_g$ v = 0 – 4, as well as for $a\ ^1\Delta_g$ v = 0 – 3 and $b\ ^1\Sigma_g^+$ v = 0 – 2.

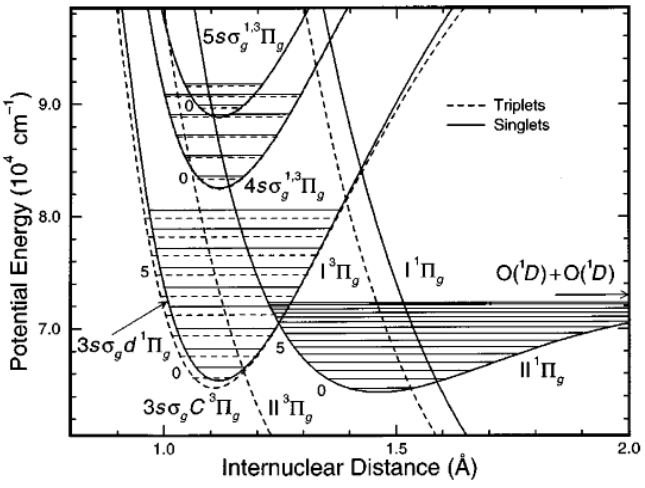

Figure 2.14: Diabatic potential-energy curve demonstrating the perturbations of the $O_2(d^1\Pi_g)$ and $(C^3\Pi_g)$ states. Morrill et al. used these potentials for their calculations of these states. Figure reprinted with permission from reference 4. Copyright JCP 1999, American Institute of Physics

Perturbations to $C\ ^3\Pi_g$ and $d\ ^1\Pi_g$ come from interactions with the nearby valence states. $O_2(d\ ^1\Pi_g)$ is perturbed in v = 1 ,2, and 3, as shown in Figure 2.14.

$O_2(d\ ^1\Pi_g)$ v = 2 and 3 have major perturbations from electrostatic interactions from the $II\ ^1\Pi_g$ valence level. This state also causes perturbations to the $d\ ^1\Pi_g$ v = 1 state. $O_2\ d\ ^1\Pi_g$ v = 4 is above the dissociation limit for the $II\ ^1\Pi_g$ state and appears to have no major perturbations. Minor perturbations are caused by predissociative electrostatic interaction from valance states including the $II\ ^1\Pi$ and $I\ ^1\Pi$ and secondary interactions by the other nearby valence states, such as the $II\ ^1\Delta_g$ state. For $C\ ^3\Pi_g$ v = 2 rotational analysis has been done and it is perturbed by the $II\ ^3\Pi_g$ state. Weak perturbations are also caused by spin orbit interaction between $C\ ^3\Pi_g$ and $d\ ^1\Pi_g$.[3-5] The perturbations result in rotational constants that change as a function of J and spectral features that can be quite far from those expected in the absence of perturbations.

The O_2^+ yield spectrum is complicated due to the perturbations as well as to the combination of aspects that contribute to its intensity. Since the photodissociation and detection laser are the same, the populations of the O_2 states produced, the absorption efficiency of the dissociation photon, the detection probability and the available REMPI transitions all play a role in the final spectrum. In the following sections the O_2^+ images will be used to determine which lower states are possible for each and then possible assignments will be given based on available transitions.

2.6.1 O_2 Image analysis

O_2 images were taken which can be used to identify transitions in the O_2 spectra. In the 321 – 329 nm range the O_2 images were obtained at the same wavelengths as the $O(^3P)$ images. At longer wavelengths they were taken to help identify different bands in the spectra. The O_2 spectrum was obtained for 321 – 346 nm. For a peak in the O_2 spectrum a photon must be absorbed to dissociate ozone, producing an O_2 state that can be ionized at the same wavelength. The populations determined from the $O(^3P_2)$ images reported in section 2.4 show which O_2 states are available at specific wavelengths, and these limit the number of lower states we need to consider for ionization. A state has to be produced by ozone dissociation in order to be available for ionization. The $O_2(X\ ^3\Sigma_g^-) + O(^1D)$ channel from ozone dissociation is also energetically available for $O_2(X\ ^3\Sigma_g^-)$ v = 0 – 3 or 4 in this range, and so those states need to be considered for all the images but have different velocities than the $O(^3P)$ channel.

The O_2 images are fit to determine which lower states need to be considered for transitions in the spectra. Peaks in the O_2 images correspond to a certain kinetic energy, similar to the $O(^3P_2)$ images, so the O_2 states that appear at the proper energy to fit the peak in the image can be determined. Once the lower O_2 state is limited, the wavelength can give an idea of the upper state. There must be a transition at the wavelength for detection of the lower state, otherwise the lower state can be discounted.

The O_2 images were transformed using BASEX in the same way as the $O(^3P_2)$ images and then converted to total kinetic energy following the same principles of

conservation of energy and momentum. O_2 lower state fits were made based on the following equations:

$$KE = E_{hv} - D_0(O_2 - O) - T_{O_2}(v) + ZPE_{O_2} - F_{vO_2}(J) - E_{O(^3P_j)}$$

$$\sum_{v=0}^{vXmax}\sum_{J=0}^{100} populationX[v,J] * e^{-\frac{(x-energyX[v,J])^2}{2*\left(\frac{1+(instrumental\ function*energyX[v,J]}{2*\sqrt{2*Ln2}}\right)^2}}$$

$$+ \sum_{v=0}^{vamax}\sum_{J=0}^{100} populationa[v,J]$$

$$* e^{-\frac{(x-energya[v,J])^2}{2*\left(\frac{1+(instrumental\ function*energya[v,J]}{2*\sqrt{2*Ln2}}\right)^2}}$$

$$+ \sum_{v=0}^{vbmax}\sum_{J=0}^{100} populationb[v,J]$$

$$* e^{-\frac{(x-energyb[v,J])^2}{2*\left(\frac{1+instrumental\ function*energyb[v,J]}{2*\sqrt{2*Ln2}}\right)^2}}$$

The main difference in the fits here is that the populations for these fits are not based on a rotational temperature. Each peak was fit with a Gaussian whose height, "population," was a number for one (or several) specific O_2 state(s) to scale it to the image. The center position of the Gaussian is based on the energy for the specific v, J state. The "instrumental function" in the equation is to account for the band-width of the laser and error within the imaging process, which gave a 12% error in energy, and is responsible for the width of the Gaussian.

The O_2 states that have populations based on the $O(^3P)$ images and those available from the $O_2(X\ ^3\Sigma_g^-)$ + $O(^1D)$ channel were considered. $O_2(X\ ^3\Sigma_g^-)$ from the $O(^1D)$ channel is notably slower than where the main peak is in many of the images

but can contribute to smaller peaks in some of the images. A few of the images had too broad of a peak or were too noisy to make a reasonable fit in this manner, and for those the vibrational state was estimated but the rotational state was not assigned. For the images in the 329 – 346 nm range, with no complementing O(^{3}P) image, initial fits are made for the vibrational state only.

Ozone dissociation at the wavelength, 321.199 nm serves as a good example image because it has a clear, relatively narrow peak, as can be seen in Figure 2.15.

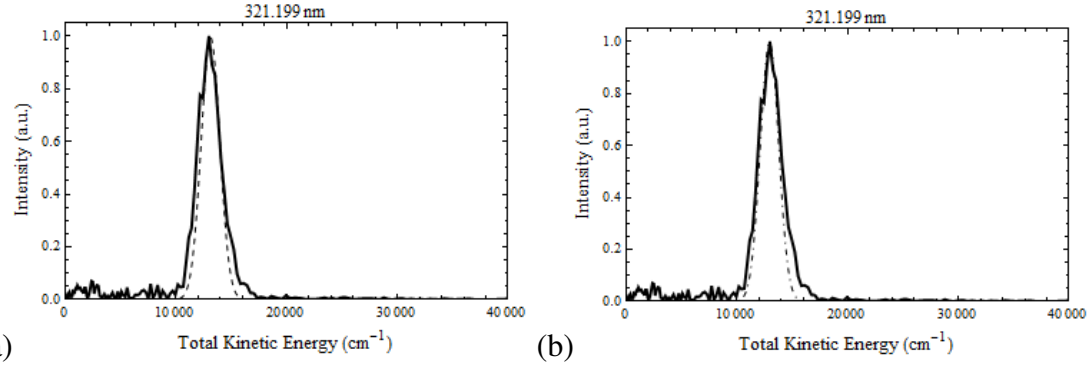

Figure 2.15: The solid black lines are the image intensity. The dashed black lines are fits to a single O_2(E,v,j) state. (a) is a fit with the state assigned by Morrill, $O_2(a^1\Delta_g)$ v = 0, j = 33. (b) is a fit to $O_2(X\,^3\Sigma_g^-)$ v = 5, J = 39. The proper fit could be a sum of two states but this will not ultimately change which states need to be considered for the transitions.

The O_2^+ spectral peak has been assigned by Morrill[3] as originating from the $O_2(a^1\Delta_g)$ v = 0, j = 33 state. At this wavelength $O_2(X\,^3\Sigma_g^-)$ v = 0 – 16, $O_2\,(a^1\Delta_g)$ v = 0 – 10 and O_2 $(b^1\Sigma_g^+)$ v = 0 – 7 are all energetically available. Considering the O(^{3}P$_2$) imaging results places limits on the possible O_2 states because only $O_2(X\,^3\Sigma_g^-)$ v = 1 – 8, O_2 $(a^1\Delta_g)$ v = 0 – 4 and $O_2\,(b^1\Sigma_g^+)$ v = 0 – 5 are created at this wavelength. This image shows no evidence of signal from the O(^{1}D) channel, no slow peak, and so this channel can be ignored for the example. The O_2 image was fit to various v, j states

according to the TKE. Only J = 0 – 40 were considered because at 500 K, the assumed temperature for the $O(^3P_2)$ fits, J above 40 has a very small relative population. Two of the possible fits are shown in Figure 2.15.

For each image a series of fits were found. For the example, 321.199 nm, not only are the two states shown in Figure 2.15 both possibilities, but also possible are $O_2(a^1\Delta_g)$ v = 1, j = 12 and $O_2(X\,^3\Sigma_g^-)$ v = 6, j = 21. The proper assignments could be a combination of two or more of these states. From these images alone it is not possible to differentiate between a single state or a combination of states since both appear to be reasonable. The possible states and a few examples of fits at each wavelength are found in Appendix D.

The fits for this procedure are quite sensitive to the j level. Changing j by ±7, as shown in Figure 2.16, gives notably worse fits. From this analysis it seems reasonable that each possible assignment has a precision of ±7 but within that range could be a single j state or a combination of several.

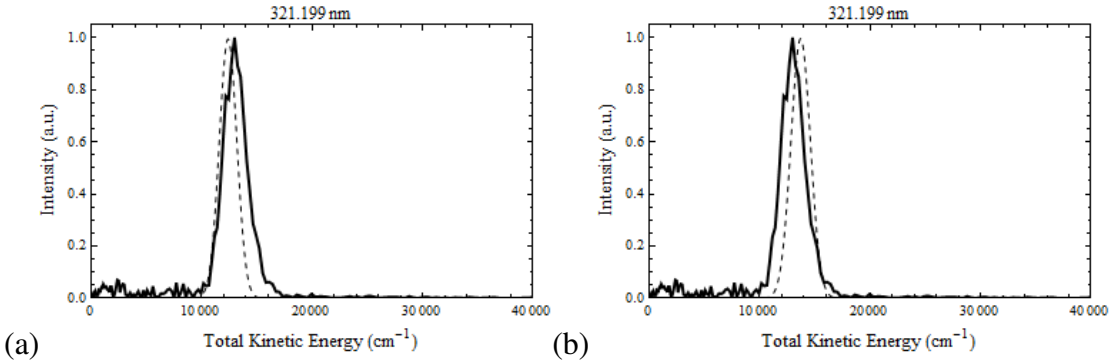

Figure 2.16: This is the same image as Figure 2.15 but with fits to state ± 7 j from Figure 2.15 a. (a) is + 7, $O_2(a^1\Delta_g)$ v = 0, j = 40 (b) is -7, $O_2(a^1\Delta_g)$ v = 0, j = 26

Table 2.5, demonstrates for the example wavelength restricting the lower states that need to be considered for the O_2 yield spectra.

Table 2.5: The first column is the dissociation wavelength, followed by the O_2 electronic states. The vibrational populations are based on the $O(^3P)$ images and given for each electronic state respectively. The possible O_2 lower vibrational (rotational) states for each electronic state are given in the fourth column.

wavelength	Electronic state	Vibrational population	O_2 image fit v(J)
321.199	$X^3\Sigma_g^-$	v = 1 – 8	5(39), 6(21)
	$a^1\Delta_g$	v = 0 – 4	0(33), 1(12)
	$b^1\Sigma_g^+$	v = 0 – 5	None

Once the possible lower states were determined only three transitions are possible: $O_2(d^1\Pi_g d\ ^1\Pi_g)$ v = 2 $\leftarrow\leftarrow$ $O_2(a\ ^1\Delta_g)$ v = 0, $O_2(d\ ^1\Pi_g)$ v = 3 $\leftarrow\leftarrow$ $O_2(X\ ^3\Sigma_g^-)$ v = 6 and $O_2(C\ ^3\Pi_g)$ v = 3 $\leftarrow\leftarrow$ $O_2(X\ ^3\Sigma_g^-)$ v = 6. The possible transitions for large peaks in the images for all the wavelengths are reported in the results section. All possible transitions for the images, including minor peaks can be found in Appendix D.

2.6.2 O_2 spectral analysis

The O_2 spectra in two well know regions, O_2 $d\ ^1\Pi_g$ v = 2 $\leftarrow\leftarrow$ $a\ ^1\Delta_g$ v = 0 and $d\ ^1\Pi_g$ v = 1 $\leftarrow\leftarrow$ $a\ ^1\Delta_g$ v = 0, were compared with literature values[3,6,7,11] to check that O_2 was being detected.

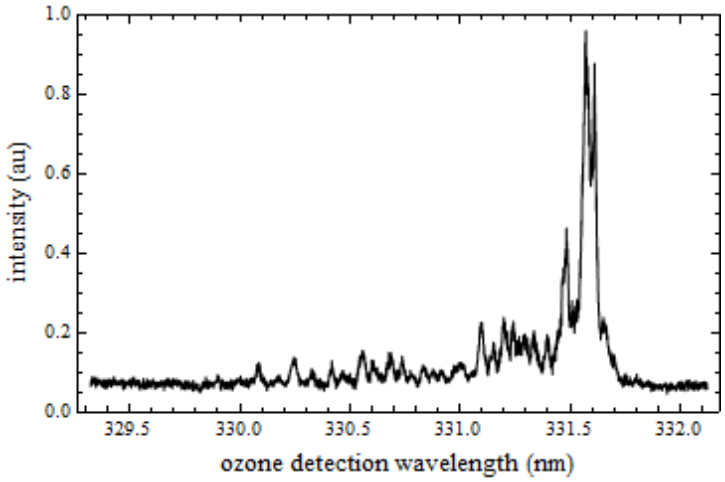

Figure 2.17: Ozone is dissociated by 298 nm and then detected by 2 + 1 REMPI of the $d\ ^1\Pi_g$ v = 1 ←← $a\ ^1\Delta_g$ v = 0 transition

For the $d\ ^1\Pi_g$ v = 1 ←← $a\ ^1\Delta_g$ v = 0 transition, 298 nm was used to dissociate the ozone, as shown in Figure 2.17. It is known the 298 nm dissociation produces $O_2(a^1\Delta_g)$ v = 0, 1 from the $O(^1D)$ channel.[23] Further confirmation can be seen in several images taken within the $d\ ^1\Pi_g$ v = 2 ←← $a\ ^1\Delta_g$ v = 0 range, for each of those $a\ ^1\Delta_g$ v = 0 was one of the states that fit with the main peak in the image.

2.7 Results

The O_2^+ yield spectrum from 321 – 329 nm is reported in Figure 2.18, which is the range that overlaps with the $O(^3P_2)$ spectrum. The short wavelength side (321 – 322 nm) shows the $d\ ^1\Pi_g$ v = 2 ←← $a\ ^1\Delta_g$ v = 0 transition. The $C\ ^3\Pi_g$ v = 2 ←← $a\ ^1\Delta_g$ v = 0 transition, identified by several groups,[3,6] is located at 325 nm and a band is seen there. The possible lower states determined from the image velocity fits are reported in Appendix D.

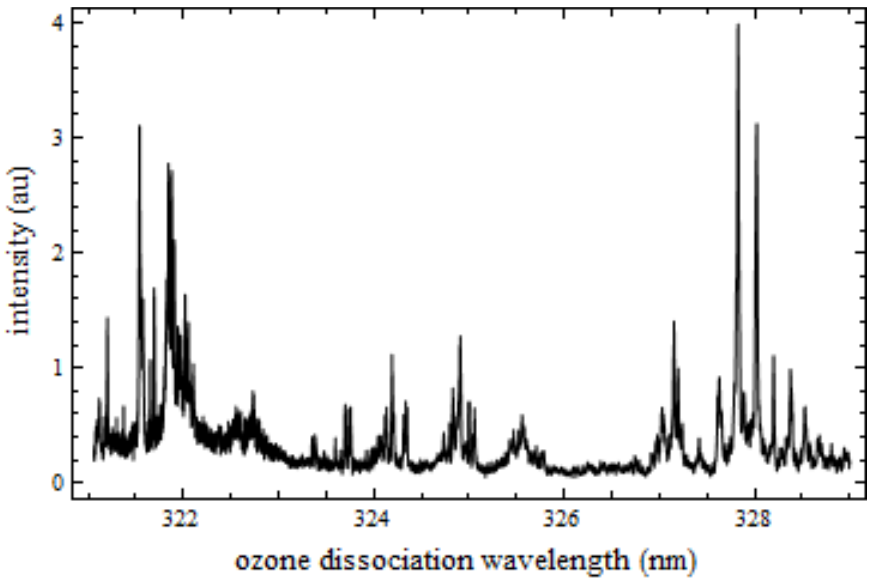

Figure 2.18: O_2^+ signal as a function of wavelength produced from O_3 dissociation and REMPI of O_2 in a single-laser experiment. The O_2^+ signal is a combination of 2+1 REMPI of O_2 ($X\ ^3\Sigma_g^-$), O_2 ($a\ ^1\Delta_g$) and O_2 ($b\ ^1\Sigma_g^+$).

Once the possible lower states are determined, comparing the nearby transitions from O_2 $X\ ^3\Sigma_g^-$, $a\ ^1\Delta_g$ and $b\ ^1\Sigma_g^+$ to $C\ ^3\Pi_g$ and $d\ ^1\Pi_g$, results in a limited number of transitions for each wavelength. The possible transitions are reported for each image along with the O_2 spectra in Figure 2.19. For O_2 images that had a broad range of features, the $O(^3P)$ population distribution was used to determine the transitions. Only the assignments based on high intensity peaks in the images are included. If multiple peaks are comparable in size all assignments are included.

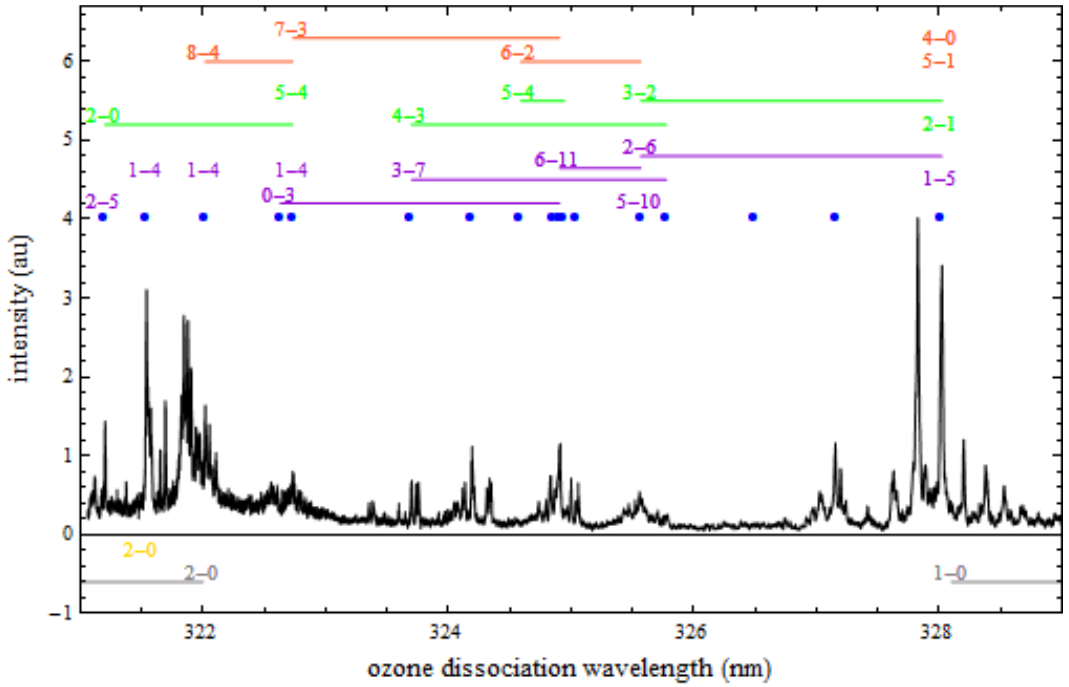

(a)

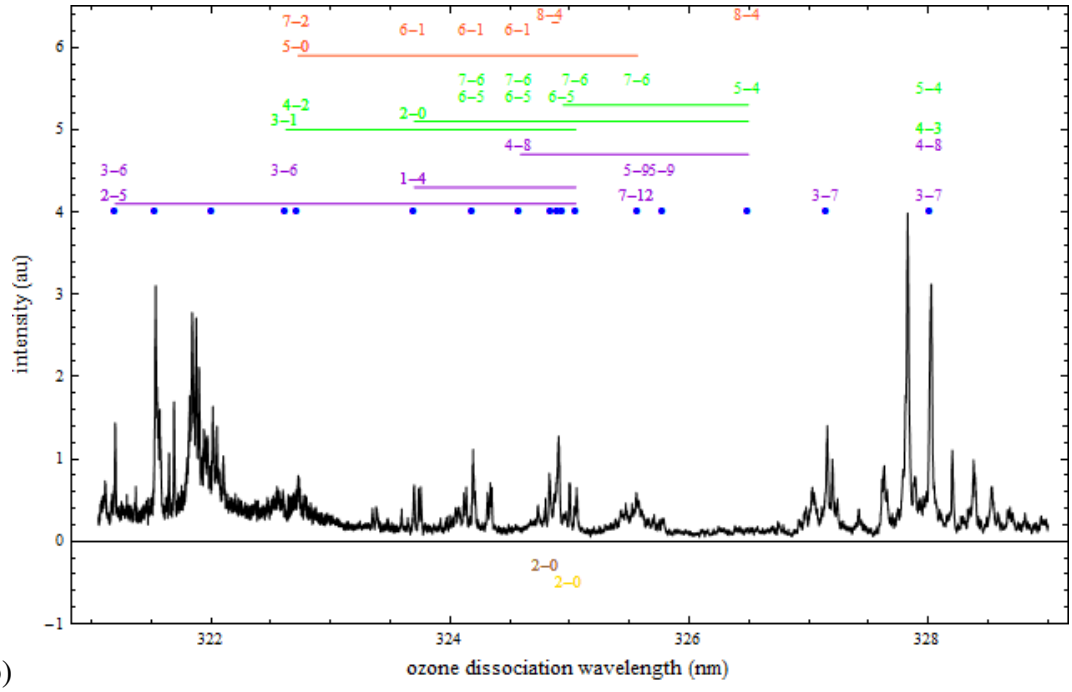

(b)

Figure 2.19: The O_2 yield spectra shown with possible assignments. Purple is for transitions originating in the $X\ ^3\Sigma_g^-$, Green in the $a^1\Delta_g$ and red in the $b^1\Sigma_g^+$. $d^1\Pi_g$ is the upper state for all in (a). $C^3\Pi_g$ is the upper state for all transitions in (b). Below the plots are assignments from references with upper states $d^1\Pi_g$ and $C^3\Pi_g$ for (a) and (b) respectively. Gray is Morrill.[3] Brown is Johnson[11] and Gold is for Ogorzalek Loo.[6,7]

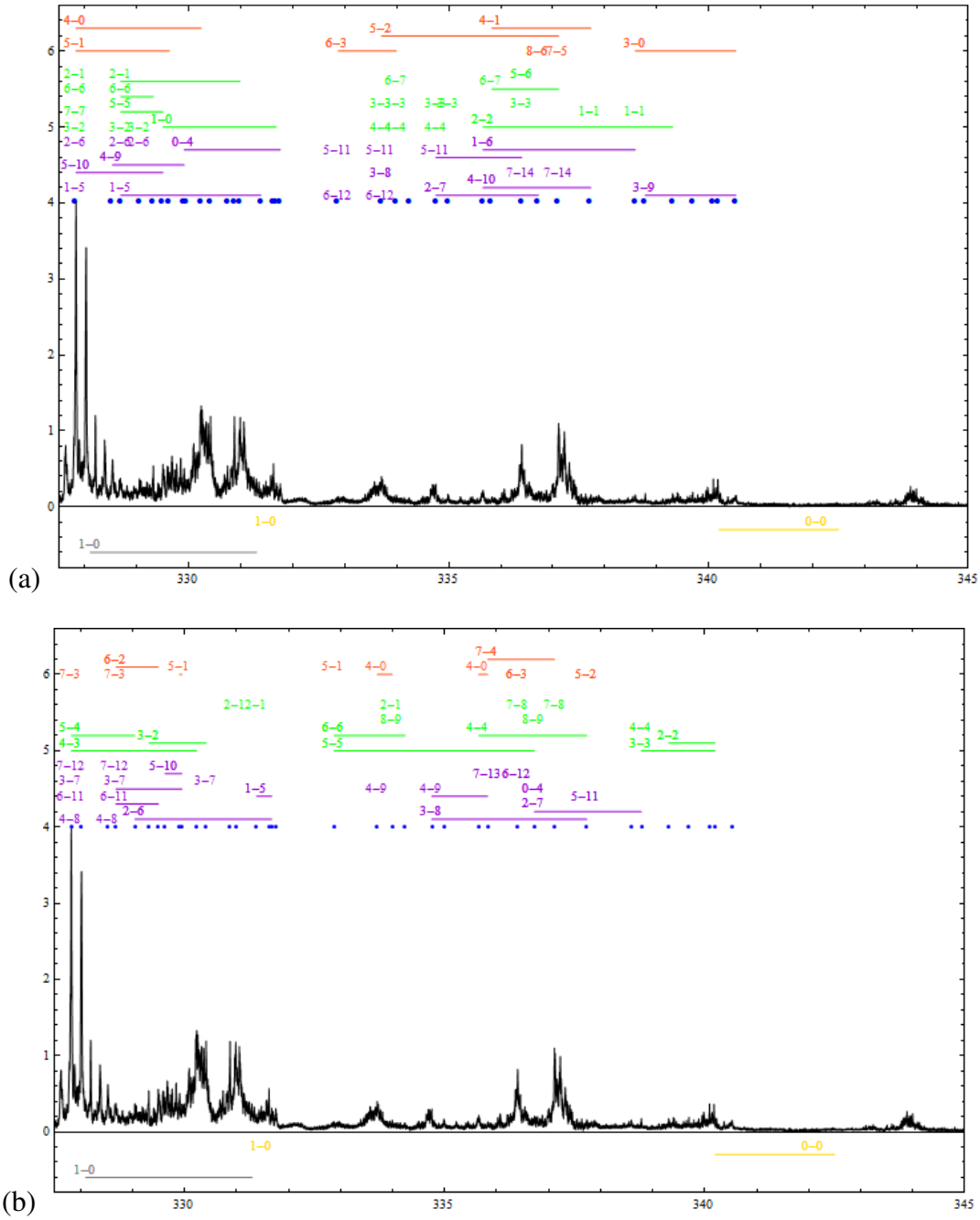

Figure 2.20: The O_2 yield spectra for the 329 – 345 nm region shown with possible assignments. Purple is for transitions originating in the $X\,^3\Sigma_g^-$, Green in the $a^1\Delta_g$ and red in the $b^1\Sigma_g^+$. $d^1\Pi_g$ is the upper state for all transitions in (a). $C^3\Pi_g$ is the upper state for all transitions in (b). Below the plots are assignments from references with upper states $d^1\Pi_g$ and $C^3\Pi_g$ for (a) and (b) respectively. Gray is Morrill.[3] and Gold is for Ogorzalek Loo.[6,7]

At the longer wavelengths, 329 – 345 nm the O_2 spectra and images were also detected. The population distribution were not determined for this region because no $O(^3P)$ data was obtained resulting in more possible states for each image taken as shown in Figure 2.20.

2.8 Discussion

Several wavelengths can be compared with data from other groups. The $d\ ^1\Pi_g$ v = 2 ←← $a\ ^1\Delta_g$ v = 0 transition is a well known transtion. The spectra from the one laser dissociation and O_2 detection is compared with 266 nm dissociation and O_2 detection in the same range, as shown in Figure 2.21. The 266 nm spectra is used as a check because it is in the main Hartley band, producing 90% $O(^1D)$ + $O_2(a\ ^1\Delta_g)$. The spectra also agrees with spectra shown by Morrill.[3]

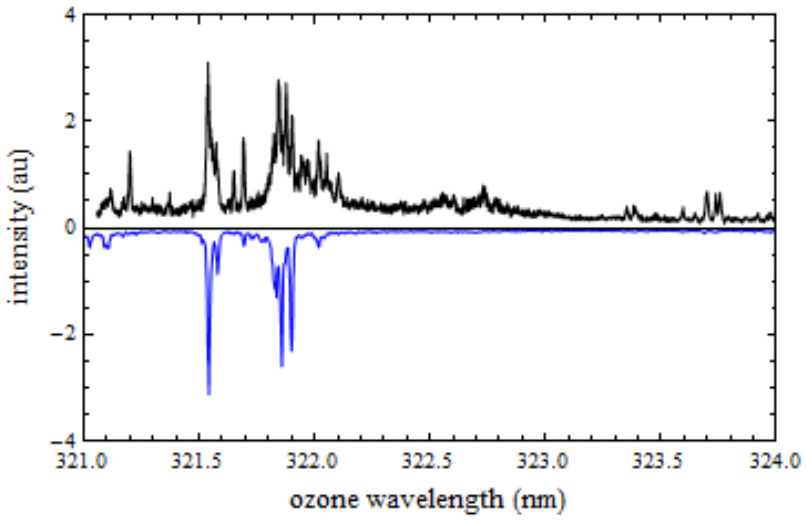

Figure 2.21: The positive plot (black) is the single laser ozone dissociation and O_2 REMPI. The negative signal (blue) is from the 266 nm dissociation and O_2 detection from 321 – 324 nm.

The images taken at 321.199 nm, 321.538 nm and 322.016 nm are all within the range of the $d^1\Pi_g$ v = 2 $\leftarrow\leftarrow$ $a^1\Delta_g$ v = 0 transition. The 321.199 nm fits with the same $a^1\Delta_g$ v = 0, J state as assigned by Morrill et al. for the same peak. Both 321.538 nm and 322.016 nm have possible assignments to $a^1\Delta_g$ v = 0 within 6 rotational states of the Morrill assignments. Of these three peaks our $a^1\Delta_g$ v = 0 possible assignment for 322.016 nm is the most different from the Morrill assignment but the frequency for this peak is also a few wavenumbers different from the frequency they detected, which may explain the shift in j. The band located around 325 nm has previously been assigned to the $C^3\Pi_g$ v = 2 $\leftarrow\leftarrow$ $a^1\Delta_g$ v = 0 transition. The images in this range all fit well with a $O_2(a^1\Delta_g)$ v = 0 assignment.

Denzer et al.[24] measured the TOF of $O_2(a^1\Delta_g)$ from dissociation of ozone at 321.9 nm and observed two peaks. They attribute the fast velocity peak to $O_2(a^1\Delta_g)$ + $O(^3P)$ and a slow velocity peak attributed to the dissociation of excited ozone to form $O_2(a^1\Delta_g)$ + $O(^1D)$. Images in this study with close dissociations wavelengths, 322.016 and 321.538 nm, can be compared to the Denzer et al. results. The 322.016 nm image does have slow and fast velocity peaks. The fast velocity peak fits well with $O_2(a^1\Delta_g)$ v = 0 from the $O_2(a^1\Delta_g)$ + $O(^3P)$ channel. While their assessment of the slow velocity peak is one possibility, the peak also fits with high vibrational levels of $O_2(b\ ^1\Sigma_g^+)$ or $O_2(X\ ^3\Sigma_g^-)$ from the $O_2(X\ ^3\Sigma_g^-)$ + $O(^1D)$ channel. There are transitions for $O_2(X\ ^3\Sigma_g^-,)$ and $O_2(b\ ^1\Sigma_g^+)$ in the range as well, so it is not clear which channel is actually causing the slow peak. Images taken at 321.538 nm and 321.199 nm only have the fast velocity peak.

2.9 Conclusion

The relative populations of the O_2 electronic and vibrational states for a variety of wavelengths in the 321 - 329 nm dissociation of ozone have been reported along with an estimated rotational temperature. The reason for the wavelength dependent change in the ratio between the three channels is still unclear. Investigation through calculation may lead to understanding of the dynamics of the photodissociation. The images have limited the possible O_2 transitions to a few choices but further analysis is needed to obtain simulated spectra and proper assignments for the entire range.

References

1) O. Tokel, J. Chen, C.K. Ulrich, P.L. Houston, *J. Phys Chem. A*, **114**, 11292 (2010)
2) O. Tokel, Ph.D. Thesis, Cornell University, 2011
3) J.S. Morrill, M.L. Ginter, E.S. Hwang, T.G. Slanger, R.A. Copeland, B.R. Lewis, S.T. Gibson, *J. of Molec. Spec.* **219**, 200 (2003)
4) J. S. Morrill, M.L. Ginter, B.R. Lewis, and S.T. Gibson, *J. Chem. Phys.* **111**, 173 (1999)
5) B.R. Lewis, S.T. Gibson; J.S. Morrill; M.L. Ginter, *J. Chem. Phys.* **111**, 186 (1999)
6) R. Ogorzalek Loo, W. J. Marinelli, P. L. Houston, S. Arepalli, J. R. Wiesenfeld, R. W. Field, *J. Chem. Phys.* **91**, 5185 (1989)
7) R. Ogorzalek Loo, Ph. D. Thesis Cornell University, 1989
8) A. Sur, L. Nguyen, N. Nikoi, *J. Chem. Phys.* **96**, 6791 (1992)
9) A. Sur, R. S. Friedman, P. J. Miller, *J. Chem. Phys*. **94**, 1705 (1991)
10) P. O'Keeffe, T. Ridley, K.P. Lawley, R.R.J. Maier, R.J. Donovan, *J. Chem. Phys*., **110**, 10803 (1999)
11) R. D. Johnson III, G. R. Long, and J. W. Hudgens, *J. Chem. Phys.* **87**, 1977 (1987)
12) D. J. Bamford, L. E. Jusinski, W. K. Bischel, *Phys. Rev. A.* **34**, 186 (1986)
13) B. Buijsse, W. J. van der Zande; A. T. J. B. Eppink, D. H. Parker; B. R. Lewis, S. T. Gibson, *J. Chem. Phys.* **108**, 7229 (1998)

14) J.D. Geiser; S.M. Dylewski; J.A. Mueller, R.J. Wilson; R. Toumi; P.L. Houston, *J. Chem. Phys.* **112**, 1279 (2000)

15) (BASEX) *Rev. Sci. Instrum.* **73**, 2634 (2002).

16) K. Takahashi, M. Kishigami, N. Taniguchi, Y. Matsumi. and M. Kawasaki, *J. Chem Phys.* **106**, 6390 (1997)

17) J.-C. Nieh, J. J. Valentini, *J. Chem. Phys.* **91** 1370 (1987)

18) L. Herzberg and G. Herzberg, *Astrophysical Journal* **105**, 353 (1947)

19) H. D. Babcock and L. Herzberg, *Astrophysical Journal* 108, 167 (1948).

20) P. O'Keeffe, T. Ridley, K.P. Lawley, R.J. Donovan, *J. Chem. Phys*., **115**, 9311 (2001)

21) Z-W Qu, H. Shu, M. Tashiro, and R. Schinke, S. C. Farantos, *J. Chem Phys.* **120**, 6811 (2004)

22) H. Lefebvre-Brion and R. W. Field, The Spectra and Dynamics of Diatomic Molecules. Elsevier Academic Press 2004.

23) S. M. Dylewski, J. D. Deiser and P. L. Houston, *J. Chem. Phys.* **115**, 7460 (2001)

24) W. Denzer, G. Hancock, J.C. Pinot de Moira, P. L. Tyley, *Chem. Phys.* **231**, 109 (1998)

CHAPTER 3

A CROSSED MOLECULAR BEAM APPARATUS: O(^{1}D) DEACTIVATION

3.1 Introduction to Bimolecular Collisions

The study of bimolecular collisions is important due to the vital role they play in atmospheric chemistry. Although photodissociation is the initial step in many atmospheric cycles, collisions of the products with other atmospheric gases can lead to the exchange of energy or to chemical reactions. Depending on the chemical interaction, energy and dynamics of the collision, the collision partners can exchange energy or react. The lifetime of the complex also plays a role in the outcome of the collision, which often can be determined from the product distribution. Upon collision energy transfers can occur redistributing the energy between partners causing changes in the state or translational energy. Collisions can also result in reactions where available reaction pathways will depend on collision energy and available internal energy of the reactants.

A convenient way to picture a molecular system is through the potential energy surface (PES) which can be calculated through experimental and theoretical methods. The potential energy surface is a plot of the energy of a system as a function of geometry, usually displayed with certain coordinates held constant. Several atmospheric examples, which will be discussed in further detail in following sections, are the collisions of O(^{1}D) with other small atmospheric molecules. An example of

collisions resulting in energy exchange is $O(^1D)$ with O_2, which can result in the production of $O(^3P) + O_2(b^1\Sigma_g^+)$. $O_2(b^1\Sigma_g^+)$ plays a role in the day glow of the earth atmosphere. An example of a reactive collision is $O(^1D)$ with N_2O, which can result in a reaction which contributes to the catalytic destruction of ozone as will be discussed in Chapter 4.

Determining the velocity and angular distribution of collision products is important for learning about the product state distributions and the mechanism of the collision. Using molecular beam techniques to study molecular collisions is beneficial because the reactant molecules have a narrow velocity distribution and thus the collision energy will be well defined. Well-defined collision partners and collision energy combined with conservation of energy and momentum allow the product velocity and angular distribution to be used to determine the states of the products. These results can be obtained using a single beam or crossed molecular beams with either a rotatable detector or an imaging apparatus. A benchmark crossed beam example is the reaction of $F + H_2$ studied by Neumark et al.[1,2] In these studies the HF flux was measured as a function of scattering angles. The angular distribution depends on the vibrational level of HF with HF v = 1 and 2 being predominantly backward scattered and v = 3 has more forward scattering. The information from the velocity flux maps, an example of which is Figure 3.1, can be used to make suggestions about the potential energy surface (PES) of the reaction.

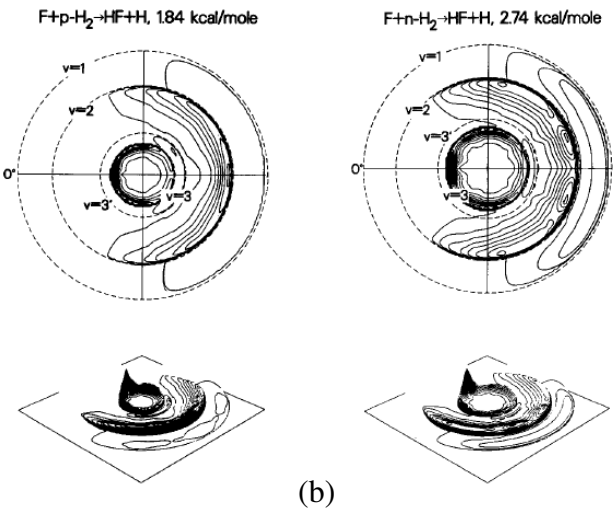

(a) (b)

Figure 3.1: Center-of-mass velocity flux contour map (a) F + p-H_2 1.84kcal/mol and (b) F + n-H_2 2.74kcal/mol. Reprinted with permission from reference 2. Copyright JCP 1985, American Institute of Physics.

Velocity mapped imaging (VMI) can be used to obtain the flux from a collision event. A benefit of this method is the detection apparatus is more compact then using a rotating detector and the full product sphere can be obtained in a single experiment. Single beam experiments generally have larger signal but the angular distribution is more difficult to determine because the observed distribution is a combination of the angular distribution from a reactant's photodissociation and the distribution from the collision. The first reactive collision studied using VMI was observed by Chandler in a single beam experiment.[3] Soon after that VMI was combined with crossed molecular beam experiments, the first being observation of an inelastic scattering event,[4] followed quickly by observation of a reactive collision.[5] The inelastic scattering of NO by Argon atoms was done by Suits et al. using the detection of state specific NO. Kitsopoulos et al.[5] imaged D ionized by 1 + 1′ REMPI from the reaction of H + D_2 at two different collision energies. Their lower collision

energy experiment agrees well with theoretical calculations. Since these initial studies, the field has continued to grow and develop.

An inelastic scattering event is more simple then a reactive scattering event, and this is why inelastic scattering was used to set up the dual beam apparatus in our study. Reactive collisions are more difficult because they involve the exchange of molecules and a consequent change in the relative velocities. A reactive collision is examined closely in the following chapter, using a single beam technique.[6,7] It was also attempted in the dual beam set up as is discussed by Tokel,[6] but the signal was too small for detailed analysis.

3.2 Inelastic Collisions: Deactivation of $O(^1D)$

Although it is a minor species in the atmosphere, $O(^1D)$ is important in atmospheric chemistry because it is in steady state concentration relationship with ozone and because it is part of several pathways that are responsible for the catalytic destruction of ozone. Even a small change in the $O(^1D)$ concentration will affect the ozone concentration, it is therefore important to understand even seemingly minor pathways in the atmospheric removal of $O(^1D)$. The electronic deactivation of $O(^1D)$ to the ground electronic state is one way it is removed from the atmosphere, so understanding processes such as 1 – 3 are important.

$$O(^1D) + N_2 \rightarrow O(^3P) + N_2 \quad (1)$$

$$O(^1D) + O_2 \rightarrow O(^3P) + O_2 \quad (2)$$

$$O(^1D) + CO_2 \rightarrow O(^3P) + CO_2 \quad (3)$$

N_2, O_2 and CO_2 are prominent in the atmosphere and have high deactivation cross sections despite the spin-forbidden nature of the deactivation by N_2 and CO_2. All three deactivations have fast rates of reaction, $2.6*10^{-11}$ cm^3 $molec^{-1}$ sec^{-1}, $4.0*10^{-11}$ cm^3 $molec^{-1}$ sec^{-1}, $1.1*10^{-10}$ cm^3 $molec^{-1}$ sec^{-1} respectively.[8] Deactivation by either N_2 or CO_2 appears to occur through the formation of a complex with a lifetime of a few vibrational periods, during which time several curve crossing events occur on the potential energy surface.

The isotope exchange reaction between $O(^1D)$ and CO_2 has been studied by Perri et al.[9,10] in a crossed molecular beam set up to determine the amount of quenching occurring in the exchange. In these studies the $^{46}CO_2$ was detected to determine the branching ratio between reaction 4 and 5, which occur through a long lived CO_3 complex, at two different collision energies.

$$^{18}O(^1D) + {}^{44}CO_2 \rightarrow {}^{16}O(^3P) + {}^{46}CO_2 \qquad (4)$$

$$^{18}O(^1D) + {}^{44}CO_2 \rightarrow {}^{16}O(^1D) + {}^{46}CO_2 \qquad (5)$$

The $^{18}O(^1D)$ reactant was produced from the dissociation of $^{36}O_2$. After collision, the time of flight spectra of the $^{46}CO_2$ is detected by a rotating detector at various angles. The CO_2 product velocity flux, shown in Figure 3.2, was determined from simulation to fit the time of flight spectra. At the higher collision energy of 7.7 kcal/mol, the isotope exchange channel was accompanied by quenching in 68% yield and by non-quenching in 32% yield. At the lower collision energy, 4.2 kcal/mol, the percent with quenching increases to 84% and that with non-quenching decreases to 16%. Only the

isotopic exchange channels are observed in this study; no information is available on the non-isotope-exchange channels.

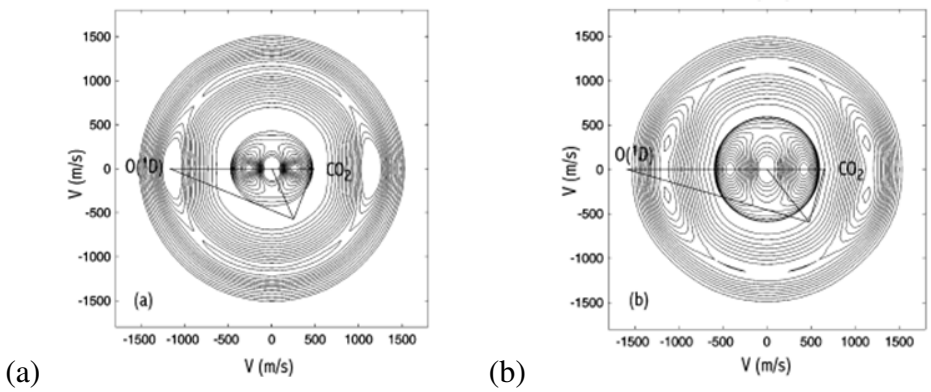

(a) (b)

Figure 3.2: The center-of-mass product velocity flux diagram of the $^{46}CO_2$ from collision with $O(^1D)$ with a collision energy of (a) 4.2 kcal/mol and (b) 7.7 kcal/mol. Figure reprinted (adapted) with permission from reference 10. Copyright 2004 American Chemical Society.

Quenching of $O(^1D)$ by N_2 has been studied both experimentally and through calculations. Tully[11] calculated with a RRKM based collision complex model that approximately 30% of the exothermicity from the quenching should go to N_2 vibrational excitation and that the cross section for quenching is large. Zahr et al.[12] theoretically found similar results as Tully: a long-lived complex resulted in a large cross section and vibrationally excited N_2. Both of these studies agree with experimental studies. Slanger and Black[13] studied $O(^1D)$ quenching by N_2 experimentally. In this study they compared the $O(^1D)$-CO system with the $O(^1D)$-N_2 and determined that 33% of the $O(^1D)$ energy is converted to N_2 vibrational energy. To do this they first observed the results of $O(^1D)$ electronic-vibrational transfer with CO then added N_2 to the system and observed the change. Matsumi et al.[14] used

vacuum ultraviolet laser induced fluorescence in a bulb set up to study the intersystem crossing of $O(^1D)$ to $O(^3P)$ from collision with several molecules including N_2. At a collision energy of 11.4 kcal/mol they found the ratio between formation of the different levels of $O(^3P_j)$ where j = 0,1,2 to be 0.23±0.05/0.35±0.05/1. They also determined that (30 ± 7) % of the electronic energy was transferred to internal excitation of N_2 based on the Doppler profiles of the $O(^3P_j)$ products. Experimental comparison of the translational relaxation and electronic quenching of hot $O(^1D)$ by collision with N_2 determined that electronic quenching is faster.[15] Matsumi et al. detected the increase in $O(^3P)$ and the change in the Doppler profiles of $O(^1D)$ from $O(^1D)$ collision with N_2 in a gas cell at room temperature. They observed that 40% of the $O(^1D)$ are electronically quenched before translational relaxation when the collision energy is 9.8 kcal/mol.

The goal of this study is to detect the $O(^3P_2)$ from electronic quenching of $O(^1D)$ from N_2 and O_2. The $O(^3P_2)$ velocity would then be used to determine the partner molecule's vibrational distribution after quenching. The second important aspect of this work is the development of a crossed molecular beam imaging apparatus which can be used for other studies of bimolecular collisions in the future.

3.3 Experiment: Deactivation of O(^{1}D) and Development of a Crossed Molecular Beam Apparatus

The experiment for studying deactivation of $O(^1D)$ was done utilizing the dual beam apparatus, whose original development has been described previously.[6] $O(^3P_2)$ from the deactivation of $O(^1D)$ was detected by 2+1 REMPI. $O(^1D)$ was obtained by

O_3 dissociation with a polarized laser in the upper beam. The laser polarization was set such that the $O(^1D)$ intersects perpendicularly with the second beam, consisting of a small atmospheric gas such as N_2 (Ultra high purity 99.999%, Airgas) or O_2 (99.997% purity, Matheson Trigas). Throughout the $O(^1D)$ deactivation study several improvements were made to the crossed beam apparatus which are discussed in the flowing sections.

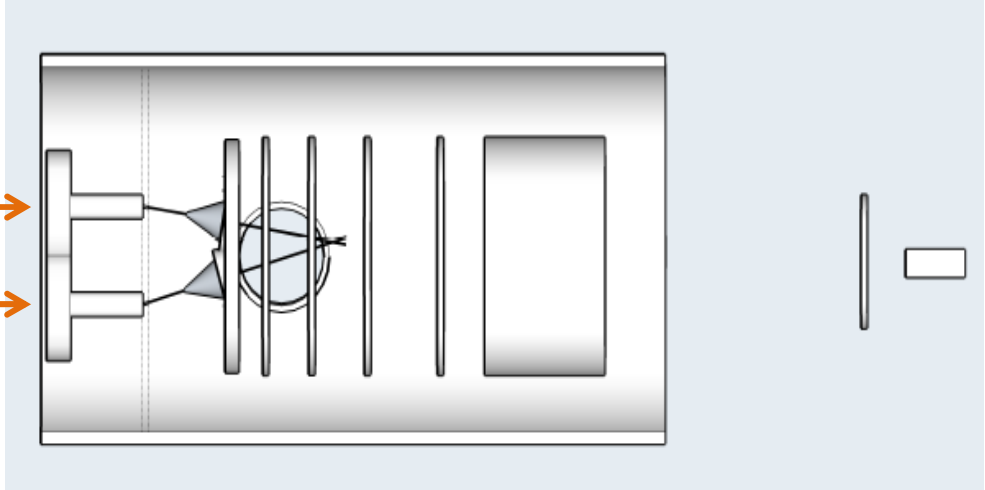

Figure 3.3: A side view of the inside of the crossed molecular beam chamber. The upper beam of O_3 is dissociated with a vertically polarized laser causing $O(^1D)$ to fly perpendicularly to the lower beam for collision with the lower beam, N_2 in the diagram. The apparatus is the same one used for the photodissociation studies described in Chapter 2. It was previously described in the dissertation by Onur Tokel.[6]

The two beams are positioned so that at the center of the interaction region they are 10 mm apart with the "lower" beam centered to the detector. The two beams are shown in Figure 3.3.

Ozone is produced in a commercial ozone generator (LG – 7, CD Laboratory) and stored on silica at -40 C. A carrier gas, such as He, or Ar is flowed over the silica

gel resulting in a mixture consisting of approximately 6 % ozone for the upper beam. The carrier gas contributes to the velocity of the $O(^1D)$ thus affecting when and where it reached the lower beam. Both Ar and He were used periodically to change the properties of the $O(^1D)$ in attempts to increase the $O(^3P)$ signal. The lower beam consists of another small atmospheric gas; both O_2 and N_2 were tried in this work. The gases were supersonically expanded through their respective nozzle and skimmer into the interaction region, defined as the region between a high voltage repeller and an extractor electrode.

A disadvantage of the experimental setup was that it employed a single source chamber for the two beams.

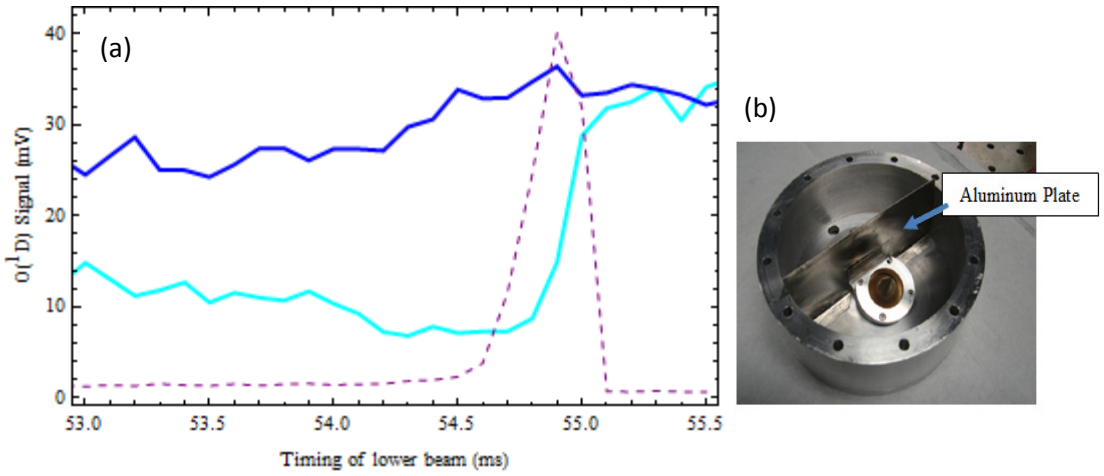

Figure 3.4: The $O(^1D)$ signal with dark blue (—) and without, light blue (—) nozzle separation by an aluminum plate. The dashed line (- - -) is the temporal location of the lower beam. b: close up of nozzles with plate.

In this configuration, the beams originally interfered with each other when operating simultaneously, as demonstrated in Figure 3.4 a. Inserting a small aluminum plate

between the two nozzle and skimmer pairs, shown in Figure 3.4 b, provided a simple solution.

3.3.1 O(^{1}D) Reactant

Determining the characteristics of the O(^{1}D) beam was an important first step in the experiment. The O(^{1}D) is formed by dissociation of the ozone in the upper beam by vertically polarized light so that the O(^{1}D) intensity in the lower beam is maximized. The wavelength of the dissociation laser controls the velocity of the O(^{1}D) and therefore the collision energy. Several wavelengths were used: 266, 280, 285 and 290 nm. The 266 nm light was created from the forth harmonic of a Nd:Yag laser (Spectra Physics GCR 270). Wavelengths from 280 – 290 nm were created from doubling the output of a tunable dye laser (Spectra Physics Quanta Ray PDL-2) pumped by the 532 nm output from a ND:Yag laser. The O(^{1}D) was detected by 2 + 1 REMPI with 203.7 nm. It was first found in the upper beam, the probe laser was then moved down and its timing delayed until the location and time of overlap with the lower beam were determined. For each dissociation wavelength there were several O(^{1}D) peaks which can be used based on the vibrational state of the partner $O_2(a^1\Delta_g,)$ as shown in Figure 3.5. As can be seen in Figure 3.5, there are several peaks of O(^{1}D) signal that can be used for the deactivation based on the dissociation laser used. Because the likelihood of collision decreases with reactant velocity for collisions involving attractive forces, it seems intuitive to use O(^{1}D) with slower velocity. However often in the O(^{1}D) case the channels creating slower O(^{1}D) are produced less

efficiently then the fast O(^{1}D). A balance must be struck between the amount and velocity of O(^{1}D) to maximize the potential signal from collision.

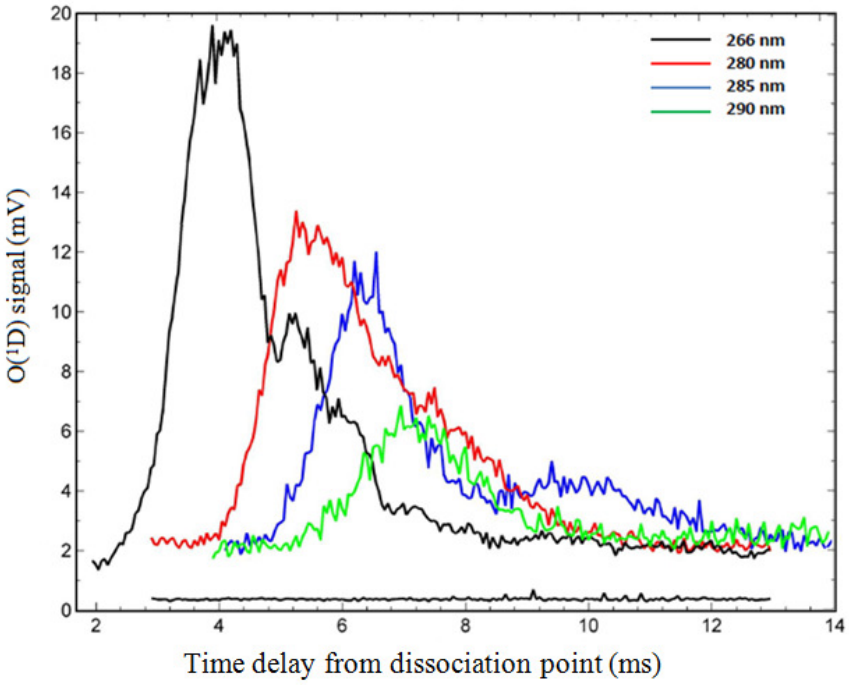

Figure 3.5: O(^{1}D) signal at the lower beam from ozone dissociation in the upper beam with several dissociation wavelengths.

Ultimately the effect of collision energy on the electronic deactivation of O(^{1}D) could be determined by using several of the O(^{1}D) peaks with different velocities for the collision.

3.3.2 Deactivation of O(^{1}D)

The location of ozone dissociation and the location of the probe laser in the lower beam were chosen so that the O(^{1}D) velocity was perpendicular to the direction of the lower beam. Probing of O(^{3}P$_2$) was performed by 2+1 REMPI, via the O(3p^3P$_2$

$\leftarrow\leftarrow 2p^3P_2$) transition.[17] One mJ/pulse of 225.65 nm light was used from the doubled output of dye laser (Spectra Physics Quanta Ray PDL-2 or Scanmate 2E) pumped by the 355 nm from a Nd:Yag laser (Spectra Physics GCR 230). The 225.65 nm was aligned to overlap the 203.7 nm to ensure proper overlap with the collision region.

The $O(^3P_2)$ created by the collision were ionized by the 225.65 nm light at a location between two high voltage electrodes. The voltages of the repeller and extractor were set to allow the ions to fly through the center holes of two grounded electrodes and through a field-free flight tube to a position-sensitive dual plate MCP/Phospher set up. For measurement of total ion flux, a PMT recorded the light from the phosphor, while for velocity mapped images, the light was focused onto a CCD camera. As the ions moved from the dissociation point to the detector they expanded according to the velocity resulting from the collision event. The detector was gated to allow for the detection of O^+ ions based on the time of flight.

3.3.3 Improvements: Decreasing the background

Several background sources greatly impede obtaining the experimental signal. One background source is signal from ionization of heavy molecules or atoms from the dissociation laser that reach the detector at the same time as the $O(^3P)$ from the probe laser. These molecules are ambient in the chamber or enter with the upper beam. Because the dissociation laser arrives in the chamber earlier than the probe laser, these heavier ions can reach the detector at the same time as the $O(^3P)^+$ ions from the probe laser.

One strategy to limit the background signal from this source was to pulse the voltage on the repeller in the ion optics rather than to use a constant voltage. The repeller is held at a low voltage until approximately 50 ns before the probe laser enters the chamber at which point it increases to the proper voltage for the ion optic lens to focus the O ions to the detector. This ensures that only ions created by the probe laser will reach the detector, as can be seen in Figure 3.6.

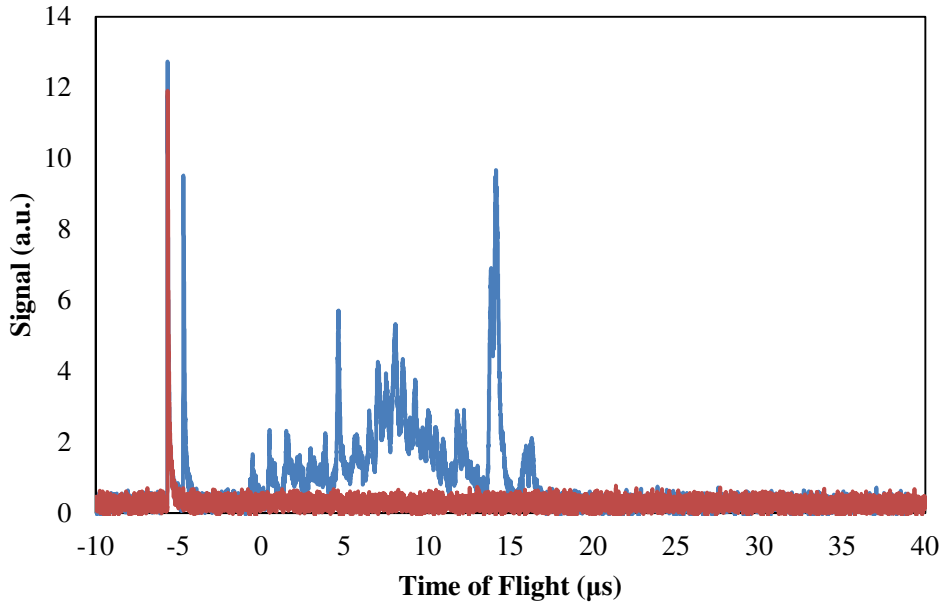

Figure 3.6: Background signal from 285 nm laser with (blue) the repeller voltage constant and with (red) the repeller pulsing such that the repeller turns on after the 285 nm laser is in the chamber but before the probe laser arrives.

Dissociation of ozone in the Hartley band produces $O(^3P)$ as well as $O(^1D)$ although in a much smaller amount, 90 % $O(^1D)$: 10 % $O(^3P)$. This signal from the dissociation laser appears as a dot, or short line, off center from the collision because the $O(^3P)$ is travelling faster than the $O(^1D)$. This background source is unavoidable

but should be easily subtracted from the overall signal because its velocity and angular distribution is very different from the experiment signal.

A third background source is caused by dissociation of ozone by the probe laser at 225.65 nm. Adjusting the timing of the beams and lasers and putting the aluminum plate to separate the two nozzles, significantly reduces this background, but there is still some residual in the center of the images. As can be seen in Figure 3.7, the largest signal from the probe dissociation is less than 1200 mm/sec. This background will overlap with any $O(^3P)$ from the full experiment that is partnered with high vibrational levels of N_2, the slowest $O(^3P)$.

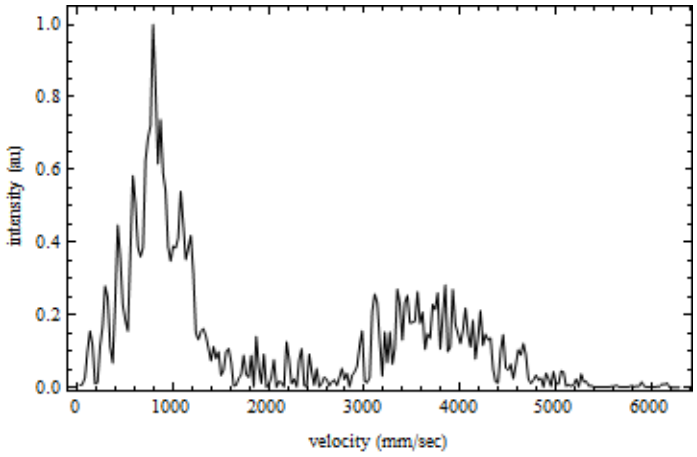

Figure 3.7: The velocity distribution of $O(^3P_2)$ from ozone dissociation by the probe laser, 225.65nm.

3.4 Expected Signal

Based on the velocity of the reactants, $O(^1D)$ and N_2 or O_2, the possible velocity of the product $O(^3P)$ can be calculated. A straight forward way to do this is

through Newton diagrams. A Newton diagram puts the reactants into the center-of-mass frame which through conservation of energy and momentum can be used to determine the product relative velocities. An example of this can be seen in Figure 3.8.

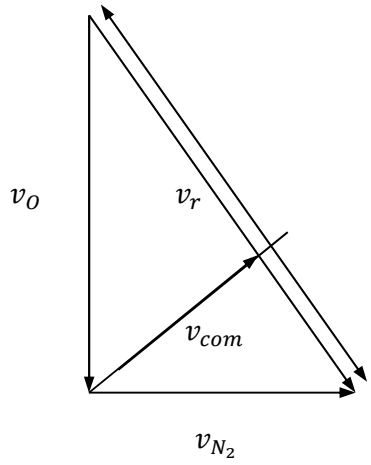

Figure 3.8: The Newton diagram for the collision of O + N_2. The figure would be the same for O_2 except $\boldsymbol{m_{O_2} v_{O_2}{}^2}$ replaces $\boldsymbol{m_{N_2} v_{N_2}{}^2}$ in the following equations. The $\boldsymbol{v_O}$ will depend on the dissociation laser wavelength.
$\boldsymbol{KE = \frac{1}{2} m_O v_O{}^2 + \frac{1}{2} m_{N_2} v_{N_2}{}^2} \quad \boldsymbol{KE = \frac{1}{2} \mu v_r{}^2 + \frac{1}{2} M v_{com}{}^2}$

Electronic quenching of O(^{1}D) to O(^{3}P) releases 1.996 eV of energy. That energy combined with the collision energy is available for vibrational excitation of N_2 and translational energy of N_2 and O(^{3}P) products. The expected velocities can be determined for O(^{3}P) from O(^{1}D) + N_2 corresponding to the various vibrational levels of N_2 that can be reached, as shown in Figure 3.9, but the actual distribution will depend on which of the N_2 states are populated.

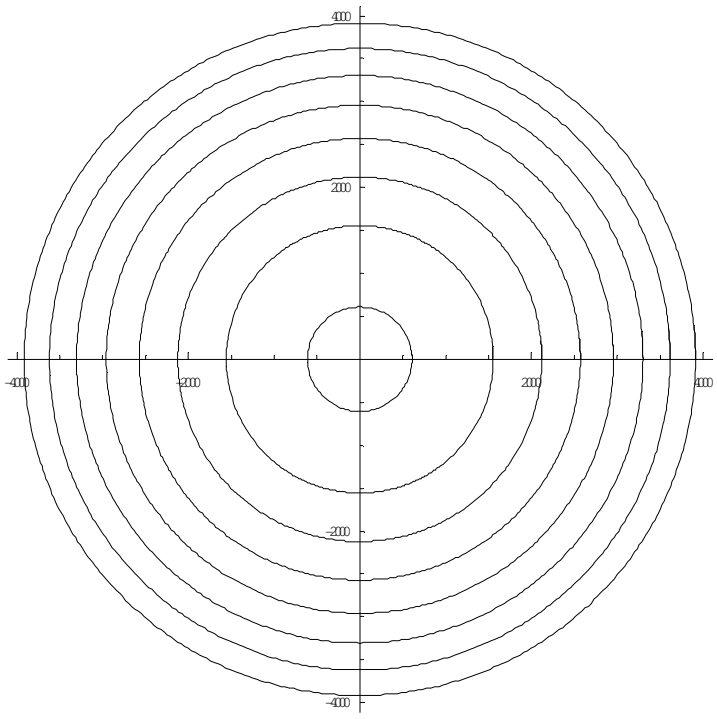

Figure 3.9: The calculated $O(^3P)$ corresponding to N_2 v = 0 – 7, J = 0 from the collision of N_2 with $O(^1D)$. The $O(^1D)$ is from the dissociation of ozone with 285 nm.

The calculated rings are based on only N_2 vibrational excitation with rotational levels of j = 0 giving the maximum velocity for $O(^3P)$ corresponding to each N_2 vibrational state. In reality multiple rotational levels would be populated which would broaden and shift the actual signal.

The possible velocity of $O(^3P)$ from quenching of $O(^1D)$ by O_2 can be calculated in the same way. $O(^3P)$ from $O(^1D) + O_2$ can only reach three vibrational levels of O_2 and thus three circles are seen in Figure 3.10.

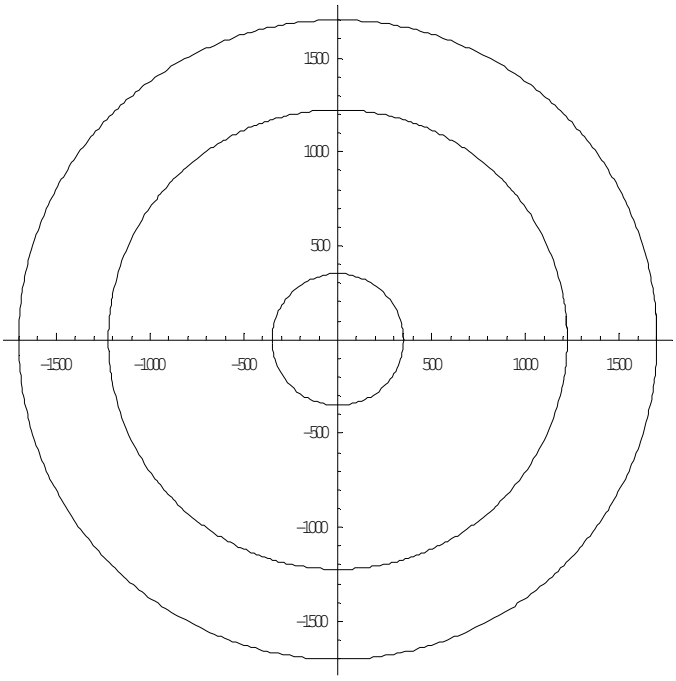

Figure 3.10: The calculated $O(^3P)$ corresponding to O_2 v = 0 – 2, J = 0 from the collision of O_2 with $O(^1D)$. The $O(^1D)$ is from the dissociation of ozone with 285 nm.

As with the $O(^3P)$ from N_2 diagram, only the j = 0 levels are calculated for simplicity. In the quenching by O_2 case there is an extra background source that needs to be addressed. The O_2 reactant is dissociated by the 225.65 nm probe laser resulting in $O(^3P)$ which can be detected by that same laser. This signal will fall close to the $O(^3P)$ from quenching corresponding to the O_2 v = 1 state. Although unavoidable, this signal is a narrow peak and hopefully can be subtracted from the overall signal to obtain the quenching signal.

3.5 Initial Results

The initial images of the $O(^1D) + N_2 \rightarrow O(^3P) + N_2$, appeared to have some signal but the background was too large to determine the velocity from the signal, Figure 3.11.

(a) 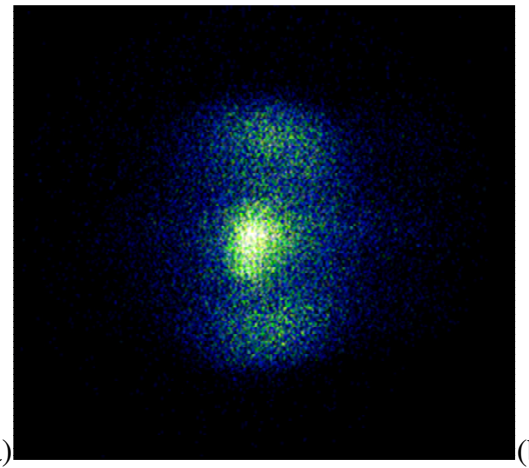 (b) 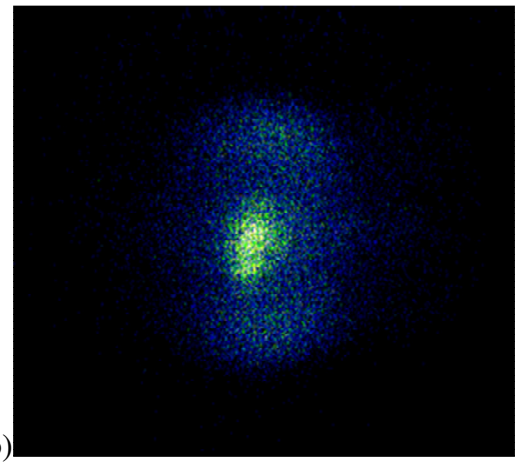

Figure 3.11: The original images of $O(^1D)$ quenching by N_2. (a) Has all lasers and molecular beams at the correct timing to give the expected signal while (b) has the N_2 beam timing set so that no N_2 will be in the interaction region with the $O(^1D)$ and probe laser. Most of the signal can be attributed to $O(^3P)$ from ozone dissociation by the probe laser although the difference between (a) and (b) suggest signal from the experiment.

Despite decreasing the background and attempts to increase the amount of $O(^1D)$ reactant the signal , Figure 3.12, appears to be there but is still too small to analyze.

(a) 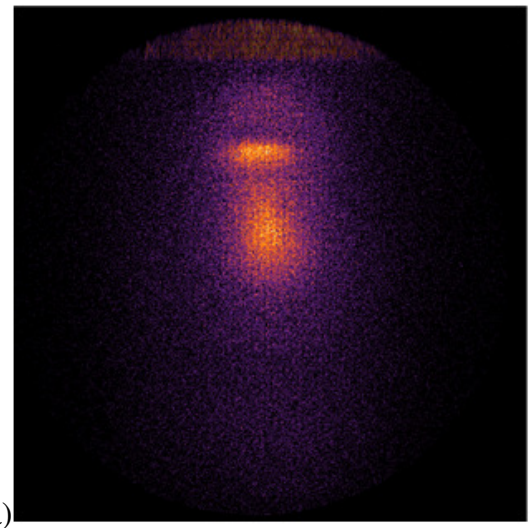 (b) 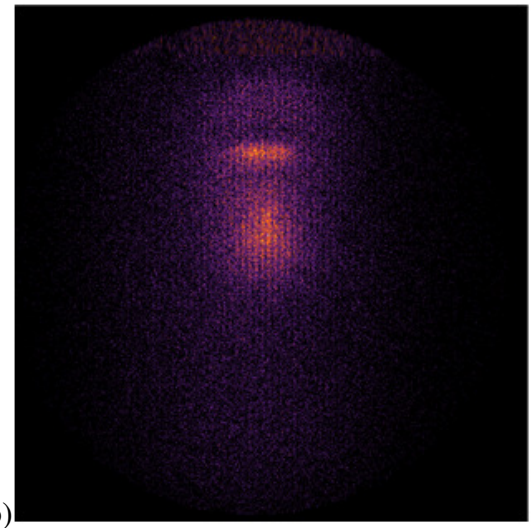

Figure 3.12: $O(^3P_2)$ from the deactivation by N_2 is shown in (a) while the same set up is shown in (b) without N_2 in the lower beam, thus showing only the background signal.

Comparing the two images in Figure 3.12, demonstrates a distinct difference between them. The center spot, which is signal from the probe dissociation of ozone is still apparent but much smaller than previously. The off-center signal, which is $O(^3P)$ from the dissociation laser in the upper beam is now obvious demonstrating clearly the sensitivity of the set up. Unfortunately although it seems that there is some signal from the overall experiment it is too small to determine the velocity and angular distributions. Despite the experiment signal being too small for analysis, the development of the crossed beam apparatus and improved methods to minimize background shows great potential. Other inelastic or reactive collision with large cross-sections and small potential background sources can be attempted in the future.

A single molecular beam can be used to study some collisions. The angular distribution from the images is more difficult to analyze in single beam experiments, but the ion signal is stronger. For the deactivation experiments, the $O(^3P)$ from ozone dissociation by the probe laser is too strong for this to be a reasonable approach, but the $O(^1D) + N_2O$ reaction detecting the NO channel is a good candidate. Here the probe laser produces some background but the signal from the reaction is stronger. This reaction is very important environmentally and is discussed further in the next chapter.

References

1) D. M. Neumark, A. M. Wodtke, G. N. Robinson, C. C. Hayden, and Y. T. Lee, *Phys. Rev. Lett*., **53**, 226, (1984).
2) D. M. Neumark, A. M. Wodtke, G. N. Robinson, C. C. Hayden, and Y. T. Lee, *J. Chem. Phys.*, **82** (7) 3045 (1985)
3) M. A Buntine, D. P. Baldwin, R. N. Zare, D. W. Chandler, *J. Chem. Phys.* **94**, 4672 (1991)
4) A. G. Suits, L. S. Bontuyan, P. L. Houston, and B. J. Whitaker, *J. Chem. Phys.*, **96**, 8618, (1992).
5) T. N. Kitsopoulos, M. A. Buntine, D. P. Baldwine, R. N. Zare, and D. W. Zare, *Science*, **260**, 1605, (1993).
6) O. Tokel, Ph.D. thesis, Cornell University, 2011
7) O. Tokel, J. Chen, C.K. Ulrich, P.L. Houston, *J. Chem. Phys.*, **114**, 11292 (2010)
8) W.B. DeMore, S.P. Sander, D.M. Golden, R.F. Hampson, R.E. Huie, M.J. Kurylo, C.J. Howard, A.R. Ravishankara, C.J.Kolb, and M.J. Molina, "Chemical Kinetic and Photochemical Data for Use in Stratospheric Modeling: Evaluation No. 12 of the NASA Panel for Data Evaluation, JPL Publication 97 – 4 (April, 1997)
9) M. J. Perri, A. L. Van Wyngarden, K. A. Boering, J. J. Lin, and Y. T. Lee, *J. Chem. Phys.,* **119** (16), 8213, (2003).

10) M. J. Perri, A. L. Van Wyngarden, J. J. Lin, Y. T. Lee, and K. A. Boering, *J. Phys. Chem. A,* **108** (39), 7995 (2004)

11) J. C. Tully, *J. Chem. Phys.*, **61** (1), 61, (1974)

12) G. E. Zahr, R. K. Preston, and W. H. Miller, *J. Chem. Phys.* **62** (3), 1127, (1975)

13) T. G. Slanger and G. Black, *J. Chem. Phys.* **60**, 468 (1974)

14) Y. Matsumi, Y. Inagaki, G. P. Morley, and M. Kawasaki, *J. Chem. Phys.*, **100**, 315 (1994)

15) Y. Matsumi and A. M. Sarwaruddin Chowdhury, *J. Chem. Phys.*, **104**, 7036, (1996)

16) S. M. Dylewski, J. D. Geiser, P. L. Houston, *J. Chem. Phys.*, **115** (16), 7460 (2001).

17) D. J. Bamford, L. E. Jusinski, W. K. Bischel, *Phys. Rev. A.* **34**, 186, (1986)

18) P. L. Houston, *Chemical Kinetics and Reaction Dynamics,* 2001, McGraw-Hill Companies Inc. New York

CHAPTER 4

$O(^1D) + N_2O$ REACTION: NO VIBRATIONAL AND ROTATIONAL DISTRIBUTION

4.1 Introduction

The reaction between $O(^1D)$ and N_2O is both of importance to atmospheric chemistry and interesting from the point of view of a multichannel reaction:

$$O(^1D) + N_2O \rightarrow N_2 + O_2 \qquad k = 4.9 \times 10^{-11}\ cm^3\ molec^{-1}\ s^{-1} \qquad \textbf{(1a)}$$

$$\rightarrow NO + NO \qquad k = 6.7 \times 10^{-11}\ cm^3\ molec^{-1}\ s^{-1} \qquad \textbf{(1b)}$$

The reaction rate increases as the relative velocity between the $O(^1D)$ and N_2O decreases. The reaction is important to atmospheric chemistry because the branching ratio between the two channels is fundamental to the steady-state concentration of ozone.[1] N_2 and O_2 are major constituents of the stratosphere, so reaction to this channel is neutral to the concentration of ozone. Production of two NO molecules, however, decreases the ozone concentration because NO is a catalyst in a scheme which converts two ozone molecules to three molecules of oxygen. Thus, not only is the odd oxygen species $O(^1D)$ destroyed in **(1b)**, but the products go on to catalyze the destruction of further odd oxygen.

There is considerable uncertainty concerning the vibrational distribution of the NO products from reaction **(1b)**; we summarize previous results briefly here and return to this issue in the discussion section. Brouard et al.[2-3] reported the

stereochemistry of the reaction by probing NO in v=15 and 16. Akagi et al.[4-6] reported that two different NO molecules were formed, a "new" one from the abstraction of an N atom by $O(^1D)$ from N_2O and the other from the "old" NO left behind. By using isotopic labeling they found that the new NO had a peak in the vibrational distribution at high vibrational levels, whereas the old one peaked at v=0. Pisano et al. reported the distribution from v=0 to v=12 and found it to peak at v=7.[7] Hancock and Haverd measured time-resolved infrared emission of NO(v=1-14) and concluded that the vibrational distribution for these states decreased monotonically from a maximum population at v=1.[8] An earlier paper using this technique was reported by Wang et al.[9] Finally, Lu, Liang and Lin have recently investigated the translational energy distribution of the $N_2 + O_2$ and NO + NO products from the $O(^1D) + N_2O$ reaction.[10] For the NO + NO products, they report that the translational energy release consumes 31% of the available energy. It is unclear from these studies both what the vibrational distribution actually is and why so many measurements differ from one another. All attempts to measure the nascent rotational distribution find that it is very hot. Kawai et al.[11] report temperatures up to 20,000 K, while Tsurumaki et al.[12] found 10,000 K.

The reaction of $O(^1D)$ with N_2O has also been investigated in clusters, typically by photodissociation of one N_2O of the N_2O dimer.[13,14] This "pre-aligned" reaction produces NO vibrational excitation, but it may be somewhat different from that of the normal reaction. In particular, it appears that the rotational temperatures of the NO products are typically colder, on the order of 60-100 K, than those reported for the normal reaction described above.

Theoretical investigations of the $O(^1D) + N_2O$ reaction are limited. Gonzalez and coworkers performed trajectory calculations using both A′ and A″ surfaces calculated at the CASPT2/CASSCF level.[15-17] Last et al. have investigated the $O(^1D) + N_2O$ reaction on an *ab initio* surface calculated using the Møller-Plesset method.[18] More recently, Akagi et al.[19] developed a surface at the CASPT2/cc-pVDZ level for the reaction, and Takayanagi and Akagi have reported the results of classical trajectory studies.[20] Finally, Takayanagi has performed mixed quantum-classical wavepacket calculations to explore this system.[21]

In this paper we report a detailed investigation of the vibrational and rotational distribution of the NO product of **(1b)** using multiphoton ionization to probe the NO product following reaction of $O(^1D)$ and N_2O in a molecular beam.

4.2 Experimental

Figure 4.1 presents a schematic drawing of the experimental apparatus. The molecular beam setup is a modified version of the single beam ion imaging apparatus described elsewhere.[7] In a manner similar to the setup first described by Welge and coworkers,[22] a second nozzle has been added parallel to the first one in preparation for future reaction product imaging studies. The apparatus has been equipped with additional electrodes for DC or pulsed slice imaging capabilities when desired.

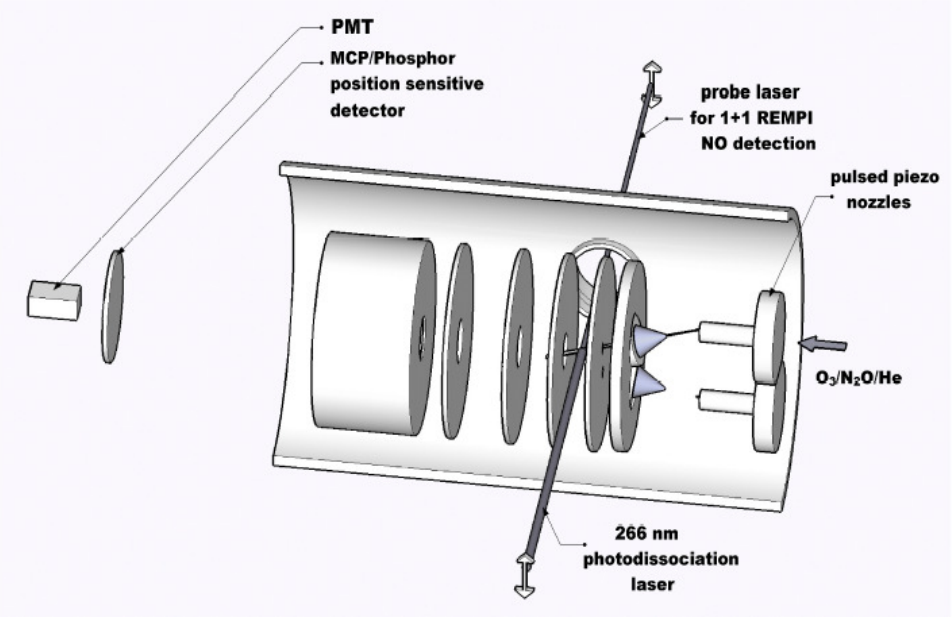

Figure 4.1: Scaled diagram of the experimental apparatus.

A mixture of O_3 (1%) and N_2O (6%) seeded in He (-78° C, backing pressure 2 psi) was expanded supersonically through a 500 μm diameter nozzle, and collimated with a 500 μm diameter skimmer located 2 cm from the nozzle. Two unfocused counter-propagating laser beams intersected the molecular beam at right angles in the center of repeller and extractor electrodes and 7.5 cm from the nozzle. One laser dissociated the O_3 molecules to generate $O(^1D)$ atoms, while the other state selectively ionized the resulting $NO(X\ ^2\Pi)$ molecules formed in the $O(^1D)+N_2O \rightarrow 2\ NO(X\ ^2\Pi)$ reaction. The ion cloud was then extracted through an optimized velocity-map spectrometer and impinges onto a gated dual micro-channel plate coupled to a fast phosphor screen (Burle, P-47) located at the end of the time-of-flight tube. The ion intensity was measured with a PMT (Thorn EMI) and passed to a computer, where a boxcar records the NO signal strength as a function of laser wavelength.

The O_3 molecules were dissociated by the linearly polarized 266 nm laser light generated by the fourth harmonic of a Nd-YAG laser (Spectra-Physics GCR-6) operating at 10 Hz. Typical energies were 5-6 mJ/pulse. The laser beam size was apertured to 5 mm, which gave the maximum signal to noise ratio under our detection conditions. The polarization axis of the dissociation light was vertical to the plane defined by the molecular beam and the 266 laser direction.

The $O(^1D)$ ions created by a 203.7 nm, 2+1 REMPI processes,[23] were used to check the molecular beam properties and to optimize production of this species. The 203.7 nm light was generated by doubling the output of a Nd-YAG (Spectra-Physics GCR-270) pumped dye laser (PDL-2) in a KDP crystal and then summing the fundamental with the doubled light in a BBO crystal. Typical powers were 0.9 mJ/pulse at 10 Hz.

NO molecules were state-selectively detected by a 1+1 REMPI processes.[24,25] The tunable 220-246 nm laser light used to probe the NO molecule was generated by doubling the output of a Nd-YAG (GCR-230) pumped Scanmate OPPO laser (Lambda Physik). The probe laser polarization was the same as that of the 266 nm laser. The probe laser was set to arrive 20 ns after the 266 nm laser. To generate the appropriate light, three types of dyes were used: Coumarin 450, 460 and 480. Typical energies were 0.9-1 mJ/pulse or 0.5-0.6 mJ/pulse. The pulse energy levels were chosen so that the NO ion signal did not saturate. Care was also taken by routinely monitoring the signal under small magnetic fields to ensure that no electrons generated by secondary processes caused any ion background. A series of overlapping 1.5 nm scans were

recorded at 30 laser shots/step, monitoring the laser pulse energies before and after each scan.

Ultrahigh purity N_2O (99.99%) and He (99.999%) were purchased from Matheson Tri-Gas and Airgas, respectively, and used without any further purification. O_3 was generated by a commercial ozonator and kept in a silica gel trap at -78° C.[26]

4.3 Results

4.3.1 Background Sources

There are three possible NO background sources in the experiment. First, some residual NO molecules are in thermal contact with the chamber walls. At 300 K these molecules account for almost all the thermal NO molecules populating v=0 and around 0.01% of those populating the v=1 level. This source was very small compared to our signal, 3-4% for v=0. The signal for NO(X $^2\Pi$) (v=0) from this source has been characterized, as shown in Figure 4.2(a), which is a scan of the probe laser with the molecular beam off.

A second background source is the NO generated and detected by the interaction of N_2O and the probe laser; that is the background is there even when there is no ozone in the beam mixture and when the 266 nm light is blocked. The background was weak; we estimate it to account for less the 7% of the signal in v = 0. To characterize this background source, we put pure N_2O in the beam and scanned the probe laser wavelength over strong transitions used for NO(X $^2\Pi$) v=1, 2 and 3 detection. Figure 4.2(b) shows the N_2O + probe laser scan for NO(X $^2\Pi$) (v=1).

Similar but much weaker beam-dependent spectra have been obtained for NO(X $^2\Pi$) v=2 and 3, with rotational temperatures close to 300 K, but the signal was too weak for a proper fit.

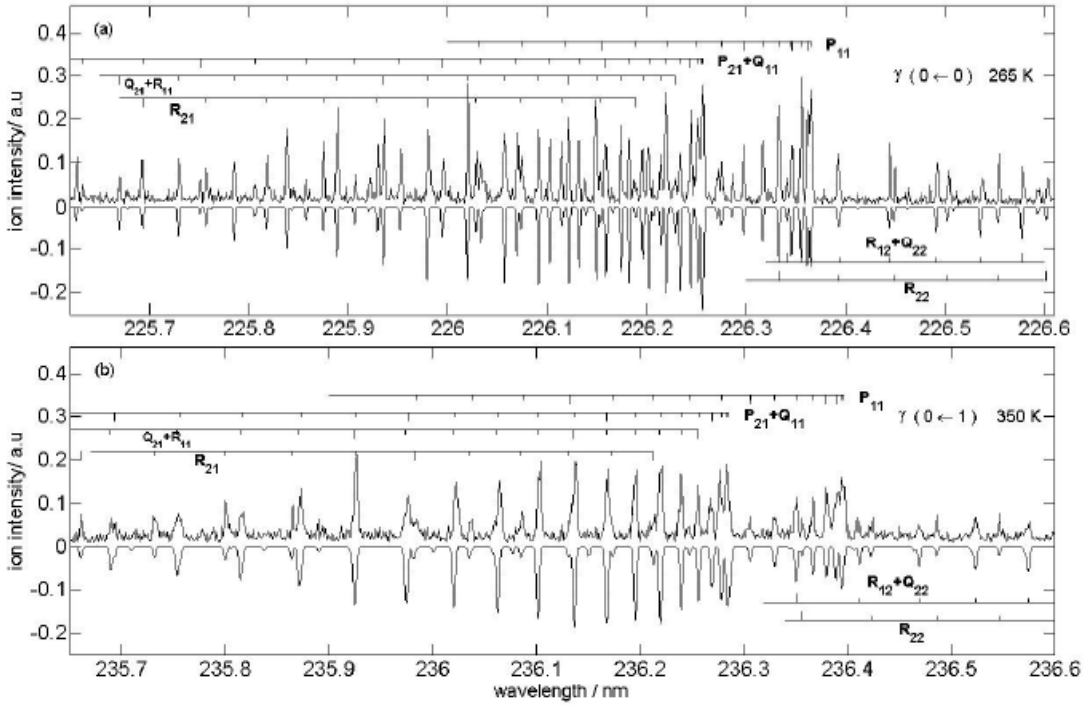

Figure 4.2: NO^+ ion signal from (a) probe laser, v=0 and (b) probe + N_2O, v=1. The upper plot shows the data and the lower one is the simulated spectra.

Honma and coworkers have shown that N_2O dimers formed in the molecular beam can be photolyzed by 193 nm photons, creating NO(X $^2\Pi$) through the $O(^1D)\cdot N_2O$ reactant pair.[13] Gödecke et al.[14] have recently studied the same reaction. They report rotational temperatures around 150 K, whereas Honma and coworkers report 60-100 K for all vibrational levels up to v=7. Our v=1 scan showed a rotational

temperature around 350 K, much higher than that found from the dimer experiments. Thus, it seems unlikely that dimers are the source of this background.

Whatever the source of the background, in our experiments performed with the O_3/N_2O mixture, the v=0 background contribution from this beam dependent source is less than 7% of our net signal, and higher levels are absent. Apart from their small intensity in the experiment, both the first and second background sources have a T_{rot} around 300 K, much lower in comparison to that found for vibrational levels monitored in the full experiment on the O_3/N_2O mixture. In summary, the second background makes a small contribution, but only to v=0.

The total background in the scans is around 10-15%, and much of this belongs to a third source of NO. Analysis of this source shows that it is a scaled down version of our actual experimental signal. This can be understood as a result of dissociation of O_3 by the probe laser.

Dissociation of ozone is through the Hartley band, which peaks at 254 nm. Absorption of a photon in this band results mostly in photodissociation through two channels, both of which create translationally hot $O(^1D)$ atoms.[27,28] The $O_3 + h\nu \rightarrow O_2$ ($a\ ^1\Delta_g$) + $O(^1D)$ channel opens for $\lambda < 310$ nm, whereas the $O + h\nu \rightarrow O$ ($b\ ^1\Sigma^+_g$) + $O(^1D)$ channel opens for $\lambda < 267$ nm. About 90% of the dissociation in this band proceeds by the first channel. Since our probe laser scans extend to the middle of the Hartley band, it is to be expected that some O_3 molecules will dissociate by this channel after absorbing the probe laser light. The resulting $O(^1D)$ atoms would react with the N_2O, creating NO molecules, which are then ionized by the same pulse.

Fortunately, this is a multiphoton process, so the signal is not too large with our unfocused laser pulses. Furthermore, the O_3 absorption cross section at the wavelengths used for probing NO is small compared to that at 266 nm, and the probe pulse energy is a factor of 5 smaller than that of the 266 pulse. All of these factors result in small magnitude for the background signal caused by the probe laser. That this background closely mimics the actual signal is not surprising, considering that the difference between the relative collision energies of the precursor $O(^1D)$ atoms created by two lasers is much smaller than the large exothermicity of the reaction.[15,27]

4.3.2 Analysis Procedure

A preliminary analysis of the 1+1 REMPI spectrum was required due to the very hot rotational temperature observed. Pisano et al. have showed that the rotationally cooled spectrum is dominated by gamma transitions.[7] A cross-correlation algorithm was written for calibrating the spectrum with gamma transitions only, simulated with LIFBASE[29] software, assuming an initial rotational and vibrational temperature.

To determine the relative population of each NO($X\ ^2\Pi$) vibrational level produced in the reaction, we modeled the NO gamma and beta transitions with Pgopher.[30] Fermi's golden rule states that the one photon transition probability is proportional to the square of the $\langle \mu \cdot E \rangle$ matrix element, where E is the polarization vector of our linearly polarized probe laser and μ is the molecule's transition dipole moment. Therefore, we need to use only first-order spherical transition moments in the simulation, i. e., electric dipole moments. The spectroscopic constants for the

ground state NO(X $^2\Pi$) are taken from Amiot[31] and Engelman et al.,[32,33] and NO(B $^2\Pi$) state from Huber and Herzberg[34] and Hamilton et al.[35] The NO(A $^2\Sigma$) state has been recently revisited by Danielak and coworkers.[36] Since the observed spectrum is rotationally hot, the rotational constants B_v and D_v are statistically significant. For the β system, the D_v values are less certain, so we used the set of rotational constants from Hamilton et al., derived from the literature in a self-consistent manner.

The following procedure was followed for the analysis. First, a constant rotational temperature, T_{rot} is assumed for all vibrational levels. A section of the data is picked and an iterative fitting is performed for all individual γ bands extending into the chosen region. Because the γ and β bands are two competing absorption systems with different ionization efficiencies, one needs to also check for β bands in each region.[37] Thus, the same iteration is repeated for β transitions in each data segment. After an initial fit, the iteration moves to a neighboring section. Once a reasonable fit is obtained to all the data segments, the iteration set is repeated over the whole of the spectrum again, but this time including the T_{rot} as a fitting parameter in the set. The iterations are continued until satisfactory convergence is attained to the data.

The second step is to relax the universal temperature constraint for the main bands contributing to the data; a band by band individual T_{rot} fit is performed, allowing for differences in T_{rot} with vibrational level. A Boltzmann rotational distribution is assumed in all fits.

4.4 Discussion

4.4.1 The Vibrational Distribution

A portion of the recorded spectrum[38] is shown in Figure 4.3, along with the best fit that resulted from the procedure described above. Figure 4.4 shows an expanded version in more detail.

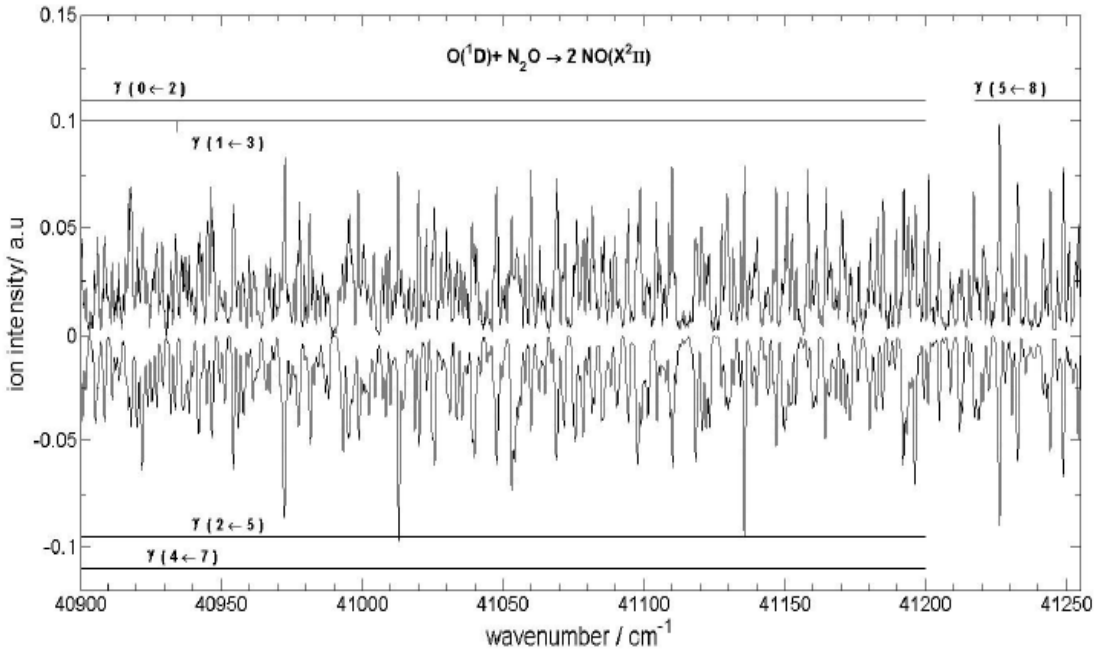

Figure 4.3: 1+1 REMPI spectrum of NO(X $^2\Pi$) from O(^{1}D) + N_2O → 2 NO(X $^2\Pi$) reaction. Features from the A ← X (0,2) ; (1,3); (2,5); and (4,7) bands span the whole range. The (5,8) band head and (1,3) band origin are also shown. The upper plot shows the data and the lower one is the simulation with T_{rot} = 4500 K

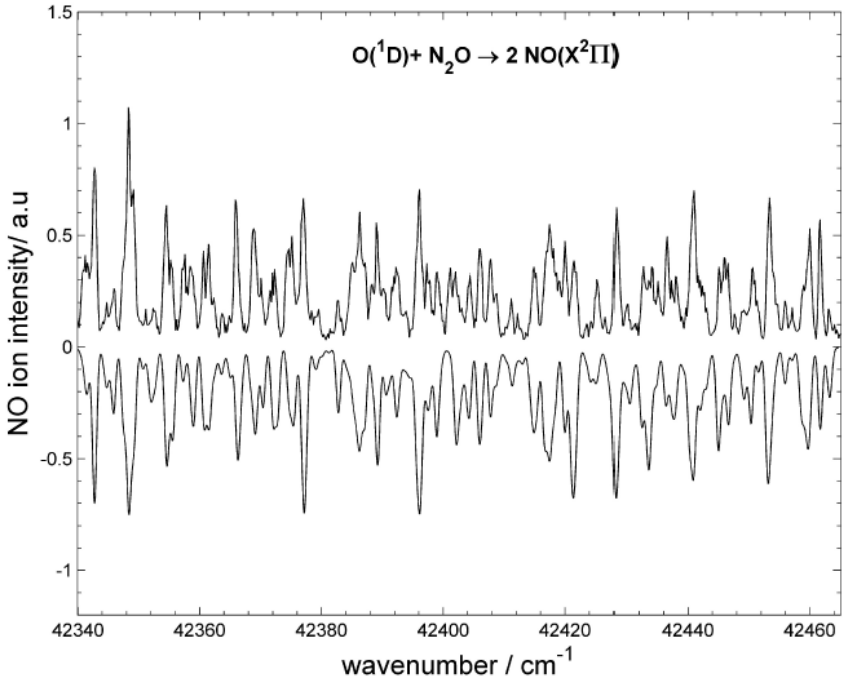

Figure 4.4: 1+1 REMPI spectrum of NO(X $^2\Pi$) from the O(^{1}D)+N_2O → 2 NO(X $^2\Pi$) showing a smaller spectral region expanded so as to demonstrate the degree of agreement between the measured spectrum (upper plot) and the calculated one (lower plot). The γ(0,1) and γ(3,5) transitions span the entire area with contributions from the γ(4,6) transitions.

The individual T_{rot} fits showed that the observed vibrational transitions can be well represented by a Boltzmann rotational distribution with a universal T_{rot} around 4500-5000 K. Tsurumaki et al.[12] have measured the rotational temperature of NO(v=0) with Doppler-resolved LIF, via the γ (0,0) band for the same reaction, using 193 nm laser pulses to generate the O(^{1}D) precursor from N_2O. Their reported T_{rot} of 10000 K contrasts with the 300 K reported by Brouard et al.[2] for the same system. However, both observed very high rotational temperatures for $v > 0$, with Brouard et al. reporting T_{rot} = 5500 K, for v=1. The discrepancy at v=0 was probably because of the thermal NO (v=0) in the chamber, dominating the LIF signal in the latter experiment. Kawai

et al.[11] recently determined the rotational temperature as ≈ 20 000 K for NO (v=0, 1, 2) for the part of the distribution with J < 80, as measured under flow conditions. For J > 80, they observe a faster decrease in their distribution, corresponding to a somewhat lower rotational temperature. In our fits to the data, we did not observe strong differences from a Boltzmann distribution for J > 80 populations.

The contributing transitions in the 220-246 nm range were found to be only the γ transitions. Akagi[4,6] have used the B $^2\Pi$(v=0-2) ← X $^2\Pi$(v=12-15) transitions for the LIF detection, and Pisano et al.[7] observed the NO β system REMPI for this reaction, but both had rotationally cooled sources, allowing them to isolate these tiny signals from the otherwise congested spectrum. The NO molecule is very efficiently detected with REMPI processes,[37] so under cooled conditions the β system would be an additional source of information.

The electric dipole transition matrix element fit parameter input to the PGOPHER program can be converted to relative vibrational populations for each band, using the known electronic transition moments, $R_e(r_{v',v''})$[39] and Franck-Condon factors.[39,40] The relative vibrational populations are given in Table 4.1.

4.4.2 Origin of Vibrational Excitation

The origin of the inverted vibrational distributions can be qualitatively understood by considering the two competing factors affecting it, the energy randomization rate in the intermediate and the available time for this randomization to take place.

Table 4.1: NO($X^2\Pi$) Vibrational State Distribution of the $O(^1D) + N_2O \rightarrow 2$ NO($X\ ^2\Pi$)

vibrational state	observed transition(s)	relative populations[a]	weighted average[b]
0	γ(0,0)	0.088±0.008	0.089±0.008
1	γ(0,1)	0.036±0.003	0.039±0.010
	γ(1,1)	0.075±0.014	
2	γ(0,2)	0.041±0.004	0.043±0.003
	γ(2,2)	0.047±0.009	
3	γ(1,3)	0.125±0.010	0.116±0.015
	γ(2,3)	0.095±0.014	
4	γ(3,4)	0.098±0.015	0.100±0.015
5	γ(4,5)	0.134±0.021	0.212±0.026
	γ(3,5)	0.220±0.011	
	γ(2,5)	0.242±0.019	
6	γ(4,6)	0.128±0.014	0.130±0.015
7	γ(6,7)	0.095±0.026	0.124±0.024
	γ(5,7)	0.103±0.016	
	γ(4,7)	0.173±0.021	
8	γ(6,8)	0.118±0.025	0.093±0.015
	γ(5,8)	0.084±0.014	
9	γ(6,9)	0.053±0.015	0.053±0.015

[a] The relative vibrational distribution from each band is given before averaging and weighing the data. Since the fluctuations of error in the bands occurring in the same spectral region are correlated, about a ±15% fit precision to peak height is assumed in the error calculations. The uncertainties include the estimated uncertainty in the transition probabilities. Transition probabilities for bands $\gamma(6,7)$, $\gamma(6,8)$, and $\gamma(6,9)$ were taken from ref 40 and carry higher uncertainties because a Morse oscillator wave function is assumed

[b] The weighted mean and error in the weighted mean are calculated using eqs 4.21 and 4.22 from ref 41. Following averaging, the weighted mean is normalized to a sum of unity over all observed levels.

Ab initio calculations of potential energy surfaces[16,17,43] show that the NO + NO products correlate on two 1A″ surfaces and one 1A′ surface to $O(^1D) + N_2O$. All surfaces for $O(^1D) + N_2O$ leading to NO + NO products pass through a dimer configuration. The lifetime of the intermediate for this reaction is estimated to be on the order of 1 ps or less,[12,44] on the order of the rotational period of the cis-NO dimer.[12] Considering the large exothermicity and the barrierless PES for the reaction, with this seemingly short-lived intermediate, the NO can be expected to show characteristics of a non-statistical vibrational distribution, rather like the inverted vibrational distribution for the new OH product in the $O(^1D) + H_2O$[45,46] reaction, as compared to the old OH from the original water, which shows a colder vibrational distribution in comparison to a statistical one. However, in the reaction we are studying this effect is counterbalanced by intramolecular vibrational relaxation (IVR), which is proportional to the density of states in the intermediate and to the square of the effective coupling between the vibrational states. The two similar masses of the NO molecules is likely to increase the density of states available in the intermediate, as discussed by Akagi et al.[5] Kawai et al. confirms that the stretching modes are strongly coupled for the reaction path which passes through the trans-minimum.[43] These two competing mechanisms are likely to end up leaving NO molecules with an inverted vibrational distribution under high energy collisions with a direct mechanism, and possibly with more chance of energy redistribution at lower energy collisions.

4.4.3 The importance of $O(^1D)$ velocity relaxation

An important question to address is why there is so much discrepancy between the various measurements of the NO vibrational distribution produced following reaction of $O(^1D)$ with N_2O. Hancock and Haverd provided a very thoughtful discussion of the potential problems in each of the reported experiments, but they were still at a loss to explain the discrepancies shown in their Figure 4.[8] These distributions, along with results from the current study (plotted as weighted averages from Table 4.1), are shown in Figure 4.5.

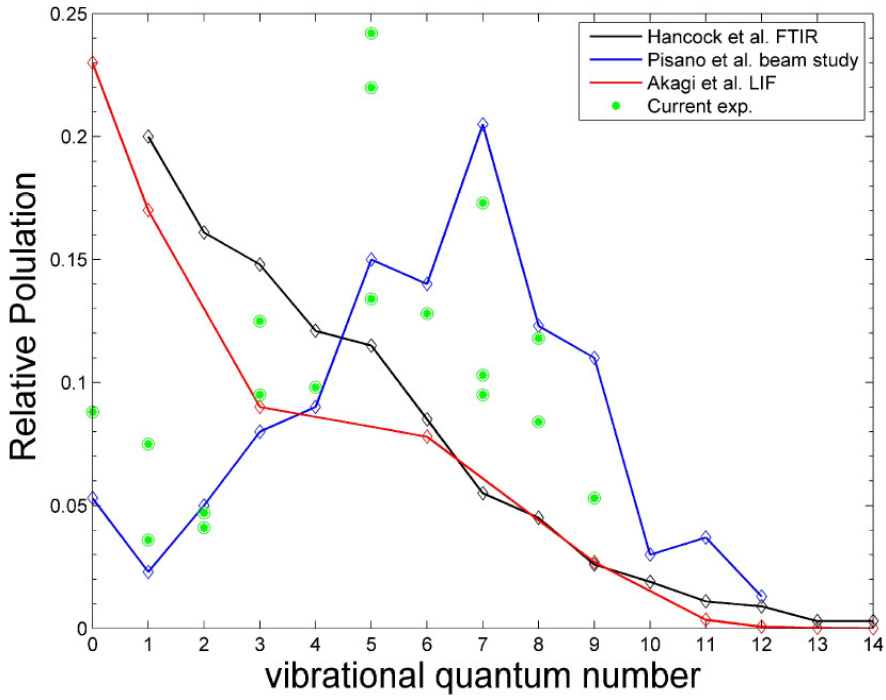

Figure 4.5: Comparison of the relative NO(X $^2\Pi$) vibrational level population results from the current experiment with those from previous molecular beam and bulk studies. A shoulder is observed at the v = 4 - 8 range in the bulk studies, whereas an inverted population is observed in the molecular beam studies.

An alternate approach is to ask if there might be some hidden variable that has hitherto been unaccounted for; perhaps all the measurements are correct, but there is a difference in conditions that has not been noticed. We argue here that the hidden variable is the velocity distribution associated with the collision between $O(^1D)$ and N_2O.

The experiments are of two broad types. The first type are those done in a molecular beam, including that by Pisano et al.,[7] that by Lu, Laiang, and Lin,[10] and the current experiment. The second type are those done in static or flowing bulb experiments. The conditions for the latter are as follows. Akagi et al. generated $O(^1D)$ from 266 nm photolysis of O_3 and performed the experiment at a total pressure of 1.0 torr at a delay time of 5 μs.[4,6] Brouard et al. used 193-nm photodissociation of N_2O as an $O(^1D)$ source and performed the experiment at a total pressure of up to 200 mtorr with a delay time of 200 ns.[2,3] Hancock and Haverd used a similar source with total pressures of 0.3-1.0 torr and a delay time of around 40 μs.[8]

The conditions for the molecular beam experiments are as follows. Pisano et al.[7] used a molecular beam experiment in which an O_3/N_2O mixture was photolyzed at 266 nm near the throat of a nozzle expansion. Most $O(^1D)$ atoms flew out of the beam before reacting, but those that reacted did so within roughly a single collision. The resulting NO was rotationally relaxed by collisions in the expansion, but vibrational relaxation under such conditions is negligible. The NO products were detected downstream, in the collisionless part of the beam, by a 1+1′ REMPI scheme. Because of the rotational relaxation, the spectra were simpler to interpret than those in the

current experiment. The conditions for the current experiment are similar to those used by Pisano et al. in that a molecular beam of an O_3/N_2O mixture is employed with photodissociation at 266 nm, but both dissociation and detection are accomplished in the collisionless part of the beam. Again, most of the $O(^1D)$ products escape from the beam, but a few collide with N_2O to produce NO products, which are probed within a delay time of 20 ns. These products presumably have the vibrational and rotational distributions characteristic of a single collision at high velocity. The velocity distribution of the $O(^1D)$ in the current and Pisano et al. experiments is peaked at 2.2 x 10^5 cm/s. Lu, Liang, and Lin used a crossed molecular beam apparatus.[10] The $O(^1D)$ was produced by 157-nm photolysis of O_2 , giving a velocity of 2.1 x 10^5 cm/s.

While much attention in the bulb experiments has been focused on the possibility of vibrational relaxation of the NO, the possibility of velocity relaxation of the $O(^1D)$ has not been considered. We hypothesize that "slow" $O(^1D)$ reacts with N_2O to give a statistical vibrational distribution, perhaps through an insertion/complex-forming process, whereas "fast" $O(^1D)$ reacts to give an inverted distribution, through a more direct mechanism. For any individual experiment, the result would then be a weighted sum of the statistical distribution, given by the data of Akagi et al.,[6] in our Figure 4.5, and an inverted distribution given by the current data, also shown in our Figure 4.5. The distributions of Akagi et al.(Figure 3),[6] and of Hancock and Haverd (Figure 5)[8] do seem to show a shoulder at v = 4-8 on top of a more statistical distribution, albeit one that peaks at the lowest vibrational level. Thus, our hypothesis is that the $O(^1D)$ reacts from a relaxed velocity distribution in the bulb experiments, favoring the statistical branch of the NO vibrational distribution. In the

beam experiments, on the other hand, if the $O(^1D)$ produced by the reaction does not react on its first collision with N_2O, it leaves the beam and does not react at all. Thus, it reacts with the velocity provided by the O_3 dissociation, a velocity high enough to favor the stripping branch of the NO vibrational distribution.

The only potential counterexample to this interpretation is the result by Lu, Liang and Lin.[10] Although they do not directly measure the NO vibrational or rotational distribution, they find that the translational energy deposition in the reaction is 31% (28 kcal/mol out of 89.7 kcal/mol available), a value too high in their view to allow for the high vibrational and rotational excitation observed in the current experiments and those of Pisano et al. Our own measurement of the rotational temperature suggests that the total rotational energy for the two fragments is less than 20 kcal/mol (out of 91.5 kcal/mol available). That would still leave roughly 42 kcal/mol available for vibration, or about 47%. While this fraction is less than the 75-87% estimate of Pisano et al., it still means that the average NO molecule would have 21 kcal/mol in vibration and would be at $v = 4$, as compared to the peak of the distribution at $v = 5$ in the current experiment. To be completely consistent with our measurement, the translational energy disposal would need to be only 18 kcal/mol, as compared with their measurement of 28 kcal/mol.

Some estimates show the plausible importance of velocity relaxation. The total rate constant for reaction of $O(^1D)$ with N_2O is 1.2×10^{-10} cm^3 $molec^{-1}$ s^{-1}. Measurements have been made on the relaxation of $S(^1D)$ velocities in collisions with He, Ar, and Xe[47] and of $O(^1D)$ velocities in collisions with He, Ne, Ar, N_2, and O_2.[48,49]

For $O(^1D)$ with N_2, the rate of velocity relaxation is 1.99 x 10^{-10} cm^3 $molec^{-1}$ s^{-1}. Assuming the velocity relaxation cross section for $O(^1D) + N_2O$ to be similar to that for $O(^1D) + N_2$, velocity relaxation is 1.7 times faster than the total reaction rate. Thus, the $O(^1D)$ in bulb experiments is cooling translationally nearly twice as fast as it is reacting. While the $O(^1D) + N_2O$ relaxation rate might be somewhat dissimilar from that for $O(^1D) + N_2$, the fact that the rates of velocity relaxation of $O(^1D)$ and $S(^1D)$ by nearly all measured partners are comparable suggests that the conclusion that velocity relaxation competes effectively with reaction is likely to be a robust one. Repetition of previous experiments but with N_2O as the target could confirm this conclusion. However, given the current state of knowledge it appears plausible that under the bulb conditions, the reaction might favor predominantly a statistical distribution whereas under beam conditions it might favor predominantly an inverted distribution.

A molecular beam experiment might be designed to check this hypothesis by using slower $O(^1D)$ atoms to initiate the reaction. In such an experiment in the current apparatus, ozone would need to be dissociated with wavelengths longer than 290 nm for the reaction to have small collision energies comparable to those in a cell experiment. Unfortunately, the ozone dissociation cross section is about an order of magnitude smaller at these wavelengths. Our estimate is that the ratio of signal to "probe laser and beam background" would be only around one. Furthermore, the probe laser would still create fast $O(^1D)$ atoms which would complicate the interpretation. Thus, this experiment was not attempted.

4.5 Conclusions

An inverted vibrational and a very hot rotational distribution is observed in the NO product channel of N_2O collisions with fast $O(^1D)$ atoms. The translational relaxation of $O(^1D)$ in bulb experiments probing the same reaction is hypothesized to play a role in their observation of colder and more statistical NO vibrational distributions.

We conclude that an inverted vibrational distribution in this channel is likely be the result of a direct reaction mechanism, whereas a statistical outcome can dominate at lower collision energies through an insertion type mechanism and with the help of efficient coupling of NO stretching modes in the collision complex.

Extending the reduced dimensionality QCT calculations[42,44] to full three dimensions may shed light on the origins of the observed distribution. Experimentally, isotopically labeled species can be used to get more information on this channel, if a two-fold congested spectrum can be similarly analyzed. A more informative study would be state-selected crossed molecular beam studies, which is currently underway in our lab. In this experiment, ozone is dissociated in one beam, and the product $O(^1D)$ flies to a beam of N_2O, where reaction takes place. Separating the location of the probe laser from the ozone source circumvents creation of fast $O(^1D)$ by the probe laser, but the signal is still expected to be small due to the necessity of creation of slow $O(^1D)$ at wavelengths where ozone does not absorb strongly.

References

1) J. R. Wiesenfeld, *Acct. Chem. Res*. **1982**, *15*, 110–116.

2) M. Brouard, S. P. Duxon, P. A. Enriquez, R. Sayos, J. P. Simons, *J. Phys. Chem.* **1991**, *95*, 8169–8174.

3) M. Brouard, S. P. Duxon, P. A. Enriquez, J. P. Simons, *J. Chem. Phys.* **1992**, *97*, 7414–7422.

4) H. Akagi, Y. Fujimura, O. Kajimoto, *J. Chem. Soc. Faraday Trans*. **1998**, *94*, 1575–1581.

5) H. Akagi, Y. Fujimura, O. Kajimoto, *J. Chem. Phys.* **1999**, *110*, 7264–7272.

6) H. Akagi, Y. Fujimura, O. Kajimoto, *J. Chem. Phys*. **1999**, *111*, 115–122.

7) P. J. Pisano, M. S. Westley, P. L. Houston, *Chem. Phys. Lett.* **2000**, *318*, 385–392.

8) G. Hancock, V. Haverd, *Phys. Chem. Chem. Phys.* **2003**, *5*, 2369–2375.

9) X. B. Wang, H. Z. Li, Q. H. Zhu, F. N. Kong, H. G. Yu, *J. Chin. Chem. Soc.* **1995**, *42*, 399–403.

10) Y.-J. Lu, C.-W. Liang, J. J. Lin, *J. Chem. Phys.* **2006**, *125*, 133121.

11) S. Kawai, Y. Fujimura, O. Kajimoto, T. Takayanagi, *J. Chem. Phys*. **2004**, *120*, 6430–6438.

12) H. Tsurumaki, Y. Fujimura, O. Kajimoto, *J. Chem. Phys*. **1999**, *111*, 592–599.

13) K. Honma, Y. Fujimura, O. Kajimoto, G. Inoue, *J. Chem. Phys*. **1988**, *88*, 4739–4747.

14) N. Gödecke, C. Maul, A. I. Chichinin, S. Kauczok, K. H. Gericke, *J. Chem. Phys.* **2009**, *131*, 054307–1–054307–11.

15) M. Gónzales, D. Troya, M. P. Puyuelo, R. Sayós, P. A. Enríquez, *Chem. Phys. Lett.* **1999**, *300*, 603–612.

16) M. Gónzales, R Valero, J. M. Anglada, R. Sayós, *J. Chem. Phys.* **2001**, *115*, 7015–7031.

17) M. Gónzales, R. Sayós, R. Valero, *Chem. Phys. Lett.* **2002**, *355*, 123–132.

18) I. Last, A. Aguilar, R. Sayos, M. Gonzalez, M. Gilibert, *J. Phys. Chem. A*. **1997**, *101*, 1206–1215.

19) H. Akagi, A. Yokoyama, Y. Fujimura, T. Takayanagi, *Chem. Phys. Lett.* **2000**, *324*, 423-429.

20) T. Takayanagi, A. Akagi, *Chem. Phys. Lett.* **2002**, *363,* 298-306.

21) T. Takayanagi, *Chem. Phys.* **2005**, *308*, 211–216.

22) L. Schnieder, K. Seekamp-Rahn, F. Liedeker, H. Steuwe, K. H. Welge, *Faraday. Discuss. Chem. Soc.* **1991**, *91*, 259–269.

23) S. T. Pratt, P. M. Dehmer, J. L. Dehmer, *Phys. Rev. A.* **1991**, *43*, 4702–4711.

24) M. Hippler, J. Pfab, *Chem. Phys. Lett*. **1995**, *243*, 500–505.

25) R. Uberna, R. D. Hinchliffe, J. Cline, *J. Chem. Phys.* **1996**, *105*, 9847–9858.

26) R. E. Stevens, C. W. Hsiao, L. L. N. J. Curro, B. J. Monton, B. Y. Chang, C. Y. Kung, C. Kittrell, J. L. Kinsey, *Rev. Sci. Instrum.* **1998**, *69*, 2504–2508.

27) S. M. Dylewski, J. D. Geiser, P. L. Houston, *J. Chem. Phys.* **2001**, *115*, 7460–7473.

28) K. Takahashi, N. Taniguchi, Y. Matsumi, M. Kawasaki, *Chem. Phys.* **1998**, *231*, 171–182.

29) J. Luque, D. Crowley, LIFBASE: Database and spectral simulation (version 1.5), **1999**.

30) C. Western, Pgopher, a Program for Simulating Rotational Structure. http://pgopher.chm.bris.ac.uk/.

31) C. Amiot, *J. Mol. Spectrosc.* **1982**, *94*, 150–172.

32) R. Engelman, P. E. Rouse, H. M. Peek, V. D. Baiamonte, The Beta and Gamma Systems of Nitric Oxide; Los Alamos Scientific Report LA-4364, **1970**.

33) R. Engelman, P. E. Rouse, *J. Mol. Spectrosc.* **1971**, *37*, 240–251.

34) K. P. Huber, G. Herzberg, V. Nostrand, *Molecular Spectra and Molecular Structure: IV.Constants of Diatomic Molecules*; **1970**.

35) P. A. Hamilton, A. J. Phillips, R. Windsor, *Chem. Phys. Lett.* **1997**, *264*, 245–251.

36) J. Danielak, U. Domin, R. K.pa, M. Rytel, M. Zachwieja, *J. Mol. Spectrosc*. **1997**, *181*, 394–402.

37) D. C. Jacobs, R. N. Zare, *J. Chem. Phys.* **1986**, *85*, 5457–5468.

38) O. Tokel, Ph.D. Thesis, **2010**, to be published.

39) J. Luque, D. R. Crosley, *J. Chem. Phys.* **1999**, *111*, 7405–7415.

40) H. A. Ory, A. P. Gittleman, J. P. Maddox, *Astrophys. J*. **1964**, *139*, 346–356.

41) P. R. Bevington, D. K. Robinson, *Data Reduction and Error Analysis for the Physical Sciences*.

42) T. Takayanagi, A. Wada, *Chem. Phys.* **2001**, *269*, 37–47.

43) S. Kawai, Y. Fujimura, O. Kajimoto, T. Yamashita, C. B. Li, T. Komatsuzaki, M. Toda, *Phys. Rev. A*. **2007**, *75*, 022714–1–022714–11.

44) S. Kawai, Y. Fujimura, O. Kajimoto, T. Yamashita, *J. Chem. Phys*. **2006**, *124*, 184315–1–184315–9.

45) C. B. Cleveland, J. R. Wiesenfeld, *J. Chem. Phys*. **1992**, *96*, 248–255.

46) D. G. Sauder, J. C. Stephenson, D. S. King, M. P. Casassa, *J. Chem. Phys.* **1992**, *97*, 952–961.

47) G. Nan, P. L. Houston, *J. Chem. Phys.* **1992**, *97*, 7865–7872.

48) Y. Matsumi, S. M. Shamsuddin, Y. Sato, M. Kawasaki, *J. Chem. Phys.* **1994**, *101*, 9610–9618.

49) N. Taniguchi, K. Hirai, K. Takahashi, Y. Matsumi, *J. Phys. Chem. A*, **2000**, *104*, 3894–3899

APPENDICES

APPENDIX A

Anisotropy parameter value per pixel for the O($^3P_2$) images.

The plots are of the O($^3P_2$) signal intensity (solid line), the weighted average β (dashed lines) and the segment of points averaged for the reported β (colored points, a different color is used for each β, βa (•), βb (■), βc (◆), βd (▲)). Each plot is labeled with the dissociation wavelength.

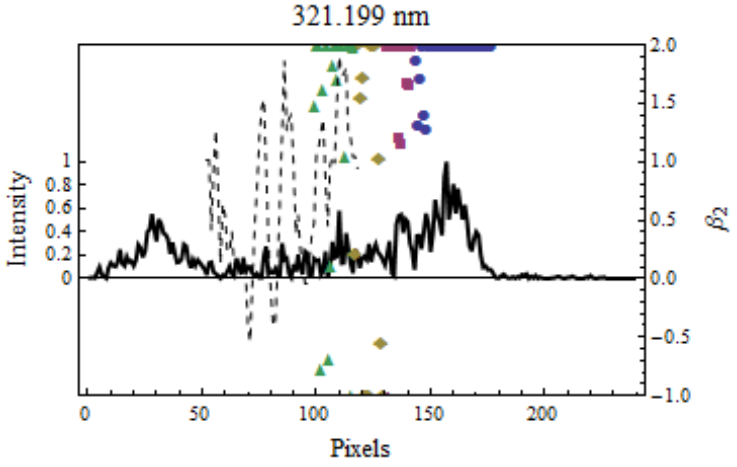

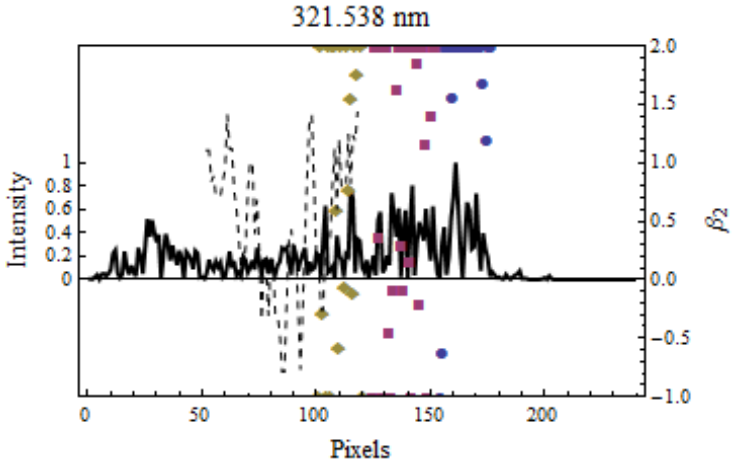

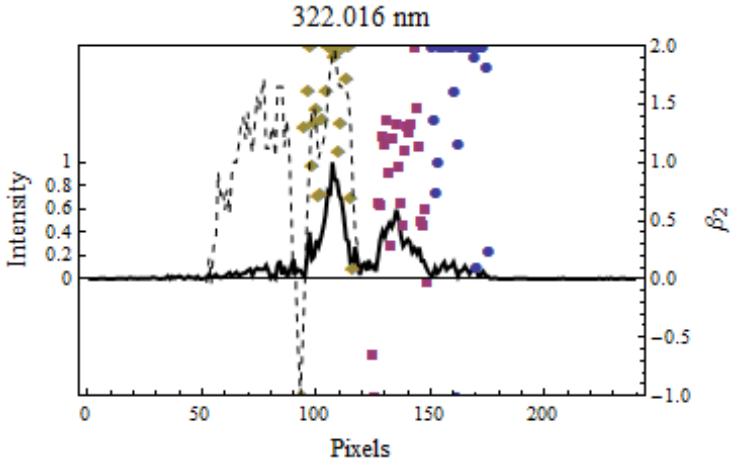
322.016 nm
Intensity
Pixels
β_2

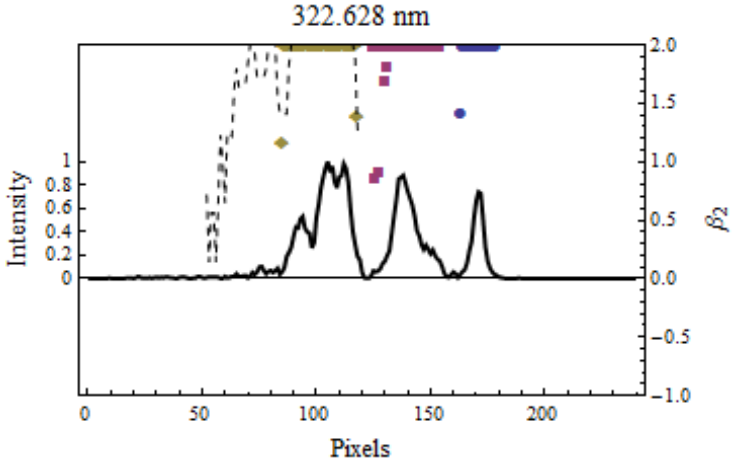
322.628 nm
Intensity
Pixels
β_2

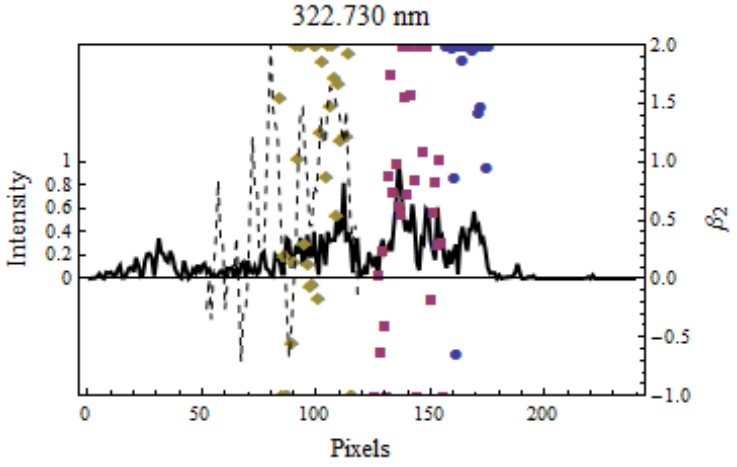
322.730 nm
Intensity
Pixels
β_2

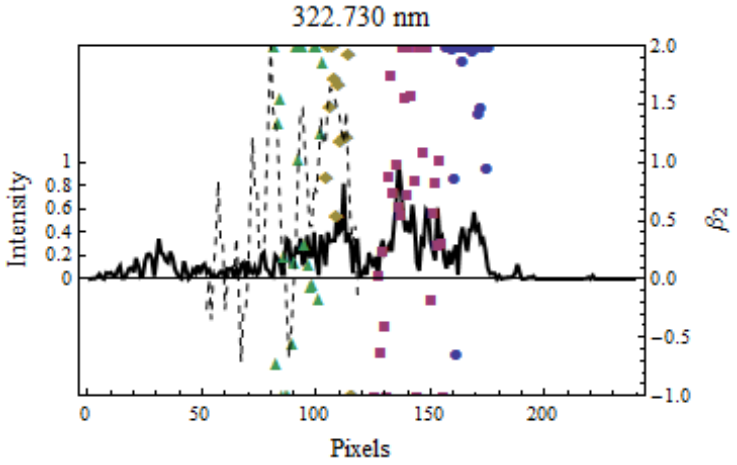
322.730 nm
Intensity
Pixels
β_2

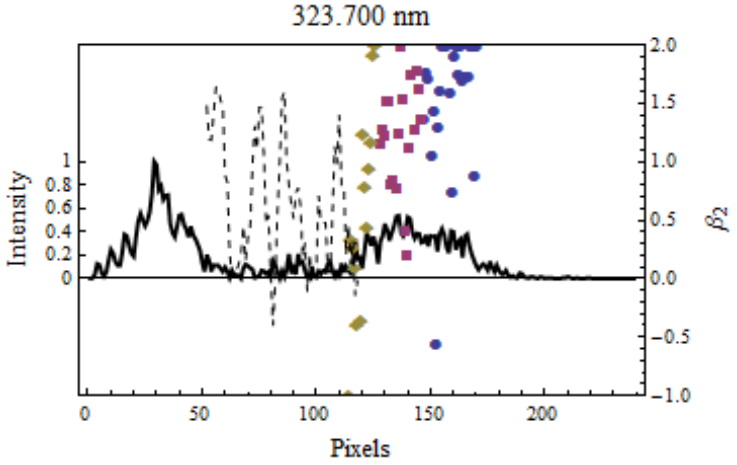
323.700 nm
Intensity
Pixels
β_2

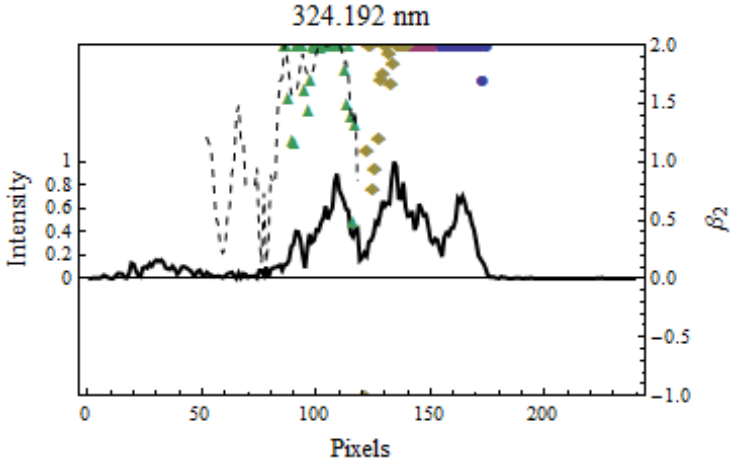
324.192 nm
Intensity
Pixels
β_2

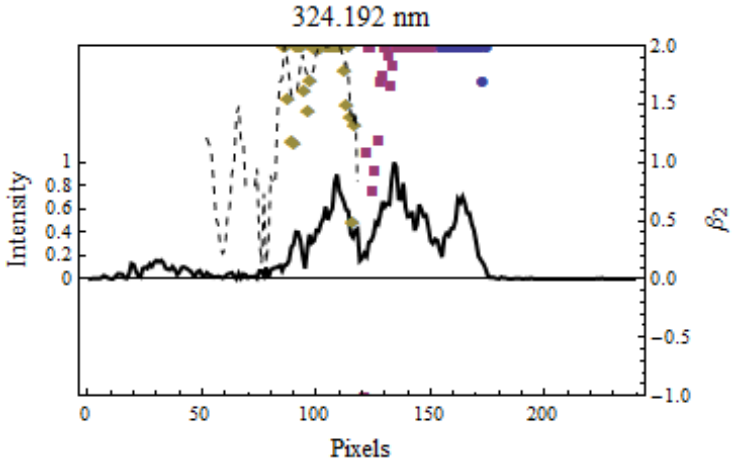
324.192 nm
Intensity
Pixels
β_2

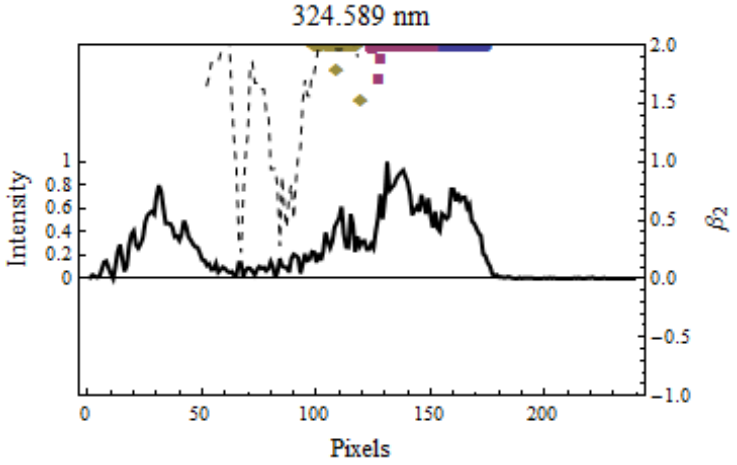
324.589 nm
Intensity
Pixels
β_2

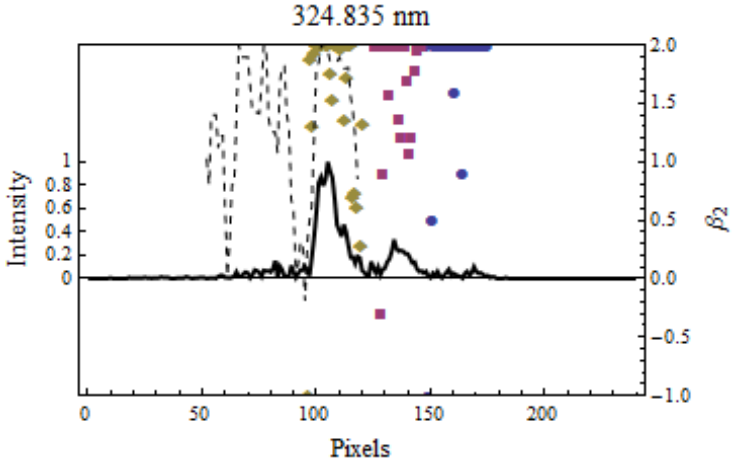
324.835 nm
Intensity
Pixels
β_2

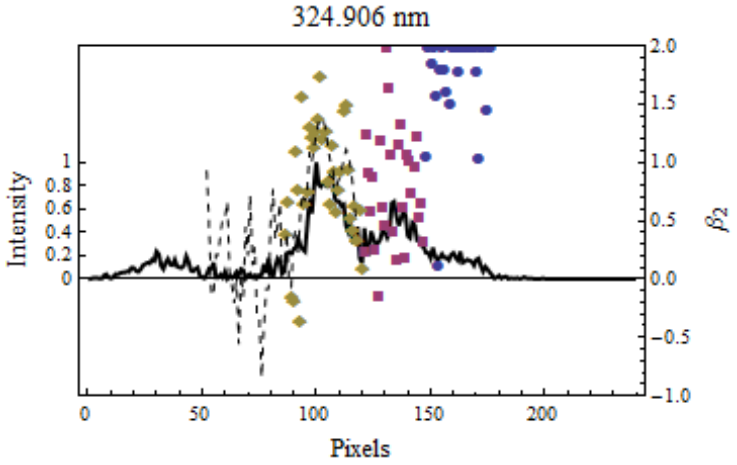
324.906 nm
Intensity
Pixels
β_2

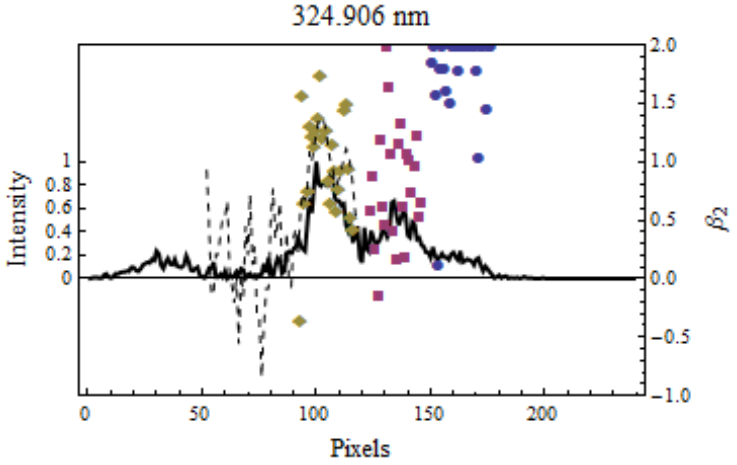
324.906 nm
Intensity
Pixels
β_2

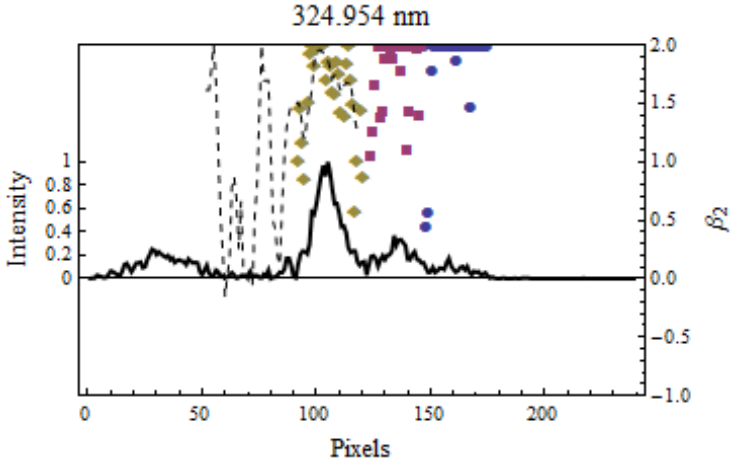
324.954 nm
Intensity
Pixels
β_2

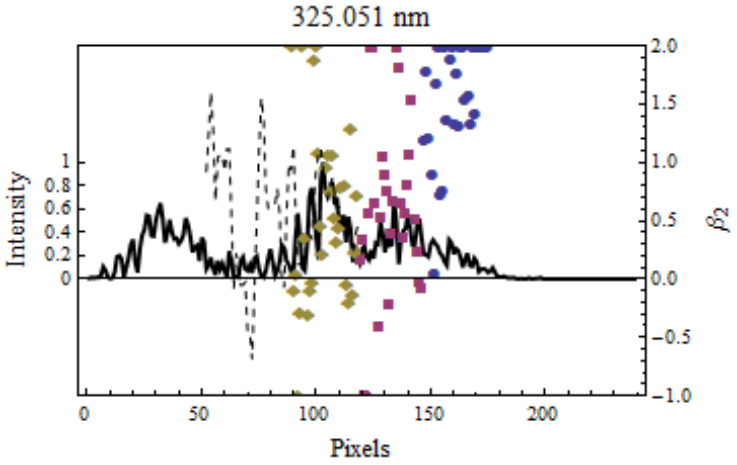
325.051 nm
Intensity
Pixels
β_2

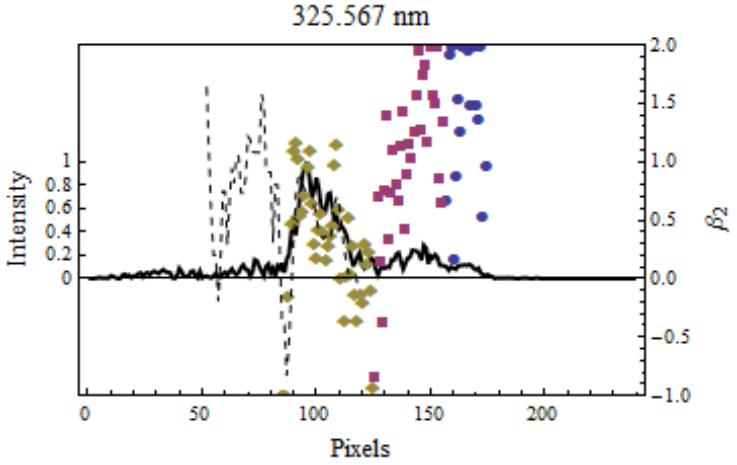
325.567 nm
Intensity
Pixels
β_2

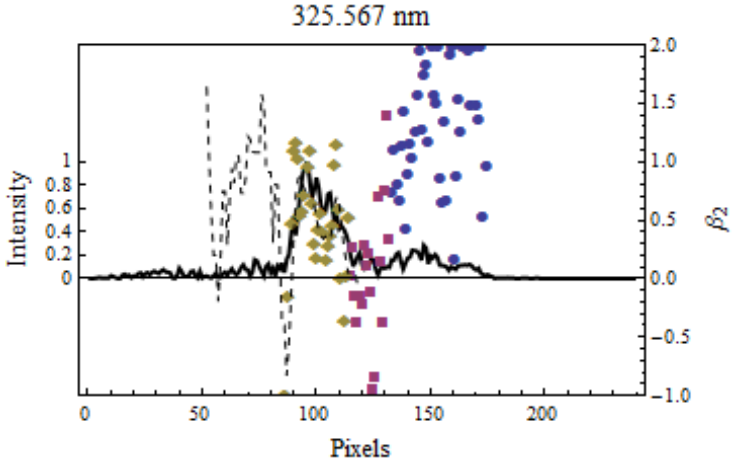
325.567 nm
Intensity
Pixels
β_2

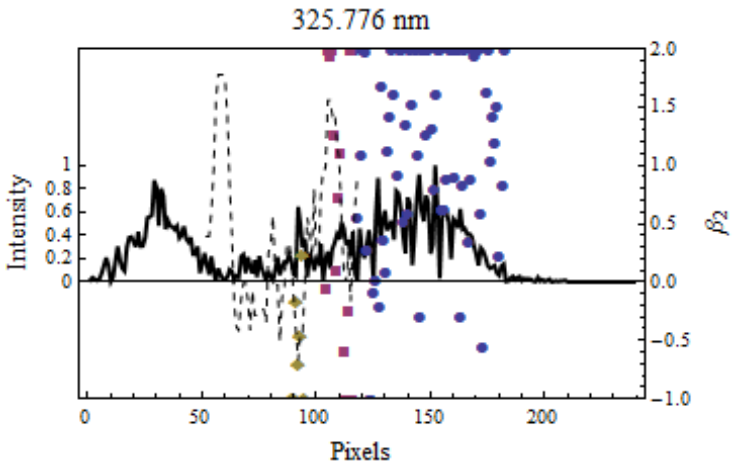
325.776 nm
Intensity
Pixels
β_2

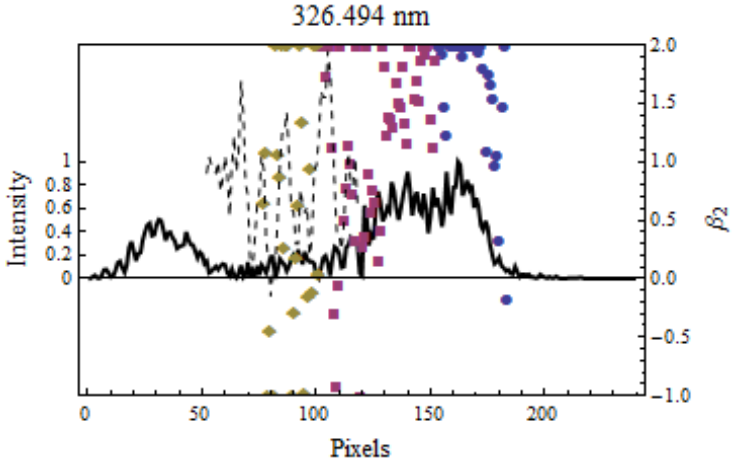
326.494 nm
Intensity
Pixels
β_2

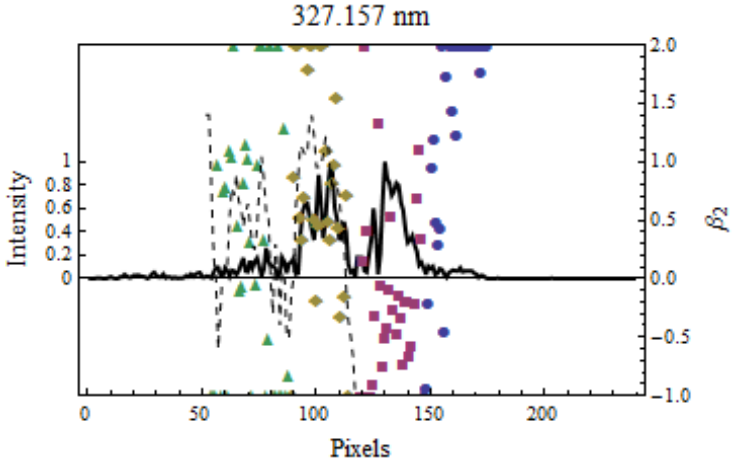
327.157 nm
Intensity
Pixels
β_2

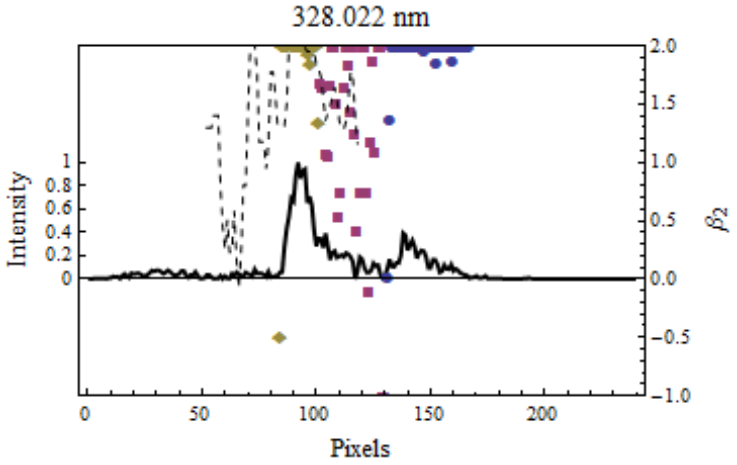
328.022 nm
Intensity
Pixels
β_2
0
0.2
0.4
0.6
0.8
1
0
50
100
150
200
−1.0
−0.5
0.0
0.5
1.0
1.5
2.0

APPENDIX B

The simulated fits to the $O(^3P_2)$ images used to obtain the relative population for O_2 from ozone dissociation in the 321 – 329 nm range.

All figures are labeled with the dissociation wavelength. The heavy dark line is the signal intensity for the total kinetic energy of the $O(^3P_2)$ image from the dissociation of O_3. The green, pink and blue lines are overlay of the $O_2(X\ ^3\Sigma_g^-)$, $O_2(a^1\Delta_g)$ and $O_2(b^1\Sigma_g^+)$ respectively. The red dashed line is the sum of all three O_2 ($X\ ^3\Sigma_g^-$), $O_2(a^1\Delta_g)$ and $O_2(b^1\Sigma_g^+)$ states. In the cases where there are two possible fits both are given and are labeled accordingly.

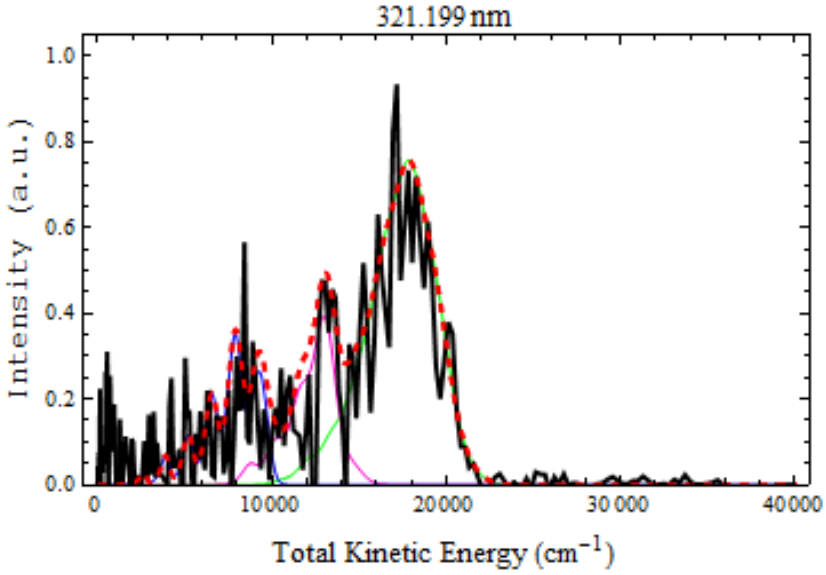

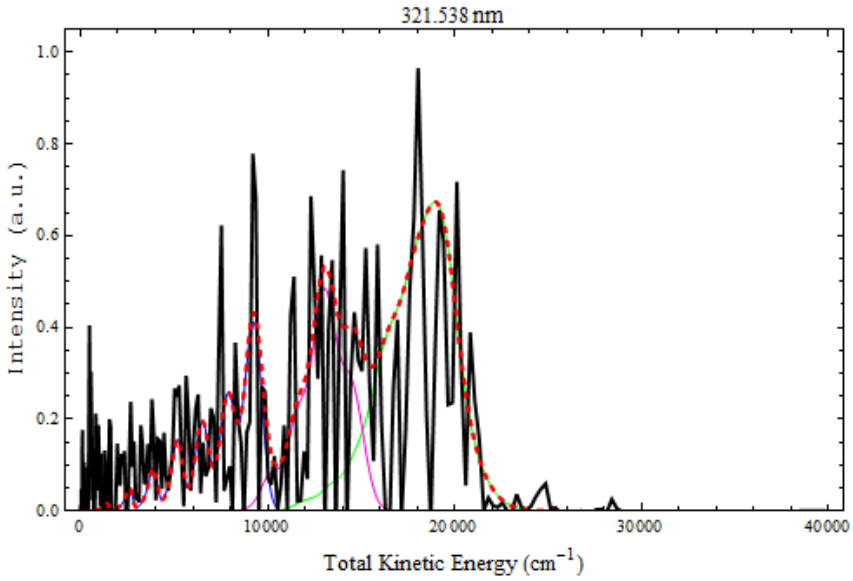
321.538 nm
Intensity (a.u.)
1.0
0.8
0.6
0.4
0.2
0.0
0
10000
20000
30000
40000
Total Kinetic Energy (cm^{-1})

Fit 1:

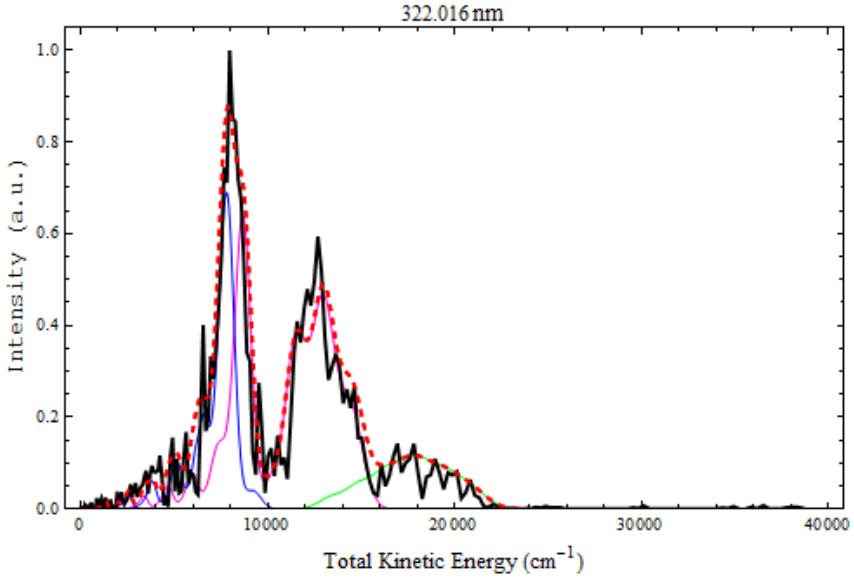
322.016 nm
Intensity (a.u.)
1.0
0.8
0.6
0.4
0.2
0.0
0
10000
20000
30000
40000
Total Kinetic Energy (cm^{-1})

Fit 2:

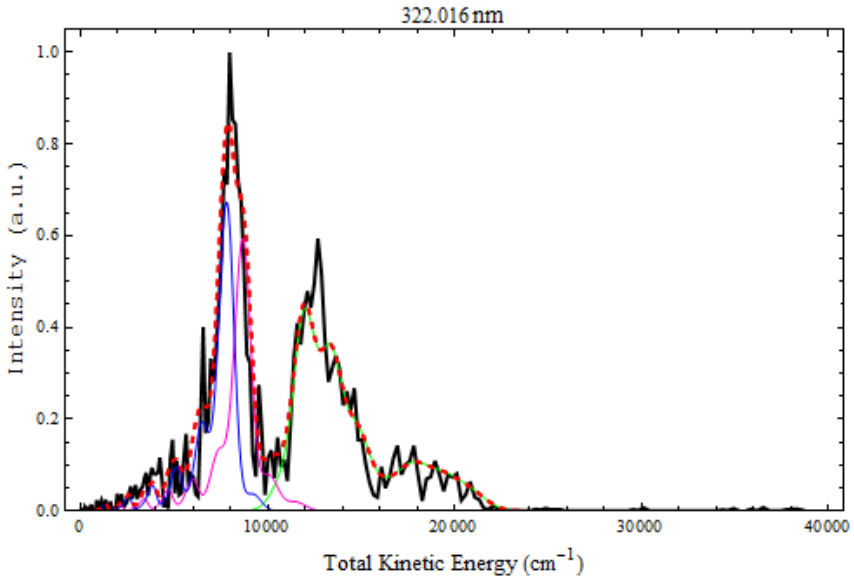
322.016 nm
Intensity (a.u.)
1.0
0.8
0.6
0.4
0.2
0.0
0
10000
20000
30000
40000
Total Kinetic Energy (cm^{-1})

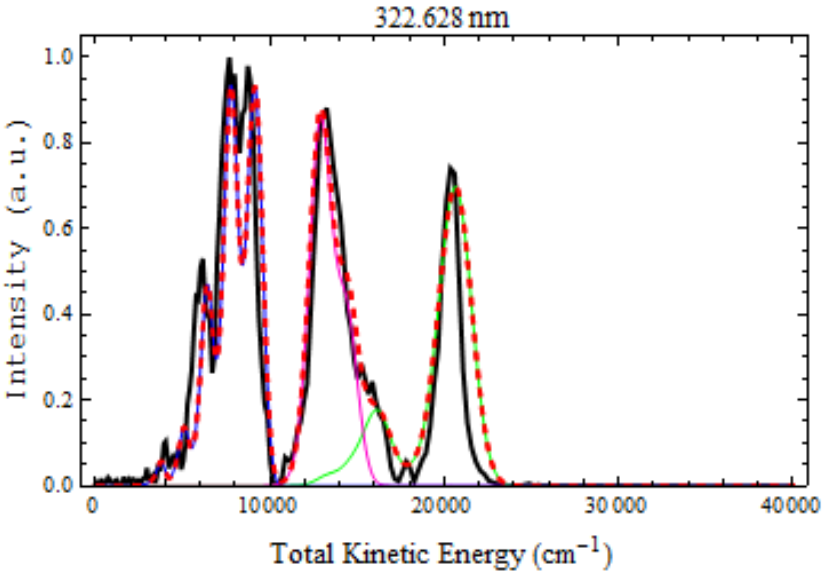
322.628 nm
Intensity (a.u.)
0.0
0.2
0.4
0.6
0.8
1.0
0
10000
20000
30000
40000
Total Kinetic Energy (cm^{-1})

Fit 1:

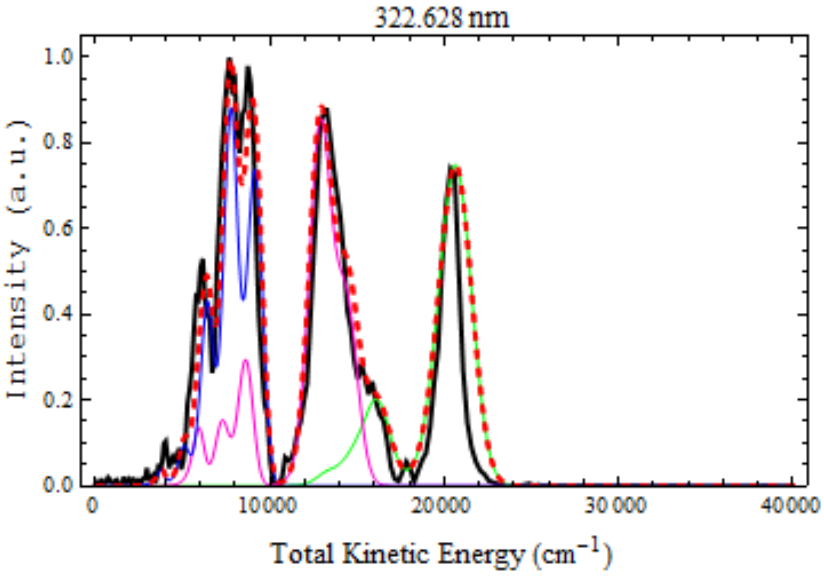
322.628 nm
Intensity (a.u.)
0.0
0.2
0.4
0.6
0.8
1.0
0
10000
20000
30000
40000
Total Kinetic Energy (cm^{-1})

Fit 2:

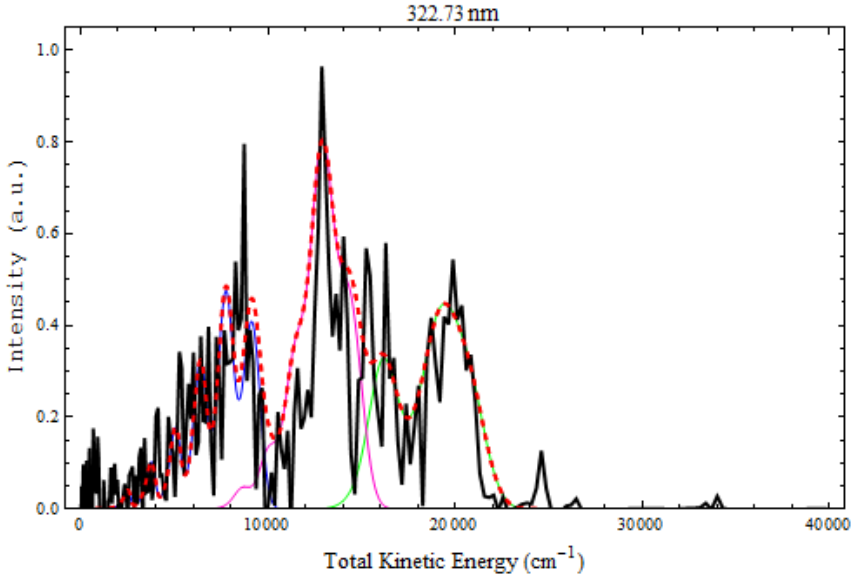
322.73 nm
Intensity (a.u.)
1.0
0.8
0.6
0.4
0.2
0.0
0
10000
20000
30000
40000
Total Kinetic Energy (cm^{-1})

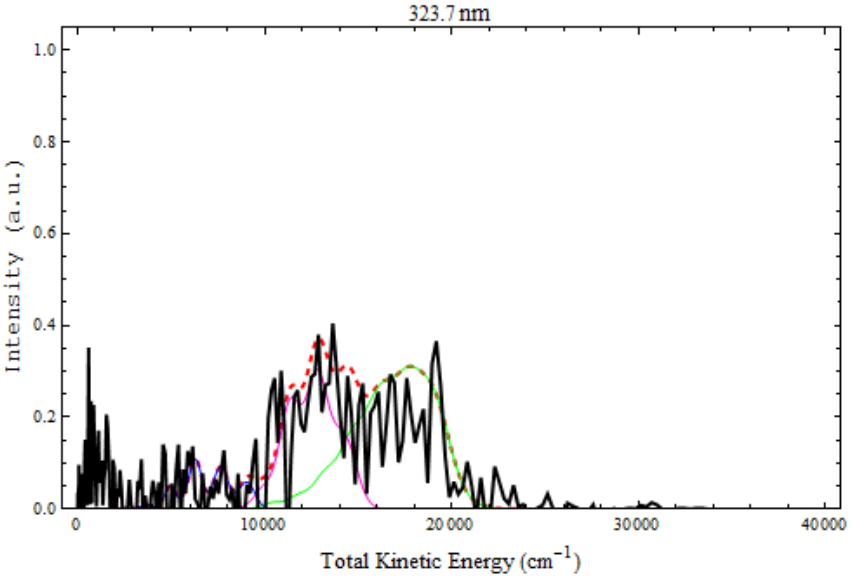
323.7 nm
Intensity (a.u.)
1.0
0.8
0.6
0.4
0.2
0.0
0
10000
20000
30000
40000
Total Kinetic Energy (cm^{-1})

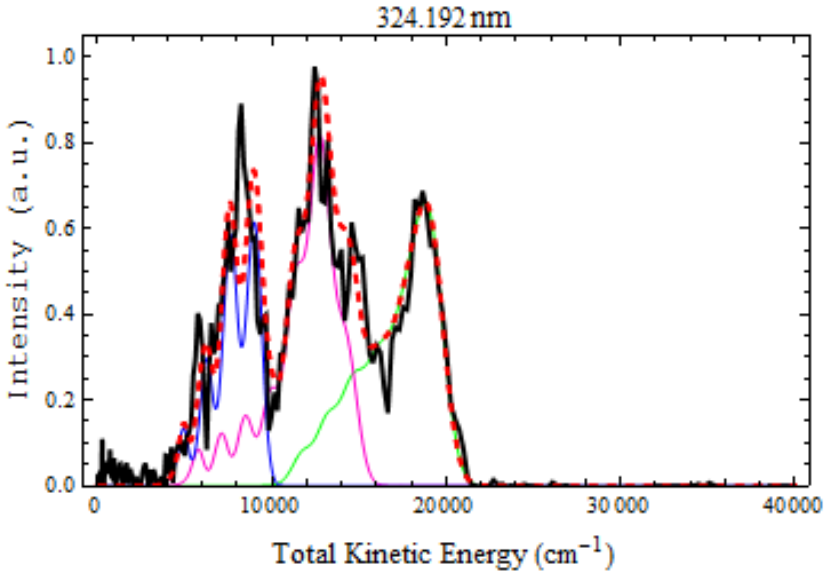
324.192 nm
Intensity (a.u.)
1.0
0.8
0.6
0.4
0.2
0.0
0
10000
20000
30000
40000
Total Kinetic Energy (cm^{-1})

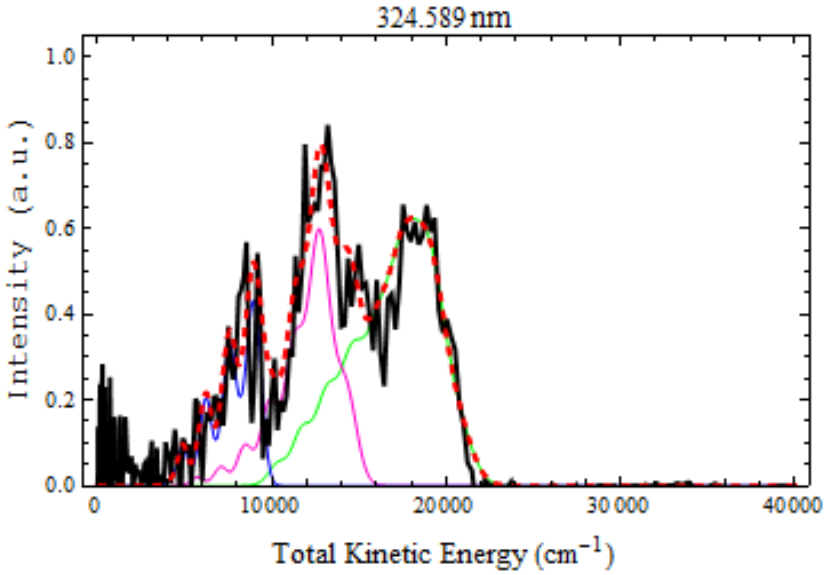
324.589 nm
Intensity (a.u.)
1.0
0.8
0.6
0.4
0.2
0.0
0
10000
20000
30000
40000
Total Kinetic Energy (cm^{-1})

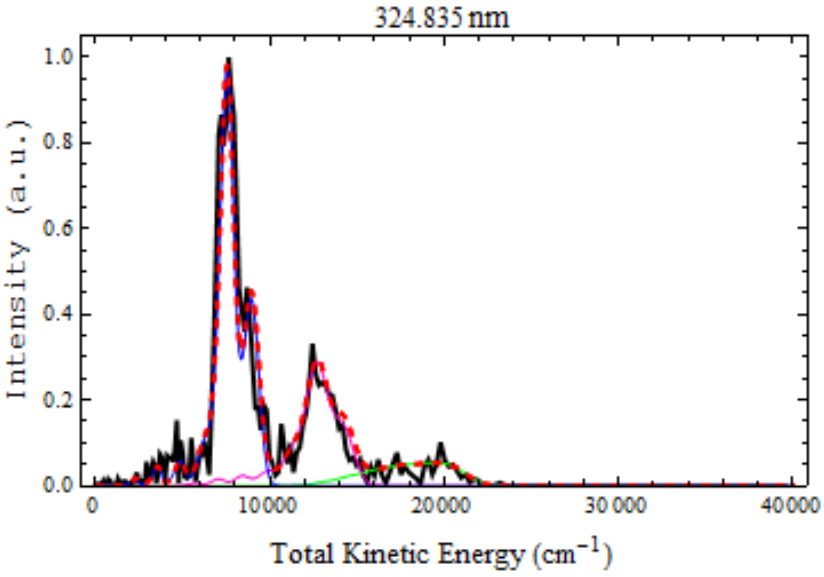
324.835 nm
Intensity (a.u.)
1.0
0.8
0.6
0.4
0.2
0.0
0
10000
20000
30000
40000
Total Kinetic Energy (cm^{-1})

Fit 1:

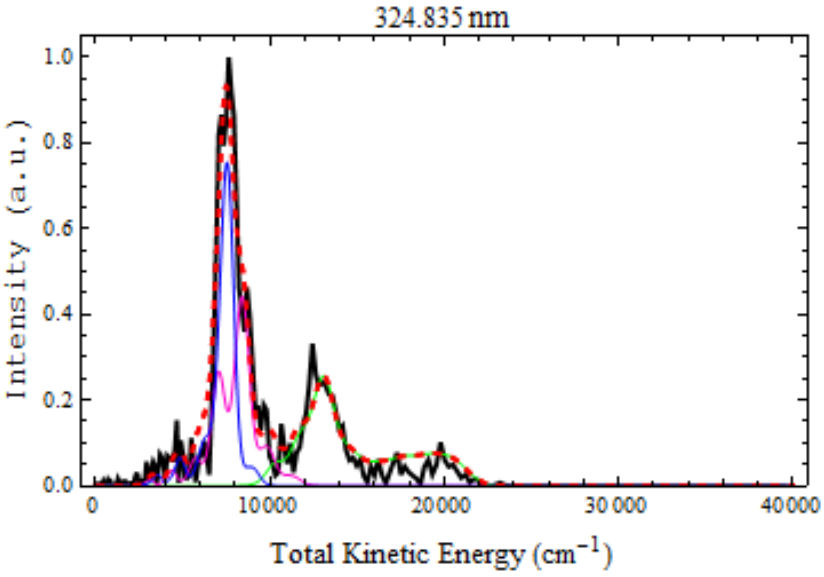
324.835 nm
Intensity (a.u.)
1.0
0.8
0.6
0.4
0.2
0.0
0
10000
20000
30000
40000
Total Kinetic Energy (cm^{-1})

Fit 2:

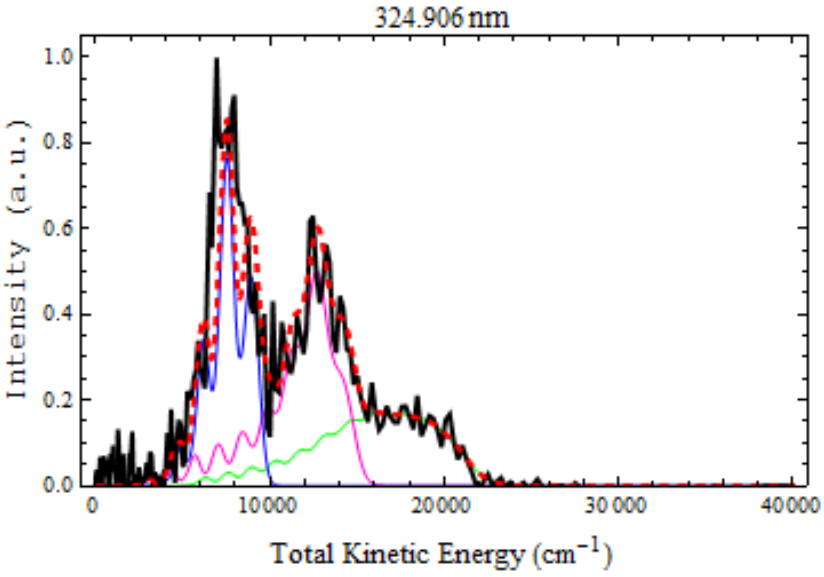
324.906 nm
Intensity (a.u.)
0.0
0.2
0.4
0.6
0.8
1.0
0
10000
20000
30000
40000
Total Kinetic Energy (cm^{-1})

Fit 1:

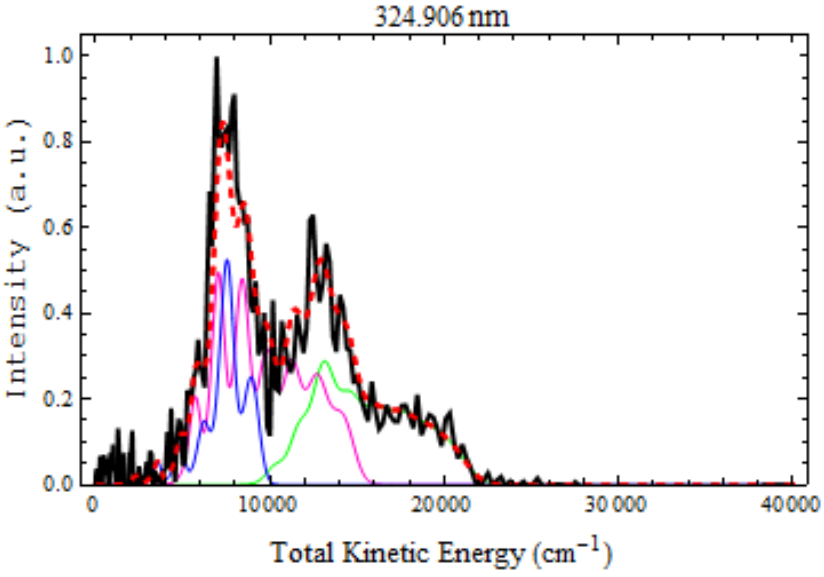
324.906 nm
Intensity (a.u.)
0.0
0.2
0.4
0.6
0.8
1.0
0
10000
20000
30000
40000
Total Kinetic Energy (cm^{-1})

Fit 2:

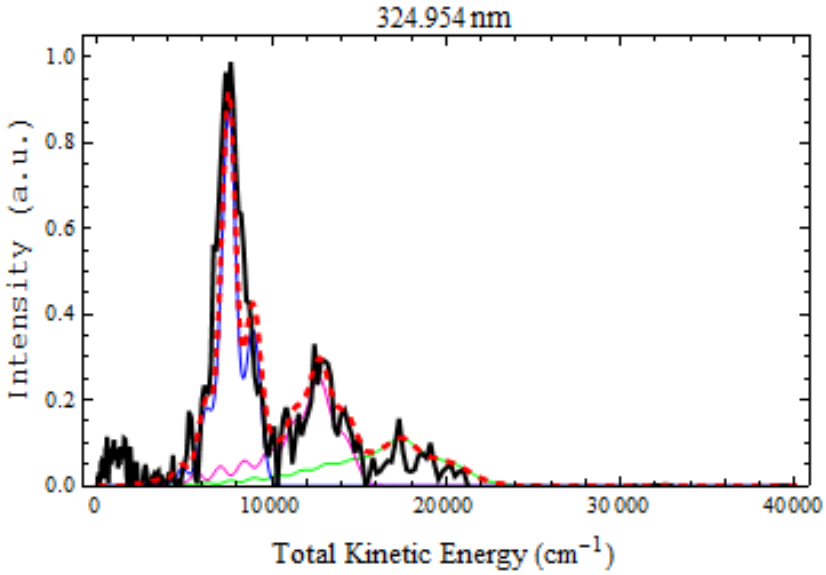
324.954 nm
Intensity (a.u.)
1.0
0.8
0.6
0.4
0.2
0.0
0
10000
20000
30000
40000
Total Kinetic Energy (cm^{-1})

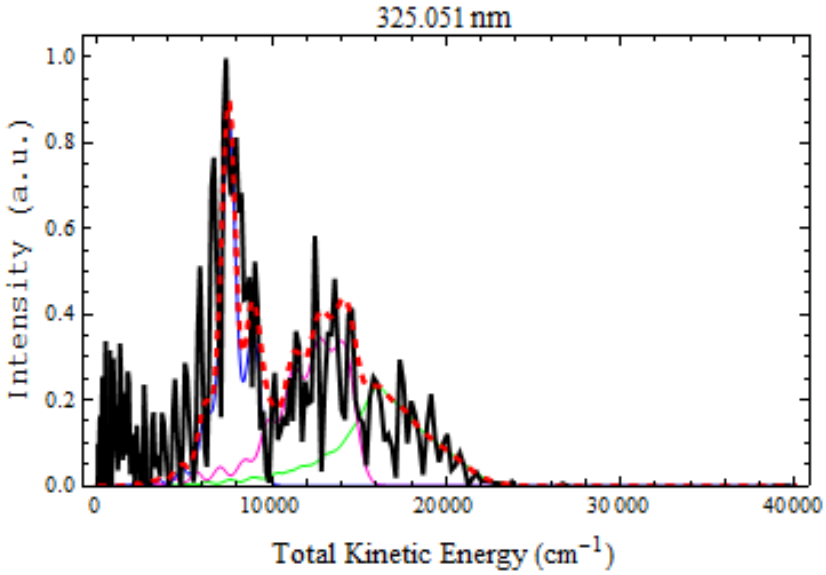
325.051 nm
Intensity (a.u.)
1.0
0.8
0.6
0.4
0.2
0.0
0
10000
20000
30000
40000
Total Kinetic Energy (cm^{-1})

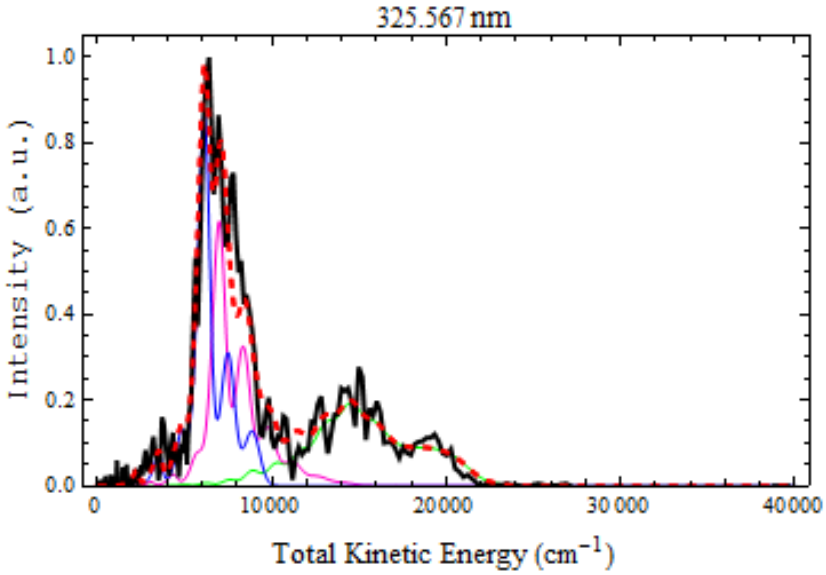
325.567 nm
Intensity (a.u.)
1.0
0.8
0.6
0.4
0.2
0.0
0
10000
20000
30000
40000
Total Kinetic Energy (cm^{-1})

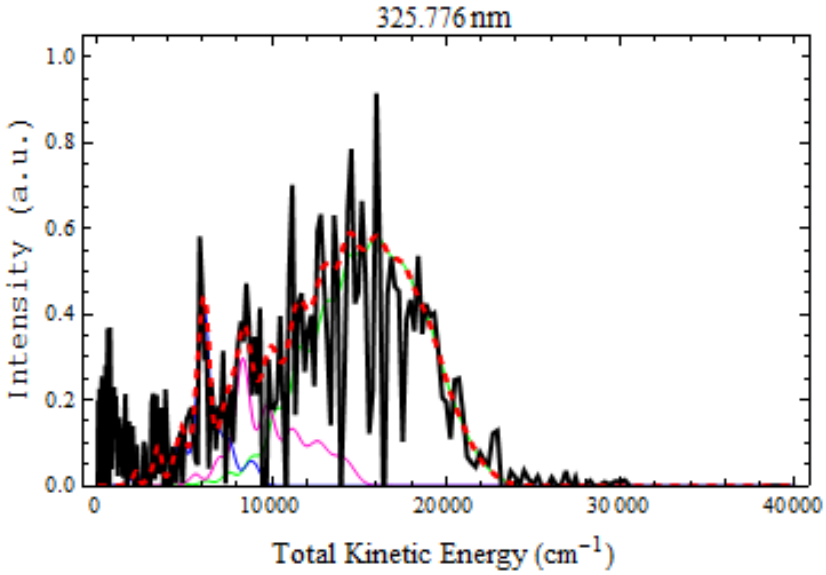
325.776 nm
Intensity (a.u.)
1.0
0.8
0.6
0.4
0.2
0.0
0
10000
20000
30000
40000
Total Kinetic Energy (cm^{-1})

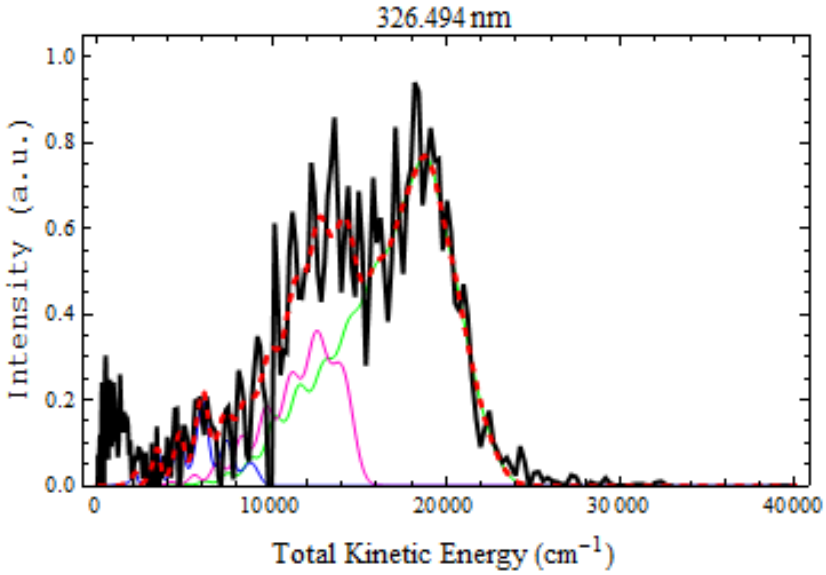
326.494 nm
Intensity (a.u.)
1.0
0.8
0.6
0.4
0.2
0.0
0
10000
20000
30000
40000
Total Kinetic Energy (cm^{-1})

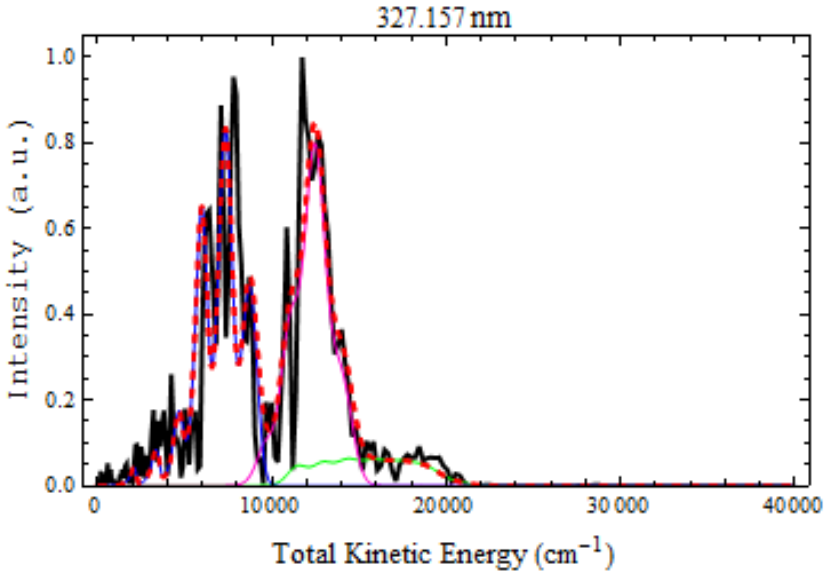
327.157 nm
Intensity (a.u.)
1.0
0.8
0.6
0.4
0.2
0.0
0
10000
20000
30000
40000
Total Kinetic Energy (cm^{-1})

Fit 1:

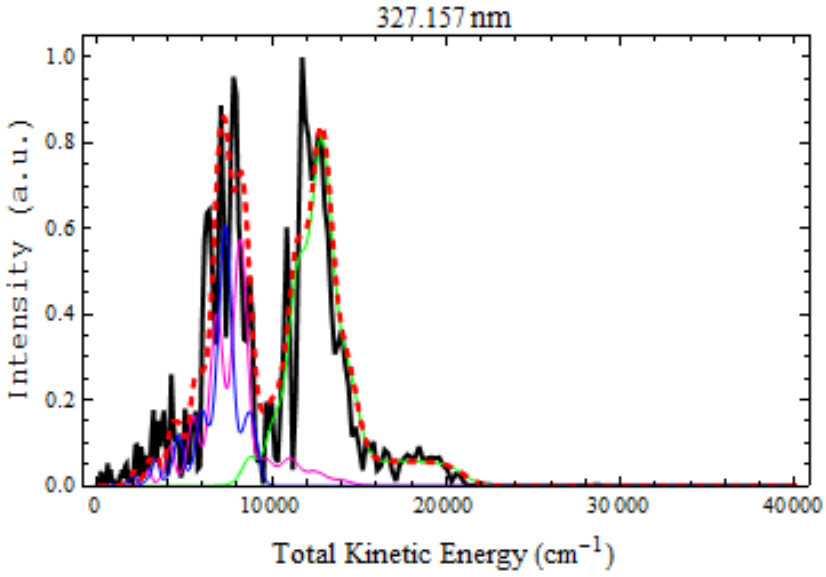
327.157 nm
Intensity (a.u.)
1.0
0.8
0.6
0.4
0.2
0.0
0
10000
20000
30000
40000
Total Kinetic Energy (cm^{-1})

Fit 2:

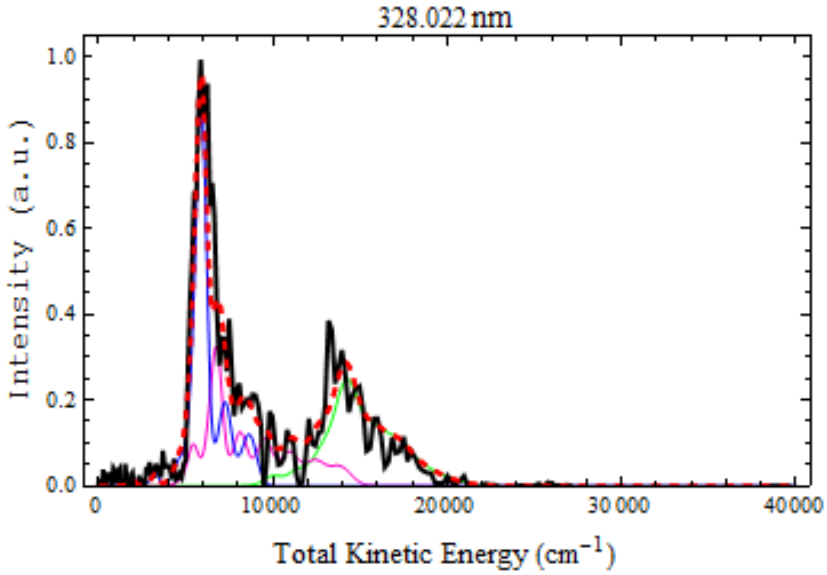
328.022 nm
Intensity (a.u.)
1.0
0.8
0.6
0.4
0.2
0.0
0
10000
20000
30000
40000
Total Kinetic Energy (cm^{-1})

APPENDIX C

Change in the relative vibrational population of O_2 as the absorption of ozone to ν_1 or ν_2 changes.

The following plots demonstrate the change in O_2 vibrational population as the ozone absorption changes. In all the figures blue green and red points are the relative vibrational populations for the $O_2(X\ ^3\Sigma_g^-)$, $O_2(a^1\Delta_g)$ and $O_2(b^1\Sigma_g^+)$ states respectively. The plots are done twice once using Fit 1 and once using Fit 2. Each plot is labeled with the appropriate vibrational level.

The effect of ν_1 for Fit 1:

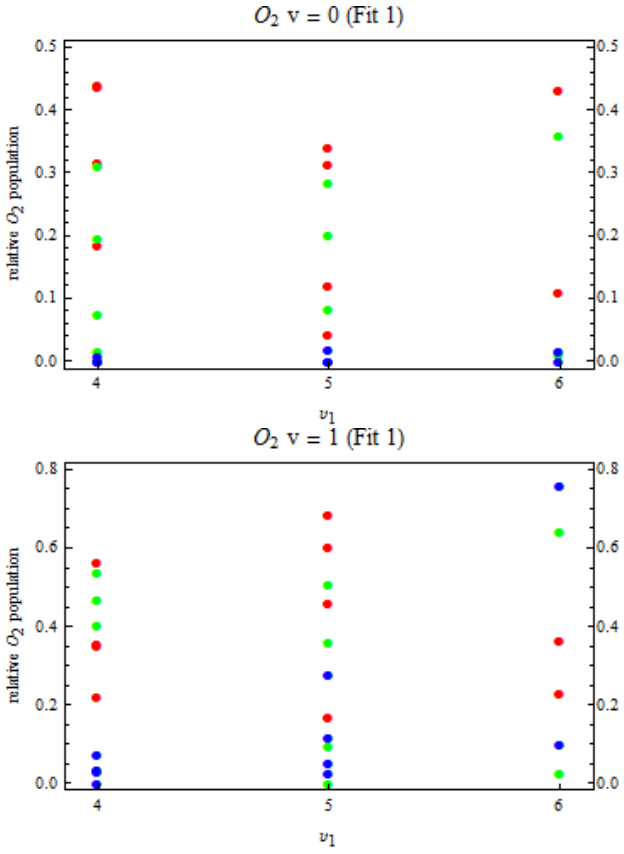

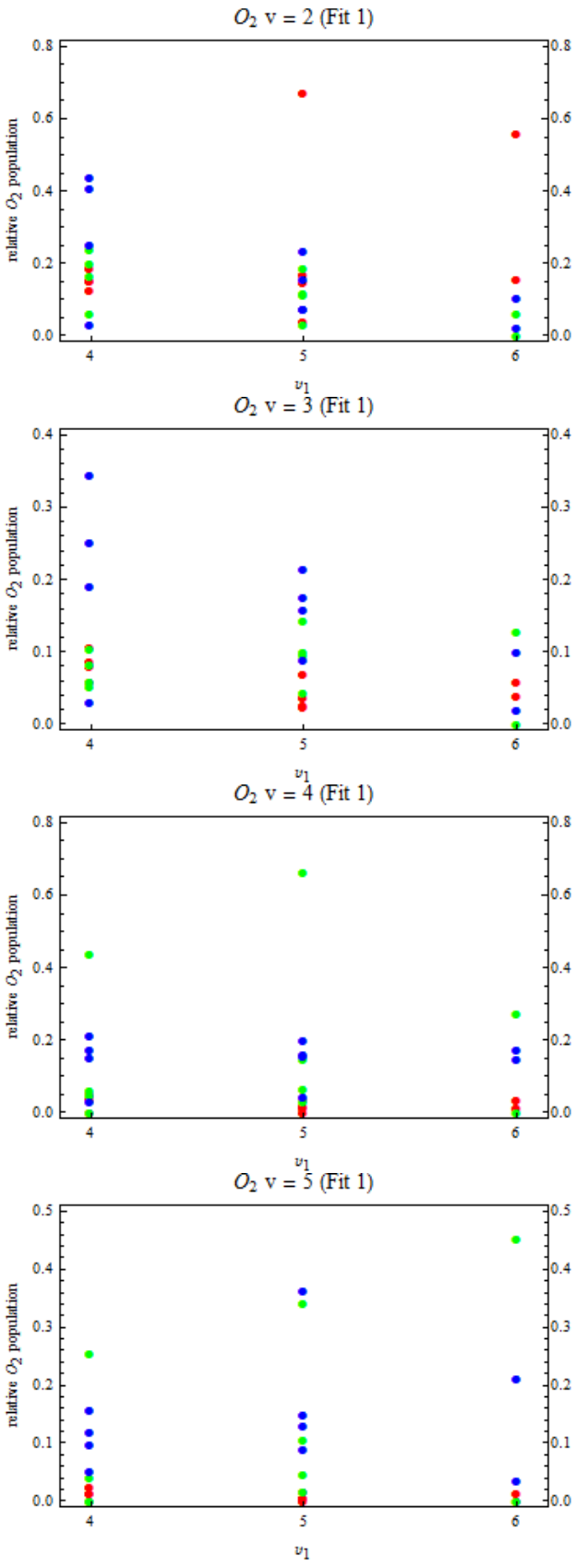
O_2 v = 2 (Fit 1)
relative O_2 population
v_1
O_2 v = 3 (Fit 1)
relative O_2 population
v_1
O_2 v = 4 (Fit 1)
relative O_2 population
v_1
O_2 v = 5 (Fit 1)
relative O_2 population
v_1

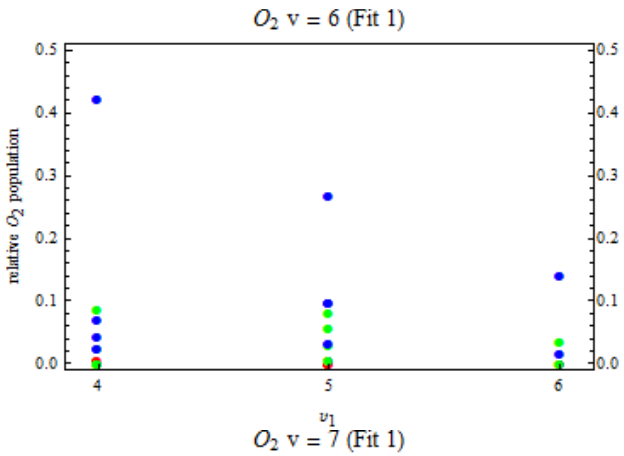
O_2 v = 6 (Fit 1)
relative O_2 population
0.5
0.4
0.3
0.2
0.1
0.0
4
5
6
v_1

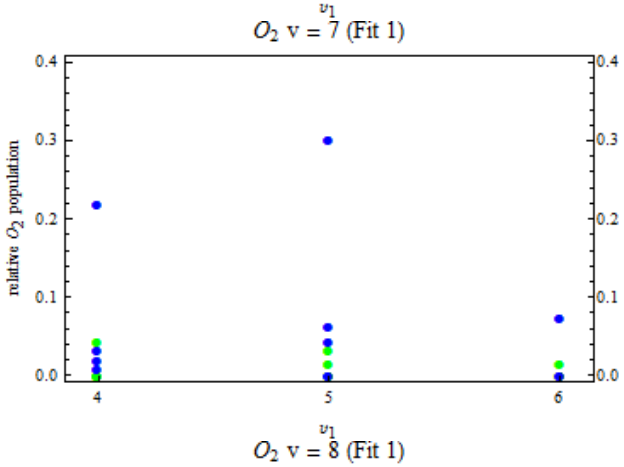
O_2 v = 7 (Fit 1)
relative O_2 population
0.4
0.3
0.2
0.1
0.0
4
5
6
v_1

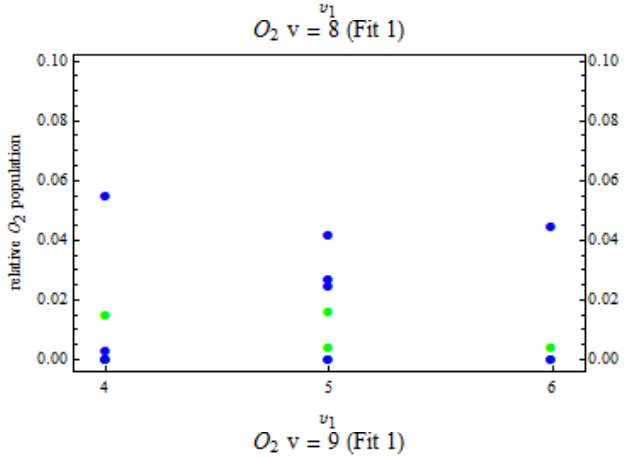
O_2 v = 8 (Fit 1)
relative O_2 population
0.10
0.08
0.06
0.04
0.02
0.00
4
5
6
v_1

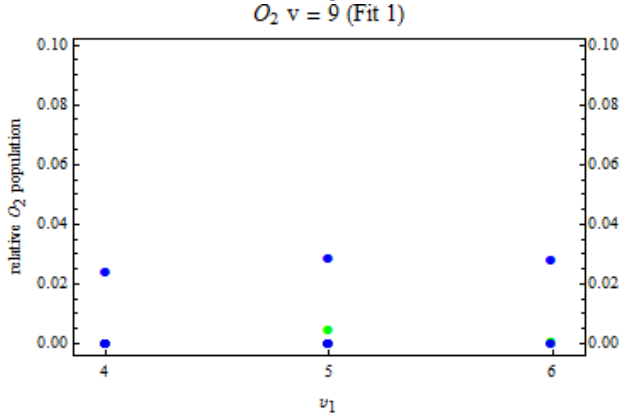
O_2 v = 9 (Fit 1)
relative O_2 population
0.10
0.08
0.06
0.04
0.02
0.00
4
5
6
v_1

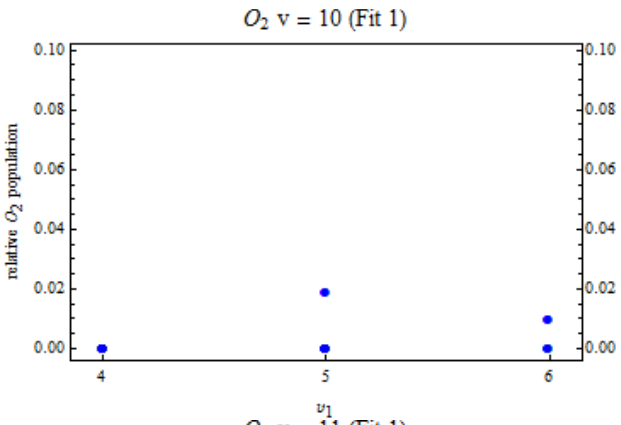
O_2 v = 10 (Fit 1)
relative O_2 population
0.10
0.08
0.06
0.04
0.02
0.00
4
5
6
v_1

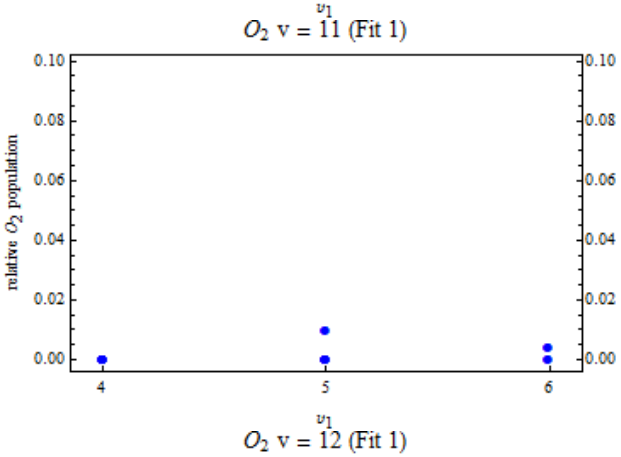
O_2 v = 11 (Fit 1)
relative O_2 population
0.10
0.08
0.06
0.04
0.02
0.00
4
5
6
v_1

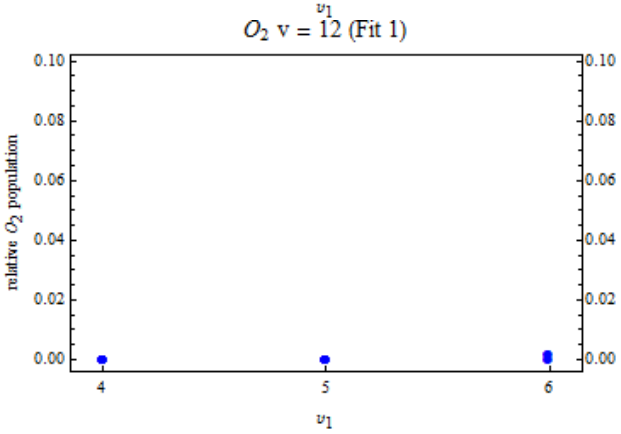
O_2 v = 12 (Fit 1)
relative O_2 population
0.10
0.08
0.06
0.04
0.02
0.00
4
5
6
v_1

The effect of ν_2 for Fit 1:

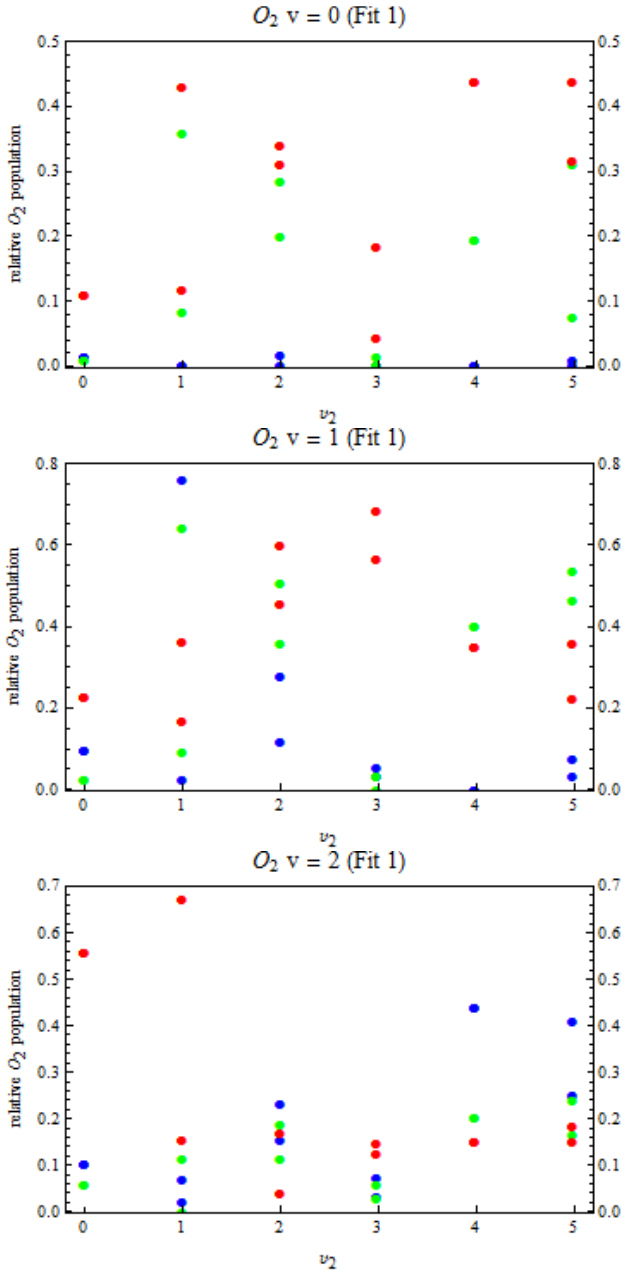

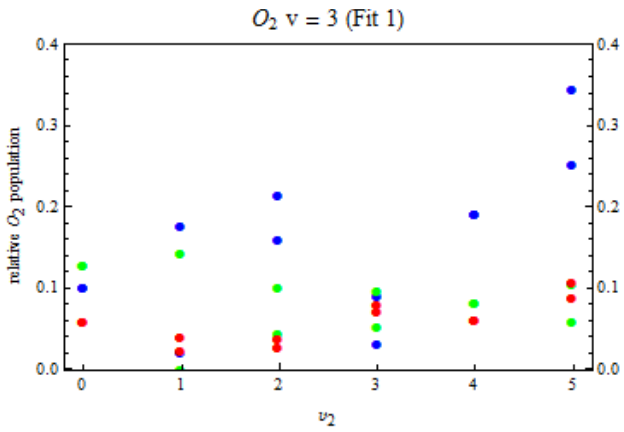
O_2 v = 3 (Fit 1)
relative O_2 population
v_2

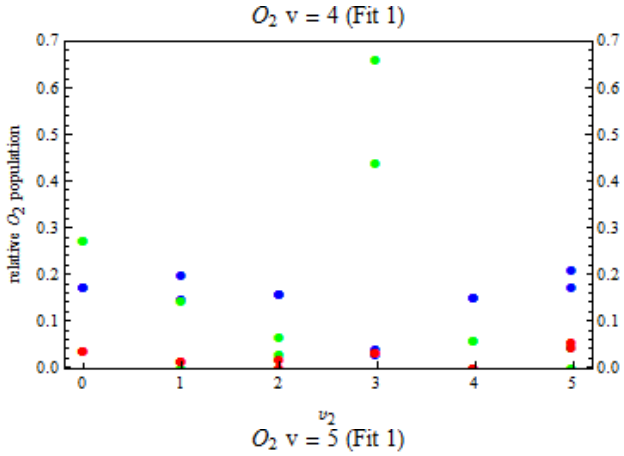
O_2 v = 4 (Fit 1)
relative O_2 population
v_2

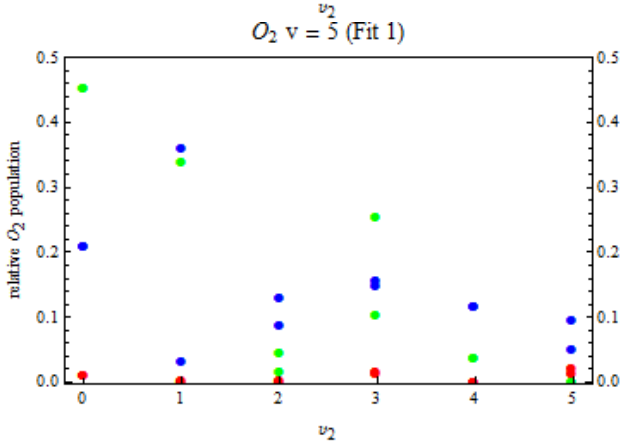
O_2 v = 5 (Fit 1)
relative O_2 population
v_2

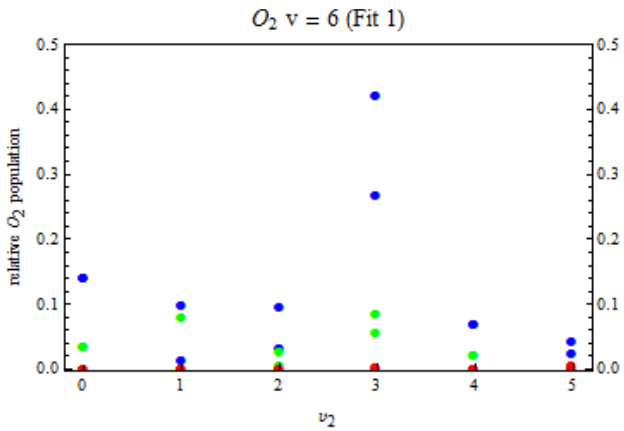
O_2 v = 6 (Fit 1)
relative O_2 population
v_2

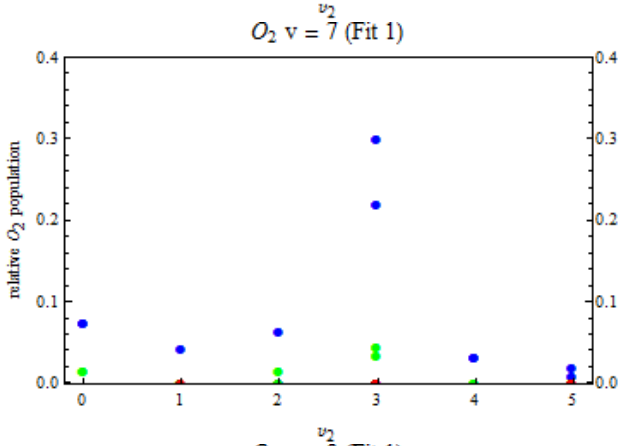
O_2 v = 7 (Fit 1)
relative O_2 population
v_2

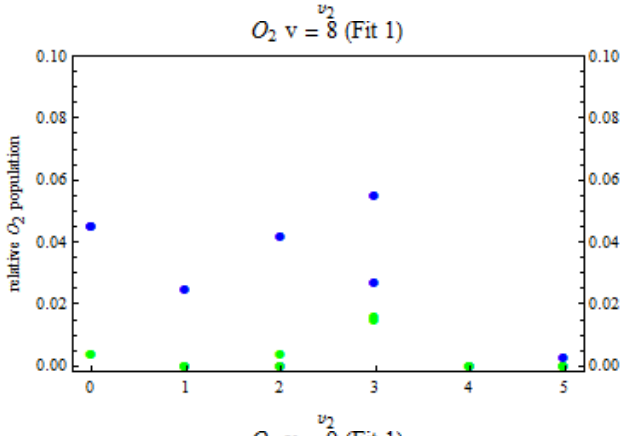
O_2 v = 8 (Fit 1)
relative O_2 population
v_2

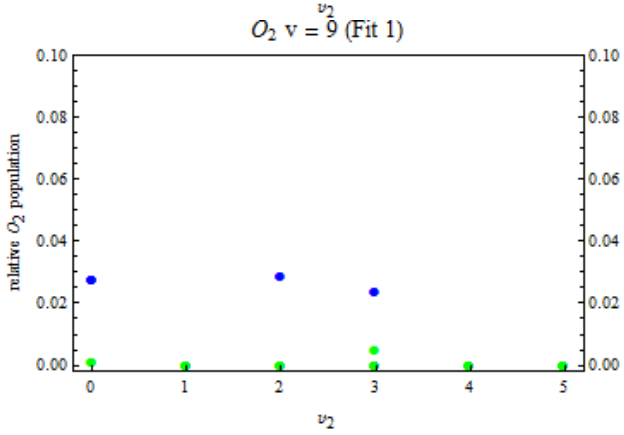
O_2 v = 9 (Fit 1)
relative O_2 population
v_2

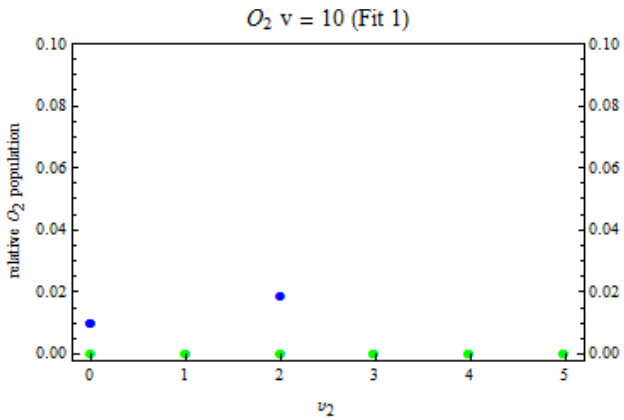
O_2 v = 10 (Fit 1)
relative O_2 population
0.10
0.08
0.06
0.04
0.02
0.00
0
1
2
3
4
5
v_2

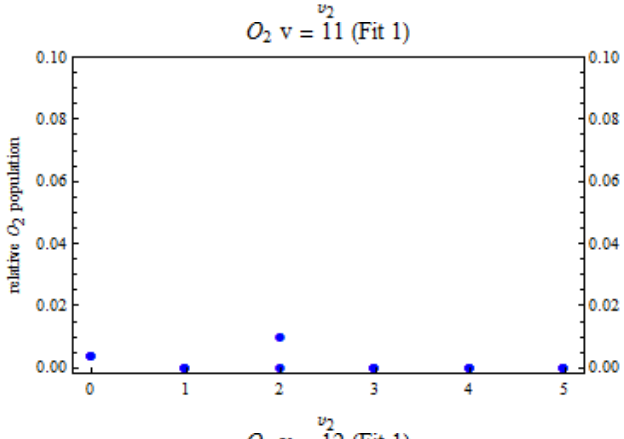
O_2 v = 11 (Fit 1)
relative O_2 population
0.10
0.08
0.06
0.04
0.02
0.00
0
1
2
3
4
5
v_2

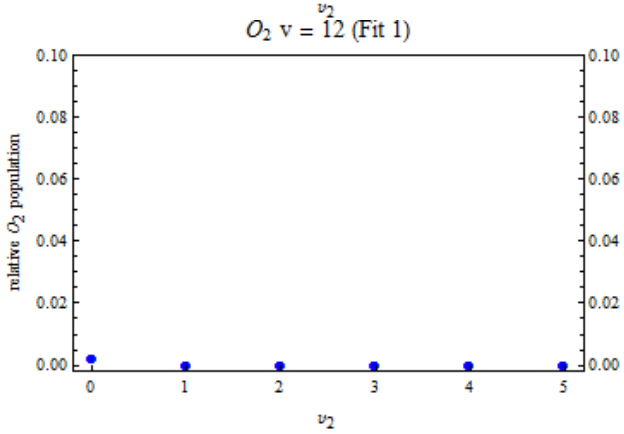
O_2 v = 12 (Fit 1)
relative O_2 population
0.10
0.08
0.06
0.04
0.02
0.00
0
1
2
3
4
5
v_2

The effect of ν_1 for Fit 2:

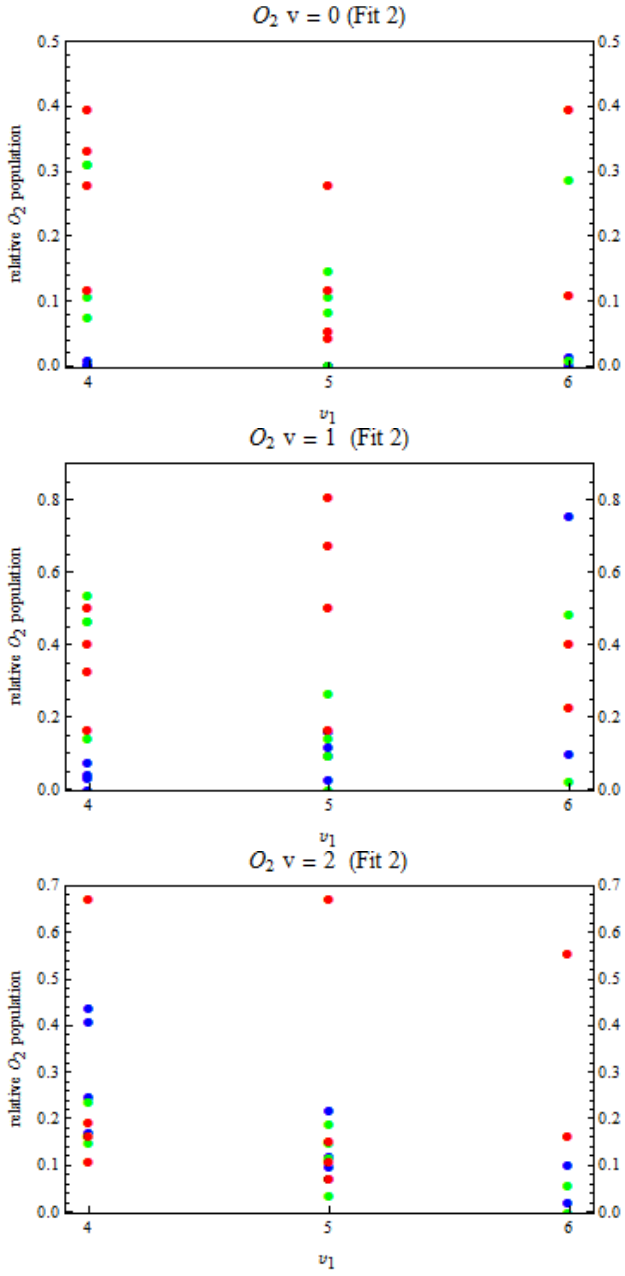

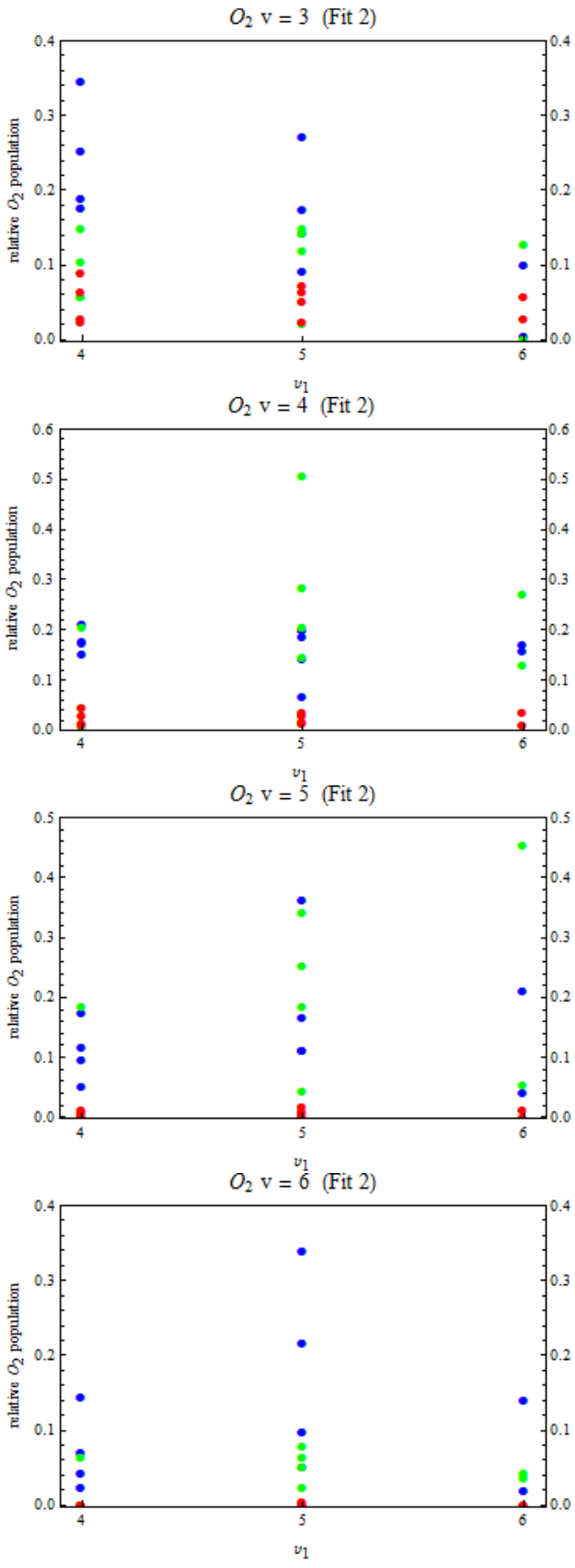
O_2 v = 3 (Fit 2)
relative O_2 population
v_1
O_2 v = 4 (Fit 2)
relative O_2 population
v_1
O_2 v = 5 (Fit 2)
relative O_2 population
v_1
O_2 v = 6 (Fit 2)
relative O_2 population
v_1

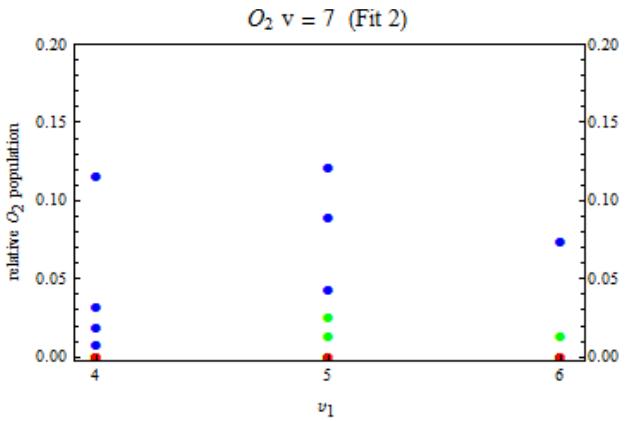
O_2 v = 7 (Fit 2)
relative O_2 population
0.20
0.15
0.10
0.05
0.00
4
5
6
v_1

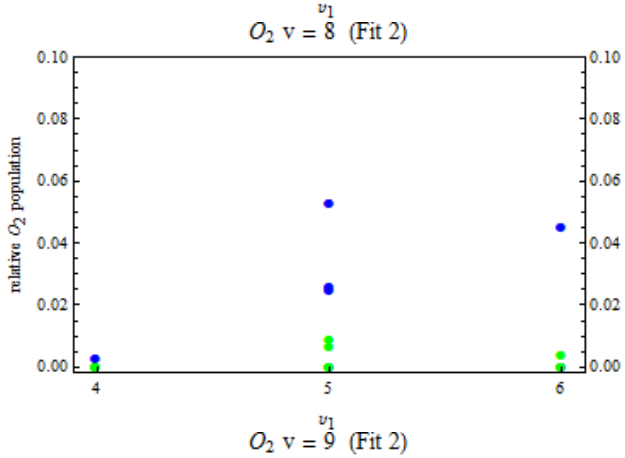
O_2 v = 8 (Fit 2)
relative O_2 population
0.10
0.08
0.06
0.04
0.02
0.00
4
5
6
v_1

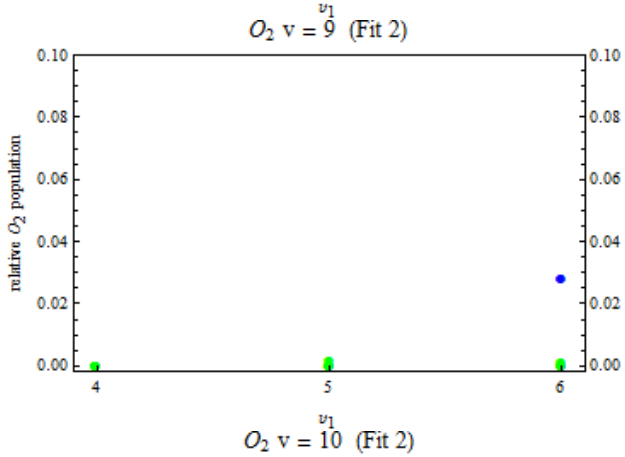
O_2 v = 9 (Fit 2)
relative O_2 population
0.10
0.08
0.06
0.04
0.02
0.00
4
5
6
v_1

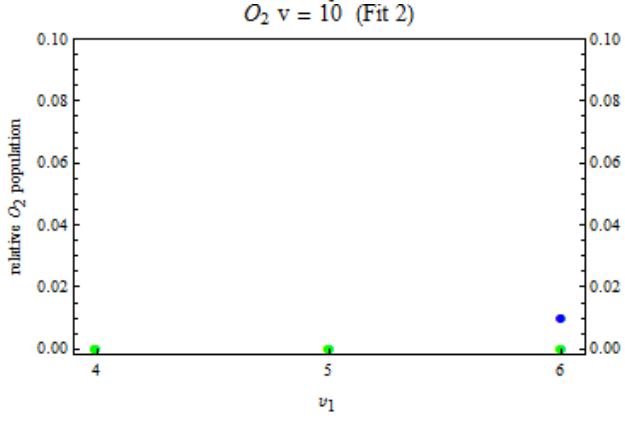
O_2 v = 10 (Fit 2)
relative O_2 population
0.10
0.08
0.06
0.04
0.02
0.00
4
5
6
v_1

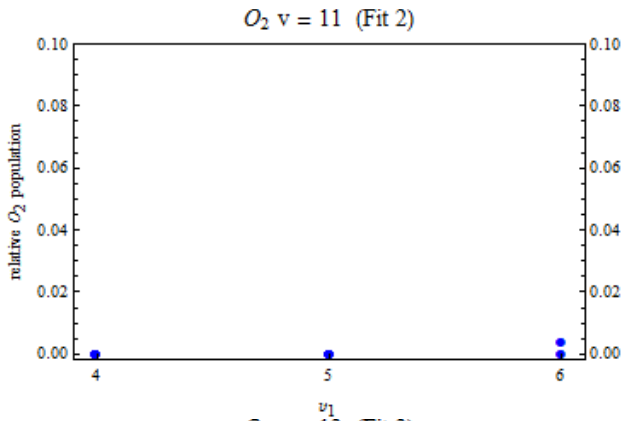
O_2 v = 11 (Fit 2)
relative O_2 population
0.10
0.08
0.06
0.04
0.02
0.00
4
5
6
v_1

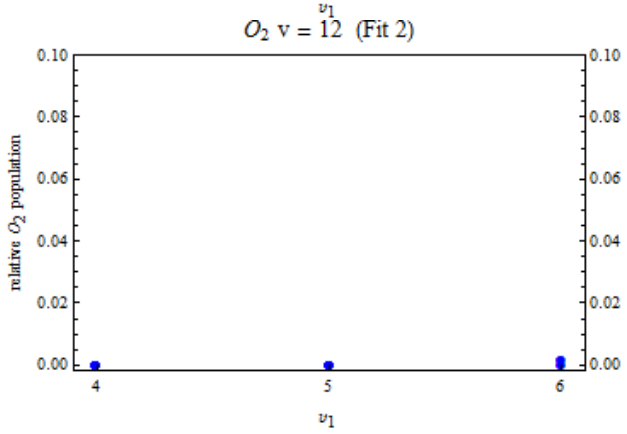
O_2 v = 12 (Fit 2)
relative O_2 population
0.10
0.08
0.06
0.04
0.02
0.00
4
5
6
v_1

The effect of ν_2 for Fit 2:

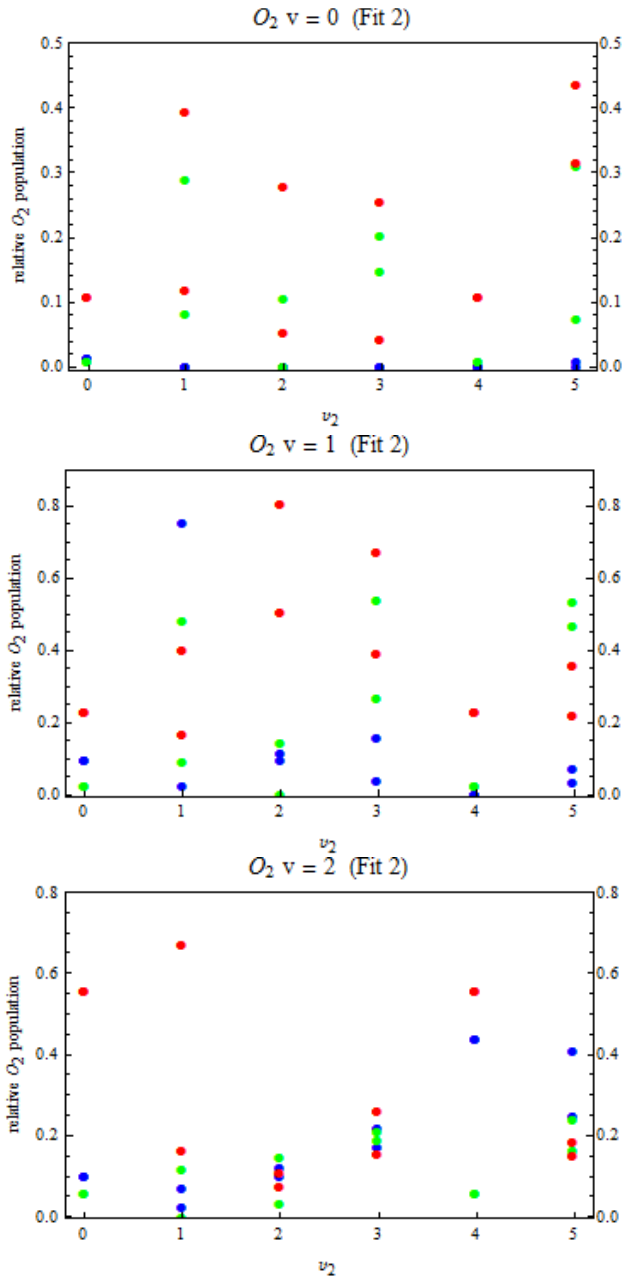

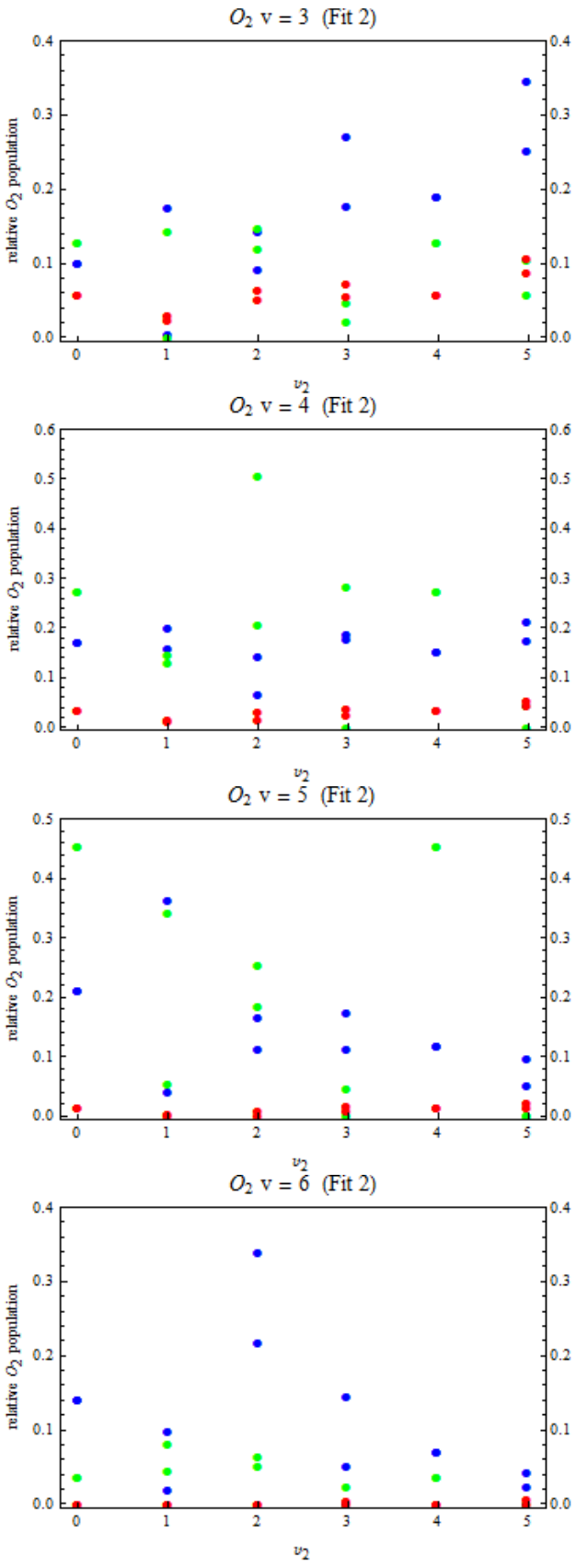
O_2 v = 3 (Fit 2)
relative O_2 population
v_2
O_2 v = 4 (Fit 2)
relative O_2 population
v_2
O_2 v = 5 (Fit 2)
relative O_2 population
v_2
O_2 v = 6 (Fit 2)
relative O_2 population
v_2

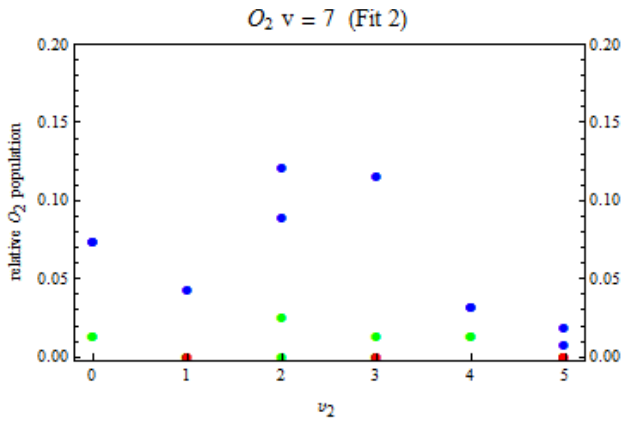
O_2 v = 7 (Fit 2)
relative O_2 population
0.20
0.15
0.10
0.05
0.00
0
1
2
3
4
5
v_2

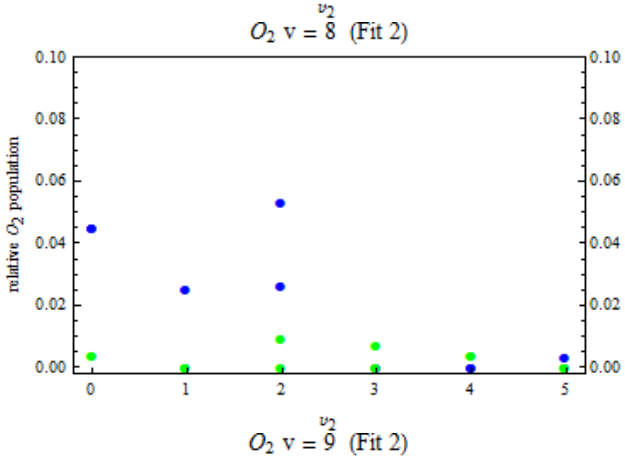
O_2 v = 8 (Fit 2)
relative O_2 population
0.10
0.08
0.06
0.04
0.02
0.00
0
1
2
3
4
5
v_2

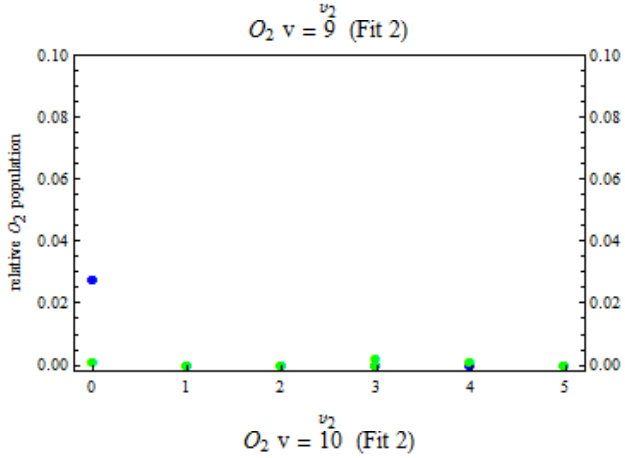
O_2 v = 9 (Fit 2)
relative O_2 population
0.10
0.08
0.06
0.04
0.02
0.00
0
1
2
3
4
5
v_2

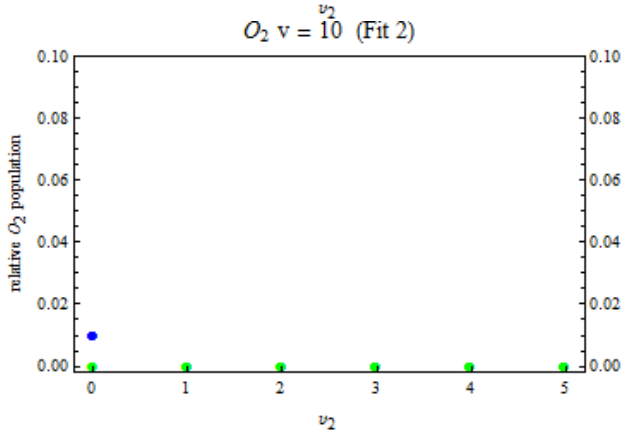
O_2 v = 10 (Fit 2)
relative O_2 population
0.10
0.08
0.06
0.04
0.02
0.00
0
1
2
3
4
5
v_2

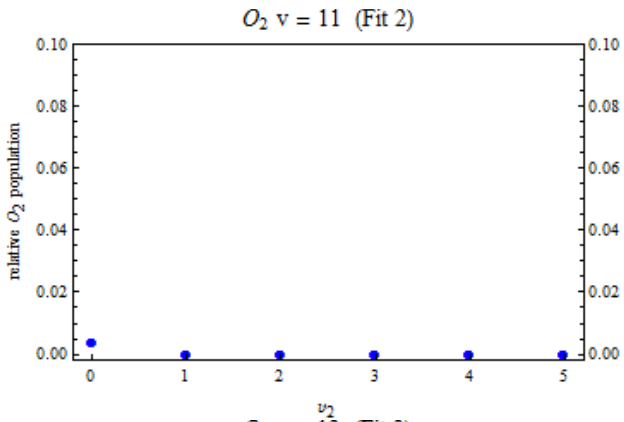
O_2 v = 11 (Fit 2)
relative O_2 population
0.10
0.08
0.06
0.04
0.02
0.00
0
1
2
3
4
5
v_2

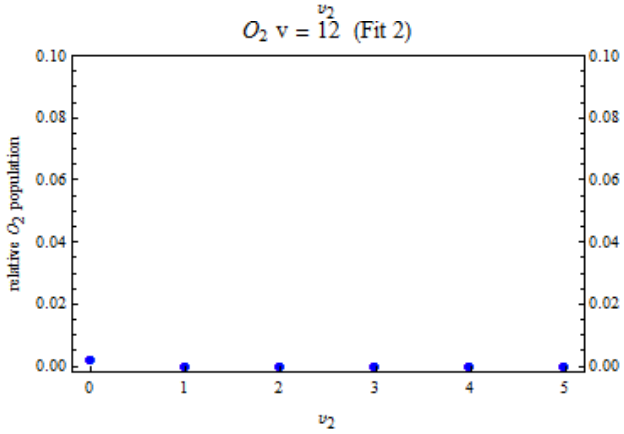
O_2 v = 12 (Fit 2)
relative O_2 population
0.10
0.08
0.06
0.04
0.02
0.00
0
1
2
3
4
5
v_2

APPENDIX D

O_2 images fits to gain insight to the O_2 REMPI spectra.

The possible O_2 lower vibrational states, transitions to the O_2 $d\ ^1\Pi_g$ and $C\ ^3\Pi_g$ states and example fits for all of the O_2 images are given. The images are separated into two groups, the first have corresponding O_2 population data.

The following table displays possible transitions from the three lower states of $O_2(X^3\Sigma_g^-)$, $O_2(a^1\Delta_g)$ and $O_2(b^1\Sigma_g^+)$ to the upper states of O_2, $d\ ^1\Pi_g$ and $C\ ^3\Pi_g$. Transitions within 2 nm of the calculated value, J = 0, were considered due to the broad spectra and the lack of specific knowledge of the upper states, particularly for high vibrational levels.

Wavelength	Lower electronic state	$d\ ^1\Pi_g$ upper electronic state	$C\ ^3\Pi_g$ upper electronic state
321.199	$X^3\Sigma_g^-$ $a^1\Delta_g$ $b^1\Sigma_g^+$	(2 - 5 (1.5)) 2-0 (0.27)	(2-5(1.8)), 3-6(0.08)
321.538	$X^3\Sigma_g^-$ $a^1\Delta_g$ $b^1\Sigma_g^+$	1- 4 (0.23) 2- 0 (0.07)	(2-5(1.5))
322.016	$X^3\Sigma_g^-$ $a^1\Delta_g$ $b^1\Sigma_g^+$	1-4 (0.245) 2- 0 (0.54), 9-9 (0.38) 8-4 (0.49)	(2-5(1.1))
322.628	$X^3\Sigma_g^-$ $a^1\Delta_g$ $b^1\Sigma_g^+$	(0 - 3 (1.2)) (2 - 0 (1.2)) (8-4 (1.1))	2-5(0.45), (3-6(1.3)) 3-1(0.68)
322.73	$X^3\Sigma_g^-$ $a^1\Delta_g$ $b^1\Sigma_g^+$	1-4 (0.96), (0-3 (1.1)) (2-0 (1.3)) 5-4 (0.48) 7-3 (0.89) (8-4 (1.2))	2-5(0.34) 3-1(0.58), (4-2(1.2)) (5-0(1.6)),(7-2(1.7))
323.7	$X^3\Sigma_g^-$ $a^1\Delta_g$ $b^1\Sigma_g^+$	0-3 (0.15) (3-7 (1.3)) (4-3 (1.54)) 7-3 (0.08)	(1-4(1.5)),2-5(0.63) (2-0(1.2)), 3-1(0.39) (6-1(1.1)), 5-0(0.63)
324.192	$X^3\Sigma_g^-$ $a^1\Delta_g$ $b^1\Sigma_g^+$	0-3 (0.34), 3-7 (0.76) (4-3 (1.1)) 5-4 (0.98) (6-2 (1.5)) 7-3(0.58)	(1-4(1)),(2-5(1.2)) 2-0(0.68), 3-1(0.88), (6-5(1.1)), 7-6 (0.61) (6-1(1.6)), 5-0(0.14)

wavelength	Lower electronic state	$d\ ^1\Pi_g$ upper electronic state	$C\ ^3\Pi_g$ upper electronic state
324.589	$X^3\Sigma_g^-$ $a^1\Delta_g$ $b^1\Sigma_g^+$	0-3 (0.74), 3-7 (0.37) 4-3 (0.65) (5-4 (1.4)) (6-2(1.1)) 7-3 (0.97)	1-4(0.63),(2-5(1.5)),(4-8(2)) 2-0(0.28), (3-1(1.3)), (6-5(0.72)),(7-6 (1)) (6-1(2)), 5-0(0.26)
324.835	$X^3\Sigma_g^-$ $a^1\Delta_g$ $b^1\Sigma_g^+$	0-3 (0.99) 3-7 (0.12) 4-3 (0.41) (5-4 (1.6)) (7-7 (1.2)) 8-8 (0.98) 6-2 (0.87) (7-3(1.2)) (9-6(1.2))	1-4(0.38),(2-5(1.8)),(4-8(1.7)) 2-0(0.04),(3-1(1.5)) (8-4(1.6)), 5-0(0.51)
324.906	$X^3\Sigma_g^-$ $a^1\Delta_g$ $b^1\Sigma_g^+$	(0-3(1.1)) 3-7(0.05) 6-11(0.21) 4-3 (0.34) (5-4 (1.7)) (7-7 (1.2)) (8-8 (1.1)) 6-2 (0.8) (7-3(1.2))	1-4(0.31),(2-5(1.8)),(4-8(1.6)) 2-0(0.03),(3-1(1.6)) (8-4(1.5)), 5-0(0.58)
324.954	$X^3\Sigma_g^-$ $a^1\Delta_g$ $b^1\Sigma_g^+$	3-7 (0.002) 4-3 (0.29 (5-4 (1.7)) 6-2(0.75)	1-4(0.26),(2-5(1.9)),(4-8(1.6)) 2-0(0.08),(3-1(1.6)),6-5(0.35) 5-0(0.63)
325.051	$X^3\Sigma_g^-$ $a^1\Delta_g$ $b^1\Sigma_g^+$	3-7 (0.1) 6-11 (0.06) 4-3 (0.19) 6-2 (0.66)	1-4(0.16),(2-5(2)),(4-8(1.5)) 2-0(0.18), (3-1(1.7)), 6-5(0.25), (7-6 (1.5))
325.567	$X^3\Sigma_g^-$ $a^1\Delta_g$ $b^1\Sigma_g^+$	(2-6 (1.7)) 3-7 (0.61) 5-10 (2) 6-11 (0.45) (3-2 (1.7)) 4-3 (0.32) 6-2 (0.14) (3,6 for small)	4-8(0.98),(5-9(1.2)),(7-12(1.7)) 2-0(0.7), 6-5(0.26), (7-6 (2)) (5-0(1.2))
325.776	$X^3\Sigma_g^-$ $a^1\Delta_g$	(2-6 (1.4)) 3-7 (0.8) (3-2 (1.5)) 4-3 (0.53)	4-8(0.77),(5-9(1.4)) 2-0 (0.9)
326.494	$X^3\Sigma_g^-$ $a^1\Delta_g$ $b^1\Sigma_g^+$	(6, 7, 10, 11) (2, 3, 6, 7) (1, 2, 5)	4-8(0.05) (6-5 (1.2)),5-4(0.7),(2-0(1.6) 8-4(0.06)
327.157	$X^3\Sigma_g^-$ $a^1\Delta_g$ $b^1\Sigma_g^+$	2-6 (0.06) 3-2 (0.12) 5-1 (0.64) (6-2 (1.4))	(3-7(1.6))
328.022	$X^3\Sigma_g^-$ $a^1\Delta_g$ $b^1\Sigma_g^+$	(1-5 (1.5)) 2-4 (0.8) (2-1 (1.3)) 3-2 (0.74) 5-1 (0.22), 4-0(1.8)	3-7(0.71),(4-8(1.5)) 5-4(0.83),(4-3(1.1))

The following figures are single example fits for each O_2 image corresponding to the dissociation wavelengths in the above table. Listed below each example fit are all the possible lower states based on the kinetic energy, denoted vibrational state (rotational state). The heavy black line is the signal intensity. The red dashed line is the sum of all individual simulated states. The thin, black, dashed lines are the individual simulated O_2 states.

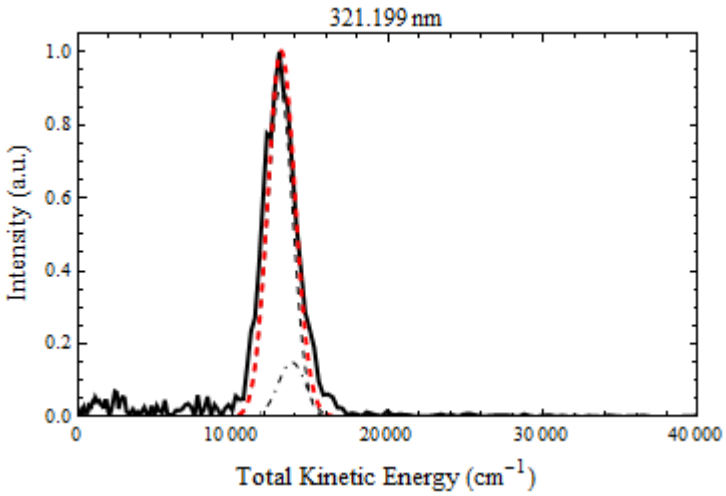

The given fit for dissociation at 321.199 nm is O_2 $X^3\Sigma_g^-$ 5(30), $a^1\Delta_g$ 0(34). The other possible lower states (v(j)) for the large peak are O_2 $X\ ^3\Sigma_g^-$ 5(39), 6(21) and $a^1\Delta_g$ 0(33), 1(12)

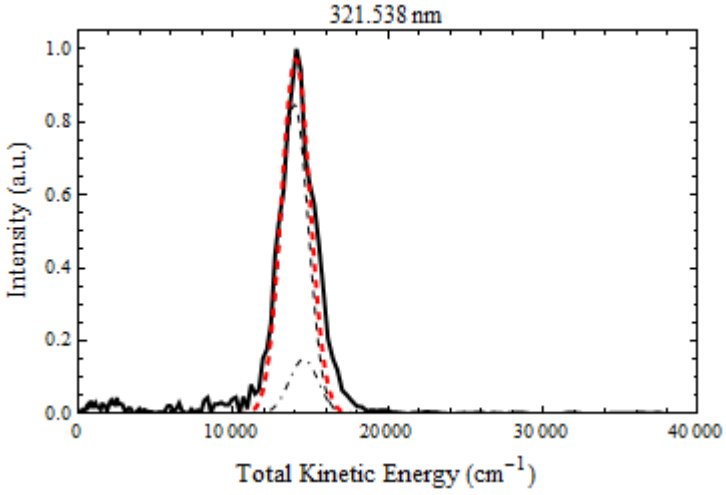

The given fit for dissociation at 321.538 nm is O_2 $X^3\Sigma_g^-$ 5(18), $a^1\Delta_g$ 0(22). The other possible lower states (v(j)) for the large peak are O_2 $X\ ^3\Sigma_g^-$ 4(40), 5(25) and $a^1\Delta_g$ 0(20)

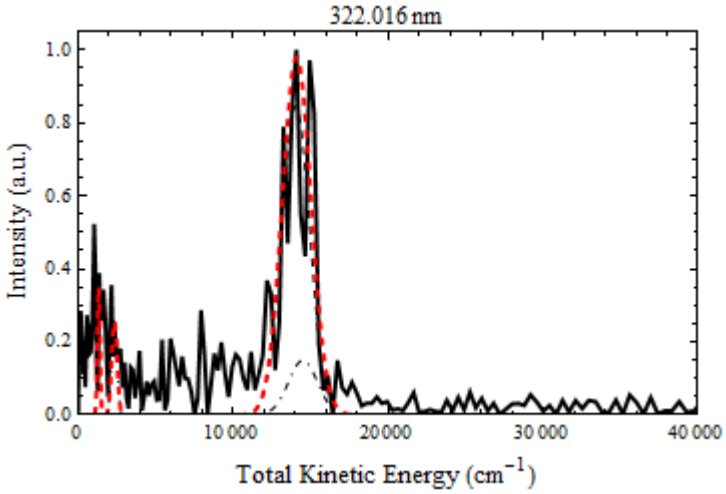

The given fit for dissociation at 322.016 nm is O_2 $X^3\Sigma_g^-$ 5(18) ($O(^3P)$ channel), 2(40) ($O(^1D)$ channel), $a^1\Delta_g$ 0(20), $b^1\Sigma_g^+$ 5(15). The other possible lower states (v(j)) are O_2 X $^3\Sigma_g^-$ 4(40), 5(23,25) and $a^1\Delta_g$ 0(20) for the largest peak and $O_2(a^1\Delta_g)$ 9(27), 8(40) and $O_2(b^1\Sigma_g^+)$ 4(35), 5(10), 6(5) for the smaller slow peak.

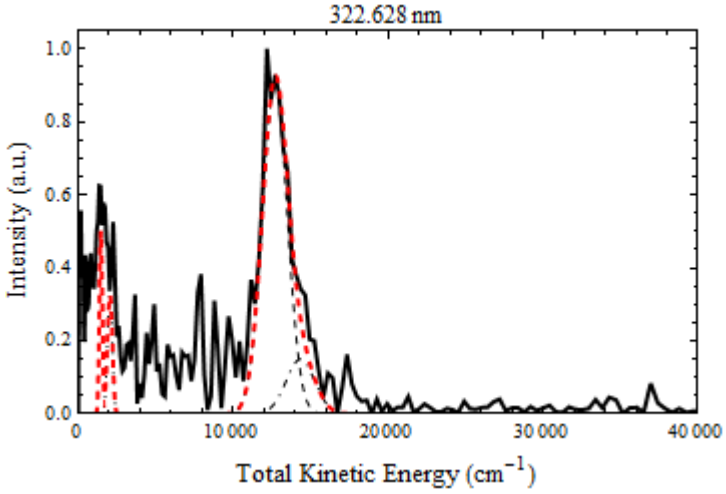

The given fit for dissociation at 322.628 nm is O_2 $X^3\Sigma_g^-$ 5(20) ($O(^3P)$ channel), 3(20) ($O(^1D)$ channel), $a^1\Delta_g$ 0(36), $b^1\Sigma_g^+$ 5(20). The other possible lower states (v(j)) are $O_2(X^3\Sigma_g^-)$ 5(40), 6(22), $O_2(a^1\Delta_g)$ 0(35), 1(15) for the large, fast peak. The slow peak can come from $O_2(b^1\Sigma_g^+)$ 4(40) 5(30) or $O_2(X^3\Sigma_g^-)$ v = 0-4 from the $O(^1D)$ channel.

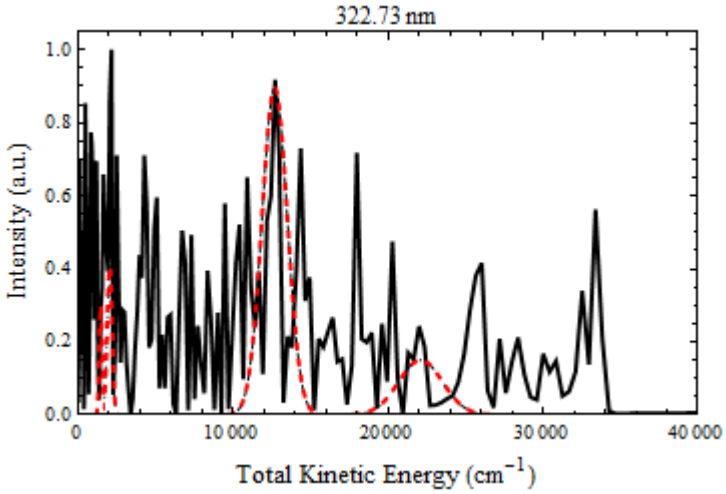

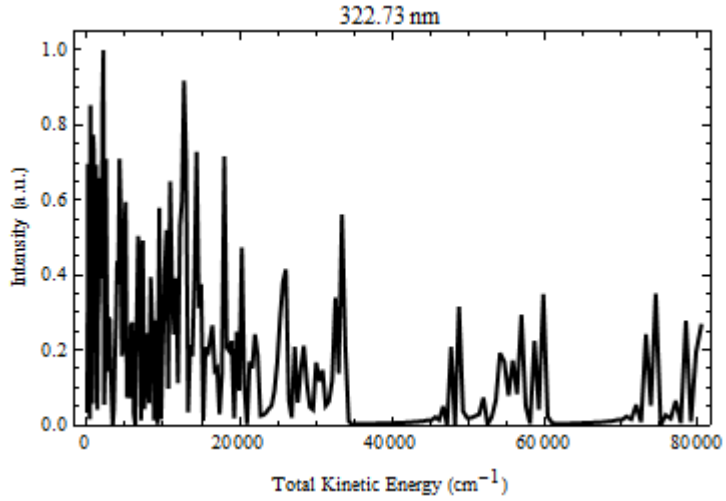

The given fit for dissociation at 322.730 nm is O_2 $X^3\Sigma_g^-$ 0(15) ($O(^3P)$ channel), 3(20) ($O(^1D)$ channel), $a^1\Delta_g$ 0(36), $b^1\Sigma_g^+$ 5(20). The other possible lower states (v(j)) are O_2 $X\ ^3\Sigma_g^-$ v = 1-5, $a^1\Delta_g$ v = 0-4 and $b^1\Sigma_g^+$ v = 0-5 based on the population data. The fastest red peak is $O_2(X^3\Sigma_g^-)$ 0(15), the higher energy signal must have another source.

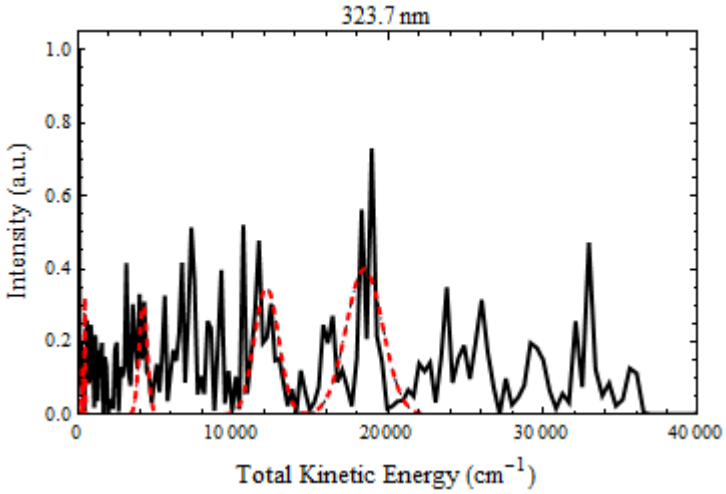

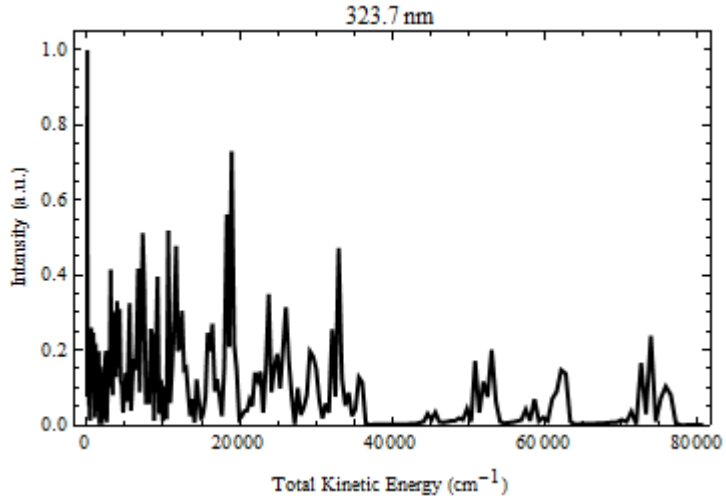

The given fit for dissociation at 323.7 nm is O_2 $X^3\Sigma_g^-$ 1(40) ($O(^3P)$ channel), 0(40) ($O(^1D)$ channel), $a^1\Delta_g$ 0(40), $b^1\Sigma_g^+$ 5(40). The other possible lower states (v(j)) are $O_2(X^3\Sigma_g^-)$ v = 1-7, $O_2(a^1\Delta_g)$ v = 0-3 and $O_2(b^1\Sigma_g^+)$ v = 0-4 based on the population data. The fastest red peak is $O_2(X^3\Sigma_g^-)$ 1(40), the higher velocity signal must have another source.

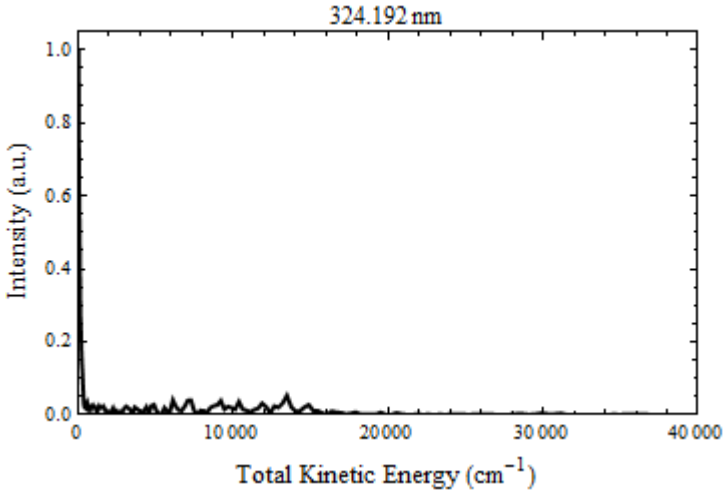

The main feature for the image at 324.192 nm is the center (zero velocity) peak. This makes other signal too small to analyze. This can originate from $O_2(X^3\Sigma_g^-)$ in the molecular beam or from $O_2(X^3\Sigma_g^-)$ v = 0-4 from the O(^{1}D) channel.

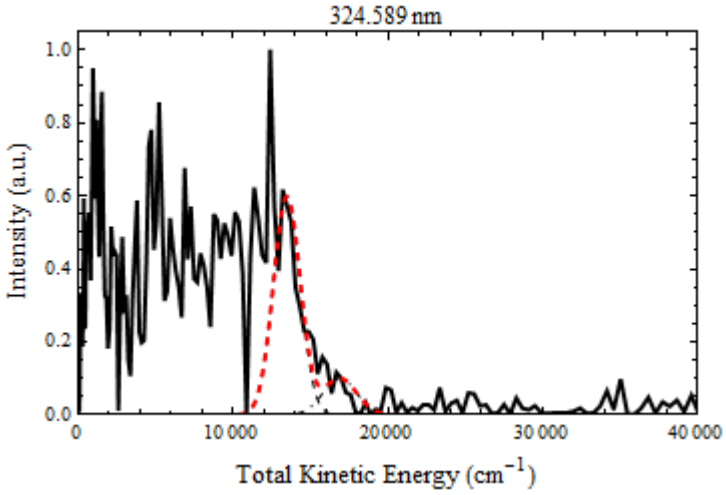

The given fit for dissociation at 324.589 nm is O_2 $X^3\Sigma_g^-$ 2(40) (O(^{3}P) channel), $a^1\Delta_g$ 0(25). The other possible lower states (v(j)) are $O_2(X^3\Sigma_g^-)$ 2(40) – v = 8, $O_2(a^1\Delta_g)$ 0(25) – v=6 and $O_2(b^1\Sigma_g^+)$ v = 0-3. The initial v(j) states are based on the above fit while rest of the vibrational states are from the population.

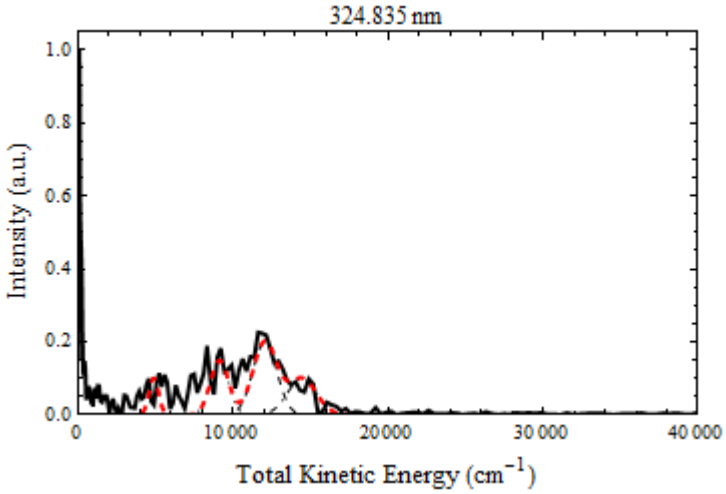

The given fit for dissociation at 324.835 nm is O_2 $X^3\Sigma_g^-$ 4(35) ($O(^3P)$ channel), 1(0) ($O(^1D)$ channel), $a^1\Delta_g$ 0(40), $b^1\Sigma_g^+$ 0(0). The other possible lower states (v(j)) are $O_2(X^3\Sigma_g^-)$ v = 0-4 and v = 4-8 (O(3P) channel), $O_2(a^1\Delta_g)$ v = 0-8 and $O_2(b^1\Sigma_g^+)$ v = 0-6. The highest v states (or O_2 in the beam) account for the 0 energy peak.

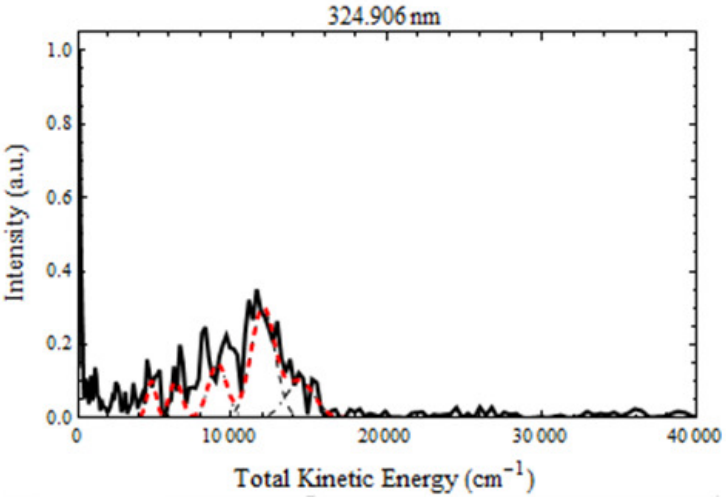

The given fit for dissociation at 324.906 nm is O_2 $X^3\Sigma_g^-$ 4(35) ($O(^3P)$ channel), 0(0) ($O(^1D)$ channel), $a^1\Delta_g$ 0(40), $b^1\Sigma_g^+$ 0(0). The other possible lower states (v(j)) are $O_2(X^3\Sigma_g^-)$ v = 0-4 and v = 4-8, $O_2(a^1\Delta_g)$ v = 0-8 and $O_2(b^1\Sigma_g^+)$ v = 0-5. The highest v states (or O_2 in the beam) account for the 0 energy peak.

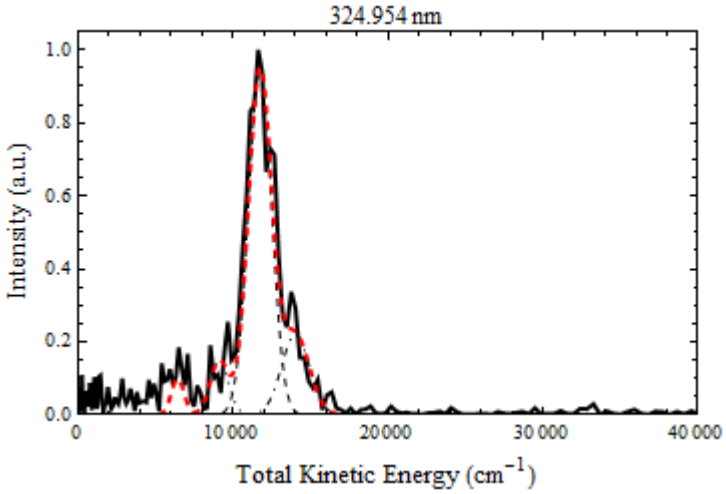

The given fit for dissociation at 324.954 nm is O_2 $X^3\Sigma_g^-$ 4(39) ($O(^3P)$ channel), 0(0) ($O(^1D)$ channel), $a^1\Delta_g$ 1(28), $b^1\Sigma_g^+$ 0(0). The other possible lower states (v(j)) are O_2 $X\ ^3\Sigma_g^-$ 6(33), 7(13) (smaller contributions from v = 4, 5, 8), $a^1\Delta_g$ 0(40), 1(28), 2(0) (smaller contributions from v = 3-5) and $b^1\Sigma_g^+$ v = 0-2 could contribute to the smaller peaks.

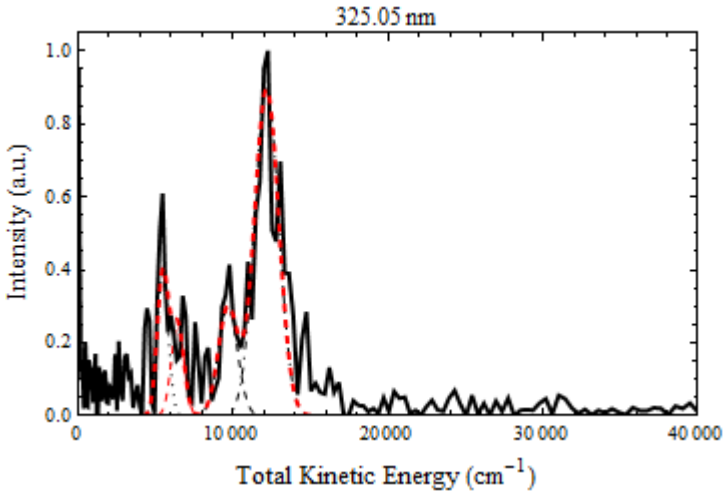

The given fit for dissociation at 325.05 nm is O_2 $X^3\Sigma_g^-$ 6(28) ($O(^3P)$ channel), 0(0) ($O(^1D)$ channel), $a^1\Delta_g$ 2(35), $b^1\Sigma_g^+$ 1(40). The other possible lower states (v(j)) are O_2 $X\ ^3\Sigma_g^-$ 5(40), 6(28) 8(22) (v=7 smaller contributions), 10(40) 11(20) and v = 0-4 (from the $O(^1D)$ channel) can account for the zero energy peak. $a^1\Delta_g$ 0(40), 1(20), 2(35), 3(0), 6(10) (v=5 minor contributions) and $b^1\Sigma_g^+$ 1(40), 2(22) also fit the two higher energy peaks.

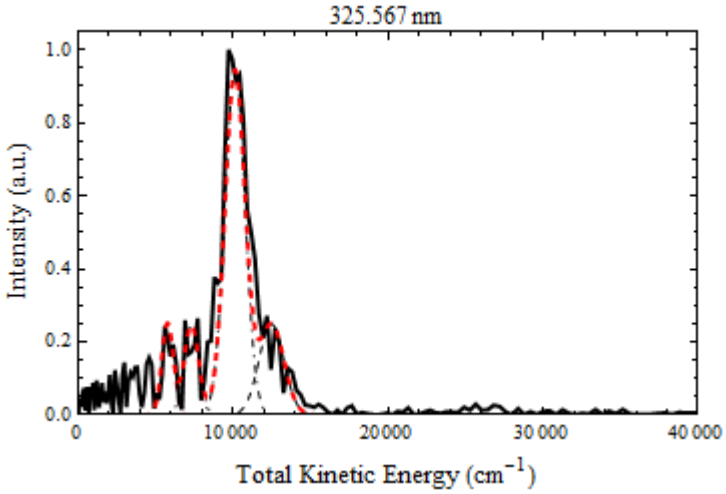

The given fit for dissociation at 325.567 nm is O_2 $X^3\Sigma_g^-$ 7(35) ($O(^3P)$ channel), 0(20) ($O(^1D)$ channel), $a^1\Delta_g$ 1(15), $b^1\Sigma_g^+$ 0(35). The other possible lower states (v(j)) are O_2 X $^3\Sigma_g^-$ 8(0), 7(35) (smaller contributions v = 5, 6, 9-12), $a^1\Delta_g$ 2(30), 3(0), (5(30), 6(30), v = 0 and 1 fit smaller peaks), $b^1\Sigma_g^+$ v = 0 – 2 can contribute to the smaller peaks.

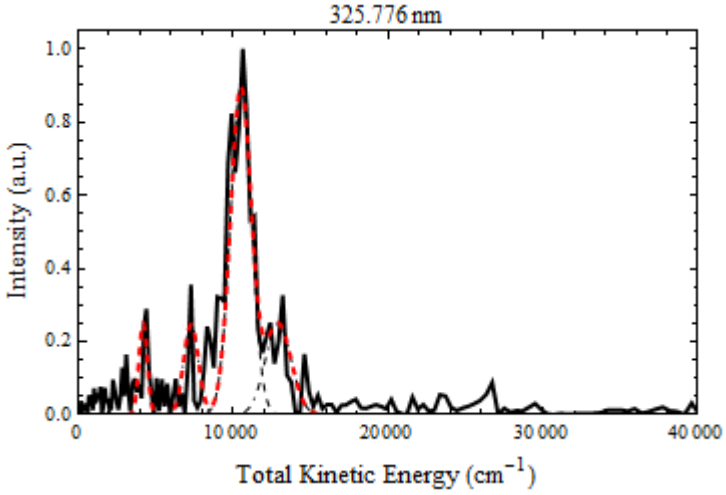

The given fit for dissociation at 325.776 nm is O_2 $X^3\Sigma_g^-$ 5(35) ($O(^3P)$ channel), 1(20) ($O(^1D)$ channel), $a^1\Delta_g$ 1(40), $b^1\Sigma_g^+$ 0(35). The other possible lower states (v(j)) are O_2 X $^3\Sigma_g^-$ 7(30), 8(0), $a^1\Delta_g$ 1(40), 2(25) for the main peak. $O_2(X\ ^3\Sigma_g^-)$ v = 5, 6, 9, $a^1\Delta_g$ v = 0, 3 and $b^1\Sigma_g^+$ v = 0 fit the minor peaks.

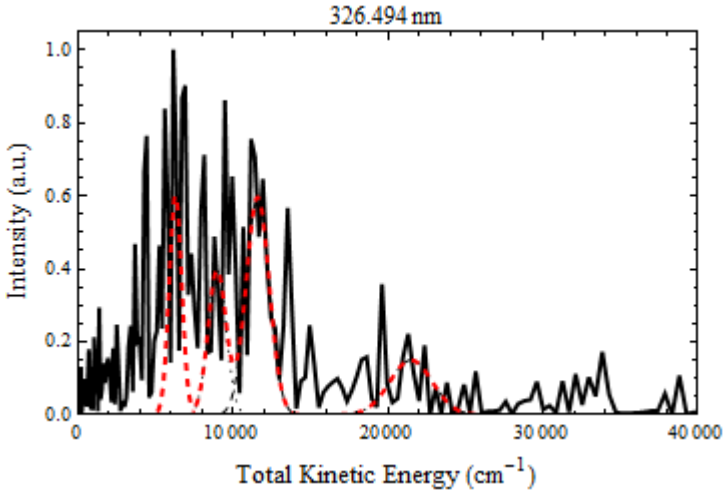

The given fit for dissociation at 326.494 nm is O_2 $X^3\Sigma_g^-$ 0(20) ($O(^3P)$ channel), 0(0) ($O(^1D)$ channel), $a^1\Delta_g$ 1(28), $b^1\Sigma_g^+$ 0(0). The other possible lower states (v(j)) are $O_2(X^3\Sigma_g^-)$ v = 5 - 9, $O_2(a^1\Delta_g)$ v = 1-7 and $O_2(b^1\Sigma_g^+)$ v = 0-5 for the main feature. The fastest red peak is $O_2(X^3\Sigma_g^-)$ 0(20) which could make a minor contribution.

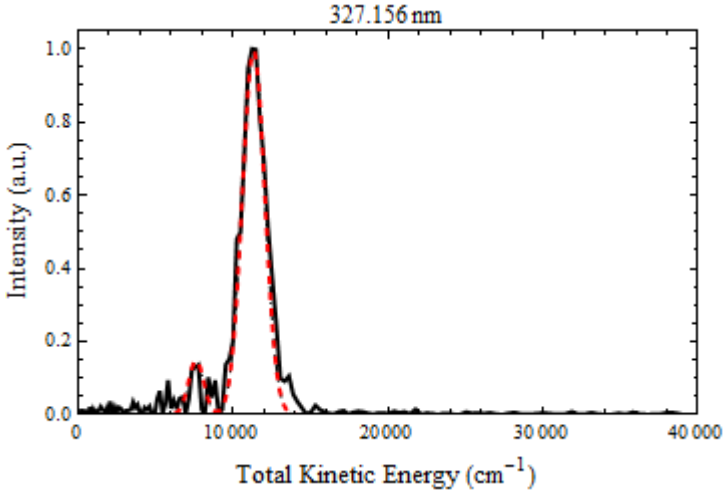

The given fit for dissociation at 327.156 nm is O_2 $X^3\Sigma_g^-$ 7(15) ($O(^3P)$ channel), $b^1\Sigma_g^+$ 0(30). The other possible lower states (v(j)) are O_2 X $^3\Sigma_g^-$ 6(35) and $a^1\Delta_g$) 1(30), 2(0) for the main peak. $O_2(b^1\Sigma_g^+)$ v = 0 and 1 could make small contributions.

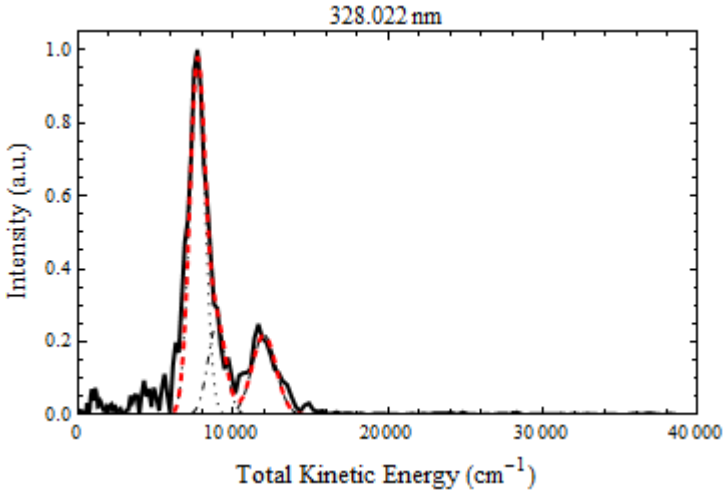

The given fit for dissociation at 328.022 nm is O_2 $X^3\Sigma_g^-$ 8(30) ($O(^3P)$ channel), $a^1\Delta_g$ 1(20), $b^1\Sigma_g^+$ 0(28). The other possible lower states (v(j)) are O_2 $X\ ^3\Sigma_g^-$ 8(40), $a^1\Delta_g$ 3(38), 4(20) and $b^1\Sigma_g^+$ 0(28) 1(0). The smaller peak could be O_2 $X\ ^3\Sigma_g^-$ 5(40), 6(25), 7(0) or $a^1\Delta_g$ 0(40), 1(20), 2(0).

The following table displays possible transitions from the three lower states of $O_2(X^3\Sigma_g^-)$, $O_2(a^1\Delta_g)$ and $O_2(b^1\Sigma_g^+)$ to the two upper states of O_2, $d\ ^1\Pi_g$ and $C\ ^3\Pi_g$ for the wavelengths with O_2 images only. These images do not have population data. All transitions within 2 nm of the calculated value, J= 0, were considered because of the broad spectra due to the perturbations and the lack of specific knowledge of the upper state particularly for high vibrational levels.

wavelength	Lower electronic state	$d\ ^1\Pi_g$ upper electronic state	$C\ ^3\Pi_g$ upper electronic state
340.525	$X^3\Sigma_g^-$ $a^1\Delta_g$ $b^1\Sigma_g^+$	None None 3-0 (-0.46)	None None None
340.087	$X^3\Sigma_g^-$ $a^1\Delta_g$ $b^1\Sigma_g^+$	3 - 9 (0.07) None 3-0(-0.02)	None 3-3(0.9), 2-2(1.1) None
340.196	$X^3\Sigma_g^-$ $a^1\Delta_g$ $b^1\Sigma_g^+$	3 - 9 (0.04) None 3-0(0.13)	None 3-3(1),2-2(1) None
339.695	$X^3\Sigma_g^-$ $a^1\Delta_g$ $b^1\Sigma_g^+$	3 - 9 (0.46) None 3-0(0.37)	None 3-3(0.5),2-2(1.5) None
339.309	$X^3\Sigma_g^-$ $a^1\Delta_g$ $b^1\Sigma_g^+$	3 - 9 (0.86) (2 -2 (1.9)) 3-0(0.76)	None 3-3(0.2), 2-2(1.9) None
338.781	$X^3\Sigma_g^-$ $a^1\Delta_g$ $b^1\Sigma_g^+$	(3 - 9 (1.4)) (2 -2 (1.4)) 3-0(1.3)	2-7(0.1) 4-4(1.9), 3-3(0.4) None
338.590	$X^3\Sigma_g^-$ $a^1\Delta_g$ $b^1\Sigma_g^+$	(1-6(1.1)) (1-1(1.1)),(2 -2 (1.2)) 3-0(1.5)	2-7(0.06) None None
337.734	$X^3\Sigma_g^-$ $a^1\Delta_g$ $b^1\Sigma_g^+$	(1-6(0.24)), 4-10(0.31) (1-1(2)), 2 -2 (0.31) 4-1(0.02)	2-7(0.9), 3-8(1.3), 5-11(1.3) 4-4(0.8) 5-2(1.9)
337.113	$X^3\Sigma_g^-$ $a^1\Delta_g$ $b^1\Sigma_g^+$	(1-6(0.38)), 4-10(0.31), 7-14(0.77) 2 -2 (0.31), (6 - 7 (1.5)) 4-1(0.6),5-2(1.75),7-5(0.8)	2-7(1.5), 3-8(0.7) 4-4(0.2)7-8(0.8) 7-4(1.7)
336.725	$X^3\Sigma_g^-$ $a^1\Delta_g$ $b^1\Sigma_g^+$	(1-6(0.77)), (2-7(1.8)), 4-10(0.7) 2 -2 (0.7), (6 - 7 (1.1)) 4-1(1), 5-2(1.4), 8-6(1.4)	2-7(1.9), 3-8(0.3), 0-4(1(D)) 4-4(0.5), 5-5(2), 8-9(0.8) 7-4(1.3)
336.403	$X^3\Sigma_g^-$ $a^1\Delta_g$ $b^1\Sigma_g^+$	(1-6(1.1)), (2-7(1.4)) 4-10(1) 5-11(1.7), 7-14(0.1) (2 -2 (1)), 6 - 7 (0.77), 5-6(1.7), 3-3(1.2) 4-1(1.3), 5-2(1)	3-8(0.001), 6-12 (0.1) 4-4(1.1), 5-5(1.7), 7-8(1.5) 6-3(1), 7-4(1)

wavelength	Lower electronic state	$d\ ^1\Pi_g$ upper electronic state	$C\ ^3\Pi_g$ upper electronic state
335.829	$X^3\Sigma_g^-$	(1-6(1.7)), 2-7(0.88) 4-10(1.6) 5-11(1.1)	3-8(0.6), 4-9(1.9),7-13 (1.7)
	$a^1\Delta_g$	(2 -2 (1.6)), 6 - 7 (0.19)	4-4(1.3), 5-5(1.1)
	$b^1\Sigma_g^+$	4-1(1.9), 5-2(0.5)	4-0(1.9)7-4(0.4)
335.657	$X^3\Sigma_g^-$	(1-6(1.8)), 2-7(0.7) 4-10 (1.8) 5-11(0.9)	3-8(0.7), 4-9 (1.7)
	$a^1\Delta_g$	(2 -2 (1.8))	4-4(1.9), 5-5(0.9)
	$b^1\Sigma_g^+$	5-2(0.3)	4-0(1.8)
334.986	$X^3\Sigma_g^-$	2-7(0.03) 5-11(0.25)	3-8(1.4), 4-9 (1)
	$a^1\Delta_g$	3-3(0.14)	5-5(0.2)
	$b^1\Sigma_g^+$	5-2(0.4)	None
334.753	$X^3\Sigma_g^-$	2-7(0.2) 5-11 (0.02)	3-8(1.7), 4-9(0.8)
	$a^1\Delta_g$	4-4(1.9), 3-3(0.4)	5-5(0.01)
	$b^1\Sigma_g^+$	5-2(0.6)	None
334.240	$X^3\Sigma_g^-$	None	None
	$a^1\Delta_g$	None	5-5(0.5), 6-6(1.6)
	$b^1\Sigma_g^+$	5-2(1.1)	None
333.992	$X^3\Sigma_g^-$		
	$a^1\Delta_g$	6-7(1.6), 4-4(1.1), 3-3(1.1)	2-1(1.1), 5-5(0.7), 6-6(1.4), 8-9(1.9)
	$b^1\Sigma_g^+$	5-2(1.4), 6-3(1)	4-0(0.1)
333.707	$X^3\Sigma_g^-$	3-8 (1.2) 5-11 (1) , 6-12 (1.6)	4-9(0.3)
	$a^1\Delta_g$	4-4(0.9), 3-3(1.4)	5-5(1), 6-6(1.1)
	$b^1\Sigma_g^+$	5-2(1.7) 6-3(0.7)	4-0(0.2)
332.873	$X^3\Sigma_g^-$	5-11(1.9), 6-12(0.79)	None
	$a^1\Delta_g$		5-5(1.9), 6-6(0.2)
	$b^1\Sigma_g^+$	6-3(0.15)	5-1(1)
327.827	$X^3\Sigma_g^-$	1-5(1.7), 2-6(0.6), 5-10(0.3)	3-7(0.9), 4-8(1.3), 6-11(1.5), 7-12(0.6)
	$a^1\Delta_g$	7-7(1.7), 6-6(0.5), 3-2(0.5), 2-1(1.5)	4-3(1.3), 5-4(0.6)
	$b^1\Sigma_g^+$	4-0(2), 5-1(0.03)	7-3(0.3)
331.758	$X^3\Sigma_g^-$		
	$a^1\Delta_g$		
	$b^1\Sigma_g^+$		
331.678	$X^3\Sigma_g^-$	0-4(0.14)	1-5(1.4), 2-6(0.9)
	$a^1\Delta_g$	1-0(0.3)	None
	$b^1\Sigma_g^+$	None	None
331.625	$X^3\Sigma_g^-$	0-4(0.2)	1-5(1.5), 2-6(0.9)
	$a^1\Delta_g$	1-0(0.2)	None
	$b^1\Sigma_g^+$	None	None
331.387	$X^3\Sigma_g^-$	0-4(0.4) 1-5(1.9)	1-5(1.7), 2-6(0.6)
	$a^1\Delta_g$	1-0(0.01)	2-1(1.5)
	$b^1\Sigma_g^+$	None	None

wavelength	Lower electronic state	$d\ ^1\Pi_g$ upper electronic state	$C\ ^3\Pi_g$ upper electronic state
330.986	$X^3\Sigma_g^-$ $a^1\Delta_g$ $b^1\Sigma_g^+$	0-4(0.8) 1-5(1.5) 1-0(0.4), 2-1(1.7) None	2-6(0.2) 2-1(1.9) None
330.876	$X^3\Sigma_g^-$ $a^1\Delta_g$ $b^1\Sigma_g^+$	0-4(0.9) 1-5(1.4) 1-0(0.5), 2-1(1.6) None	2-6(0.1) None None
330.744	$X^3\Sigma_g^-$ $a^1\Delta_g$ $b^1\Sigma_g^+$	0-4(1.1)1-5(1.2) 1-0(0.6), 2-1(1.4) None	2-6(0.001) None None
330.416	$X^3\Sigma_g^-$ $a^1\Delta_g$ $b^1\Sigma_g^+$	0-4(1.4)1-5(0.9) 1-0(1), 2-1 (1.1) None	2-6(0.3), 3-7(1.7) 3-2(0.7) None
330.236	$X^3\Sigma_g^-$ $a^1\Delta_g$ $b^1\Sigma_g^+$	0-4(1.6)1-5(0.7) 4-9(0.26) 1-0(1.1),2-1(0.9) 4-0(0.35)	2-6(0.5) 3-2(0.9), 4-3(1.1) None
329.950	$X^3\Sigma_g^-$ $a^1\Delta_g$ $b^1\Sigma_g^+$	0-4(1.8) 1-5(0.4) 4-9 (0.02) 1-0(1.4),2-1(0.6) 4-0(0.06)	2-6(0.8), 3-7(1.2), 5-10(1.7) 3-2(1.2), 4-3(0.8) 5-1(1.9)
329.908	$X^3\Sigma_g^-$ $a^1\Delta_g$ $b^1\Sigma_g^+$	0-4(1.9) 1-5 (0.4) 4-9 (0.07) 1-0(1.5),2-1(0.6) 4-0(0.02)	2-6(0.8), 3-7(1.2), 5-10(1.7) 3-2(1.2), 4-3(0.8) 5-1(2)
329.627	$X^3\Sigma_g^-$ $a^1\Delta_g$ $b^1\Sigma_g^+$	1-5 (0.1)4-9(0.35) 1-0(1.8),2-1(0.3) 4-0(0.26), 5-1(1.8)	2-6(1.1), 3-7(0.9), 5-10(2) 3-2(1.5), 4-3(0.5) None
329.498	$X^3\Sigma_g^-$ $a^1\Delta_g$ $b^1\Sigma_g^+$	1-5(0.01) 4-9 (0.48) 5-10 (2) 1-0(1.9), 2-1(0.2) 5-5(1.1) 4-0(0.?), 5-1(1.7)	2-6(1.2), 3-7(0.8), 6-11(0.2) 3-2(1.6), 4-3(0.4) 6-2(0.4)
329.317	$X^3\Sigma_g^-$ $a^1\Delta_g$ $b^1\Sigma_g^+$	1-5 (0.2) 4-9 (0.66) 5-10(1.8) 2-1(0.01), 5-5(1.3), 6-6(1) 4-0(0.57), 5-1(1.5)	2-6(1.4), 3-7(0.6), 6-11(0.01) 3-2(1.8), 4-3(0.2) 6-2(0.6)
329.048	$X^3\Sigma_g^-$ $a^1\Delta_g$ $b^1\Sigma_g^+$	1-5(0.5) 2-6(1.8) 4-9 (0.92) 5-10 (1.5) 2-1(0.3), 3-2(1.8), 5-5(1.5), 6-6(0.7) 4-0(0.84), 5-1(1.3)	2-6(1.7), 3-7(0.3), 6-11(0.3) 4-3(0.1), 5-4(1.9) 6-2(0.9)
328.685	$X^3\Sigma_g^-$ $a^1\Delta_g$ $b^1\Sigma_g^+$	1-5(0.8) 2-6(1.5) 4-9(1.3) 5-10(1.2) 2-1(0.6), 3-2(1.4), 5-5(1.9), 6-6(0.4) 4-0(1.2), 5-1(0.9)	3-7(0.05), 6-11(0.6), 7-12(1.5) 4-3(0.4), 5-4(1.5) 6-2(1.2), 7-3(0.5)
328.528	$X^3\Sigma_g^-$ $a^1\Delta_g$ $b^1\Sigma_g^+$	4-9(1.4) 5-10 (1) None 4-0(1.4), 5-1(0.7)	4-8(2) 4-3(0.6), 5-4(1.3) None

The following figures are for the O_2 images with no population data. Each dissociation wavelength image was converted to total kinetic energy, and is given (black solid line) with one possible fit (red dashed line). Following each figure the vibrational states whose energy fit the image data are listed corresponding to each electronic state. The three O_2 + $O(^3P)$ channels and the O_2 $X^3\Sigma_g^-$ +$O(^1D)$ channel are included.

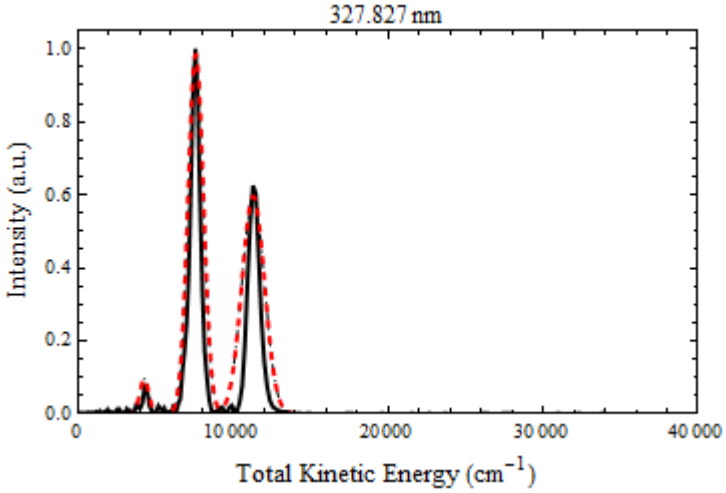

The given fit for dissociation at 327.827nm is O_2 $X^3\Sigma_g^-$ 7(14) ($O(^3P)$ channel), $a^1\Delta_g$ 3(39), $b^1\Sigma_g^+$ 2(36). Other possible O_2 vibrational states are $X^3\Sigma_g^-$ v = 5-12 ($O(^3P)$ channel) and 0,1 ($O(^1D)$ channel, small peak), $a^1\Delta_g$ v = 0 - 7 and $b^1\Sigma_g^+$ v = 0 – 3.

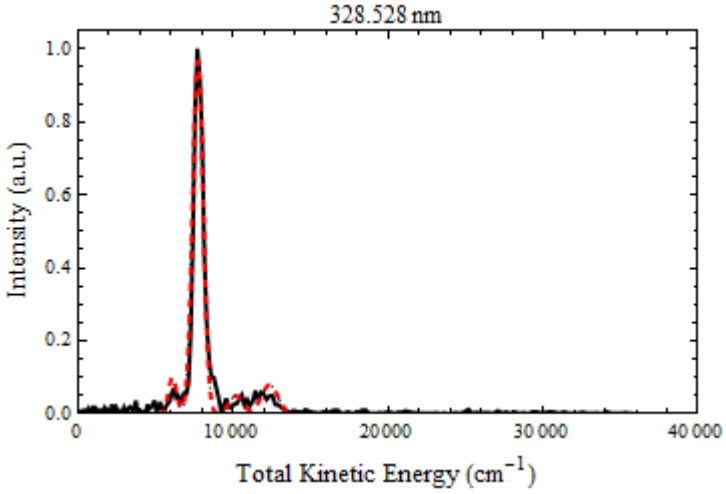

The given fit for dissociation at 328.528 nm is O_2 $X^3\Sigma_g^-$ 5(38) ($O(^3P)$ channel), 0(0) ($O(^1D)$ channel), $a^1\Delta_g$ 2(25), $b^1\Sigma_g^+$ 0(27). Other possible states that are O_2 $X^3\Sigma_g^-$ v = 8-10 (O(3P) channel), O_2 $a^1\Delta_g$ v = 3,4 and O_2 $b^1\Sigma_g^+$ v = 0,1.

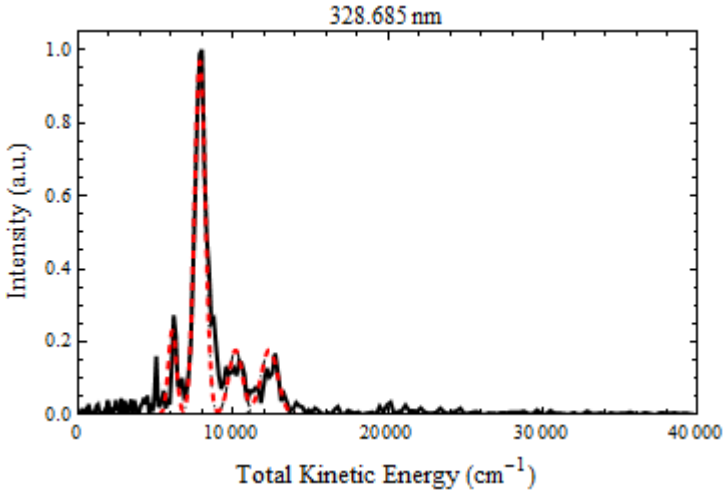

The given fit for dissociation at 328.685 nm is O_2 $X^3\Sigma_g^-$ 5(38) ($O(^3P)$ channel), 0(0) ($O(^1D)$ channel), $a^1\Delta_g$ 2(25), $b^1\Sigma_g^+$ 0(25). Other possible states that could fit are O_2 $X^3\Sigma_g^-$ v = 4-12 (O(3P) channel), v = 0, ($O(^1D)$ channel), O_2 $a^1\Delta_g$ v = 0-6 and O_2 $b^1\Sigma_g^+$ v = 0-3.

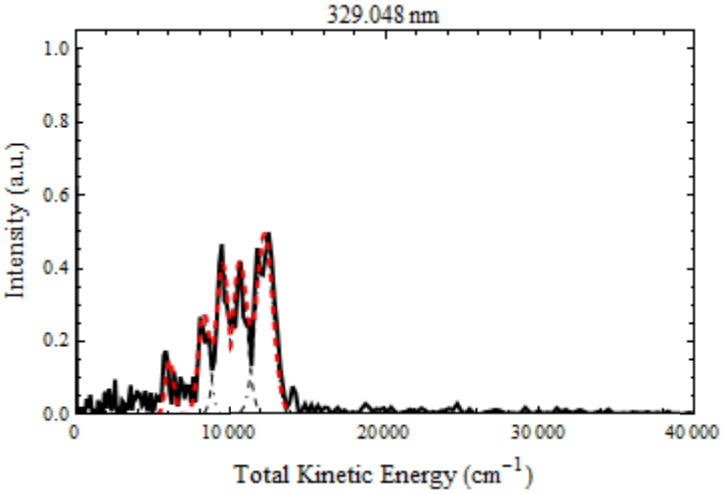

The given fit for dissociation at 329.048 nm is O_2 $X^3\Sigma_g^-$ 5(38) ($O(^3P)$ channel), 0(0) ($O(^1D)$ channel), $a^1\Delta_g$ 2(15), 2(33), $b^1\Sigma_g^+$ 0(18). Other possible states that could fit are O_2 $X^3\Sigma_g^-$ v = 5-11(some contribution from 4) ($O(^3P)$ channel), v = 0, ($O(^1D)$ channel), O_2 $a^1\Delta_g$ v = 0-5 (some possible contribution from 6) and O_2 $b^1\Sigma_g^+$ v = 0-2.

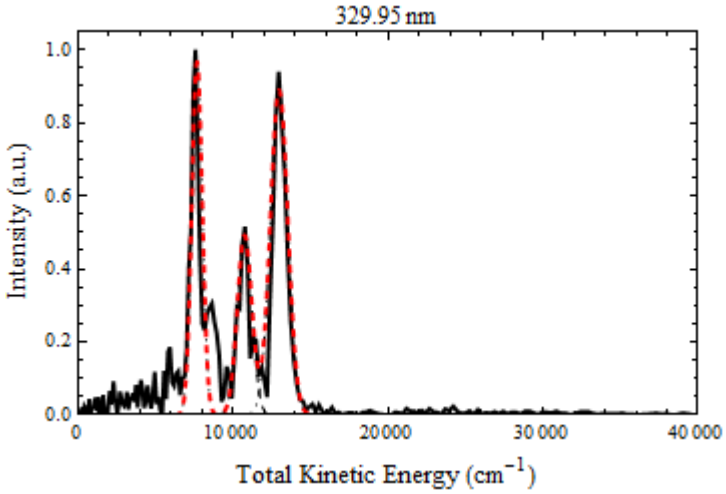

The given fit for dissociation at 329.950 nm is O_2 $X^3\Sigma_g^-$ 5(30), $a^1\Delta_g$ 1(34), $b^1\Sigma_g^+$ 0(26). Other possible states that could fit are O_2 $X^3\Sigma_g^-$ v = 5-10 (some possible contribution from 6) (O(3P) channel), O_2 $a^1\Delta_g$ v = 0-4 and O_2 $b^1\Sigma_g^+$ v = 0,1.

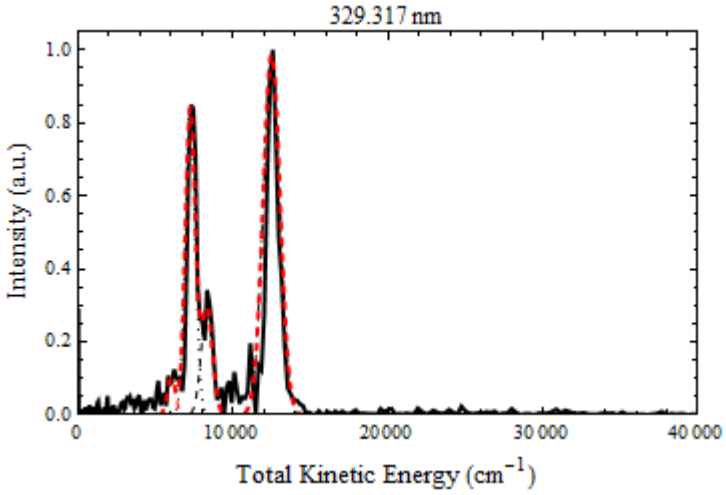

The given fit for dissociation at 329.317 nm is O_2 $X^3\Sigma_g^-$ 5(36) ($O(^3P)$ channel), 0(0) ($O(^1D)$ channel), $a^1\Delta_g$ 3(30), $b^1\Sigma_g^+$ 0(32). Other possible states that could fit are O_2 $X^3\Sigma_g^-$ v = 5-11(some contribution from 4) ($O(^3P)$ channel), v = 0, ($O(^1D)$ channel), O_2 $a^1\Delta_g$ v = 0-6 and O_2 $b^1\Sigma_g^+$ v = 0-2.

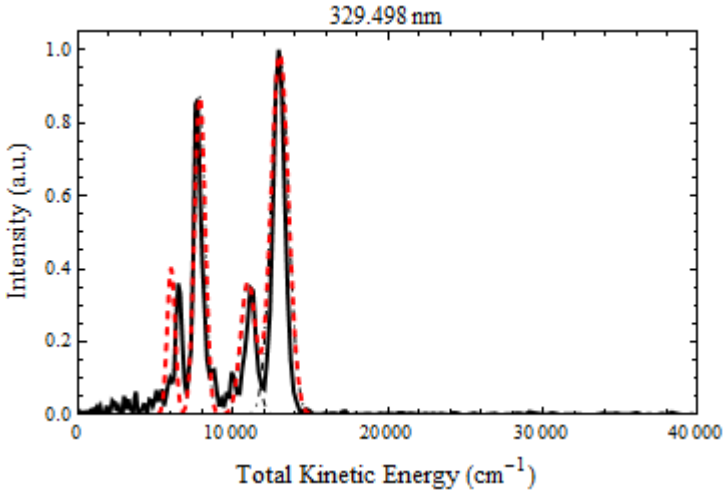

The given fit for dissociation at 329.498 nm is O_2 $X^3\Sigma_g^-$ 5(30) ($O(^3P)$ channel), 0(0) ($O(^1D)$channel), $a^1\Delta_g$ 1(32), $b^1\Sigma_g^+$ 0(24). Other possible states that could fit are O_2 $X^3\Sigma_g^-$ v = 4-10(some contribution from 11) ($O(^3P)$ channel), v = 0, ($O(^1D)$ channel), O_2 $a^1\Delta_g$ v = 0-5 and O_2 $b^1\Sigma_g^+$ v = 0, 1, and small contribution from 2.

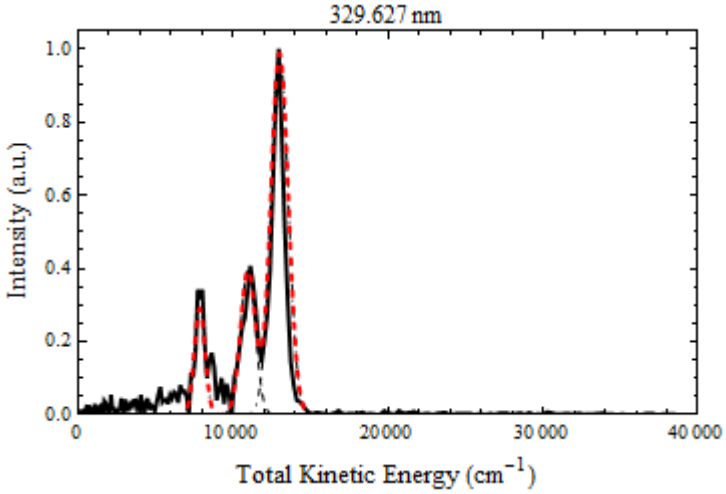

The given fit for dissociation at 329.627 nm is O_2 $X^3\Sigma_g^-$ 5(30), $a^1\Delta_g$ 1(32), $b^1\Sigma_g^+$ 0(24). Other states that could fit are O_2 $X^3\Sigma_g^-$ v = 5-9 (small contribution from 4, 10) (O(3P) channel), O_2 $a^1\Delta_g$ v = 0-4 and O_2 $b^1\Sigma_g^+$ v = 0, 1.

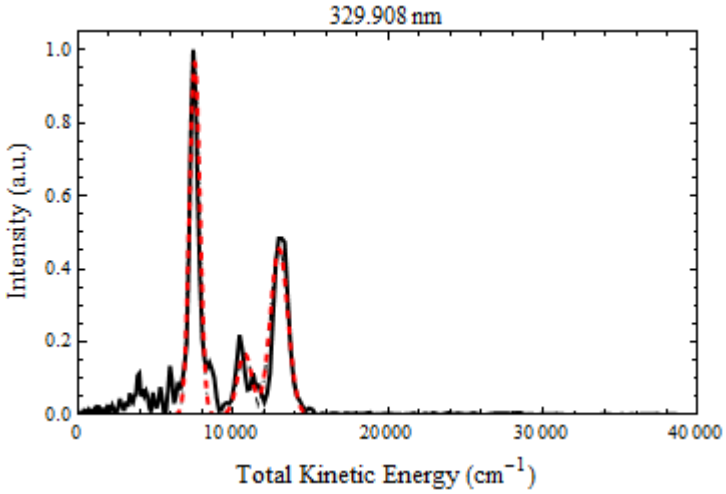

The given fit for dissociation at 329.908 nm is O_2 $X^3\Sigma_g^-$ 5(30), $a^1\Delta_g$ 1(34), $b^1\Sigma_g^+$ 0(28). Other possible states that could fit are O_2 $X^3\Sigma_g^-$ v = 4-10 ($O(^3P)$ channel), O_2 $a^1\Delta_g$ v = 0-4 and O_2 $b^1\Sigma_g^+$ v = 0, 1.

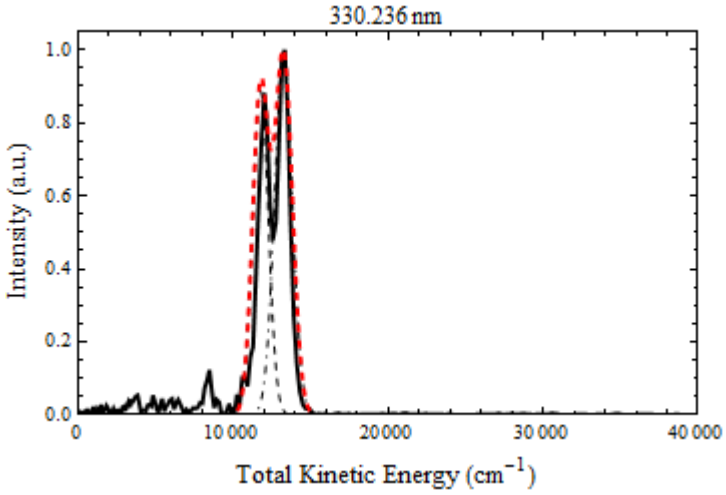

The given fit for dissociation at 330.236 nm is O_2 $X^3\Sigma_g^-$ 5(26), $a^1\Delta_g$ 0(38). Other possible states that could fit are O_2 $X^3\Sigma_g^-$ v = 4-9 (O(3P) channel), O_2 $a^1\Delta_g$ v = 0-4 and O_2 $b^1\Sigma_g^+$ v = 0.

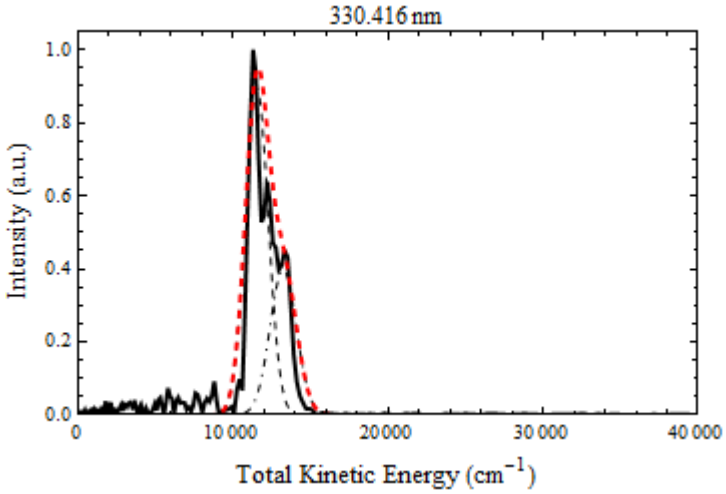

The given fit for dissociation at 330.416 nm is O_2 $X^3\Sigma_g^-$ 5(26), $a^1\Delta_g$ 0(40). Other possible states that could fit are O_2 $X^3\Sigma_g^-$ v = 5-7 (small contribution from 4) (O(3P) channel), O_2 $a^1\Delta_g$ v = 0, 1 (small contribution from 2).

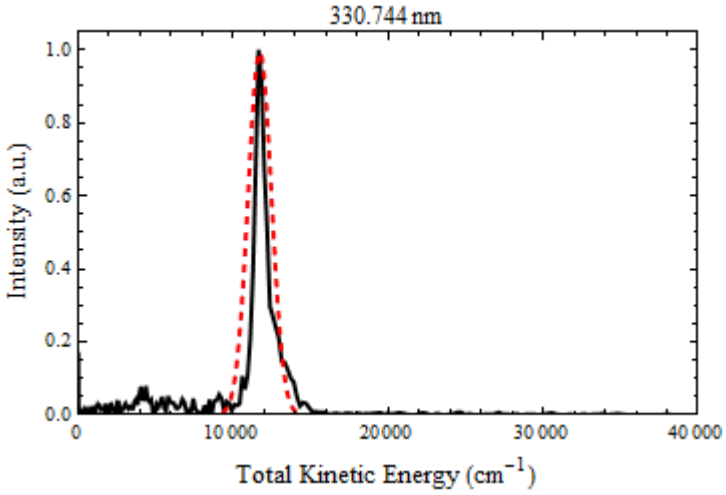

The given fit for dissociation at 330.744 nm is O_2 $a^1\Delta_g$ 0(38). Other possible states that could fit are O_2 $X^3\Sigma_g^-$ v = 5, 6 (small contribution from 4, 7) (O(3P) channel), O_2 $a^1\Delta_g$ v = 0, 1.

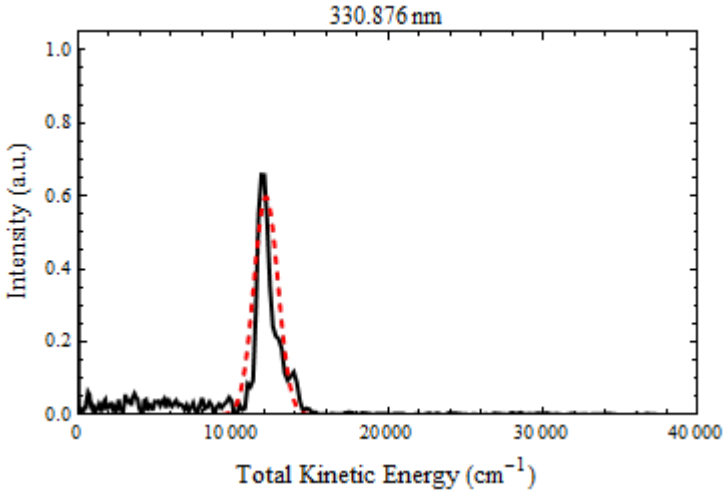

The given fit for dissociation at 330.876 nm is O_2 $a^1\Delta_g$ 0(34). Other possible states that could fit are O_2 $X^3\Sigma_g^-$ v = 5, 6 (small contribution from 4, 7) (O(3P) channel), O_2 $a^1\Delta_g$ v = 0, 1.

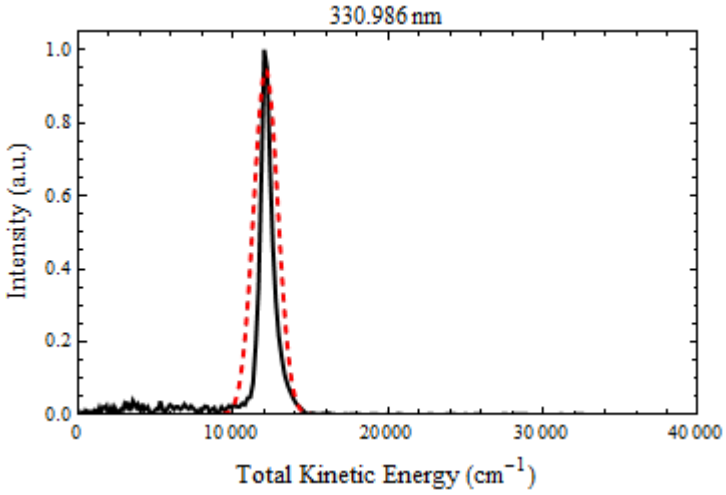

The given fit for dissociation at 330.986 nm is O_2 $a^1\Delta_g$ 0(34). Other possible states that could fit are O_2 $X^3\Sigma_g^-$ v = 5, 6 (small contribution from 4, 7) (O(3P) channel), O_2 $a^1\Delta_g$ v = 0, 1.

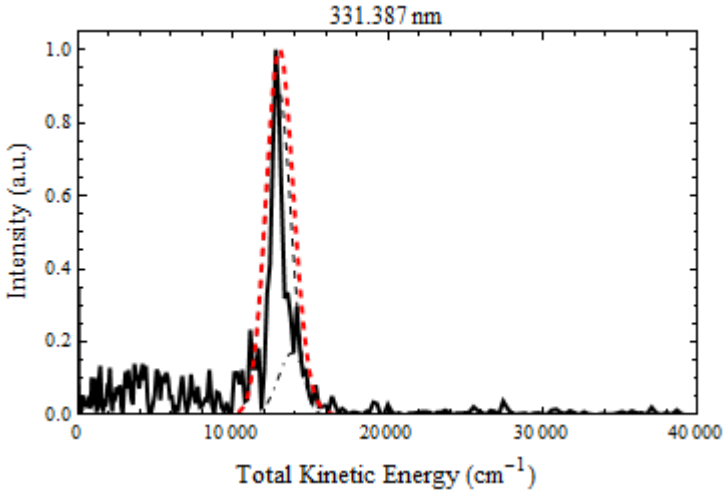

The given fit for dissociation at 331.387 nm is O_2 $X^3\Sigma_g^-$ 5(14) ($O(^3P)$ channel), $a^1\Delta_g$ 0(24). The other possible vibrational states that fit the main peak are O_2 $X^3\Sigma_g^-$ v = 4, 5 (small contribution from 3, 6) ($O(^3P)$ channel), O_2 $a^1\Delta_g$ v = 0 (small contribution from 1).

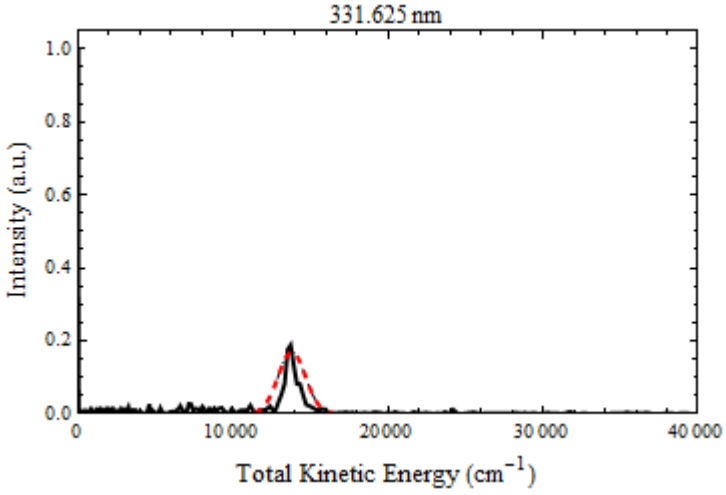

The given fit for dissociation at 331.625 nm is O_2 $X^3\Sigma_g^-$ 5(14) ($O(^3P)$ channel). The other possible vibrational states that fit the main peak are O_2 $X^3\Sigma_g^-$ v = 4, 5 (small contribution from 3, 6) ($O(^3P)$ channel), O_2 $a^1\Delta_g$ v = 0. There is also a zero velocity peak which can be O_2 in the beam or the highest vibrational levels from the dissociation.

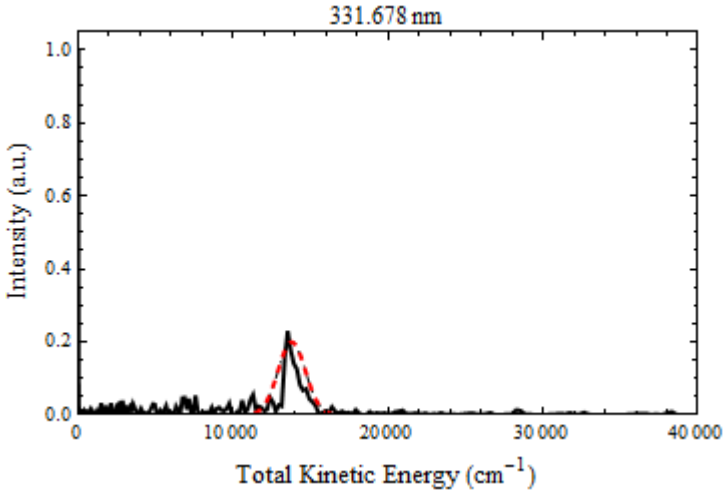

The given fit for the dissociation at 331.678 nm is O_2 $X^3\Sigma_g^-$ 5(14) ($O(^3P)$ channel). The other possible vibrational states that fit the main peak are O_2 $X^3\Sigma_g^-$ v = 4, 5 (small contribution from 3, 6) ($O(^3P)$ channel), O_2 $a^1\Delta_g$ v = 0. There is also a zero velocity peak which can be O_2 in the beam or the highest vibrational levels from the dissociation.

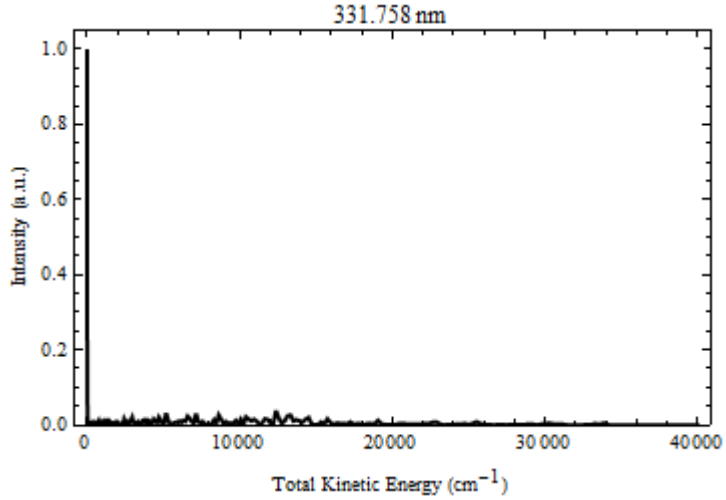

Ozone dissociation at 331.758 nm results in a large approximately zero velocity peak. It can be O_2 in the beam or O_2 from dissociation at the highest vibrational levels possible. $X^3\Sigma_g^-$ v ~ 15, 16 (or 0, 1 from $O(^1D)$ channel), $a^1\Delta_g$ v ~ 9, 10 and $b^1\Sigma_g^+$ v ~ 5, 6.

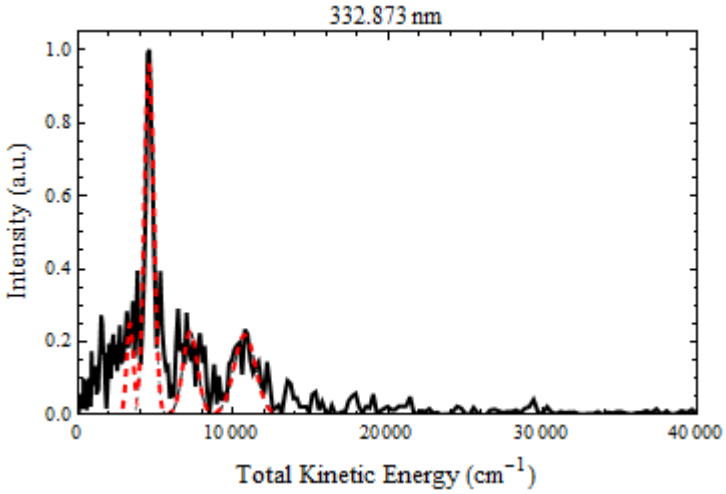

The given fit for dissociation at 332.873 nm is O_2 $X^3\Sigma_g^-$ 7(16), ($O(^3P)$ channel), 0(40)($O(^1D)$ channel), $a^1\Delta_g$ 3(38), $b^1\Sigma_g^+$ 2(27). The other possible vibrational states that fit are O_2 $X^3\Sigma_g^-$ v = 11, 12 (small contribution from 10) ($O(^3P)$ channel) or v = 0 ($O(^1D)$ channel), O_2 $a^1\Delta_g$ v = 5, 6 and $b^1\Sigma_g^+$ v = 1-3.

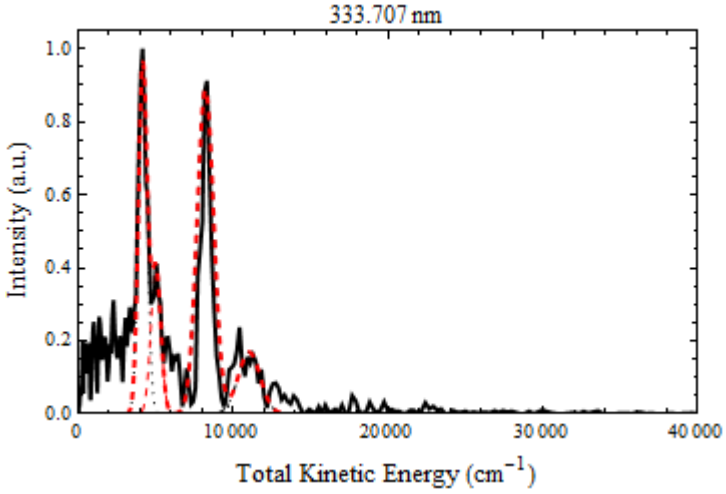

The given fit for dissociation at 333.707 nm is O_2 $X^3\Sigma_g^-$ 7(0), ($O(^3P)$ channel), 0(20) ($O(^1D)$ channel), $a^1\Delta_g$ 3(26), $b^1\Sigma_g^+$ 3(0). The other possible vibrational states that could fit are O_2 $X^3\Sigma_g^-$ v = 8, 9, 11, 12 (small contribution from 10) ($O(^3P)$ channel) or v = 0, 1 ($O(^1D)$ channel), O_2 $a^1\Delta_g$ v = 2, 3, 5, 6 (small contribution from 4) and $b^1\Sigma_g^+$ v = 0, 2, 3 (small contribution from 1).

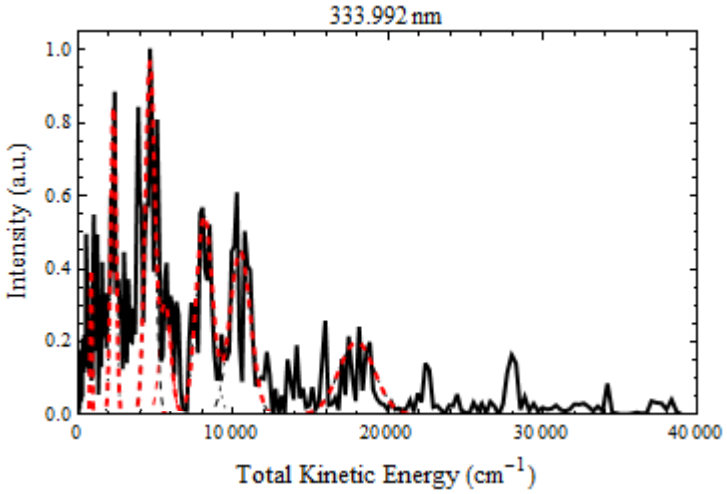

The given fit for dissociation at 333.992 nm is O_2 $X^3\Sigma_g^-$ 2(15), 7(20), ($O(^3P)$ channel), 0(0), 3(10), ($O(^1D)$ channel), $a^1\Delta_g$ 5(36), $b^1\Sigma_g^+$ 0(10), 4(20). Essentially all vibrational states for the $X^3\Sigma_g^-$, $a^1\Delta_g$ and $b^1\Sigma_g^+$ could give some contribution.

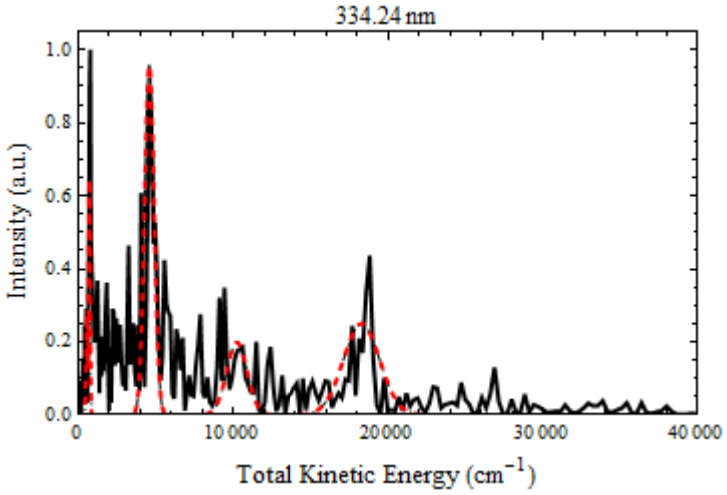

The given fit for dissociation at 334.240 nm is O_2 $X^3\Sigma_g^-$ 2(0), 6(40), ($O(^3P)$ channel), $a^1\Delta_g$ 5(36), $b^1\Sigma_g^+$ 4(40). The other possible vibrational states that could fit are O_2 $X^3\Sigma_g^-$ v = 0, 1 ($O(^3P)$ channel) or 0 ($O(^1D)$ channel), O_2 $a^1\Delta_g$ v = 5, 6 and $b^1\Sigma_g^+$ v = 1, 2. There can be smaller contributions from many other states.

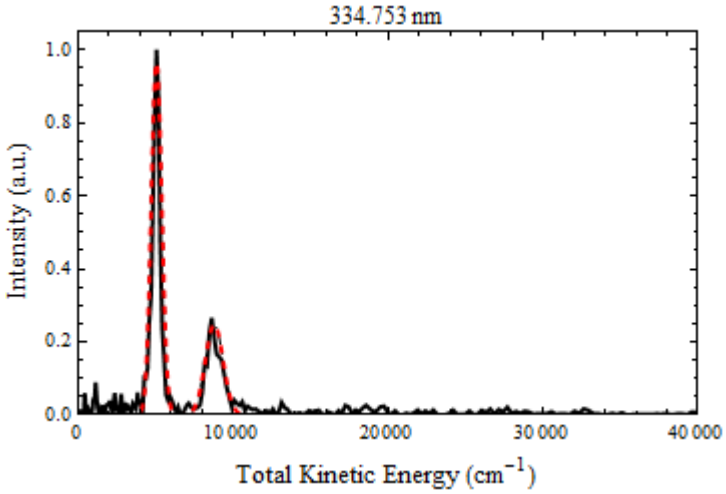

The given fit for dissociation at 334.753 nm is O_2 $X^3\Sigma_g^-$ 7(40), ($O(^3P)$ channel), $a^1\Delta_g$ 5(30). The other possible vibrational states that could fit are O_2 $X^3\Sigma_g^-$ v = 7, 8, (faster smaller peak) 10, 11 (larger, slower peak) ($O(^3P)$ channel) or v = 0 ($O(^1D)$ channel, large slow peak only), O_2 $a^1\Delta_g$ v = 2, 3,(small peak) 5, 6 (large peak) (small contribution from 4) and $b^1\Sigma_g^+$ v = 1, 2 (large peak only).

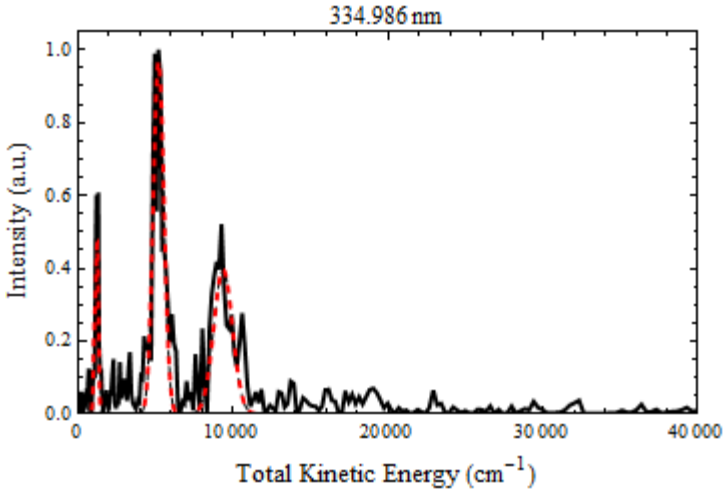

The given fit for dissociation at 334.986 nm is O_2 $X^3\Sigma_g^-$ 7(34), ($O(^3P)$ channel), $a^1\Delta_g$ 5(28), $b^1\Sigma_g^+$ 4(34). The other possible vibrational states that could fit are O_2 $X^3\Sigma_g^-$ v = 6, 7, 8, 10, 11 ($O(^3P)$ channel) or v = 0 (small contribution from 1) ($O(^1D)$ channel), O_2 $a^1\Delta_g$ v = 1-6 and $b^1\Sigma_g^+$ v = 1, 2.

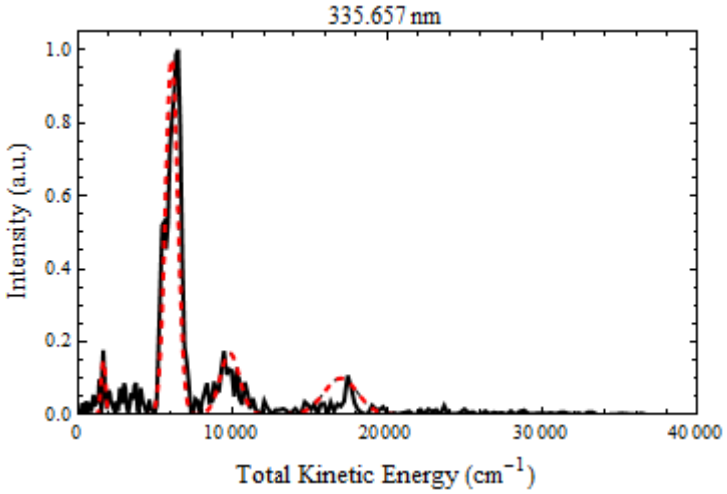

The given fit for dissociation at 335.657 nm is O_2 $X^3\Sigma_g^-$ 2(28), 7(28), ($O(^3P)$ channel), $a^1\Delta_g$ 5(11), $b^1\Sigma_g^+$ 4(28). The other possible vibrational states that could fit are O_2 $X^3\Sigma_g^-$ v = 1, 2, 6, 7, 8, 9, 10, 11 ($O(^3P)$ channel) or v = 0 ($O(^1D)$ channel), O_2 $a^1\Delta_g$ v = 1, 2, 4, 5 and $b^1\Sigma_g^+$ v = 0, 1, 2.

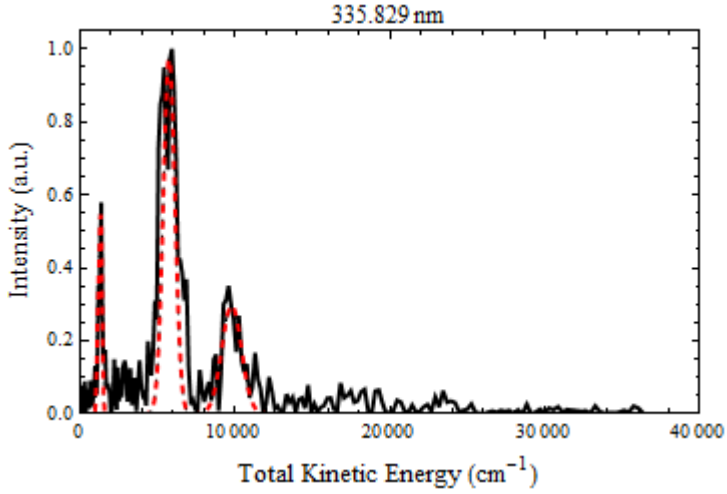

The given fit for dissociation at 335.829 nm is O_2 $X^3\Sigma_g^-$ 7(28), ($O(^3P)$ channel), $a^1\Delta_g$ 5(18), $b^1\Sigma_g^+$ 4(32). The other possible vibrational states that could fit are O_2 $X^3\Sigma_g^-$ v = 6, 7, 8, 9, 10, 11, 13 ($O(^3P)$ channel) or v = 0, 1, 2 ($O(^1D)$ channel), O_2 $a^1\Delta_g$ v = 1, 2, 4, 5, 7, 8 and $b^1\Sigma_g^+$ v = 0, 1, 2, 4, 5.

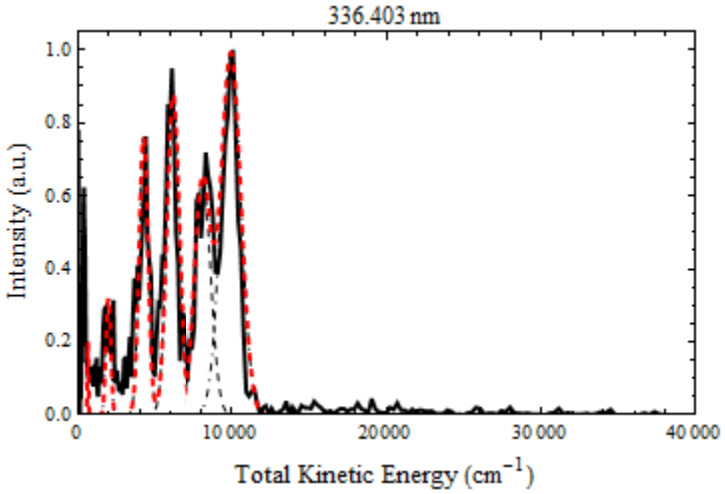

The given fit for dissociation at 336.403 nm is O_2 $X^3\Sigma_g^-$ 7(25), 11(30) ($O(^3P)$ channel), 3(10)($O(^1D)$channel), $a^1\Delta_g$ 3(24), 5(3), $b^1\Sigma_g^+$ 4(22). The other possible vibrational states that could fit are O_2 $X^3\Sigma_g^-$ v = 6 - 12, (smaller contributions from 13, 14) ($O(^3P)$ channel) or v = 0, 1, 2 ($O(^1D)$ channel), O_2 $a^1\Delta_g$ v = 1 - 6, (smaller contribution from 7, 8) and $b^1\Sigma_g^+$ v = 0 - 3, (smaller contribution from 4).

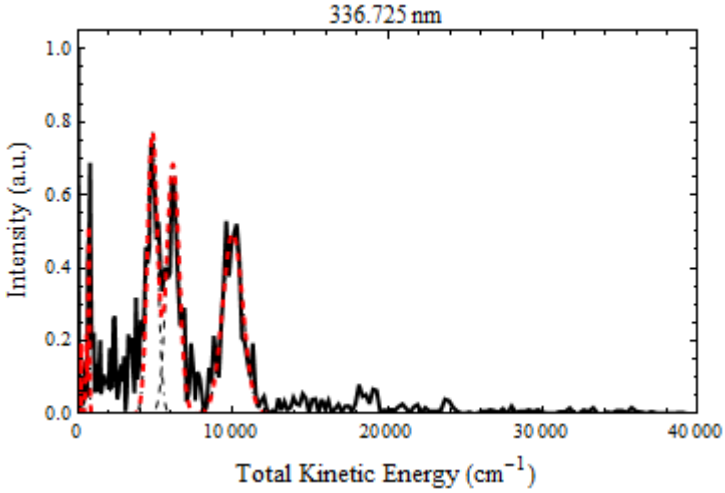

The given fit for dissociation at 336.725 nm is O_2 $X^3\Sigma_g^-$ 6(40), 10(38) ($O(^3P)$ channel), 3(20)($O(^1D)$channel), $a^1\Delta_g$ 5(0), $b^1\Sigma_g^+$ 5(22). The other possible vibrational states that could fit are O_2 $X^3\Sigma_g^-$ v = 6, 7, 8, 10, 13, 15 (small contribution possible from 9) ($O(^3P)$ channel) or v = 0, 2, 4 ($O(^1D)$ channel), O_2 $a^1\Delta_g$ v = 1, 2, 4, 5, 7, 9 and $b^1\Sigma_g^+$ v = 1, 2, 4, 6 (small contribution possible from 0).

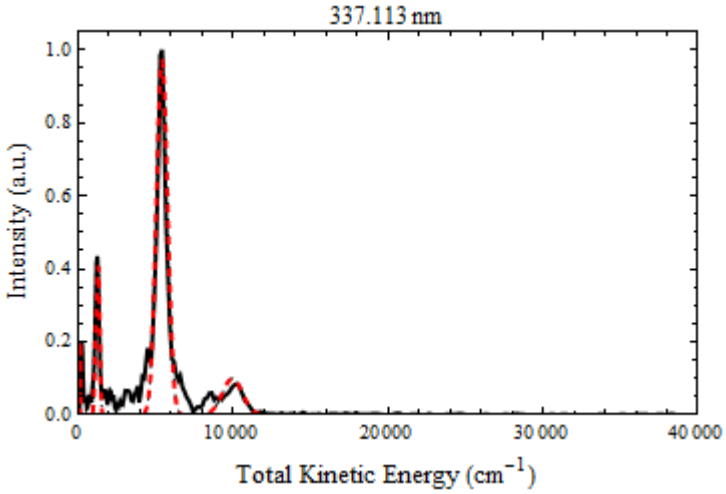

The given fit for dissociation at 337.113 nm is O_2 $X^3\Sigma_g^-$ 6(40)($O(^3P)$ channel), 3(20)($O(^1D)$ channel) $a^1\Delta_g$ 5(22), $b^1\Sigma_g^+$ 5(0). The other possible vibrational states that could fit are O_2 $X^3\Sigma_g^-$ v = 6, 7, 8, 10, 13, 14 (small contribution possible from 9) ($O(^3P)$ channel) or v = 0, 2, 3 ($O(^1D)$ channel), O_2 $a^1\Delta_g$ v = 1, 2, 4, 5, 7, 8 and $b^1\Sigma_g^+$ v = 1, 2, 4, 5 (small contribution possible from 0).

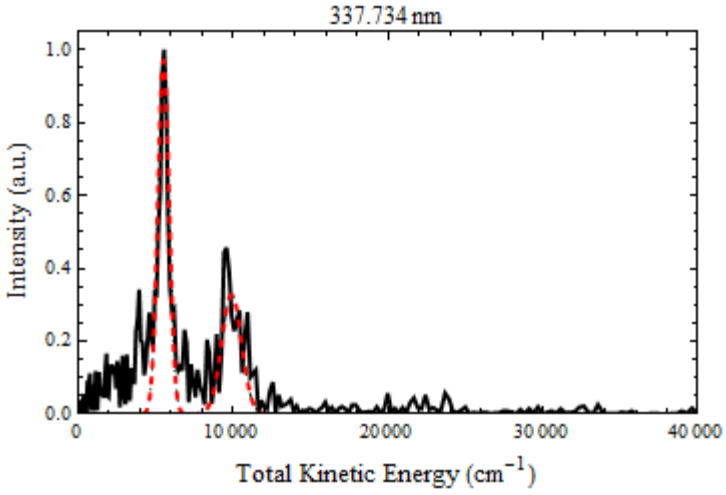

The given fit for dissociation at 337.734 nm is O_2 $X^3\Sigma_g^-$ 6(40), $b^1\Sigma_g^+$ 1(27). The other possible vibrational states that could fit are O_2 $X^3\Sigma_g^-$ v = 6, 7, 9, 10, 11 ($O(^3P)$ channel), O_2 $a^1\Delta_g$ v = 1, 2, 4, 5 and $b^1\Sigma_g^+$ v = 0, 1 (small contribution possible from 2).

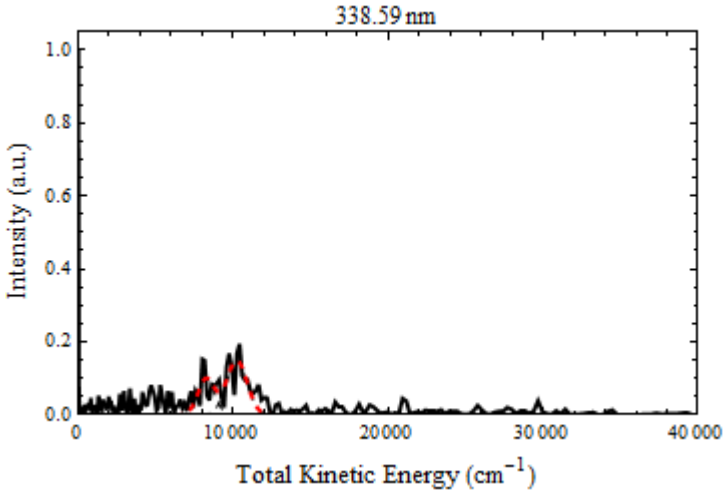

The given fit for dissociation at 338.590 nm is O_2 $X^3\Sigma_g^-$ 6(36), $a^1\Delta_g$ 3(18). The main feature is a large approximately 0 energy peak. It can be O_2 in the beam or O_2 from dissociation at the highest vibrational levels possible. $X^3\Sigma_g^-$ v ~15, 16 (or 0, 1 from O(^{1}D) channel), $a^1\Delta_g$ v ~ 8, 9 and $b^1\Sigma_g^+$ v ~5, 6. The faster broad peak(s) could be $X^3\Sigma_g^-$ v = 6, 7 (O(^{3}P) channel), $a^1\Delta_g$ v = 1, 2 and $b^1\Sigma_g^+$ v = 0(small contribution).

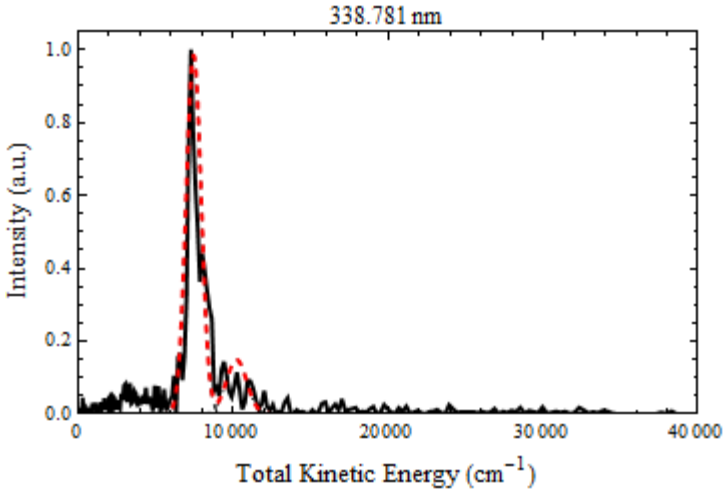

The given fit for dissociation at 338.781 nm is O_2 $X^3\Sigma_g^-$ 6(36), $a^1\Delta_g$ 3(30). The other possible vibrational states that could fit are O_2 $X^3\Sigma_g^-$ v = 8, 9 (possibly a small contribution from 7)(O(^{3}P) channel), O_2 $a^1\Delta_g$ v = 3, 4 (small contribution from 2) and $b^1\Sigma_g^+$ v = 0.

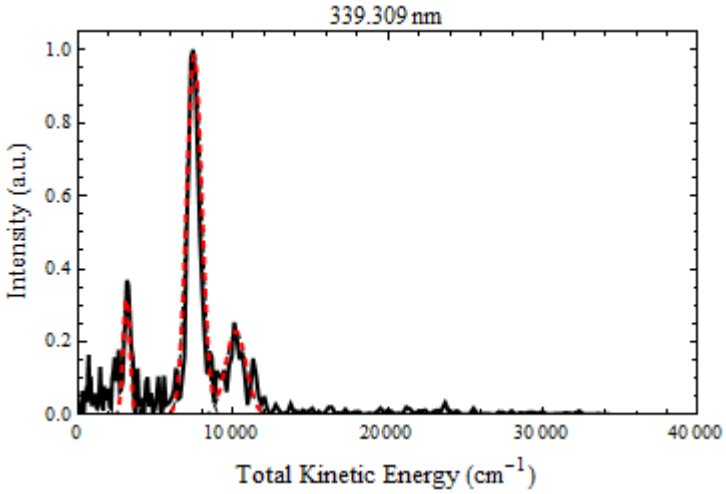

The given fit for dissociation at 339.309 nm is O_2 $X^3\Sigma_g^-$ 6(36), $a^1\Delta_g$ 3(29), $b^1\Sigma_g^+$ 3(20). The other possible vibrational states that could fit are O_2 $X^3\Sigma_g^-$ v = 8, 9 ($O(^3P)$ channel), O_2 $a^1\Delta_g$ v = 3, 4(small contribution from 2) and $b^1\Sigma_g^+$ v = 0.

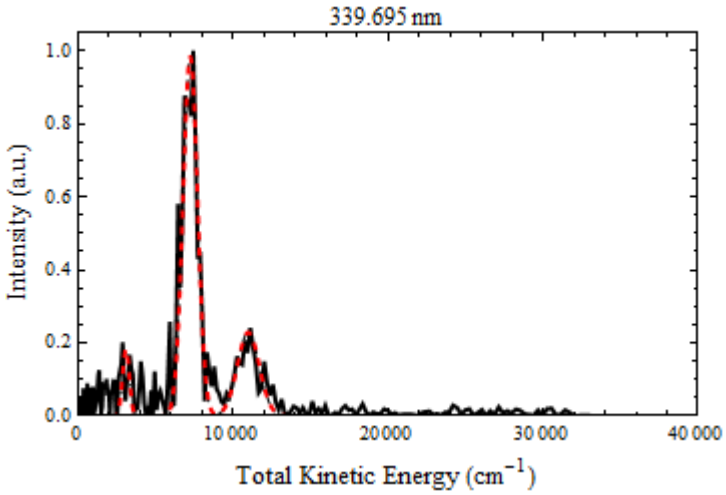

The given fit for the figure from dissociation at 339.695 nm is O_2 $X^3\Sigma_g^-$ 6(26), $a^1\Delta_g$ 4(0), $b^1\Sigma_g^+$ 3(20). The other possible vibrational states that could fit are O_2 $X^3\Sigma_g^-$ v = 8, 9 ($O(^3P)$ channel), O_2 $a^1\Delta_g$ v = 3, 4(small contribution from 2) and $b^1\Sigma_g^+$ v = 0.

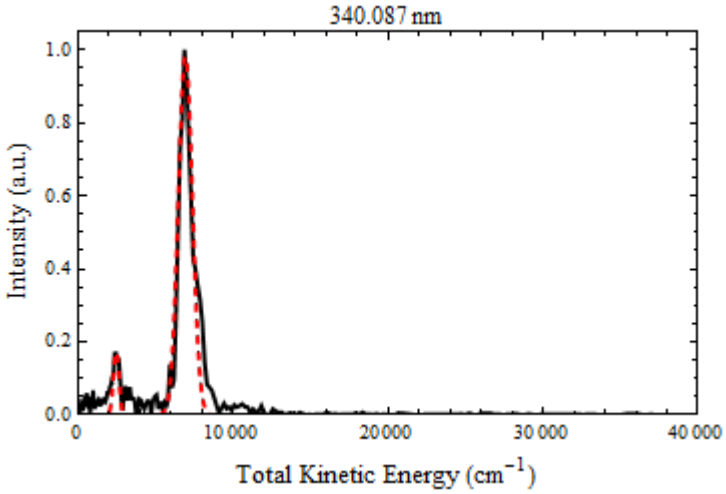

The given fit for the figure from dissociation at 340.087 nm is O_2 $a^1\Delta_g$ 4(14), $b^1\Sigma_g^+$ 3(29). The other possible vibrational states that could fit are O_2 $X^3\Sigma_g^-$ v = 8, 9 ($O(^3P)$ channel), O_2 $a^1\Delta_g$ v = 3, 4and $b^1\Sigma_g^+$ v = 0.

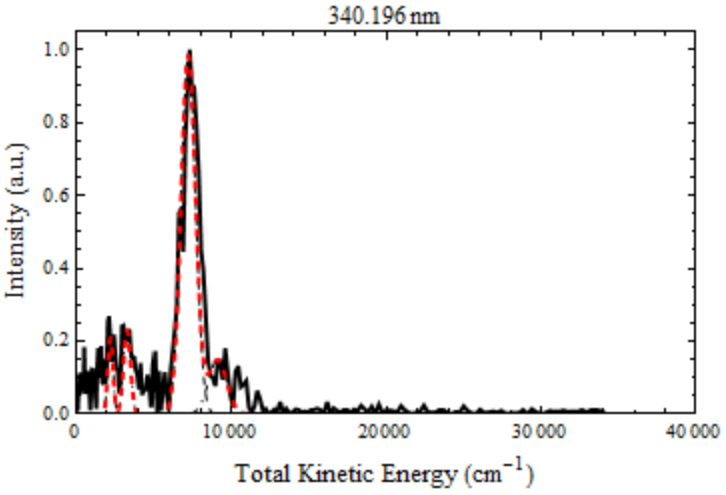

The given fit for the figure from dissociation at 340.196 nm is O_2 $X^3\Sigma_g^-$ 8(0), 13(15), $a^1\Delta_g$ 4(0), $b^1\Sigma_g^+$ 3(15). The other possible vibrational states that could fit are O_2 $X^3\Sigma_g^-$ v = 8, 9 ($O(^3P)$ channel), O_2 $a^1\Delta_g$ v = 3, 4(small contribution from 2) and $b^1\Sigma_g^+$ v = 0. There could be some smaller contributions from higher vibrational states making up the broad slow feature in the image.

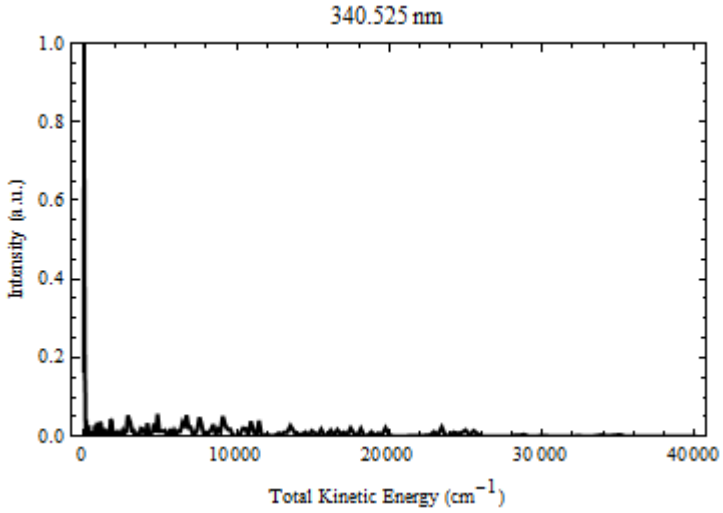

Ozone dissociation at 340.525 nm results in a large approximately 0 velocity peak. It can be O_2 in the beam or O_2 from dissociation at the highest vibrational levels possible. $X^3\Sigma_g^-$ v ~ 15, 16 (or 0, 1 from O(^{1}D) channel), $a^1\Delta_g$ v ~ 8, 9 and $b^1\Sigma_g^+$ v ~ 5, 6.

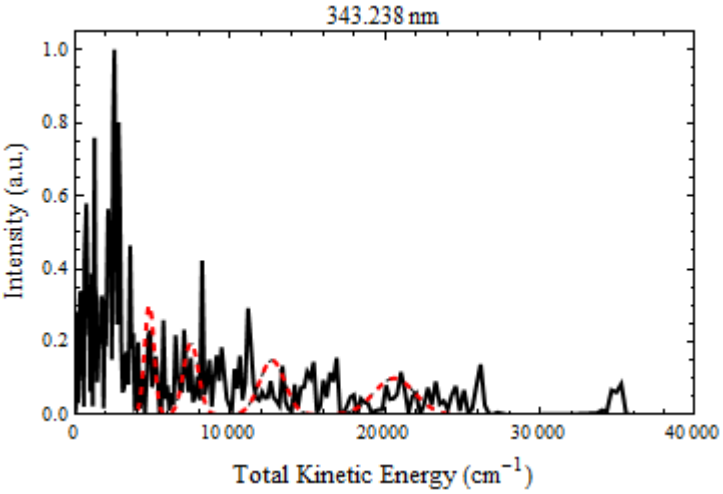

The 343.238 nm dissociation figure shows v = 0 for each electronic state. Any vibrational state can make a contribution. The biggest part of the figure can consist of $X^3\Sigma_g^-$ v > 9 (or 0, 1, 2 from O(^{1}D) channel), $a^1\Delta_g$ v > 5 and $b^1\Sigma_g^+$ v > 2.

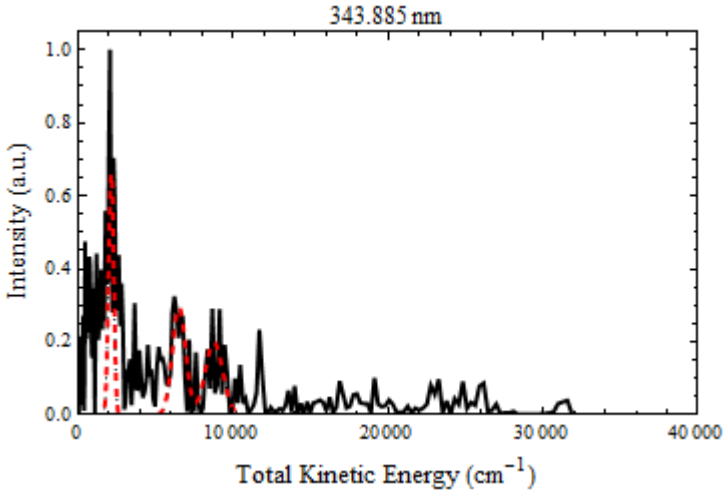

The given fit for the figure from dissociation at 343.885 nm is O_2 $X^3\Sigma_g^-$ 8(0), $a^1\Delta_g$ 4(16), $b^1\Sigma_g^+$ 3(29). Many other vibrational states are possible: O_2 $X^3\Sigma_g^-$ v = 8 - 14 ($O(^3P)$ channel) 0, 1 ($O(^1D)$ channel), O_2 $a^1\Delta_g$ v = 3 - 8 and $b^1\Sigma_g^+$ v = 0 - 4.